MOLECULAR BEAM INVESTIGATIONS OF OPEN-SHELL VAN DER WAALS MOLECULES

A thesis submitted for the degree of

Doctor of Philosophy

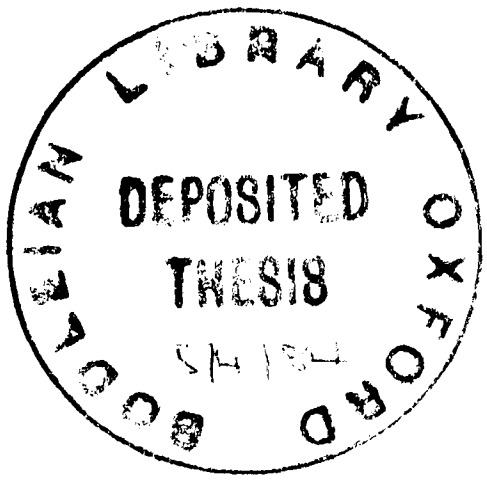
of the University of Oxford

by

Paul D. A. Mills

Brasenose College

Michaelmas Term 1983



MOLECULAR BEAM INVESTIGATIONS OF OPEN-SHELL VAN DER WAALS MOLECULES

A thesis submitted for the degree of

Doctor of Philosophy

of the University of Oxford

by

Paul D. A. Mills

Brasenose College Michaelmas Term 1983

Van der Waals molecules are complexes of two or more atoms or molecules bound by weak intermolecular forces rather than a conventional chemical bond. This thesis contains a high resolution molecular beam study of the rotational spectra of two such species, ArNO and NeNO.

A new hamiltonian is presented to account for the spectra of these open-shell complexes. The theory is similar to that already known for the uncomplexed diatom, nitric oxide, but is modified to an asymmetric top form appropriate for these non-linear species. Two novel interactions require inclusion. The first models a slight quenching of the NO orbital angular momentum by the rare gas atoms. The second is a large centrifugal distortion associated with the effects of the bending motion on the projection of the electronic angular momentum on the complex's a-inertial axis.

A comparatively rich, though incomplete, spectrum is obtained for ArNO. Most of the transitions that originate from the lower rotational states are assigned and fitted to within a few MHz using the modified open-shell hamiltonian. Possible sources are suggested for the origins of the small residual errors between the observed and calculated transition frequencies. A vibrationally-averaged structure is derived from the fitted molecular parameters indicating an equilibrium geometry which is quite close to a T-shape. The hyperfine structure in the spectrum which is associated with the ^{14}N nucleus is well fitted by the hamiltonian; however, the magnetic hyperfine parameters are significantly perturbed from the values that best fit the lambda-doubling spectrum of the uncomplexed diatom. The implications of this with respect to the nature of the rare gas-nitric oxide intermolecular interaction are discussed.

Greater experimental difficulties are encountered in trying to record the radiofrequency and microwave spectrum of NeNO and so fewer transitions have been measured than for ArNO. A partial analysis yields approximate values for the structural parameters. The complex exhibits a larger deviation from the T-shaped geometry than is observed for ArNO. The spectrum also provides an estimate of the magnitude of the quenching of the orbital angular momentum. The quenching interaction is somewhat larger in the neon complex.

To My Darling,

Chris

Acknowledgments

It is a great pleasure to be able to acknowledge here my gratitude for the assistance, advice and good company of many friends from Oxford and further afield. It is entirely appropriate that I should thank first my supervisor, Dr. Brian Howard. Not only has Brian provided a seemingly limitless supply of ideas and enthusiasm, but he has also given freely and patiently of his time to explain or clarify new pieces of science for me. Within the molecular beams group itself I have benefited greatly from conversations with, and practical help from, all the other members of the group. I should particularly like to thank Dr. Colin Western, Paul Bartlett and Adrian Hough for assistance with the experiments, the legacy of some elegant pieces of software and for many useful and stimulating conversations. My thanks are also due to the Workshop, Electronics, Technical Drawing and Administrative staff of the P.C.L.

A further debt of gratitude is owed to Mark Thomas for enormous help and stalwart support during the production of this thesis. Thanks to Mark I am now an avid disciple of "Wordstar". I have also enjoyed immensely the friendship and company of many other members of the Hulme, Junior and Senior Common Rooms of The King's Hall and College of Brasenose.

Not for the first time I am able to acknowledge my gratitude to my parents for their continuing help and support throughout seven happy years in Oxford. Finally I should like to express my thanks to Chris for her help with many of the diagrams and for putting up with me whilst I was writing and producing this thesis.

Paul Mills

CONTENTS

CHAPTER 1 : A Survey of the Structure and Properties of Van Der Waals Molecules

CHAPTER 2 : The Molecular Beam Electric Resonance Spectrometer

CHAPTER 3 : A Theory for the Rotational Energy Levels of Rare Gas - Nitric Oxide Complexes

CHAPTER 4 : ArNO - An Open-Shell Van Der Waals Molecule

CHAPTER 5 : The Rotational Spectrum and Analysis of NeNO

APPENDICES

Chapter 1 : A Survey of the Structure and Properties of van der Waals Molecules

1.1 Introduction to van der Waals Molecules - Their Importance in Physical Chemistry

1.2 The Classification and Range of Weakly Bound Complexes

1.3 Experimental Methods

1.3 a) Rotational Spectroscopy

1.3 b) Vibrational Spectroscopy

1.3 c) Electronic Spectroscopy

1.3 d) Miscellaneous Methods

1.4 Theoretical Aspects of van der Waals Molecules - The Intermolecular Potential

1.4 a) Ab Initio and Semi-Empirical Approaches

1.4 b) The Electron Gas Model

1.4c)Intermolecular Potential Energy Surfaces from Experimental Data

1.5 The Nature of the van der Waals Interaction

1.5 a) Stereospecificity in van der Waals Molecules - Incipient Chemical Bonding ?

1.5 b)The Extent of Charge Transfer in a van der Waals Bond

1.1 Introduction to van der Waals Molecules - Their Importance in Physical Chemistry

Van der Waals molecules are complexes of two or more atoms or molecules for which the binding energy has its origins in the weak intermolecular force rather than a conventional chemical bond. As a consequence these binding energies are generally quite small and of the order of 1 kJ/mole . In a bulk gas a small concentration of van der Waals molecules exists in equilibrium with their uncomplexed counterparts. For example gaseous argon or hydrogen near their respective boiling points contain about 1% of the species Ar_2 or $(H_2)_2$.

As a result of the small binding energy, these weakly bound complexes are unstable with respect to molecular collisions. Their lifetime when studied under equilibrium conditions is therefore governed by the collision number and hence by the ambient pressure. This dependence is reflected in the spectroscopic linewidths observed for these species. A typical infrared linewidth is 0.3 cm-1 for a bulk pressure of one atmosphere at 300 K. This corresponds to an average lifetime of 10^{-10}s before collisional dissociation. The structure, properties and spectroscopy of van der Waals molecules have been the subject of several reviews some of the more recent being by Ewing, Le Roy and Howard.[1-5]

The main motivation for the study of weakly bound complexes concerns the nature of the intermolecular potential acting between their constituent atoms or molecules. The traditional sources for this information have included measurements of viscosity,[6] second virial coefficients,[7] pressure broadening of rotational linewidths[8] and rotational energy transfer.[9] For the

first two only an effective isotropic average from an anisotropic potential is obtained. This problem has been elegantly tackled in the work of McCourt where transport properties have been measured in electric and magnetic fields.[10] For the rotational processes the anisotropy is clearly critical but the inversion of experimental data is difficult. In fact it has not always proved straightforward to derive an effective isotropic potential which models bulk gas properties of an anisotropic system although Smith and Tindell have recently made progress in this field.[11]

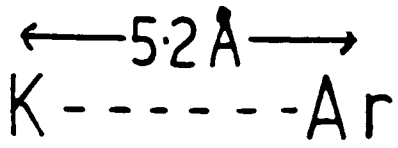
Thus it is largely in the derivation of realistic anisotropic potentials that the analysis of the structure and spectra of van der Waals molecules has become so valuable. There are also, however, a number of other physical phenomena for which the study of these complexes has proved illuminating. These include the evaluation of termolecular reaction mechanisms in the gas phase,[12] the kinetics and mechanism of nucleation[13,14] and solvation and many aspects of rotational energy transfer processes.[15]

1.2 The Classification and Range of van der Waals Species

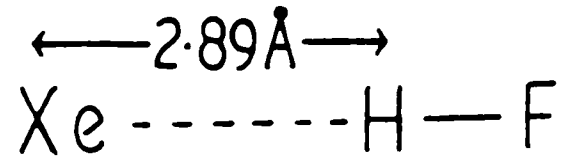
Under favourable conditions almost any pair of atoms or molecules may coalesce to form a van der Waals molecule. An exception to this was reported by Tanaka and Yoshino[16] who claimed that the $X\ ^1\Sigma_g^+$ state formed from two ground state helium atoms supported no bound states. New calculations by Swalley seem to contradict this claim indicating that He_2 does contain a single, but very weakly bound, state. Thus there exist a diversity of complexes ranging from the simplest atom-atom systems to those involving two or more molecules. Although the best studied van der Waals molecules involve an atom bound to a small molecule, some workers have studies solvation and other effects in the gas phase using complexes containing large polycyclic aromatic systems.[17,18] In Figure 1.1 is presented a selection of van der Waals species chosen to illustrate the diversity of types. Also indicated are their experimentally determined or likely equilibrium structures.

In principle complexes may contain more than two constituents and the dividing line between, for example, a van der Waals complex of several rare gas atoms and a cluster is an arbitrary one. Levy[20] and others[19] have recorded the electronic spectra of aromatic systems and I_2 to which are bound varying numbers of rare gas atoms. The feasibility of obtaining the rotational spectra of the van der Waals trimers Ar_2NO and $Ar(NO)_2$ is evident in Chapter 4 of this thesis. It is clear, however, that the analysis of the dynamics of the spectra of such complexes will be exceedingly complicated.

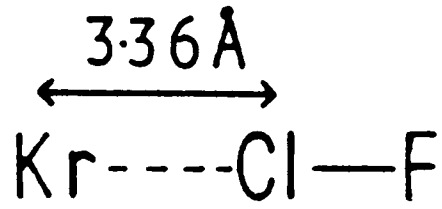
For atom-atom van der Waals complexes the intermolecular interaction is purely a function of intermolecular distance. The



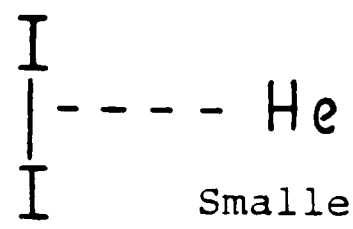
Freeman et al.
J.C.P. 64,1194,(1976)



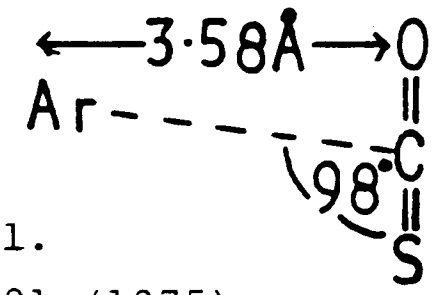
Baiocchi et al.
J.C.P. 75,2041,(1981)



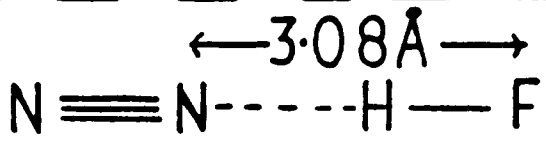
Novick et al.
Can.J.Phys. 53,2007,(1975)



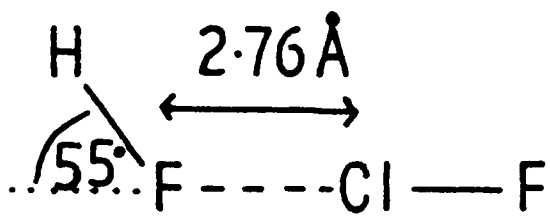
Smalley et al.
J.C.P. 68,671,(1978)



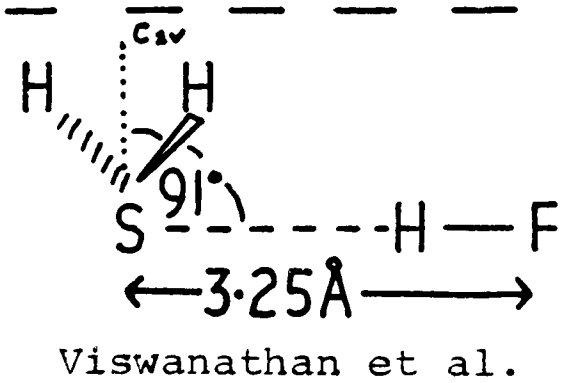
Harris et al.
J.C.P. 63,881,(1975)



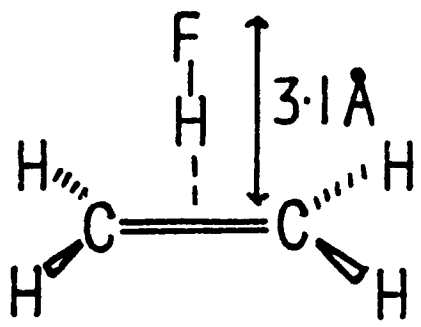
Soper et al.
J.C.P. 76,292,(1982)



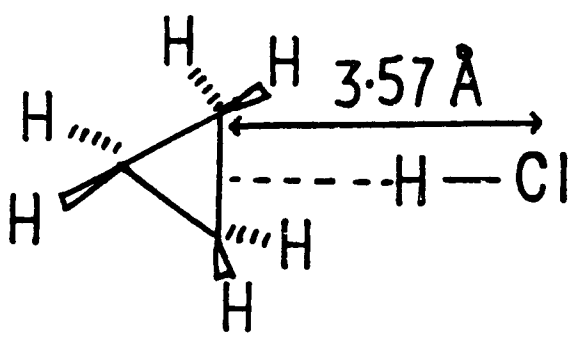
Novick et al.
J.C.P. 65,5115,(1977)



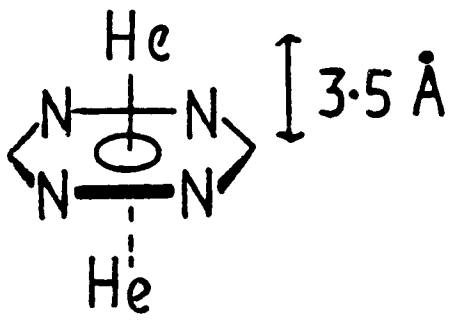
Viswanathan et al.
J.C.P. 77,1166,(1982)



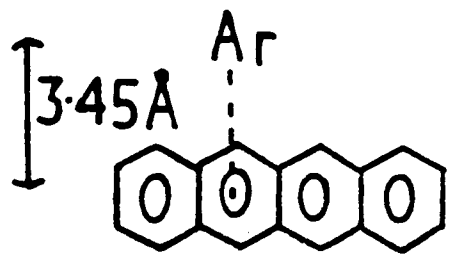
Shea et al.
J.C.P. 76,4857,(1982)



Legon et al.
J.A.C.S. 104,1486,(1982)

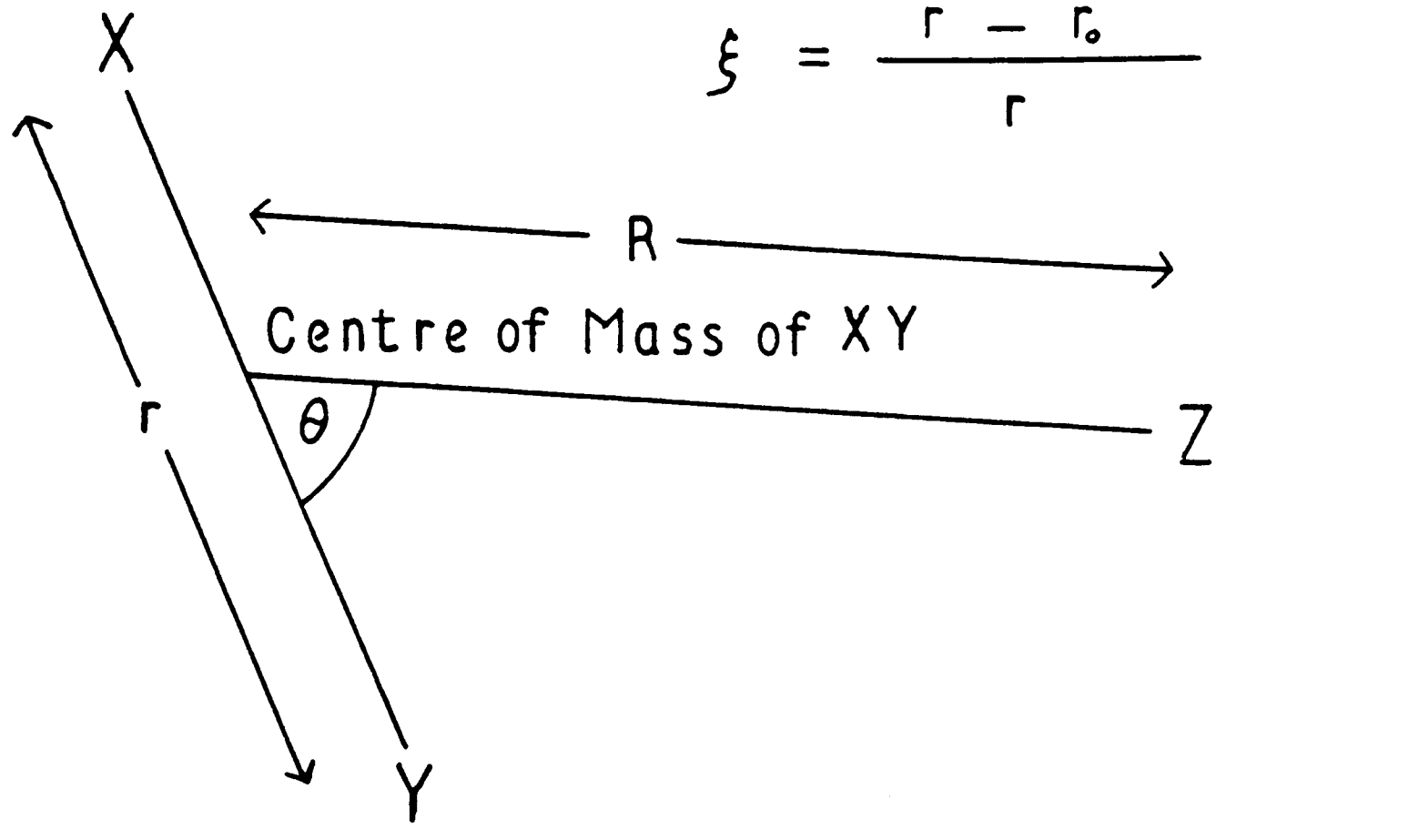


Smalley et al.
J.C.P. 68,2487,(1978)



Even et al.
Far. Disc. 73,(1982)

Figure 1.1: The Equilibrium Structures of some van der Waals Molecules.



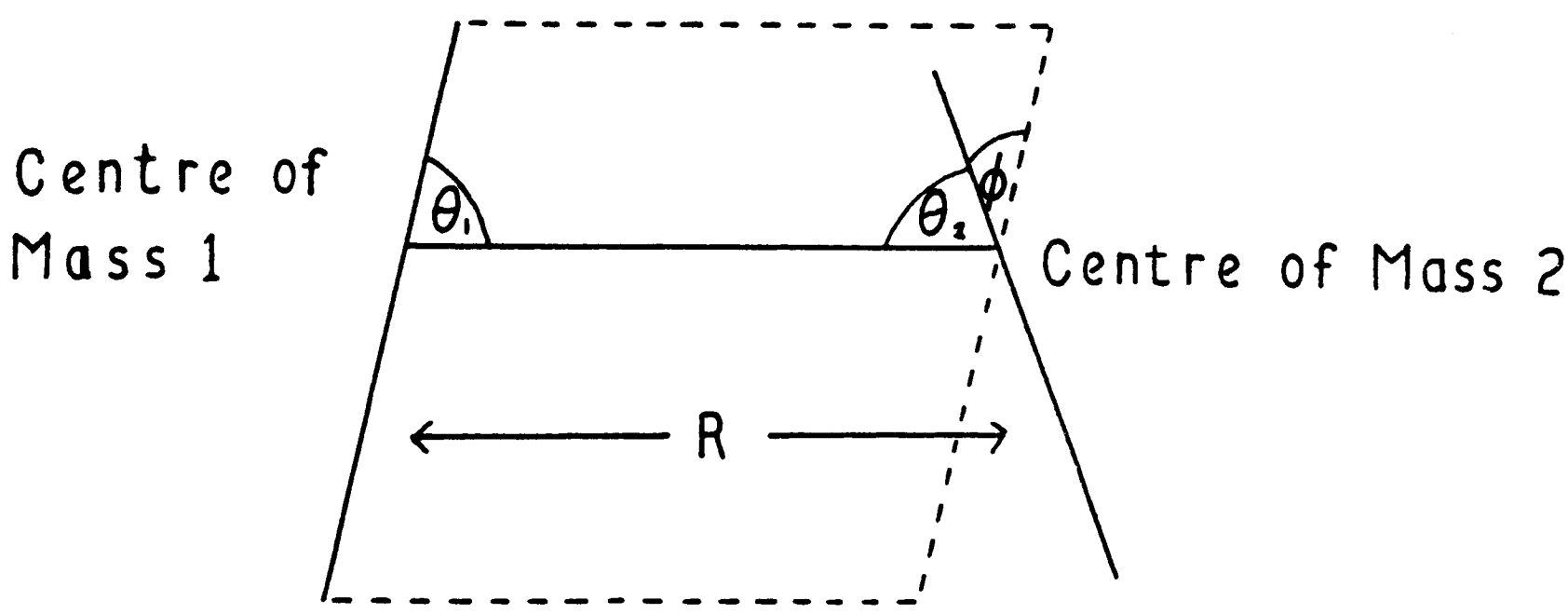


Figure 1.2: Atom-Diatom and Diatom-Diatom Coordinate Systems

analysis of the spectra of these has been closely analogous to that for conventional, chemically bound diatomic molecules. Apart from these the most thorough research has been directed towards complexes containing a rare gas atom and a diatomic molecule. The coordinate system used to describe the dynamical behaviour of these triatomic molecules is shown in Figure 1.2 . The potential is now anisotropic and may be expressed as a power series expansion in terms of Legendre polynomials. For homonuclear diatom cases this takes the form :

$$V(R,\theta,\xi) = V_0(R,\xi) + V_2(R,\xi)P_2(\mathrm{Cos}\theta) + V_4(R,\xi)P_4(\mathrm{Cos}\theta) + \ldots \qquad (1.2.1)$$

For heteronuclear diatoms the odd terms in the potential must be included. In treating the spectra of such systems it is very often assumed that the much faster motion associated with ξ and due to the vibrations of the diatom, may be factorised off in a fashion analogous to the separation of nuclear and electronic motions in the Born-Oppenheimer Approximation. Potential information so derived is therefore an average over this fast motion. Thus in practice two degrees of freedom remain corresponding to a van der Waals "bond length" and "bond angle" . On moving to a complex containing two diatoms the number of degrees of freedom is effectively doubled with three angles being necessary to specify the anisotropy of the interaction.

For the simpler atom-diatom category a classification of the spectroscopic behaviour in terms of the relative magnitudes of the anisotropy and torsional kinetic energy of the diatom was first propounded by Bratoz and Martin.[21] They treated the coupling of the various angular momenta by analogy with the well known cases of Hund. Four coupling models may conveniently be distinguished :

(i) Zero Anisotropy : This hypothetical case would arise when all terms higher than Vo vanish in Equation (1.2.1) . The quantum numbers j and N corresponding to the diatomic and "end over end" rotational angular momenta are individually conserved.

(ii) Weak Coupling : Weak anisotropic interactions induce a coupling between j and N which are no longer rigorously good quantum numbers. The total angular momentum, J, is however still a constant of the motion. As a result states with the same value of j and N but differing in J are weakly split by the anisotropic potential. Complexes such as ArH_2 are well described as weakly coupled and this behaviour is expected for a homonuclear diatom containing complex when :

$$| V_2 | << (4j + 6).B_d \qquad (1.2.2)$$

(iii) Strong Coupling : The rotational motion of the diatom is now strongly hindered and hence j precesses about the van der Waals bond axis with a projection Kj. N and Kj couple to yield the total angular momentum, J. Strictly N must also contain the remaining components of j not included in Kj. For a homonuclear complex strong coupling results when :

$$| V_2 | \leq (4j + 6).B_d \qquad (1.2.3)$$

(iv) Semi-Rigid Coupling : For the strongest anisotropies the rotation of the diatom is completely quenched and the complex is locked into a semi-rigid conformation which may be linear or T-shaped. Torsional motion of the diatom is now best regarded as a van der Waals bending vibration. Kj is replaced by Ka the projection of the total angular momentum about the a-inertial axis. Even in an asymmetric top this is usually quite a good quantum number. Semi-rigid behaviour is observed when :

$$| V_2 | > (4j + 6).B_d \quad , \text{ or } , \qquad (1.2.4)$$

$$| V_2 | > (2j + 2).B_d$$

for homonuclear and heteronuclear diatom complexes.

The molecules considered later in this thesis, ArNO and NeNO, will be treated as semi-rigid complexes in this context. This choice has been adopted for analysis of the majority of such van der Waals complexes. Deviations due to a departure from this limit towards strong coupling will, however, become apparent as a coupling between the rotational and bending vibrational motions. A final point of interest may be derived from Figure 1.1 . All of these complexes apart from KAr^{22} contained closed-shell constituents. Very little work has been reported on the spectroscopy of weakly bound, open-shell systems. In this thesis is presented the first reported work on high resolution spectroscopy of open-shell van der Waals molecules.

1.3 Experimental Methods

This section contains a brief review of some of the newer and more important experimental techniques that have been used in the study of van der Waals molecules. By their very nature these species tend to be transient and so many of the techniques have utilised non-equilibrium conditions. Indirect methods of obtaining the intermolecular potential (for example, molecular beam scattering[23]) that do not involve weakly bound complexes are not included here. However a particularly relevant and illustrative scattering study is described in some detail in Chapter 4.

1.3 a) Rotational Spectroscopy

Most of the work on the rotational spectroscopy of van der Waals molecules has been performed under non-equilibrium conditions. The technique which has been most widely used is that of molecular beam electric resonance spectroscopy (M.B.E.R.S.). Since this topic, the subject of the experiments used in this thesis, is described in detail in the next chapter only a brief outline will be given here. Van der Waals molecules are generated by a continuous supersonic expansion into a vacuum and are focussed on to a mass spectrometer detector by two electric quadrupolar fields. The beam is irradiated by R.F. or microwave sources between the focussing fields and a molecular transition will result in a change in the focussing properties of the beam-carried complexes. Thus the molecular resonance is detected as a change, normally a decrease, in the flux of molecules collected at the appropriate mass number.

The technique has many advantages. The supersonic expansion provides an enhanced concentration of van der Waals species in an effectively collision-free environment. The application of radiation at right angles to the collimated beam results in sub-Doppler linewidths and thus very high resolution. Since molecules rather than radiation are being detected, M.B.E.R.S. is a very sensitive form of spectroscopy.

A very large number of van der Waals molecules have thus been studied yielding much information on the potentials of these systems. In particular nearly all of the inert gas - hydrogen halides, RgH/DX,[24-27] (Rg = Ne,Ar,Kr,Xe ; X = F,Cl,Br) have been investigated. Recent work has been published by Klemperer and coworkers on complexes such as CO_2-HCl,[28] HF-Cl_2[29] and XeHF.[30] Dyke et al. have determined the structure of the hydrogen bonded species, H_2S-HF,[31] by the same technique. Muenter and others have investigated complexes of atmospheric interest such as Ar-O_3[32] and Ar-SO_2[33] using a similar molecular beam apparatus.

A second experiment for studying the rotational spectra of complexes under non-equilibrium conditions has been developed by Balle, Campbell, Keenan and Flygare.[34] The van der Waals molecules are produced in a pulsed nozzle expansion and pass into a Fabry-Perot cavity. Here they are subjected to a short, steady-state irradiation the duration and bandwidth of which is a function of the Q-factor of the cavity and the molecular linewidth. Following the decay of the exciting microwave pulse, the coherent emission from the polarised molecules is detected by a heterodyning process yielding a spectrum superimposed upon a 30 MHz carrier frequency. The timing for the irradiation and detection sequences is controlled by PIN diode switches. The final time domain signal is obtained by beating with a 30 MHz source and the frequency

spectrum is then recovered using a digital Fourier transform. Several (typically about ten) gas pulses may be followed per second and the resulting spectra are stored and signal-averaged by a dedicated computer.

It is instructive to make a comparison between the two techniques described above. The pulsed nozzle source permits the use of higher pressures behind the nozzle without condensation resulting and this facilitates greater rotational cooling and production of larger numbers of molecules. The shorter time for which the detector is "open" also reduces the amount of noise sampled and a further advantage to the signal to noise ratio is inherent through working in the time domain and using a Fourier transform. The M.B.E.R.S. approach on the other hand has a number of advantages over the Fourier transform experiment. The resolution is a little better with linewidths typically a factor of five smaller. Further, because it is a continuous expansion and radiation may be modulated by white noise (Chapter 2), much larger regions of the spectrum may be searched in a reasonable amount of time. The work to be described in Chapter 4 required extensive searching of a very large portion of the microwave spectrum which would prove very difficult using the Fourier transform experiment. Stark measurements and radiofrequency spectroscopy are straightforward with the electric resonance apparatus but have yet to be reported on the Flygare group's spectrometer. Finally the use of a mass spectrometer detector means that any impurity present in the expansion is unlikely to contribute spurious resonances.

Despite the search problem a large number of spectra from van der Waals molecules have already been recorded using the Flygare apparatus. These comprise some species already studied by

other workers using M.B.E.R.S. together with a large number of new hydrogen and pi-bonded systems. Recent papers published in the latter categories include the species C_2H_4-HF,[35] HCN-HCl[36] and the cyclic hydrocarbon complex C_3H_6-HCl.[37]

A major disadvantage common to both the molecular beam experiments is the failure to observe transitions in excited vibrational states. Legon, Millen[38] et al. have studied such transitions under equilibrium conditions for the species HCN-HF which is favoured by a comparatively high bond energy. This information combined with high resolution molecular beam data on the ground vibrational state permitted a more full analysis of the intermolecular force field.

1.3 b) Vibrational Spectroscopy

Most of the research to date in this field has been conducted under equilibrium conditions. Since the equilibrium concentration of complexes tends to be small, experimental conditions have proved rather critical. Most workers have therefore employed low temperatures, modest gas densities and the use of long path lengths in multiple traversal gas cells. The reviews already cited by Ewing[1-3] describe some early investigations on ArN_2 and ArH_2. Here some more recent work on long path length spectroscopy (L.P.L.S.) will be described.

McKellar has recently reported much improved spectra of ArH_2, ArHD and ArD_2.[39] Working at low pressures, a temperature of 77 K and with a total path length of 220 m, experimental linewidths of about 0.1 cm-1 were obtained. Integration times of many hours were necessary to achieve satisfactory signal to noise ratios. In several regions broadening of the spectral features was

interpreted in terms of predissociation. This work should provide a basis for refined ArH_2 intermolecular potentials. Although comparatively weakly bound, ArH_2 is a good candidate for this type of spectroscopy since the spectra are not obscured by absorption due to the free diatom. Problems are incurred, however, from the broad continuum features due to collision-pair absorption.

A more strongly bound complex, $(HF)_2$, has yielded a very rich infrared spectrum with bands that have been interpreted as arising from the "free" and hydrogen bound stretches in the molecule. Lafferty and Pine[40] working at 200 K and with a total path length of only 60 m achieved predominantly Doppler-limited resolution. Good ground state molecular constants were extracted from the spectrum as well as evidence of vibrational predissociation in the hydrogen bonded stretching band. In a very recent and exciting development Muenter[41] has used an F-centre laser to induce "flop out" transitions in the "free" hydrogen stretching band of $(HF)_2$ inside an M.B.E.R.S. apparatus. This experiment, the first of its kind, has achieved linewidths of just 30 MHz which are probably limited by residual Doppler broadening.

Working in the far infrared (14 to 240 cm-1) Boom and van der Elsken[42,43] have observed features attributable to excited bending vibrational states for the species ArHCl, KrHCl and XeHCl. Using a path length of 200 m and a Michelson interferometer they achieved a linewidth of 0.3 cm-1. The analysis was hampered by a poor signal to noise ratio and many lines corresponding to absorption by the free HCl monomer. Values of D_o, the dissociation energy for the complexes, were deduced from the temperature dependence of the absorption intensities. For ArHCl a

value of 184 ± 24 cm-1 was calculated. Bending frequencies and zero point energies were also estimated. Although uncertainty in the assignment of the lines indicates a need for caution, these results are valuable since excited bending states for these systems have not been observed in molecular beam experiments.

Finally a non-equilibrium, molecular beam technique has recently been developed by Gough, Miller and Scholes. In their experiment a collimated molecular beam is produced by a supersonic expansion and crossed by an F-centre laser. The molecular beam is detected by a liquid helium cooled, silicon doped bolometer which is sensitive to the total energy content of beam-carried species. The systems $(N_2O)_2$[44] and $(CO_2)_2$[45] were studied from the expansion of dilute mixtures of the monomer with helium as carrier gas. For the latter case features were observed near the (v1+v3) and (2v2+v3) bands of the free monomer which corresponded to an attenuation of the bolometer signal. Predissociation of the complex followed by scattering of the fragments from the beam was inferred. A predissociative lifetime of between $3x10^{-4}$ and $5x10^{-12}$ s was deduced from the time of flight.

A similar apparatus has been constructed in Oxford using a diode laser infrared source. Although monomer spectra have been recorded success has yet to be achieved with van der Waals molecules. The instability and low output power of the laser are partly responsible for these problems.[46]

1.3 c) Electronic Spectroscopy

The main species investigated under equilibrium conditions have been the rare gas dimers and mixed dimers. The spectra are

generally recorded as satellite lines in the vacuum ultraviolet emission of the rare gases. Much of the early work in this field was pioneered by Tanaka and Yoshino who have employed a diffraction grating to disperse the emission. Rotational resolution was rarely achieved but, for example, a well depth for Kr_2 of 138 cm-1 was obtained from a partial R.K.R. analysis.[47]

Subsequent studies of one of the better resolved bands ($A4s\,^1\Sigma_u^+(0u^+)$ to $X\,^1\Sigma_g^+(0u^+)$) by Colbourn and Douglas[48] resulted in the determination of good rotational and vibrational constants for low vibrational levels in the ground state. They were thus able to apply a full R.K.R. analysis and combined long range and virial coefficient data to produce a much improved potential energy curve.

The most recent work by Tanaka and Yoshino[49] using Tesla Coil excitation has produced more new bands in the Ar emission spectrum although these show mainly diffuse rotational structure. A full diagram summarising the known excited states of Ar_2 has been given. By photographing the two lowest excited states ($^3\Sigma_u^+$ and $^1\Sigma_u^+$) at higher resolution, attempts have been made to derive the form of the upper state long range potentials from the spectroscopic constants.

Laser induced fluorescence excitation spectroscopy has been the main tool used to probe the electronic structure of larger van der Waals molecules. The experiment, developed by Levy and coworkers, consists of a supersonic expansion containing the weakly bound complexes which is crossed by a tunable dye laser. The total fluorescence emitted at a given excitation frequency is then detected, normal to both the laser and molecular beam, by a photomultiplier tube. Although the complex must contain one or more suitable chromophores the technique has yielded a lot of

information on the structure and kinetic properties of a diverse selection of molecules.

The earliest systems studied consisted of halogens complexed to rare gas atoms. Of these the complex HeI_2 yielded the most information.[50] Only poor resolution of the rotational structure was achieved but this enabled the evaluation of rotational constants compatible with a T-shaped structure. The other inert gas complexes showed even less rotational structure. Further work on these systems led to estimates of the excited state binding energies for the species ArI_2, NeI_2 and HeI_2. Finally by following the intensity of spectral features as a function of the concentration of rare gases, Levy et al.[51] derived a band-shift rule for complexes of I_2 with varying numbers of He or Ne atoms. Intramolecular energy transfer was also studied for these systems by dispersing the emission from the excited I_2.

More recently studies of larger systems containing more than one chromophore have been reported. For example the dimer of s-tetrazine[52] has been found to exist in two observable conformations. Analysis of the rotational structure yielded coplanar and T-shaped geometries for the two forms. For the latter excitation of either of the non-equivalent chromophores could be distinguished. Mixed dimers with benzene were also observed.

1.3 d) Miscellaneous Methods

The preceding spectroscopic techniques are those that have made the most substantial and direct contribution to an understanding of the structure and properties of van der Waals molecules. A few other methods have been applied to a lesser

extent. Of these perhaps the four most important are mass spectroscopy,[53] Raman spectroscopy,[54] electron diffraction[55] and photoelectron spectroscopy.[56] The references given exemplify recent contributions in these fields.

1.4 Theoretical Aspects of van der Waals Molecules and the Intermolecular Potential

1.4 a) Ab Initio and Semi-Empirical Approaches

The traditional starting point for an ab initio treatment of the van der Waals interaction is the well known "supermolecule" model. This model uses S.C.F. theory to evaluate the interaction energy as the following difference :

$$\Delta E = E_{ab}(R, ..) - E_a - E_b \qquad (1.4.1)$$

Unfortunately this treatment has a number of very serious disadvantages. The first is the failure of the S.C.F calculation to model dispersion effects which, since they arise from electron correlation, require a proper configuration interaction (C.I.) calculation. As is discussed in section 1.5 the long range potential containing contributions from induction and dispersion forces is usually incorporated by a perturbation expansion in powers of the intermolecular separation :

$$\Delta E_{L.R.} = \frac{C_6}{R^6} + \frac{C_7}{R^7} + \frac{C_8}{R^8} + ...$$

The C.I. treatment has been shown to be feasible and satisfactory for small molecules like HeH_2 [57] but is prohibitively expensive in computer time for much larger systems.

A second problem is inherent in the approach. The supermolecule method requires accurate evaluation of a very small energy of interaction from the difference between two large energies. As a result the predictions of such a calculation are often basis set dependent. For example, two orderings of the atoms are possible in the following complex assuming a linear or near linear geometry :

ClF-HF HF-ClF

(Structure 1) (Structure 2)

Umeyama et al. found that calculations with a 4-31G basis set predicted that Structure 1 was the lower energy configuration.[58] A larger 4-31G** basis favoured Structure 2 which was the only form observed in an electric resonance experiment.

A third failing is the so called "basis set superposition error", B.S.S.E. This effect results from the use of restricted basis sets when calculating the energies of the isolated species, Ea and Eb. It is found that a lower energy is determined for each of the components "a" and "b" when it is calculated in the presence of the other's basis set. This leads to unrealistically deep potential minima. Burton has demonstrated for He_2 that inclusion of a ghost basis set centred away from the nuclei helps to alleviate the problem.[59]

In order to try and include the dispersion energy without recourse to a full configuration interaction calculation, a number of workers have used perturbation treatments to calculate the long range potential. This is then combined with the results of a good S.C.F. calculation to provide a better overall potential. The use of perturbation theory is sensible when treating effects such as dispersion and charge transfer. Problems do occur at close encounter distances due to exchange and overlap, however, because the perturbation may not satisfy the Pauli Principle. Stone and Hayes[60] have recently outlined such a procedure which proved satisfactory for ArHF and ArHCl. They point out that the perturbation treatment has the additional advantage of deriving the various interaction contributions separately.

1.4 b) The Electron Gas Model

The failure of S.C.F and perturbation theory treatments of van der Waals interactions at long and short ranges respectively, indicated the need for a more unified approach to such calculations. This is provided by the electron gas model. The model was shown to very satisfactory for atom-atom, closed-shell interactions by Gordon and Kim.[61] The theory was then extended by others, including Rae, and applied to atom-molecule interactions by Nielson, Parker, Snow and Pack.

The theory is based on a number of assumptions. The first is that there is no significant rearrangement of the electron densities as the two systems approach. This is clearly unreasonable where covalent bond formation can occur and hence explains the restriction to closed-shell species. This assumption was well verified for He_2 by Gordon and Kim. It is then assumed that the energy of interaction can be evaluated as the sum of four contributions :

$$\Delta E = E(R,\theta) - E(\infty,\text{any } \theta) \qquad (1.4.2)$$

$$= E_{COUL} + E_{KIN} + E_{EXC} + E_{COR}$$

Evaluation of these terms then proceeds on the fundamental, underlying approximation that the energy density at a given point may be evaluated as that of a uniform electron gas. The coulombic term is straightforward and the kinetic energy and exchange contributions have been given as simple functions of the electron density. An empirical expansion in terms of the electron density is usually employed to model the correlation energy.

Finally the actual electron density is obtained from the first assumption as a simple additive property of the constituents :

$$\rho_{ab} = \rho_a + \rho_b$$

The electron densities for "a" and "b" may be taken from any convenient theoretical or experimental source. In practice Hartree-Fock wavefunctions are commonly used.

A potential energy curve or surface may then be evaluated by calculating the interaction energy at a mesh of points and interpolating using a suitable numerical quadrature. Apart from its success in prediction the method has two great advantages. The first results from its statistical nature; it is therefore good for many-electron species where ab initio calculations are slow and inaccurate. Given the form of the separate electron densities the time taken for an electron gas calculation is quite small even for large atoms and molecules.

The major disadvantage of the electron gas model (apart from the limitations implicit in the assumptions) is that potential curves so predicted tend to rise too quickly towards zero at long range. This is because long range dispersion and induction contributions are not included in the calculation. This is usually easily overcome by splicing in an extra perturbation theory term at long range. An example of this is cited in Chapter 4 where the somewhat unorthodox application of the model to an open-shell system by Nielson, Parker and Pack is discussed.

1.4 c) Intermolecular Potential Energy Surfaces from Experimental Data

The very close connection between the study of van der Waals molecules, in particular by molecular beam spectroscopy, and the derivation of intermolecular potential energy surfaces has already been made. It therefore seems appropriate to provide a

brief account of the derivation of such surfaces. Only atom-diatom systems will be considered.

In order to test the value of a given potential an efficient means of calculating experimental observables is required. This subject is discussed in detail in the review of Le Roy and Carley. An early application of the close-coupling method of Dunker and Gordon[62] to ArHCl was found to be computationally very expensive. A much faster calculation was developed by Holmgren et al.[63] based on a Born-Oppenheimer type of separation of the complex's angular and radial motions (B.O.A.R.S.). This new approach was shown to be superior in speed to that of Dunker and Gordon whilst furnishing rigorous upper and lower bounds to the ground state energy.

A modification to this method of calculation (the corrected Born-Oppenheimer or C.B.O. method), reported by Hutson and Howard,[64] accounted for non-adiabatic terms neglected by the B.O.A.R.S. treatment. The latter were shown to be significant particularly with regard to the information content recoverable from molecular beam spectra.

The use of the C.B.O. calculation has permitted the derivation of good anisotropic potentials from a simultaneous least squares fit of data from molecular beam spectra, scattering, second virial coefficients and rotational line broadening. The technique, again developed by Hutson and Howard, has been applied to the rare gas - hydrogen chloride series.[65] The merits and shortcomings of various parameterisations presented in these surfaces has been reviewed by Howard.

1.5 The Nature of the van der Waals Interaction

Within the study of van der Waals molecules and of intermolecular forces in general, the question of the nature of the interaction is a crucial and fundamental one. Some early insight into the contributory mechanisms for the binding energy was provided by Donath and Pitzer.[66] They chose the simple system of triplet hydrogen molecules to develop their arguments and showed that a suitable wavefunction representing the various interactions could be written :

$$\Psi_{H_2} = C_{ex}\psi(H,H)+C_{ct}\psi(H^+,H^-)+C_{ind}\psi(H^*,H)+C_{disp}\psi(H^*,H^*) \qquad (1.5.1)$$

The terms represent contributions due to the energies of exchange repulsion, charge transfer, induction or polarisation and London type dispersion. Murrell and Randic[67] later used a similar formulation for a more general theory of intermolecular energy in the region of small overlap. Using perturbation expressions they argued in favour of treating the region around the potential minimum by extension of the long range potential.

Molecular beam studies, in particular, have thrown much light on the above question. In this section attention is focussed on two important aspects of the interaction: the possibility of incipient chemical bonding and the role played by charge transfer effects. Although these two are intimately connected they are treated separately here as seems appropriate for the relevant experimental evidence.

One of the motives for the study of rare gas - nitric oxide complexes was to try and address these two questions. The complexity encountered in these open-shell systems made it

difficult to place precise interpretations on the molecular constants determined, however.

1.5 a) Stereospecificity in van der Waals Molecules - Incipient Chemical Bonding ?

Much of the work described in this section is due to the Harvard group of Klemperer. They have studied two broad categories of van der Waals molecules concentrating mainly on deriving a good description of the equilibrium structure of these species.

For atom-diatom complexes it had been assumed from much strong evidence that the inert gas - hydrogen halides all possessed linear equilibrium geometries. This assumption had been made with some reservation, however, since the vibrationally averaged structures, those determined by spectroscopy, were quite different as a result of the large amplitude motion of the hydrogen atom. For this reason Klemperer et al.[68] recorded the M.B.E.R. spectrum of the complex, ArClF, for which the average and equilibrium structures would be more similar. ArClF and later KrClF[69] were indeed found to have linear equilibrium geometries with the average structures deviating from linearity by 11.1 and 10.1 degrees respectively. Using isotopic substitution the ordering of the atoms was confirmed as written.

The existence of linear equilibrium geometries for these two complexes confirmed that an additive pair potential was not responsible for the preferred structure of binding. A comparison of the approximately determined stretching and bending frequencies, 47.0 and 41.0 cm-1 respectively for ArClF, illustrated the strength of the anisotropy. Klemperer et al.

elucidated the structural analogy with the chemically bound, isovalent complex anion I_3^-. Further they pointed out that the atomic arrangement, ArClF, was consistent with the prediction from Walsh's Rule for linear, triatomic molecules. All of these features, together with the observation of a 0.3 Angstrom shrinkage in the van der Waals bond length, were cited as characteristics that could arise from a small degree of incipient chemical bonding. The hypothesis of stabilisation via a H.O.M.O. - L.U.M.O. interaction was proposed as shown below :

$$Ar..Cl\text{-}F \qquad Ar^{+}..Cl\text{-}F^{-}$$

In the ClF complexes the linear arrangement was consistent with an acceptor orbital having a σ^* nature. For a complex where this orbital had π^* character a non-linear geometry was predicted. As a result the complex ArOCS[70] was investigated and found to have an equilibrium structure very close to a T-shape. This once again fitted the Lewis acid (OCS) - base (Ar) or H.O.M.O. - L.U.M.O. model and was shown to be analogous to the isovalent anion CO_3^{2-} or its isoelectronic equivalent COS_2^{2-}.

Similar electric resonance structure determinations by the same group on two diatom-diatom complexes were just as illuminating. HF-HCl and HF-ClF[71] were characterised by three collinear atoms and a terminal hydrogen off-axis by 50 and 55 degrees respectively. Again a rationalisation in terms of a H.O.M.O. - L.U.M.O. model was presented. The lone pair donated by the HF Lewis base was assumed to be in an approximately tetrahedrally hybridised orbital whilst the acceptor atom on the Lewis acid (HCl or ClF) was attributed ls or $p\sigma$ character. The weaker bending force constant of the former (0.0066 versus 0.3100 mdyne/Å) fitted in well with the lack of directionality associated with an acceptor orbital of approximately ls

character.

Whether incipient chemical bonding may be inferred from the above evidence or not, the agreement with such predictions is impressive. It may at least be concluded that in many instances the structures can be rationalised in terms of the behaviour of analogous chemically bound counterparts. Two other groups have furthered the approach. Legon and Millen[72] have presented a similar rule for predicting the structures of hydrogen halides complexed to molecules with pi-bonds or non-bonded electron pairs. Dyke has recently reported the structure of H_2S-HF to have the triatomic plane perpendicular to the HF axis. He concludes that lone pair donation from a 3p (or 3d) orbital on the sulphur atom may stabilise such a structure. There is an analogy between the extent to which hybridisation occurs for orbitals of first and second row atoms and that proposed for the suggested donor atoms

(S and F) in the complexes H_2S-HF and HF-ClF.

Finally it should be pointed out that exceptions to the predictions of a Lewis acid - base model are known. H_2O-HF appears to be a planar species whilst OCS-HF is linear.[31] A failure to treat the short range repulsion effects may help to explain the deviation of these structures from the model.

1.5 b) The Extent of Charge Transfer in a van der Waals Bond

In the previous section some evidence was presented for the influence of charge transfer mechanisms in determining the equilibrium structure of a number of van der Waals molecules. An alternative assessment of the contribution of charge transfer may be gained from the hyperfine coupling constants of quadrupolar nuclei.

The group of Flygare have pursued this approach by recording the microwave spectra, by the pulsed Fourier transform method, of the linear species, $^{83}KrHF$[73] and $^{131}XeHCl$.[74] In both cases hyperfine structure attributable to the rare gas quadrupolar nuclei (I = 9/2 and 3/2) was observed. For the ground electronic state of these unbound rare gas atoms no such splittings would be expected because of the spherical symmetry of the electric field of the electrons. Thus the hyperfine spectral splittings give a direct probe of the electric field gradient at the rare gas nucleus arising from complex formation. For XeHCl[74] four contributions to the measured projection of this field gradient were considered :

$$q_{aa} = q_{ext}(1-\gamma) + q_{pol} + q_{rep} + q_{ct} \qquad (1.5.2)$$

The second term, arising from dipole polarisation of the rare gas electron cloud by the HCl, was estimated to be only about 1% of the measured field gradient. Likewise since this field gradient is probed at the nucleus, Flygare et al. argued that the repulsive overlap contribution could be neglected. The leading term of the equation represents the effects of the electric field gradient due to the (assumed) remote HCl. The direct contribution was evaluated as follows in terms of the permanent HCl multipole moments :

$$q_{ext} = \frac{-6.\mu.P_1(\cos\theta)}{r^4} - \frac{12.Q.P_2(\cos\theta)}{r^5} - \frac{20.\Omega.P_3(\cos\theta)}{r^6} \ldots \qquad (1.5.3)$$

It is, however, known that such a field gradient may be shielded or anti-shielded, as originally proposed by Sternheimer, by the electrons of the rare gas atom. Hence the effect of the HCl electric field is actually dominated by the Sternheimer constant, γ, which may be considerably larger than unity. Using a

value for the Sternheimer constant calculated by a variational method, they showed that the first term of Equation (1.5.2) accounted for the observed electric field gradient to within experimental error. Flygare et el. therefore concluded that the contribution of charge transfer to the measured electric field gradient was very small.

The above analysis contains some assumptions that may be questioned. Clearly the magnitude of the Sternheimer anti-shielding constant is crucial to the final conclusions. Unfortunately the variational calculation has not been published to date although other workers have vindicated the results of a similar calculation for ^{83}Kr. The errors in the calculation of γ and also of rare gas quadrupole moments may still be as high as 10 - 20%, however. Furthermore the validity of the multipole expansion and the means of estimating the hydrogen halide polarisation of the rare gas electron cloud are questionable. It seems that charge transfer does not provide the dominant contribution to the observed electric field gradient but its magnitude could be significantly higher than the estimate from the work of Flygare et al.

The same group has also analysed the rotational spectra of two larger systems containing quadrupolar nuclei which are equivalent through symmetry in the monomer, NCCN-HF[75] and N_2-HF.[76] In both these linear systems a different quadrupole coupling constant was determined for the bound and "free" nitrogen nuclei. This difference was shown to represent a lower bound (attenuated by vibrational effects) to the electrical changes brought about by complex formation. Soper et al. assumed by analogy with KrHF and XeHCl that charge transfer made a negligible contribution to the measured $\Delta\chi$. Using the same procedures they showed that the

Sternheimer anti-shielded field gradient due to the remote HF was of similar magnitude but of opposite sign to the observed Δq. This discrepancy was rationalised in terms of polarisation of the N_2 bond, that is through an intramolecular charge transfer, by the HF. A simple calculation using the Townes-Dailey model (corrected for vibrational effects) indicated a transfer of 0.03 electronic charges from one nitrogen atom to the other.

Finally a more guarded analysis of the molecule, XeHF, by Baiocchi and other workers[30] has produced similar conclusions to those above but based on additional experimental evidence. By analysing the spectra of XeHF and XeDF the measured field gradient at the Xe nucleus was shown to be directly proportional to that from the HF multipole potential. Evidence from two other experimental sources (atomic beam studies of $^3P_2$ Xe and Mossbauer spectra of XeF_2 and $XeCl_2$) showed that the measured field gradient was only 2 - 3% of that expected from a substantial intermolecular transfer of charge. It was deduced that an inductive Sternheimer effect was operative the coefficient of which could approximately be associated with the corresponding constant of proportionality. This value of the Sternheimer constant (-157) agreed well with that from Flygare's analysis of XeHCl (-159) as would be expected. Baiocchi et al. concluded that Sternheimer anti-shielding probably accounts for most of the observed field gradient but that the fraction due to charge transfer was undetermined.

Chapter 1 : References

Abbreviations For All Chapters.

a) JCP : Journal of Chemical Physics.

b) CPL : Chemical Physics Letters.

c) CP : Chemical Physics.

d) MP : Molecular Physics.

e) JACS : Journal of The American Chemical Society.

f) FD : Faraday Discussions of the Chemical Society.

g) JMS : Journal of Molecular Spectroscopy

1.B.L.Blaney and G.E.Ewing, Ann.Rev.Phys.Chem. 27, 553, (1976)

2.G.E.Ewing, Can.J.Phys. 54, 487, (1976)

3.G.E.Ewing, Acc.Chem.Research, 8, 185, (1975)

4.R.J.Le Roy and J.S.Carley, Adv.Chem.Phys. 17, 353, (1980)

5.B.J.Howard, Int.Rev.Sci.Series 2, 2, 93, (1975)

6.H.J.Hanley,J.A.Barker,J.M.Parson,Y.T.Lee and M.Klein, MP, 24, 11, (1972)

7.F.W.Crawford,E.J.R.Harris and E.B.Smith, MP, 37, 1323 (1979)

8. J.G.Kircz,G.J.Q.van der Peyl and J.van der Elsken, JCP, 69, 4606 (1978)

9.T.Oka, Adv.Atom.Mol.Phys. 9, 127, (1973)

10.F.R.McCourt, Abstracts of MOLEC III, (1980)

11.E.B.Smith and A.R.Tindell, FD, 73 (1982)

12.D.L.King,D.A.Dixon and D.R.Herschbach, JACS, 96, 3328, (1974)

13.T.A.Milne,A.E.Vandegrift and F.T.Green, JCP, 52, 1552, (1970)

14.D.L.Thompson, JCP, 77, 1269, (1982)

15.W.Klemperer, Ber.Bunsenges, 78, 128, (1974)

16.Y.Tanaka and K.Yoshino, JCP, 50, 3087, (1969)

17.A.Amirov,U.Even and J.Jortner, JCP, 75, 2489 , (1981)

18.J.Jortner,A.Amirov and U.Even, FD, 73, (1982)

19.I.Raitt,A.M.Griffiths and P.A.Freedman, CPL, 80, 225, (1981)

20.J.E.Kenny,K.E.Johnson,W.Sharfin and D.H.Levy, JCP, 72, 1109, (1980)

21.S.Bratoz and M.L.Martin, JCP, 42, 1051, (1965)

22.R.R.Freeman,E.M.Mattison,D.E.Pritchard and D.Kleppner, JCP, 64, 1194, (1976)

23.J.M.Farrar and Y.T.Lee, CPL, 26, 428, (1974)

24.S.E.Novick,P.B.Davies,S.J.Harris and W.Klemperer, JCP, 59, 2273, (1973)

25.K.C.Jackson,P.R.R.Langridge-Smith and B.J.Howard, MP, 39, 817, (1980)

26.A.E.Barton,T.J.Henderson,P.R.R.Langridge-Smith and B.J.Howard, CP, 45, 429, (1980)

27.A.E.Barton,D.J.B.Howlett and B.J.Howard, MP, 41, 619, (1980)

28.R.S.Altman and M.D.Marshall, JCP, 77, 4344, (1982)

29.F.A.Baiocchi,T.A.Dixon and W.Klemperer, JCP, 77, 1632, (1980)

30.F.A.Baiocchi,T.A.Dixon,C.H.Joyner and W.Klemperer, JCP, 75, 2041, (1981)

31.R.Viswanathan and T.R.Dyke, JCP, 77, 1166 (1982)

32.R.L.DeLeon,K.M.Mack and J.S.Muenter, JCP, 71, 4487, (1979)

33.R.L.DeLeon,A.Yokozeki and J.S.Muenter, JCP, 73, 2044, (1980)

34.T.J.Balle,E.J.Campbell,M.R.Keenan and W.H.Flygare, JCP, 72, 922, (1980)

35.J.A.Shea and W.H.Flygare, JCP, 76, 4857, (1982)

36.A.C.Legon,E.J.Campbell and W.H.Flygare, JCP, 76, 2267, (1982)

37.A.C.Legon,P.D.Aldrich and W.H.Flygare, JACS, 104, 1486, (1982)

38.A.C.Legon,D.J.Millen and S.C.Rogers, Proc.R.Soc.Lond.A. 370, 213, (1980)

39.R.W.McKellar, FD, 73, (1982)

40.A.S.Pine and W.J.Lafferty, JCP, 78, 2154, (1983)

41.J.S.Muenter, Personal Communication

42.E.W.Boom and J.van der Elsken, JCP, 69, 4606 (1978)

43.E.W.Boom and J.van der Elsken, JCP, 77, 625 (1982)

44.T.E.Gough,R.E.Miller and G.Scholes, JCP, 69, 1588, (1978)

45.T.E.Gough,R.E.Miller and G.Scholes, J.Phys.Chem. 85, 4041, (1981)

46.G.D.Hayman and J.Hodge, Personal Communication

47.Y.Tanaka,K.Yoshino and D.E.Freeman, JCP, 59, 5160, (1973)

48.E.A.Colbourn and A.E.Douglas, JCP, 65, 1741, (1976)

49.D.E.Freeman,Y.Tanaka and K.Yoshino, JCP, 71, 1780, (1979)

50.R.E.Smalley,D.H.Levy and L.Wharton, JCP, 64, 3266, (1976)

51.J.A.Blazy,B.M.DeKoven,T.D.Russell and D.H.Levy, 72, 2439, (1980)

52.D.H.Levy,C.A.Haynam and D.V.Brumbaugh, FD, 73, (1982)

53.J.M.Calo, JCP, 62, 4904, (1975)

54.L.Frommhold and M.H.Proffitt, JCP, 74, 1512, (1981)

55.L.S.Bartell,R.K.Heenan and M.Nagashima, JCP, 78, 236, (1983)

56.P.M. and J.L.Dehmer, JCP, 67, 1774, (1977)

57.J.M.Geurts,P.E.S.Wormer and A.van der Avoird, CPL, 35, 444, (1975)

58.H.Umeyama,K,Morokuma and S.Yamabe, JACS, 99, 330, (1977)

59.P.G.Burton, JCP, 67, 4696, (1977)

60.A.J.Stone and I.C.Hayes, FD, 73, (1982)

61.R.G.Gordon and Y.S.Kim, JCP, 56, 3122, (1972)

62.A.M.Dunker and R.G.Gordon, JCP, 64, 354, (1976)

63.S.L.Holmgren,M.Waldman and W.Klemperer, JCP, 67, 4414, (1977)

64.J.M.Hutson and B.J.Howard, MP, 41, 1123, (1980)

65.J.M.Hutson and B.J.Howard, MP, 45, 769, (1982)

66.W.Donath and K.S.Pitzer, JACS, 78, 4562, (1956)

67.J.N.Murrell and J.N.Randic, Proc.R.Soc.Lond.A. 284, 566, (1965)

68.S.J.Harris,S.E.Novick,W.E.Falconer and W.Klemperer, JCP, 61, 193, (1974)

69.S.E.Novick,S.J.Harris,K.C.Janda and W.Klemperer, Can.J.Phys. 53, 2007, (1975)

70.S.J.Harris,K.C.Janda,S.E.Novick and W.Klemperer, JCP, 63, 881, (1975)

71.S.E.Novick,K.C.Janda and W.Klemperer, JCP, 65, 5115, (1977)

72.D.J.Millen and A.C.Legon, FD, 73, (1982)

73.L.W.Buxton,E.J.Campbell,M.R.Keenan,T.J.Balle and W.H.Flygare, C.P. 54, 173, (1981)

74.M.R.Keenan,L.W.Buxton,E.J.Campbell,T.J.Balle and W.H.Flygare, JCP, 73, 3523, (1980)

75.A.C.Legon,P.D.Soper and W.H.Flygare, JCP, 74, 4936, (1981)

76.P.D.Soper,A.C.Legon,W.G.Read and W.H.Flygare, JCP, 76, 292, (1982)

Chapter 2: The Molecular Beam Electric Resonance Spectrometer

2.1 The Construction Of The Spectrometer

a) The Source Chamber

b) The Buffer and Main Chamber

c) The Detector Chamber

2.2 Method Of Operation

a) Detection Electronics

b) Radiation Sources

c) Amplification of Radiation

d) Signal Processing

Chapter 2 : The Molecular Beam Electric Resonance Spectrometer

The rotational spectra of ArNO and NeNO, presented in the latter chapters of this thesis, were obtained using a Rabi type of electric resonance spectrometer.[1] The basic mechanism and some of the advantages and disadvantages of this technique have already been discussed. In this chapter, therefore, only a brief description of the construction, principles and operation of the spectrometer will be given.

2.1 The Construction of the Spectrometer

A schematic diagram of the Oxford spectrometer is shown in Figure 2.1 . It comprises four chambers; the functions of each will be discussed below. The necessary high vacuum within the apparatus is achieved by differential pumping. The source, buffer and main chambers are pumped by Edwards 9" EO9 (1000 l/s), 5" EO4 (600 l/s) and 7" EO6 (1300 l/s) diffusion pumps each backed by an Edwards rotary pump. Backstreaming of oil is prevented by a gate valve on the source pump and by refrigerated chevron baffles on the other two pumps. The pressure in each chamber is monitored by Edwards 1G5G ion gauge heads. By contrast the detector chamber, requiring ultra-high vacuum conditions (10^{-9} torr) is pumped jointly by a Ferranti Diode (80 l/s) and an A.E.I. Triode (25 l/s) pumps. A V.G. Titanium Sublimation pump is also mounted on the detector chamber.

To facilitate access for maintenance, and for protection, gate valves enable complete isolation of the source and detector chambers from the combined buffer and main chamber.

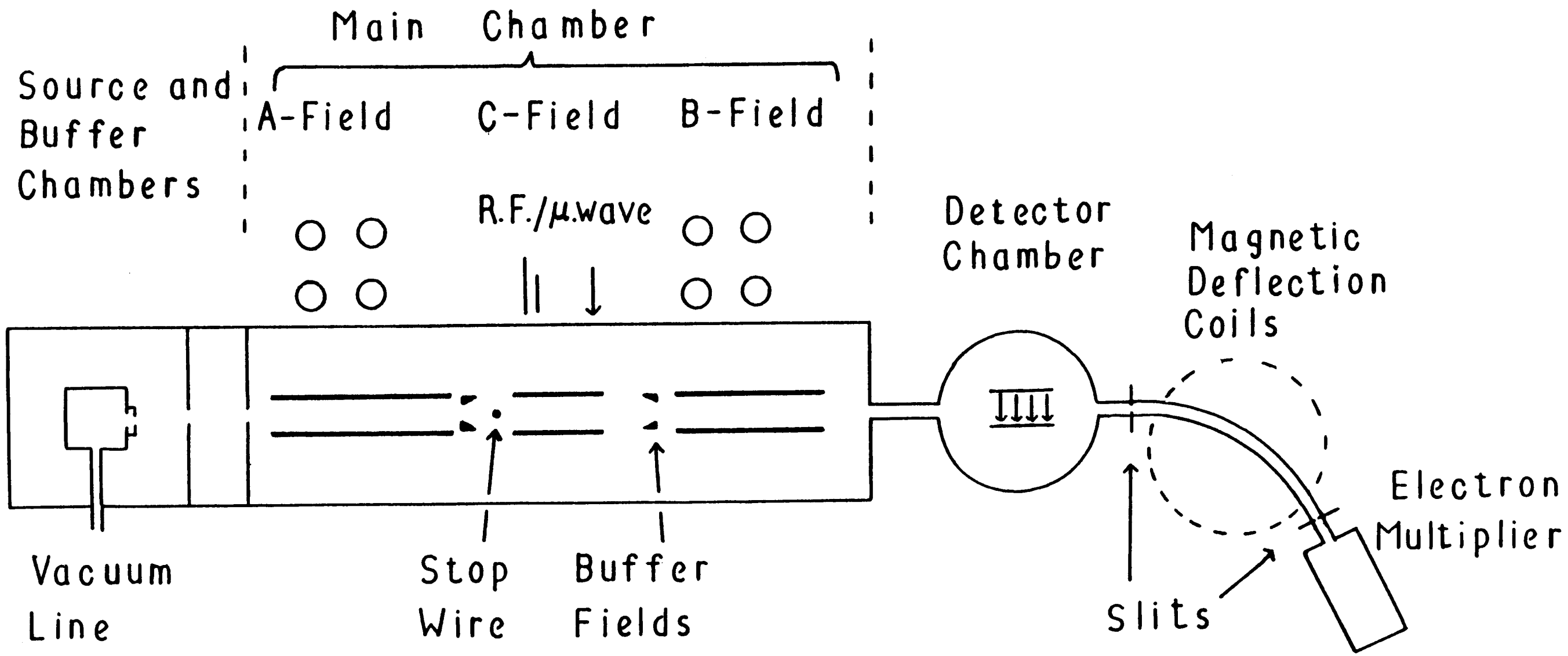


Figure 2.1: The Molecular Beam Electric Resonance Spectrometer.

2.1 a) The Source Chamber : The Supersonic Expansion

The molecular beam is generated and collimated in this chamber by a supersonic nozzle expansion. A mixture of gases is delivered to a copper block by monel tubing. The nozzle is screwed on to this block and sealed with an indium gasket. The nozzle itself comprises a small platinum pinhole (Agar Aids) secured on a stainless steel mount with Torr Seal. A few turns of resistance wire and a liquid nitrogen reservoir allow regulation of the temperature of the copper block and hence the nozzle. This temperature is monitored as the potential which develops across a chromel-alumel thermocouple which is in thermal contact with the nozzle mount. The pressure of gas behind the nozzle, the stagnation pressure, may be varied with a Nupro fine needle valve in the monel line.

Gas mixtures are made up and stored in 1 litre reservoirs on a vacuum line external to the source chamber. The composition of the gases being mixed is approximately determined using a Matheson manometer on the vacuum line.

The success of the electric resonance technique depends on the production of an enhanced concentration of complexes in low rotational states and in a collision-free environment. A brief consideration of the nature of the supersonic expansion[2] indicates how these requirements may be attained.

Under conditions of low source pressure and with an aperture dimension that is much smaller than the mean free path of the molecules, an effusive expansion results which is characterised by a velocity-weighted Maxwellian distribution. On increasing the aperture diameter and source pressure, many molecular

collisions occur during the expansion. Under these circumstances the gas behaves like a bulk fluid under compression and it undergoes a free jet supersonic expansion into a molecular beam.

The expansion is approximately isentropic and against a vacuum (no pV work). Hence the following relationship holds between the enthalpy before and after expansion and the bulk kinetic energy :

$$H_{source} = H_{beam} + 1/2.NmV^2 \qquad (2.1.1)$$

Assuming a constant heat capacity,

$$H_{source} - H_{beam} = C_p(T_{source} - T_{beam}) \qquad (2.1.2)$$

where the temperature of the beam is an effective temperature characterising the expansion and is valid only if thermal equilibrium exists between all internal degrees of freedom of the gas molecules. It is conventional to introduce the Mach number which is defined as the ratio of the flow speed to the speed of sound at that temperature :

$$M = V/c = V.\left\{\frac{Nm}{\gamma RT}\right\}^{1/2} \qquad (2.1.3)$$

Combining these equations yields the following expression for the critical low temperatures achieved in the supersonic expansion for a near perfect gas[2] :

$$T = \frac{T_{source}}{1 + \frac{1}{2}(\gamma-1)M^2} \qquad (2.1.4)$$

A much narrower velocity distribution now results which is approximately Maxwellian but with a correction due to the bulk velocity, Vo :

$$N(V) \propto V^3.T^{-3/2}.e^{-m(V-v_0)^2/2kT} \qquad (2.1.5)$$

Ashkenas and Sherman[3], treating the system as a continuum expansion, showed that the following behaviour is expected for M,

$$M \approx A(\gamma).(x/D)^{\gamma-1} \qquad (2.1.6)$$

where A is a constant and x the axial distance from the nozzle. However, as x increases the number of collisions falls off and a change to free molecular flow characterised by a terminal Mach number ensues. For argon this quantity has been shown to vary as,

$$M_T = 133.(P_o.D)^{0.4} \qquad (2.1.7)$$

where Po is the stagnation pressure in atmospheres and D the nozzle diameter in cms.[4]

Thus from this last equation it may be deduced that the most effective translational cooling is attained using large stagnation pressures and nozzles. For beams of polyatomic molecules the increased heat content, associated with the rotational and vibrational degrees of freedom, leads to lower terminal Mach numbers and less efficient cooling. Where such species are studied, seeding with an inert gas is almost always advantageous. Efficient R-T energy transfer then causes effective rotational temperatures to be close to those for translation.[5] Vibrational temperatures are frequently considerably higher, however.

The above principles illustrate how the low effective temperatures and the collision-free environment are obtained to yield beams of van der Waals molecules in the lowest few quantum states. The other main feature of interest is the variation in the number density of van der Waals dimers. Most authors have concluded that this quantity varies with Po^2D . Since the gas load for Poiseuille flow is approximately proportional to $Po\ D^4$, a compromise of fairly small nozzle diameters with high stagnation pressures proves most convenient.

A skimmer is not used on the Oxford spectrometer. The molecular beam is, however, collimated by a pair of slits at the exit of the source chamber set about 1 mm. apart and ~7cms. from

the nozzle.

2.1 b) The Buffer and Main Chambers : Electrostatic Focussing

The buffer chamber serves merely to provide an extra stage of differential pumping. Its ambient pressure is about 10^{-5} torr compared with about 10^{-4} torr for the background pressure in the source chamber.

In the main chamber (10^{-6} torr) the state selection, irradiation and state detection of van der Waals molecules is achieved. The two focussing processes occur in the A and B quadrupolar field regions. These fields consist of four cylindrical, stainless steel rods of 0.95 cms. diameter which are maintained in a parallel, clover leaf configuration by machined glass insulating supports. The lengths of the A and B quadrupoles are 48 and 37 cms. respectively (See Figure 2.2). Opposite pairs of rods are earthed whilst the other pairs are charged to a potential of up to 30 kV from Brandenburg 807-R E.H.T. power supplies. To a good approximation the electric field inside the rod assembly is given by :

$$| E | = \frac{2.r.V_0}{R^2} \qquad (2.1.8)$$

A molecule moving within this inhomogeneous electric field experiences a radial force given by the gradient operator :

$$F_r = -d/dr.W(E) = + d/dr.< \mu.E > \qquad (2.1.9)$$

where W(E) is the Stark energy. If the molecule has a positive Stark coefficient its trajectory takes it towards the position of least electric field (the centre of the quadrupole) and it is focussed. Species in negative Stark states are scattered out of

Figure 2.2 Cross Section of Quadrupole Field.

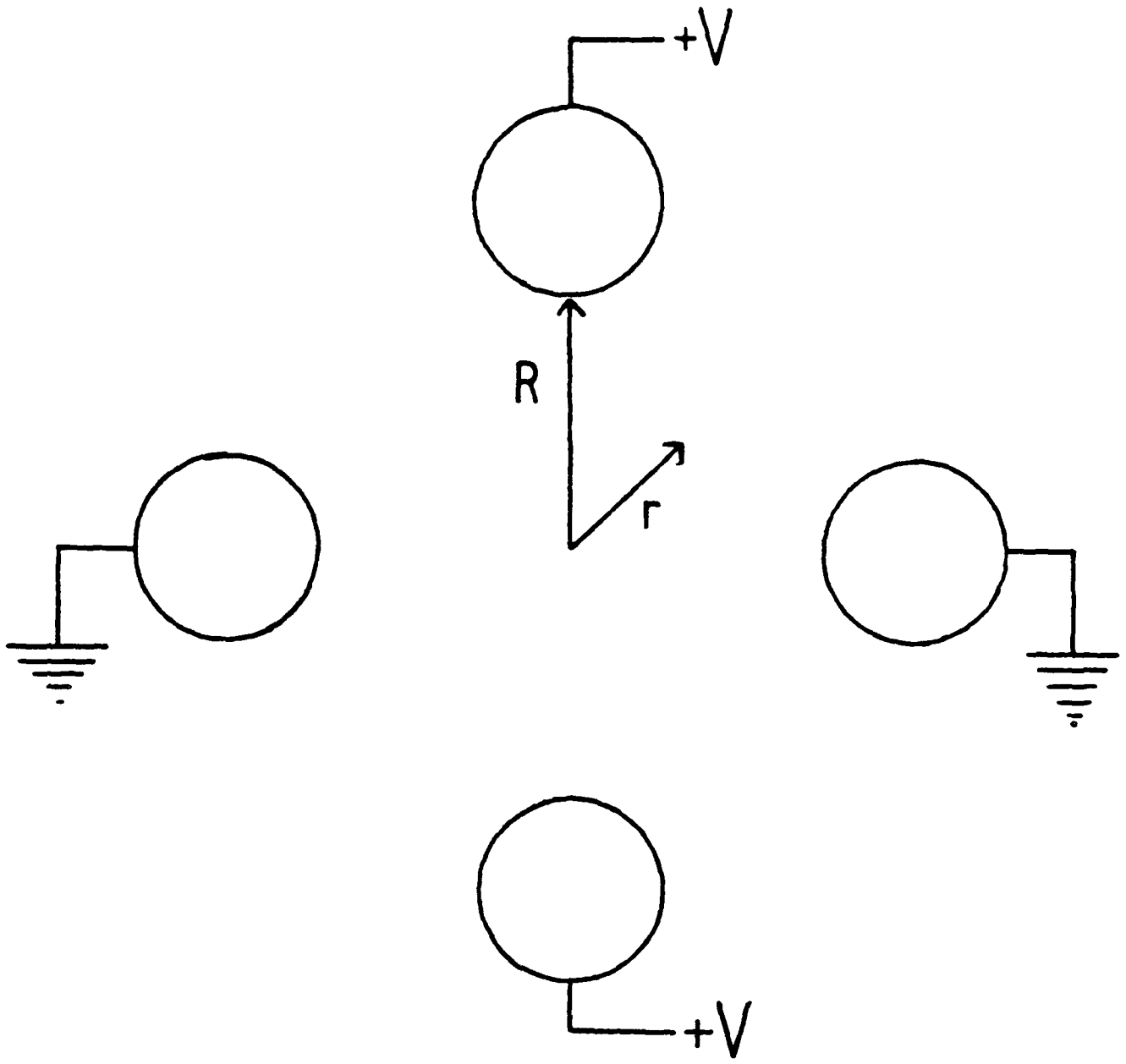
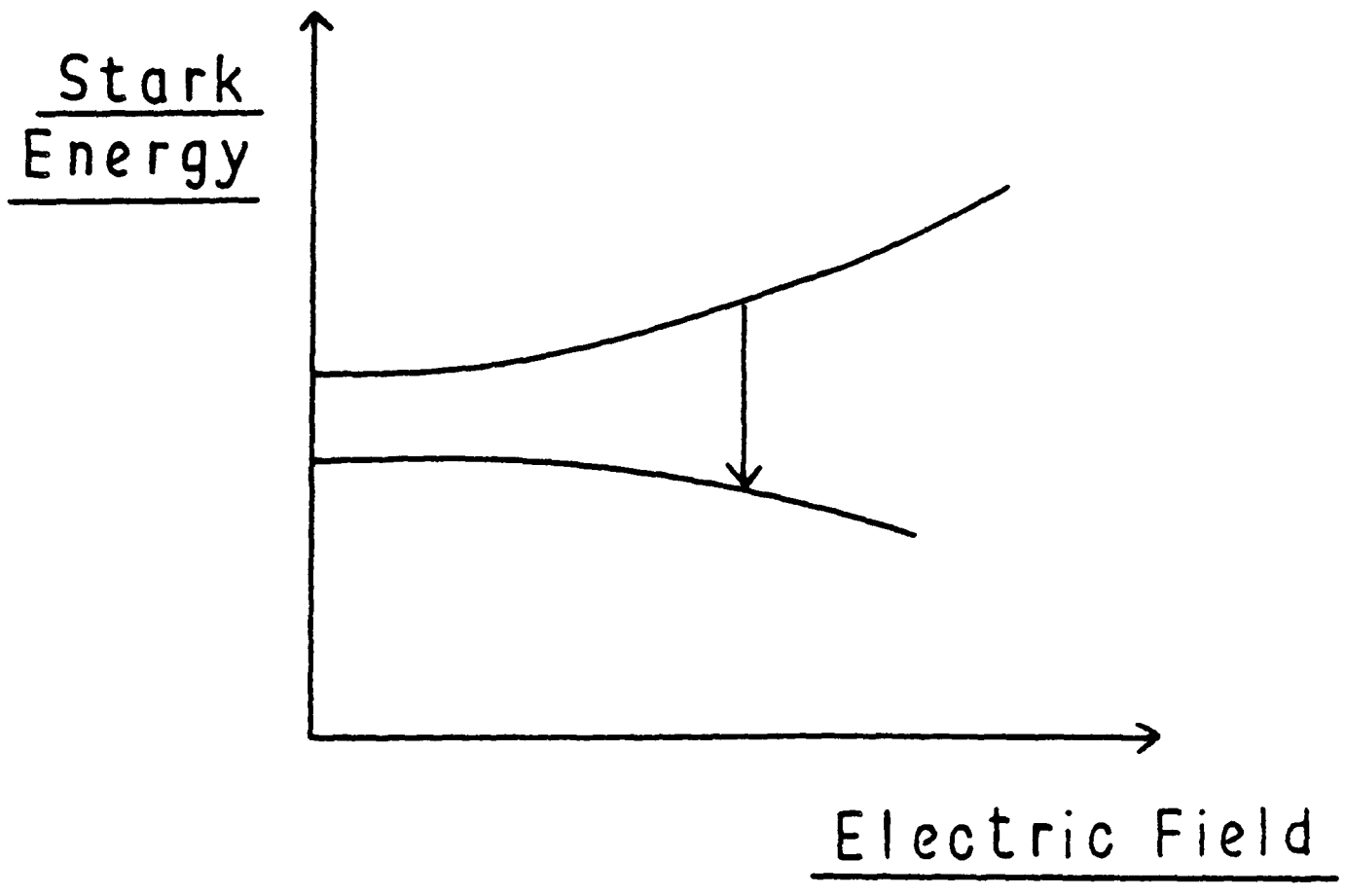


Figure 2.2 Focussing to Defocussing Transition



the beam. Thus the A and B fields can act as the analogue of an optical lens focussing molecules in positive Stark states around the stopwire and on to the detector. The purpose of the stopwire is to prevent non-polar species, particularly rare gases, from reaching the ultra high vacuum chamber.

If a spectroscopic transition occurs from a positive Stark state to a negative one; it is detected by the decrease in molecular flux at the detector (Figure 2.2). The radiation that induces these changes is applied at the C-field region normal to the molecular beam. Radiofrequency and S-band microwave radiation is coupled to the beam by a stripline field after the design of Fabricant et al.[6] This field consists of a stripline plate (of dimensions 1.6" x 10") held parallel to a ground plate at a separation of 0.32" by teflon spacers. The two are connected by a series of resistors in parallel to obtain the 50 Ohm impedance that correctly terminates the transmission line. This alleviates the problems with R.F. standing waves that have been encountered with other C-field designs. An S-band microwave horn with a coaxial transformer is also available. Higher frequency microwaves are propagated inside the main chamber from an open ended piece of X-, K- or R-band waveguide with a mica window as vacuum seal (again normal to the beam).

This perpendicular arrangement of radiation and molecular beam removes most of the Doppler broadened contribution to the spectroscopic linewidth. For the stripline field linewidths are generally limited by the molecule's transit time during irradiation. For a beam moving at about 300 ms^{-1} the time taken to traverse the field is about 1/1200 s indicating a linewidth of about 2 kHz or less. The predicted linewidth is greater for radiation delivered from the waveguide and in practice divergence

of the microwaves leaving the guides leads to some Doppler broadening. It should be pointed out that these idealised linewidths are rarely attained unless great care is taken with each transition to avoid the application of too much power. The effect of power broadening on molecular beam line shapes in terms of a 2-level model has been discussed by Dyke et al.[7]

Also located in the main chamber are two sets of buffer fields. The purpose of these is to reduce the abrupt changes in electric field that a molecule experiences on passing through and between the quadrupole field regions. Sudden changes in the electric field result in Fourier components that can excite unwanted transitions in the moving molecules. These Majorana transitions cause a loss of space quantisation but the problem is alleviated by applying a potential of 500 V or greater on the buffer fields. (This is provided by a Brandenburg 476-R (0-2.5 kV) power supply.) The maintenance of space quantisation is further assisted by arranging for two of the rods of each focussing field to be slightly (~1 cm.) longer than the other pair.

For the optimum performance of the spectrometer an accurate alignment of the A, B and C fields (as well as the detector) with the axis between the nozzle and detector entrance was found to be essential. This was checked and corrected regularly with the aid of a Spectra Physics 155 (95 mW) He-Ne laser. The accuracy of this alignment was assessed in terms of the percentage refocussing of a calibrant molecule defined by the relation :

$$\text{REFOCUSSING} = (R-S)/(T-S) \times 100\% \qquad (2.1.10)$$

where R, T and S are the refocussed, straight through (A,B=0,0 kV and stopwire out) and stopped (stopwire in) beam intensities. The two calibrants most commonly used were OCS (yielding typically

refocussing of 160% at ~300 K) and NO (up to 1000% at ~120 K).

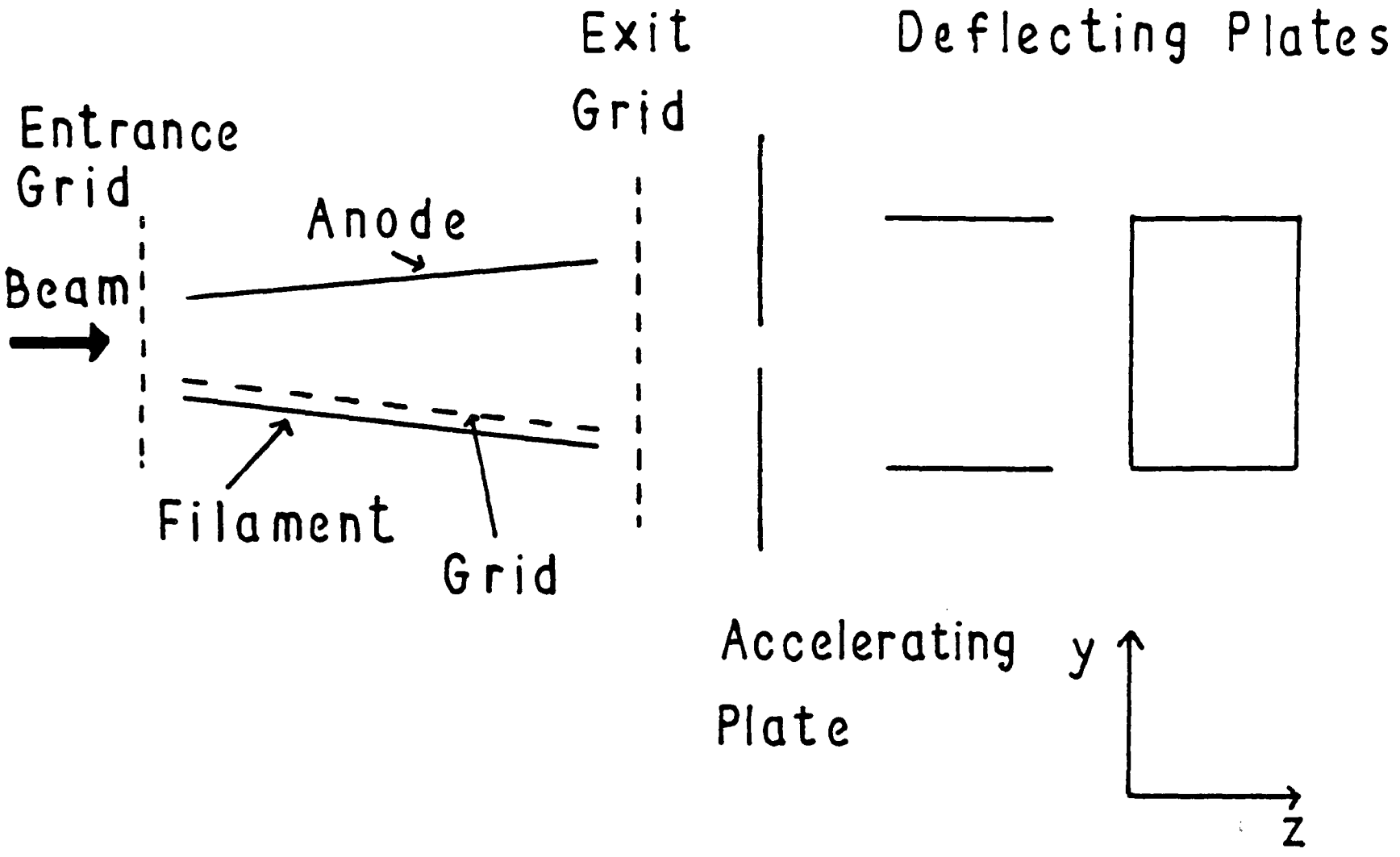
2.1 c) The Detector Chamber : The Weiss Ioniser

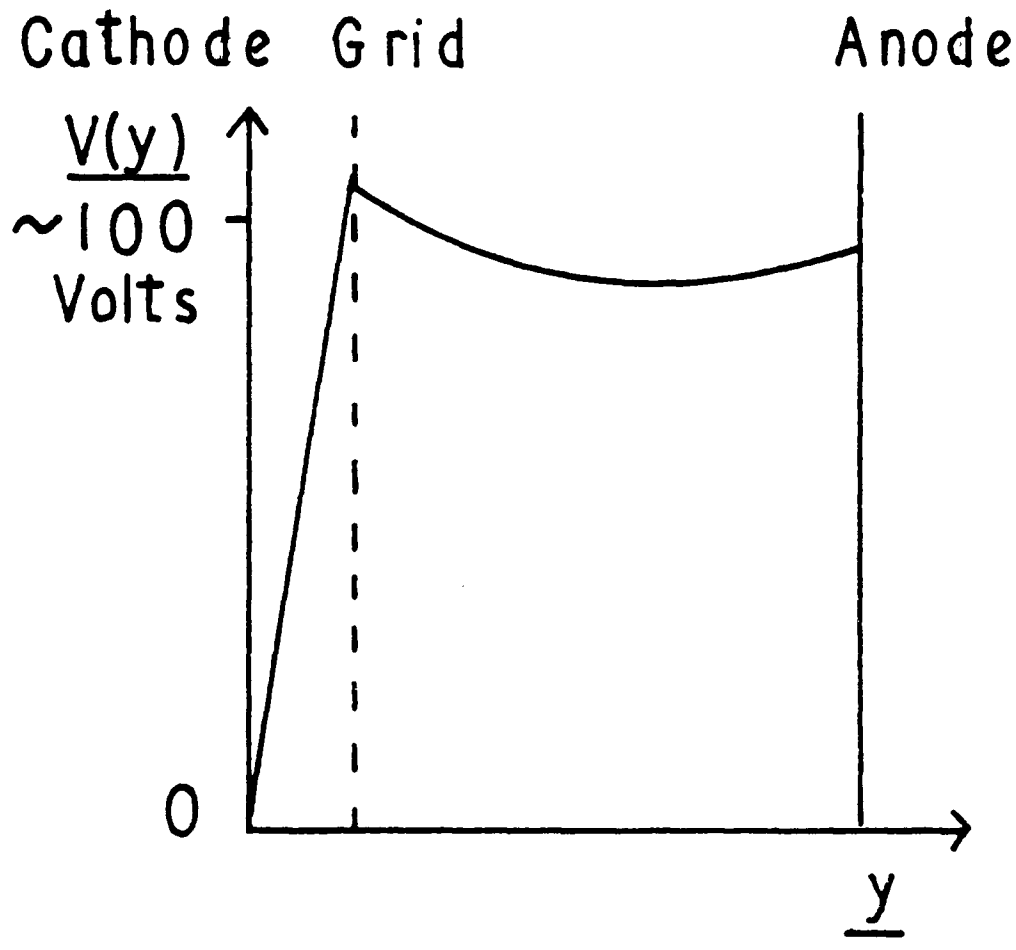
In the detector chamber the molecules in the beam are ionised, mass selected and directed on to an electron multiplier tube. The first of these processes involves a Weiss[8] ioniser; a diagram of this shown in Figure 2.3 . In this device a large thermionic emission of electrons from the filament (tungsten coated electrophoretically with thoria) causes a build up of space charge between the grid and anode. The latter two electrodes are maintained at about 80 to 100 volts . A potential minimum therefore results between them as shown in the figure . Ions produced by electron bombardment are therefore focussed into this channel in the potential. A slight divergence of the grid-anode separation and the polarity of the filament heating voltage causes the minimum in the space charge potential to become deeper along the z-direction. Hence the ions are ejected from the ioniser with a small velocity distribution.

The whole gun assembly is floated at 2.8 kV and this induces the uniform motion towards the grounded accelerating plate. The accelerated ion beam is then focussed and deflected by further electrostatic fields towards the mass analyser. Entrance and exit grids enhance the performance of the ioniser. The efficiency of the Weiss ioniser is estimated to lie between about 0.1 and 0.01%. This figure, which is high compared with values for commercial mass spectrometers, is essential to the sensitivity of the spectrometer.

The mass analyser is a 60 degree sector arrangement with two magnetic coils providing the deflection. A pair of adjustable

Figure 2.3 The Weiss Ioniser





Form of the Space Charge Potential.

slits allow higher resolution when required although extra beam intensity is usually more important at the lower mass numbers. The electron multiplier is an E.M.I. 9643/4B tube containing 11 dynodes and a gain ranging between about 600 at 1.50 kV and 120,000 at 2.45 kV. The output current, typically about 0.3×10^{-7} A for a van der Waals molecule, is measured by a Keithley 610CR solid-state D.C. electrometer.

A potentiometer driven by a synchronous motor allows a continuous sweep of the voltage on the magnetic coils. Mass spectra may therefore be recorded directly from the output of the D.C. electrometer. The presence of multiply ionised thorium peaks in the background spectrum (originating from thoria evaporation from the filament) facilitates the calibration as is illustrated later in Figures 4.7 and 5.3.

The present arrangement has two serious weaknesses. The first is that the pumping system is rather inadequate for rare gases causing a gradual increase in background pressure during operation. Purging the detector chamber with a few torr of dry oxygen alleviates the problem and regenerates the action of the ion pumps which are disabled by the rare gases. The second limitation arises because the detector is bulky and not easily moved. Hence only "flop-out" transitions can be observed effectively introducing further selection rules for allowed transitions. The use of a liquid helium cryopump or turbo-molecular pump is being considered and would enhance the removal of the rare gas background. This could be incorporated with a quadrupole mass filter to enable the observation of "flop-in" transitions but only at the expense of the high sensitivity currently achieved with the Weiss ioniser.

2.2 Method of Operation

2.2 a) The Detection Electronics

The previous paragraphs have indicated how the spectrometer yields an electrometer current which is proportional to the number of detected ions at a given mass to charge ratio. For ideal cases resonances could be observed directly as a decrease in this current for a given irradiation frequency. In practice, however, for van der Waals species it is necessary to employ phase sensitive detection to enhance the sensitivity of the experiment.

To exploit this form of detection a ~14 Hz modulation of the source radiation is applied. Thus the effects of any molecular transitions on the output current of the electrometer will also be modulated at this frequency. The output then passes through a 14 Hz notch filter and amplifier (gain ~6) and so to the input of a Brookdeal 9401 lock-in amplifier. A 14 Hz reference is provided from the modulation source. Hence the lock-in amplifier outputs a signal proportional to any 14 Hz components of the input current which bear the correct, preset phase relationship to the reference. The output from the lock-in amplifier may then be displayed directly on chart paper or directed to the Varian V-71 dedicated computer for signal processing.

In the present work two calibrations were made regularly in order to derive the maximum advantage from the detection electronics. The exact frequency for modulation was varied to correspond to the optimum bandpass of the notch filter. Once this frequency had been set the phase adjustment was made. The latter was achieved by minimising the observed signal from a strong

lambda-doubling transition (431.1905 MHz) of nitric oxide and then displacing the phase by exactly 90 degrees.

2.2 b) Radiation Sources : Search and Phase-Lock Modes

The electric resonance experiment requires tunable radiofrequency and microwave radiation sources which can be suitably modulated for phase sensitive detection. In addition, in order to take advantage of the inherently high resolution , the oscillators must be capable of high frequency stability. Two general modes of operation are distinguished. The first, the search mode, employs an artificial F.M. or white noise broadening of the radiation. This effectively increases the linewidth of a molecular transition and thus greatly increases the rate of frequency scanning. The empirical criterion for the latter is that the time taken to sweep through a linewidth should not be appreciably less than three detector time constants. Faster searching than this leads to distortion of the lineshape and ultimately to loss of intensity. Once the approximate position of a line has been determined in this search mode an accurate measurement is required. This necessitates the stabilisation of the frequency of the radiation source which is achieved by the use of a phase-locked loop.

Radiofrequency Radiation, 100 kHz - 180 MHz

The source used for this frequency range is a Solartron 4601 frequency synthesizer. This device contains internal phase-lock circuitry automatically providing radiation at a frequency stable to a few parts in 10^8 . The frequency may be set by a series of

manual digital controls or swept digitally under the control of the Varian computer. 100% amplitude modulation of the R.F. signal (necessary for phase sensitive detection) is achieved by a coaxial relay switch driven by a 14 Hz square wave. In search mode frequency modulation (up to 100 kHz) may also be applied to the sinusoidal output of the synthesizer.

R.F. and Microwave Radiation, 100 MHz - 18 GHz

The main radiation sources used to cover this region comprised a series of solid-state oscillators and heterodyne plug-in units which were all compatible with a Hewlett-Packard 8620C sweep oscillator mainframe. The maximum levelled output power of these composite devices ranged from 5 mW for the H.P.8620A (12.4 - 18.0 GHz) to 40 mW for the H.P.86330B unit (1.8 - 4.2 GHz). The experimental arrangement used for searching with these oscillators is shown in Figure 2.4a .The output frequency of the mainframe may be swept by stepping motor but, for the present work, this was achieved by voltage ramping the device. To broaden the radiation either white noise from a Zener diode circuit or a 5 kHz sine wave (from the Solartron synthesizer) was applied as frequency modulation. This modulation source was then itself 100% amplitude modulated at about 14 Hz using a solid state switch (Motorola MC 14016 BCP) driven by a square wave from a Hewlett-Packard 3311A function generator.

Thus one half cycle of the solid-state oscillator output consists of a relatively pure frequency (with about 100 kHz of "residual F.M."), whilst the other contains a broader band of frequencies displaced to either side of that of the pure half cycle. The mechanism for phase sensitive detection is therefore

Figure 2.4a) Noise Broadened Spectroscopy.

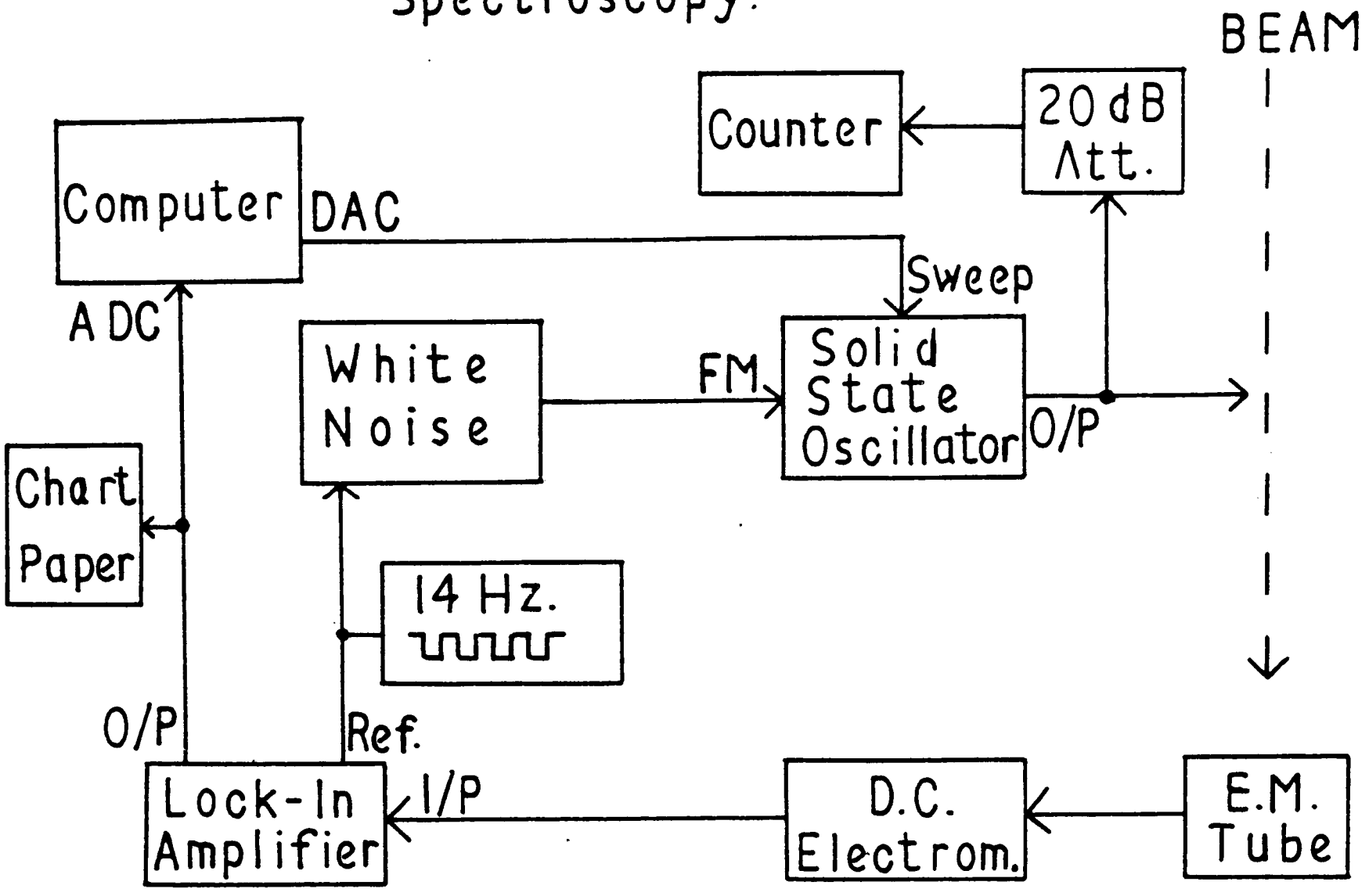
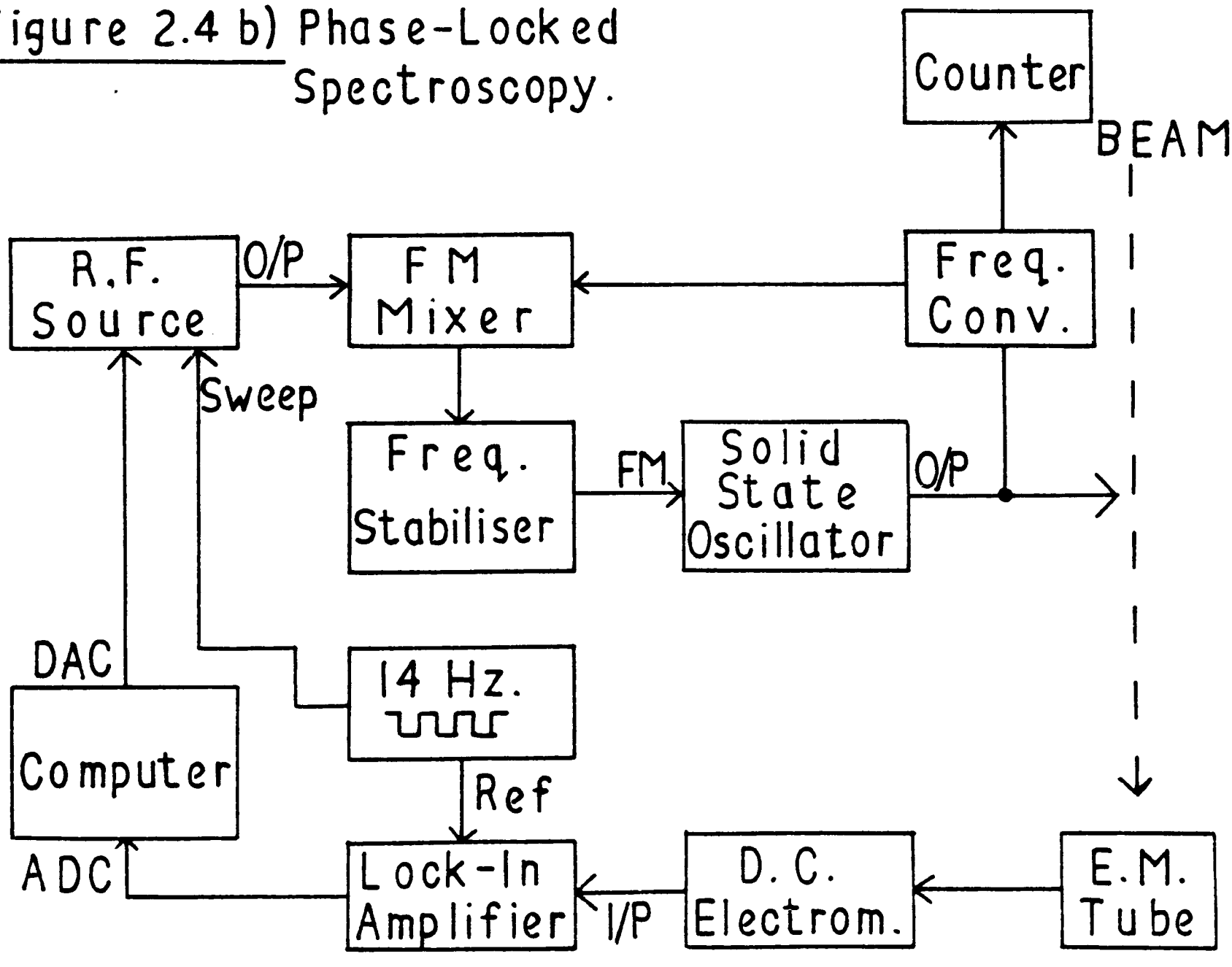


Figure 2.4 b) Phase-Locked Spectroscopy.



as follows. As a spectral line is scanned, a signal is excited first by the broadened half cycle and detected until the unmodulated frequency coincides with the transition frequency. A "modulation dip" then results since no signal is detected whilst the transition is being induced in both half cycles of the radiation. The centre frequency then passes out of resonance and a signal is observed again until the noise broadened envelope has also passed through the transition frequency.

Up to 400 MHz the output frequency of the solid state oscillator was measured directly with an H.P.5345A digital counter. The measurement of frequencies between 0.4 and 18 GHz required the additional use of plug-in frequency converters the output of which was displayed on the counter.

Once the position of a line had been established to within about 1 MHz, an accurate measurement of the centre frequency was made using a phase-locked oscillator. The experimental arrangement which was used to thus stabilise the source is shown in Figure 2.4b . Part of the output of the oscillator is fed to a frequency converter and counter. The resulting R.F. beat frequency is combined with a signal from the Solartron synthesizer using a Hatfield Mixer (Modulator type 1750, 0.5 - 300 MHz). The frequency of the Solartron is chosen such that the sum or difference beat frequency produced by the mixer is approximately equal to 40.884 MHz. The latter is the frequency of a temperature-stabilised crystal oscillator in the Microwave Systems MOS-5 frequency stabiliser. The two are thus compared and a correction voltage, generated by the latter, is applied to the solid-state oscillator completing the phase-locked loop.

The necessary frequency modulation of the output of the slave solid-state oscillator is achieved by applying a 14 Hz

square wave sweep voltage to the Solartron. This causes the frequency of the two half cycles of the latter (and hence also of the phase-locked oscillator) to differ by typically about 100 kHz. Spectral lines are therefore detected twice in a scan with the two features being of opposite sign and spaced by this phase separation. The frequency output of the solid-state oscillator is scanned by digitally sweeping the Solartron output. For accurate determination of line centres, spectra were recorded with slow scans of increasing and decreasing frequency, in order that the measured average would be free from time constant errors.

Accurate calibration of a scan is gained by measuring the exact frequencies of each phase at the two end points using the Hewlett-Packard counter. An alternative scheme for phase locking which does not require an external oscillator was utilised in a double resonance experiment illustrated in Figure 4.14 of Chapter 4.

Microwave Radiation, 8 - ~50 GHz

An alternative, though generally less convenient, source of microwave radiation is the reflex klystron. This device exploits the radiation emitted by an accelerating electron beam traversing a microwave cavity. The radiation may be tuned either, electronically over small ranges, or mechanically by varying the length of the resonant cavity. Noise broadening may be applied and phase-lock stabilisation achieved as for solid state oscillators. These devices have the advantage of higher output powers; for example, that for the OKI 20V10 ranges between 120 mW at 18 GHz and 450 mW at 22 GHz. Klystrons are susceptible to uneven rates of scanning and mode hopping, however. A cavity

wavemeter is used to measure microwave frequencies which are above 18 GHz.

2.2 c) Amplification of Radiation

As explained earlier great advantage is to be gained in the scanning rate by the application of noise broadening to the radiation. This does have the accompanying disadvantage of reducing the incident power per unit bandwidth. For the complexes studied in this thesis, ArNO and NeNO, the μa and μb components of the electric dipole moment were of the order of, or smaller than, the rather small NO moment, 0.15872 Debye. Thus the transition moments for the complexes were expected, and found to be, correspondingly small. This indicated a need for high power densities if the spectra were to be successfully recorded in a reasonable period of time. Indeed the use of R.F. and microwave amplification proved crucial to the study.

In the radiofrequency region up to 1 GHz an ENI 603L solid state power amplifier was used. This broadband device provides up to 3 Watts of R.F. power with a gain of about 40 dB. In the applications described in Chapters 4 and 5 the amplifier was driven with the output of a solid-state oscillator attenuated by 10 to 16 dB. A Bird R.F. power meter was used to monitor the power level being fed to the stripline field, to avoid damaging the termination resistors.

In the microwave frequency region two travelling wave tube (T.W.T.) amplifiers were employed: a Hughes 1177H15 (8 - 18 GHz, gain ~ 35 dB) and a Keltec CR620-10 (4 - 8 GHz, gain > 40 dB). The T.W.T. amplifier is another broadband device whose operational principles are similar to those of the klystron but

without a resonant cavity. An electron gun provides a beam of electrons produced by thermionic emission and these are focussed by magnetic fields and directed along the tube to a collector. Wound around the axis of the electron beam is a wire helix to which the R.F. signal requiring amplification is applied. The pitch of the helix is such that the R.F. phase velocity is made synchronous with the electron beam. Interaction of the two then causes velocity modulation of the electrons and a concomitant amplification of the R.F. source.

The actual gain of these devices is typically greater than 40 dB and great care is necessary to prevent damage being incurred from reflected microwave power. One or more circulators or isolators (for example, Micronde R462605 : 4 - 8 GHz) were therefore installed between the output of the amplifier and the C field. It was also found necessary to level the output of the oscillators used to drive the T.W.T. since their unlevelled output was a very uneven function of frequency. A point contact diode (Omni Spectra 20090, 0.01 - 12.0 GHz) or crystal (H.P.X424, X-band) detector was used to generate the voltage for an external levelling loop. The power applied to the C field was varied by attenuation of the microwave input power to the T.W.T. A crude estimate of the output power of the Keltec T.W.T. was made by displaying the voltage generated at the diode on a cathode ray oscilloscope and assuming a sensitivity of about 300 mV/mWatt from the manufacturer's specifications.

No amplification was available for radiation between 1 and ~3.6 GHz in the present work although lower frequency T.W.T.'s do exist. This proved to be a significant disadvantage since it transpired that many transitions in the molecule, ArNO, were expected at frequencies a little higher than 1000 MHz.

2.2 d) Signal Processing : The Varian V-71 Computer

Although a detection time constant of up to 100 seconds was available from the lock-in amplifier, the use of computer signal averaging was found to be preferable. This was because slow drifts in the source and detector conditions often caused noise with this order of time constant. For this procedure the Varian V-71 dedicated computer was used to store and average a given part of the spectrum in 511 memory locations. The computer also generated the necessary multiple digital sweeps or voltage ramps which determined the rate of scanning of the frequency synthesizer and the solid-state oscillators. An executive program ,BICEP, written by Peter Francis of Southampton University, provided the control of all the peripheral devices as well as digitising and storing the spectra. The program also enabled smoothing and plotting of the recorded spectra as shown, for example, in Figure 4.9 of Chapter 4.

Chapter 2 : References

1.N.F.Ramsey, Molecular Beams, Clarendon Press, (1956)

2.A.Kantrowitz and J.Grey, Rev.Sci.Instr. 22, 328, (1951)

3.H.Ashkenas and F.S.Sherman, Rarified Gas Dynamics, 4th. Symp. Vol II, Academic Press, (1966)

4.J.B.Anderson and J.B.Fenn, Phys.Fluids, 8, 780, (1965)

5.W.L.Meerts,G.Ter Horst,J.M.L.J.Reinartz and A.Dymanus, CP, 35, 253, (1978)

6.B.Fabricant,D.Krieger and J.S.Muenter, JCP, 67, 1576, (1977)

7.T.R.Dyke,G.R.Tomasevich,W.Klemperer and W.E.Falconer, JCP, 57, 2277, (1972)

8.R.Weiss, Rev.Sci.Instr. 32, 397, (1961)

Chapter 3 : A Theory For The Rotational Energy Levels Of Rare Gas - Nitric Oxide Complexes In The Ground Vibronic State

3.1 Introduction

3.2 The Foundations for the Derivation of the Quantum Mechanical Hamiltonian

3.3 The Choice of Basis Set

3.4 The Symmetry of the Basis Set Under Space Fixed Inversion

3.5 The Molecular Hamiltonian

3.6 Treatment of Terms Off-Diagonal in Electronic State and Estimation of Hyperfine Parameters

3.7 A Simplified Picture of the Fine Structure

3.8 Electric Dipole Transition Intensities

3.9 Postscript - Contributions from the Vibrational Hamiltonian

---

Chapter 3 : A Theory For The Rotational Energy Levels Of Rare Gas - Nitric Oxide Complexes in the Ground Vibronic State

3.1 Introduction

In this chapter a model Hamiltonian for the rotational energy levels of rare gas-nitric oxide complexes will be developed. As a starting point it is instructive to review briefly the results of previous work on the spectroscopy of more strongly bound molecules containing unpaired electrons.

The first feature of interest is that the effects attributable to the unpaired electrons depend critically upon whether the triatomic molecule has a linear equilibrium geometry. In particular, studies of species such as NCO[1] and NCS,[2] which are linear and have a degenerate ground electronic state, have revealed that the orbital motion of any unpaired electrons is essentially unquenched. Hence it might be predicted that their rotational spectra would broadly resemble those of open-shell molecules such as NO[3] or OH[4]. In practice, however, a coupling occurs between the electronic orbital angular momentum and the degenerate bending vibration. This interaction, known as the Renner or Renner-Teller Effect, complicates the spectra considerably.

The lower symmetry of non-linear, conventional triatomic molecules causes a quenching of the orbital motion of any unpaired electrons. One of the best studied examples of these molecules is HCO. Bowater, Brown and Carrington[5] have used the technique of electron paramagnetic resonance to measure the transition frequencies of hyperfine components of a K-doublet (N = 2) as a function of applied magnetic field strength. Assuming

that the orbital angular momentum was predominantly quenched, they obtained a satisfactory analysis of the spectrum in terms of a Hund's Case (b) coupling of the electronic spin to the nuclear rotation. That is :

$$\underset{\sim}{N} + \underset{\sim}{S} = \underset{\sim}{J} \qquad (3.1.1)$$

$$\underset{\sim}{J} + \underset{\sim}{I} = \underset{\sim}{F}$$

The Hamiltonian that Bowater et al. employed may be formulated as :

$$H = A_0 N_a^2 + B_0 N_b^2 + C_0 N_c^2 \qquad (3.1.2)$$

$$+ \{ \varepsilon_{aa} N_a S_a + \varepsilon_{bb} N_b S_b + \varepsilon_{cc} N_c S_c$$

$$+ 1/2(\varepsilon_{ab} + \varepsilon_{ba})(N_a S_b + S_a N_b) \}$$

+ Centrifugal Distortion, Hyperfine and

Magnetic Field Terms.

Na,b,c are the operators for the molecule-fixed components of the rotational angular momentum plus small orbital contributions due to the electrons. The latter arise from the admixture of excited electronic states via the spin-orbit interaction. The terms in Na.Sb represent the interaction between the magnetic moments of the rotating nuclear framework with that originating from the spin of the unpaired electron. In such a formulation the uncoupling of any induced orbital motion frequently results in a large magnitude for the parameter ε_{aa} .

Previous studies of the intermolecular potentials of the Ar-NO and Ne-NO systems (to be reviewed in Chapters 4 and 5) have indicated a potential minimum consistent with an equilibrium structure far removed from linearity. In the case of Ar-NO an equilibrium angle of about 90 degrees, between the NO internuclear and rare gas to NO centre of mass axes, is

predicted. In the first instance therefore it was concluded that an asymmetric rotor treatment of the complexes would be required rather than the more simple Hamiltonian for a linear complex. In fact the model subsequently developed proved appropriate to the treatment of open-shell diatomic molecules as well as asymmetric tops.

From the foregoing discussion it might be expected that a Hamiltonian such as (3.1.2) would be suitable for reproducing the rotational spectra of ArNO and NeNO. There is, however, good evidence to support a departure from an analysis following such precedents of conventional molecules.

In chemically-bound triatomic molecules such as HCO the quenching of orbital motion arises because of a lack of axial symmetry in the electric field due to the nuclei and other electrons. In ArNO and NeNO the rare gas nucleus and electrons are far more remote (a typical van der Waals "bond length" is 3 - 4 Angstroms) and hence the electrostatic potential near to the diatom will be of smaller magnitude. In competition with this quenching potential is the electronic spin-orbit interaction which induces orbital angular momentum about the NO axis. The work of Nielson, Parker and Pack[6] established an estimate of the difference potential for Ar-NO to be about 1.5 cm-1 near the potential minimum, to be compared with a value of about 120 cm-1 for the nitric oxide spin-orbit coupling constant.

An analogy may be drawn here with the orbital angular momentum contribution to the paramagnetism of transition metal complexes.[7] For the First Row transition metal ions the lowering of symmetry due to the ligand electrostatic field often causes nearly complete quenching of the orbital angular momentum. The paramagnetism is then well described by a "spin only" formula.

For much heavier ions, for example those of the Lanthanides, the effect of the ligands is small compared with the spin-orbit coupling interaction. The paramagnetism is then better interpreted in terms of a slight quenching of the orbital angular momentum under the perturbation of a crystal field environment. The behaviour of the orbital motion in rare gas - nitric oxide complexes will be closer to the latter part of this analogy; in this case it is the reduction of axial symmetry due to the rare gas atom which causes the slight quenching of orbital angular momentum.

Further evidence for the departure from conventional theory is provided by a preliminary investigation of the ArNO complex by the author.[8] He observed a large number of radiofrequency transitions (about 20 in total) at frequencies close to or less than 1 GHz. An attempt was made to analyse the spectra in terms of a Hamiltonian similar to (3.1.2) but the pattern of energy levels predicted was quite incompatible with a large number of radiofrequency transitions. It seems most likely therefore that the failure to account for such radiofrequency spectra stems from an inadequate treatment of the orbital part of the problem.

In the rest of this Chapter a Hamiltonian is developed assuming a non-linear equilibrium geometry for these complexes with only partial quenching of the orbital angular momentum of the unpaired electron. Much of the theory is similar to that already derived for open-shell diatomic molecules. However, the theory needs to be extended for use in asymmetric rotors with unquenched, or only partially quenched, orbital angular momentum.

3.2 The Foundations for the Derivation of the Quantum Mechanical Hamiltonian

The preceding discussion has indicated that a model for the rotational spectra of rare gas - nitric oxide van der Waals molecules should include explicit treatment of the spin and orbital angular momenta of the unpaired electron. In addition hyperfine effects due to the quadrupolar nitrogen nucleus (I=1, for ^{14}N) are likely to be important. In this section an outline is given of the origins of the terms that appear in the exact Hamiltonian for an open-shell, asymmetric rotor with a quadrupolar nucleus. The number of terms in the exact Hamiltonian is too large for the construction of a rigorous effective Hamiltonian for ArNO or NeNO. By the latter expression is meant a Hamiltonian which contains operators restricted to operate only within a certain vibronic state but which includes the effects of non-adiabatic operators to a prescribed order of perturbation theory. Some of the terms that would appear in such an effective Hamiltonian may still be of importance however.

The total Hamiltonian for a translating, rotating and vibrating molecule may be summarised by the following expression defined in a coordinate system fixed in space.

$$H_{tot} = \sum_{\alpha} \frac{p_{\alpha}^2}{2M_{\alpha}} + \sum_{i} \frac{p_i^2}{2m} + V(X_i, X_{\alpha}) \qquad (3.2.1)$$

$$+ H(\underset{\sim}{S}) + H(\underset{\sim}{I})$$

$$+ H(E,B)$$

In this expression the first two terms represent the kinetic energy of the nuclei and electrons and the third term includes all simple Coulombic interactions which depend on the positions

of the electrons (Xi) and nuclei (X_a). The operators H($\underset{\sim}{S}$) and H($\underset{\sim}{I}$) take into account those magnetic effects which may be attributed to electronic and nuclear spin. Finally the last term allows for the influence of an electric (E) or magnetic (B) field on the energy levels of the molecules.

It would clearly be desirable to be able to separate out from Htotal the operators describing the well known rotational, vibrational and electronic behaviour of molecules. A procedure for achieving such a separation was first described by Born and Oppenheimer.[9] More recently the factorisation of the total Hamiltonian for open-shell diatomic molecules has been reviewed by Carrington et al.[10] Other authors have extended this treatment to a general, polyatomic molecule.[11]

In order to separate the various motions of a molecule a series of transformations to a new coordinate framework is usually invoked. Thus the first and relatively straightforward transformation is to a coordinate system which translates with the molecular centre of mass (of both nuclei and electrons), but which has axes parallel to those of the space-fixed system in which Htotal was defined. The effect of such a transformation is to remove the translational motion from the Hamiltonian; this separation is completely valid in the absence of external electromagnetic fields. Since the only influence of molecular translation observed in most spectroscopic experiments is the perturbation of measured linewidths, (for example due to Doppler or Uncertainty broadening) this transformation is almost universal in the derivation of molecular Hamiltonians.

The factorisation of Htotal is further facilitated by the assumption that the nuclear motion is slow compared with that of the electrons. This enables the so called "clamped nuclei"

approximation whereby Htotal is partitioned into a sum of terms describing electronic motion in a static nuclear framework, nuclear rotation and cross terms between the two. The effect of this approximate separation is described by the equation[10]:

$$H_{tot} = H_m^e + H_r^n + H_v^n \qquad (3.2.2)$$

Hm is the approximate Hamiltonian for the motion of the electrons in a static, rigid nuclear framework and it neglects the perturbing effect of any external electric or magnetic fields. Hv and Hr contain the operators for nuclear vibration and rotation respectively. The Correction Terms include effects neglected by the previous three operators as well as cross terms between them; they are usually evaluated by perturbation theory and added to the appropriate operator He or Hn.

Associated with this factorisation of Htotal is the partitioning of the total wavefunction into the following product form appropriate for a diatomic species[10]:

$$\Psi_{tot} = \psi_\eta^e(X_i, R_\alpha).\psi_\eta^N(R_\alpha).\psi_\eta^N(X_\alpha) \qquad (3.2.3)$$

where $\psi e(Xi,R)$ denotes the essentially electronic part of the total wavefunction and $\psi n(R)$ and $\psi n(Xa)$ are the parts corresponding to nuclear vibration and rotation. R is the internuclear separation. An analogous factorisation may be effected for a polyatomic molecule but allowance must be made for the additional rotational and vibrational degrees of freedom.

In order to remove the dependence of the electronic part of the Hamiltonian (He) on the orientation of the nuclear framework in space, it is necessary to transform the electronic coordinates to the rotating axis system in which the separated nuclear motion is described. At this point a choice may be made whether to

transform the electronic spatial coordinates or both electronic spatial and spin momenta to the molecule-fixed representation. These two possibilities correspond to Hund's Coupling Cases (a) and (b) respectively. Such transformations have an important effect on the rotational part of the Hamiltonian. (This subtle effect has its origins in the transformation properties of the Laplacian operator.[10]) An operator $\underset{\sim}{R}'$ (the prime denotes that the electronic coordinates are now referred to the molecular axis system) for the rotational angular momentum of the nuclear framework is now given by the expressions :

$$\underset{\sim}{R}' = \underset{\sim}{J} - \underset{\sim}{P} \qquad \text{for Case (a)} \qquad (3.2.4)$$

$$\underset{\sim}{R}' = \underset{\sim}{K} - \underset{\sim}{L} \qquad \text{for Case (b)} \qquad (3.2.5)$$

where J denotes the total angular momentum (excluding nuclear spin), P the total electronic angular momentum and K the sum of rotational and electronic orbital momenta.

Following the coordinate transformations outlined above the total Hamiltonian has been partitioned in a way that allows the rotational motion of the molecule to be treated separately within a given vibronic state. It is still necessary, however, to understand and quantify the influence of the electrons on the rotational intervals. This requires a relativistic quantum mechanical treatment of the electron spin, the starting point for which is usually the Dirac Hamiltonian for a single electron.

At the end of this procedure the Hamiltonian relevant to the rotational spacings of a given vibronic manifold may be shown to consist of the following terms[10] :

$$H = H_r^n + H_{fs} + H_{hf} + H_z + H_e \qquad (3.2.6)$$

Hr and Hfs are operators for the rotation of the nuclei and for fine structure effects arising from the electronic motions

respectively. Hhf includes all interactions arising from any nuclear spin angular momenta present in the molecule. Finally Hz and He describe the perturbing effect of external magnetic and electric fields on the rotational energy levels.

Each of these terms is discussed in more detail in the following sections for their application to the interpretation of the spectra described in Chapters 4 and 5. The influence of the vibrational part of the total Hamiltonian, Hv, has not been included in H. This is because it makes a constant contribution to all rotational energy levels of a given vibrational state in so far as the Born-Oppenheimer Approximation is valid. When this assumption proves inadequate the neglected cross terms between the rotational and vibrational motions may be included by the perturbation procedure known as centrifugal distortion.

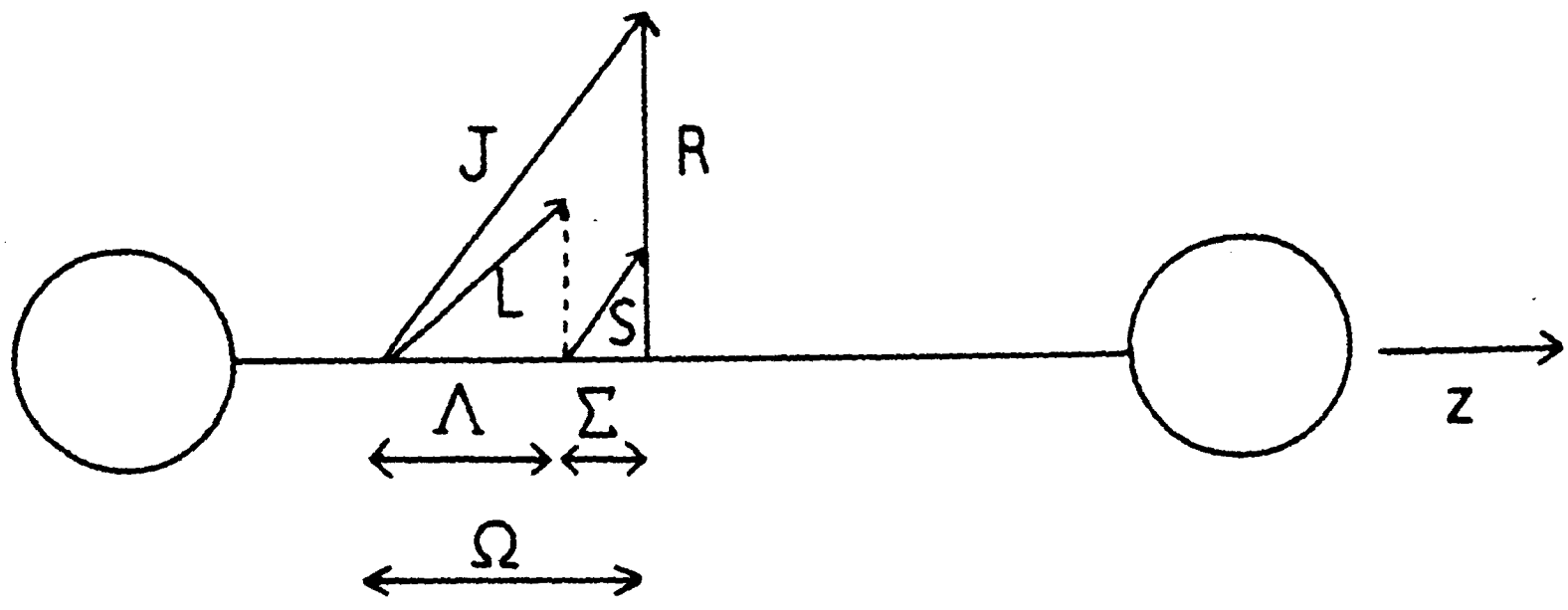


Figure 3.1: Hund's Case a) Coupling in a Diatomic Molecule.

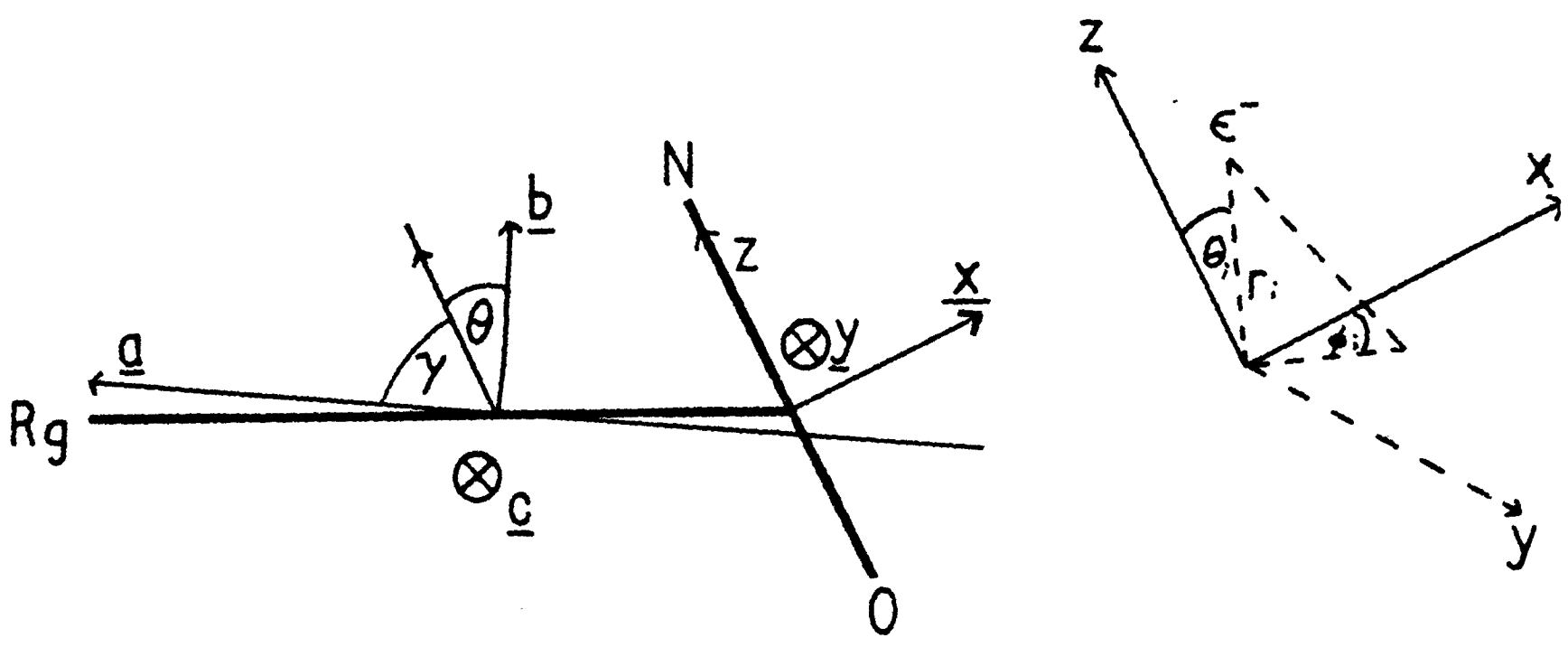


Figure 3.2: The Various Coordinate Systems For the RgNO Complexes.

3.3 The Choice of Basis Set and Molecule-Fixed Axis Systems

As described in the previous sections the form of the rotational basis set (and hence also of Hr) will depend upon the choice of angular momentum coupling scheme. For this choice the assumption is made that the motion of the unpaired electron is characteristic of the NO sub-molecule, somewhat perturbed by the presence of the rare gas atom. For NO^{12} the energy of the electronic spin-orbit interaction ($\sim$ 120 cm-1) is much greater than BJ (B_{NO} $\sim$ 1.6 cm-1) for at least moderately low J. Hund's Case (a) therefore provides a suitable description of the coupling of the angular momenta in NO and should also be adequate for the treatment of ArNO and NeNO.

A vector diagram for Hund's Case (a) coupling in a diatomic molecule is shown in Figure 3.1 . L the orbital angular momentum is strongly coupled to the internuclear axis with a component Λ . In the non-rotating limit for a diatomic molecule, Λ is a good quantum number due to the cylindrical symmetry of the electric field about the internuclear axis. The conservation of motion represented by Λ is not exact, however, in rare gas - nitric oxide complexes due to the molecular rotation and the perturbing effect of the rare gas atom on the local electric field. Nevertheless $|L\ \Lambda>$ should be a fairly good representation of the orbital wavefunction.

The electron spin, S, is also strongly coupled to the NO axis with a projection Σ as a result of the strong spin-orbit coupling. In NO the sum of $\Lambda + \Sigma = \Omega$ is then coupled to the rotation of the nuclear framework, R, to give the resultant J. J is the total angular momentum of the system excluding nuclear spin. The coupling may be summarised :

$$\underset{\sim}{J} = \underset{\sim}{R} + \underset{\sim}{L} + \underset{\sim}{S} \qquad (3.3.1)$$

Thus a suitable basis set for describing the rotational transitions of ArNO and NeNO is a simple product function :

$$|\eta\ \Lambda;S\ \Sigma;J\ K_a\ M_j\rangle = |\eta\ \Lambda\rangle\ |S\ \Sigma\rangle\ |J\ K_a\ M_j\rangle \qquad (3.3.2)$$

In this representation η labels the vibronic state and Mj is the projection of J on an arbitrary space-fixed axis. Ka is the quantum number denoting the component of J on the molecule-fixed a-inertial axis. It is important to note that these complexes may have a component of rotational angular momentum about the NO internuclear axis. (For NO itself Rz = 0.)

In selecting a representation for the symmetric rotor part of the wavefunction, |J Ka Mj>, a Ka dependent choice of phase convention must be adopted. The convention adopted here is compatible with that of Brink and Satchler[13] :

$$|J\ K_a\ M_j\rangle = \left\{\frac{2J+1}{8\pi^2}\right\}^{1/2} \mathcal{D}^{(J)*}_{M_j,K_a}(\omega) \qquad (3.3.3)$$

Figure 3.2 shows the two molecule-fixed axis systems employed to relate the various angular momenta. The principal axes of the moment of inertia tensor are denoted (a,b,c) and, since it transpires that ArNO and NeNO have equilibrium structures characteristic of prolate, near-symmetric tops, the choice of the a-axis for the quantisation of J is advantageous. (Ka is therefore a "fairly good" quantum number.) Since the electronic part of the problem arises from the NO sub-molecule, a second axis system based on that sub-molecule is useful and labelled (x,y,z). Components of the electronic angular momenta, quantised in the (x,y,z) coordinate system, are then related to the principal inertial axes via the relations :

$$L_a = -L_x\mathrm{Cos}(\theta) + L_z\mathrm{Sin}(\theta) \qquad (3.3.4)$$

$$L_b = L_x\mathrm{Sin}(\theta) + L_z\mathrm{Cos}(\theta) \qquad (3.3.5)$$

$$L_c = L_y \qquad (3.3.6)$$

with similar formulae for the components of S. Strictly speaking a correction should be made to Equations (3.3.4) to (3.3.6) to correct L for the displacement between the origin of the (x,y,z) coordinate system and the molecular centre of mass. This problem is discussed briefly in Appendix A3.1. The two axis systems are related (apart from a small translation) by a rotation of Θ about the y- or c-axis.

To evaluate matrix elements further choices of phase convention must be made. Raising and lowering operators for the rotational and electronic wavefunctions are defined by :

$$J^{\pm} = J_b \pm i\, J_c \qquad (3.3.7)$$

$$L^{+}_{-} = L_x \pm i\, L_y \qquad (3.3.8)$$

$$S^{\pm} = S_x \pm i\, S_y \qquad (3.3.9)$$

with Ja, Lz and Sz being the operators that are diagonal in this representation. The choices of phase are made to be consistent with the original prescription of Condon and Shortley[14] who defined the matrix element of the space-fixed component of an angular momentum, J_X, (in the scheme $J^{\pm} = J_X \pm iJ_Y$) to be real and positive. Equation (3.3.3) is analogous to this convention in that the matrix element of the molecule-fixed operator, Jx, is real and positive. To maintain consistency the orbital wavefunctions are taken to be :

$$|\eta\ \Lambda\rangle = Y_{L,\Lambda}(\theta,\phi) \qquad (3.3.10)$$

where the spherical harmonics, $Y_{L,\Lambda}$ (Θi, ϕi), are as tabulated in Edmonds.[15] The subscript i is appended to the polar angles to denote an electronic coordinate and to prevent confusion with the

structural angle, Θ, of the complex as defined in Figure 3.2 .

It should be recalled that the molecule-fixed components of J have anomalous commutation properties[16] compared with those of L and S. Hence J+ is a lowering operator :

$$[J_a, J_b] = -i\, J_c \qquad (3.3.11)$$

$$[L_x, L_y] = i\, L_z \qquad (3.3.12)$$

$$[S_x, S_y] = i\, S_z \qquad (3.3.13)$$

In conclusion, if hyperfine effects are to be understood the nuclear spin angular momentum, I, must be accommodated into the basis. In this work a coupled representation will be used and so the full Case (a) basis wavefunction may be written as :

$$|n\ \Lambda;S\ \Sigma;J\ K_a;I\ F\ M_F\rangle \qquad (3.3.14)$$

3.4 The Symmetry of the Basis Set under Space-Fixed Inversion

Assuming that rare gas - nitric oxide complexes have a non-linear equilibrium geometry, they have only one molecular symmetry operation; that is, reflection in a plane containing the nuclei. ArNO and NeNO therefore belong to the Cs molecular point group.

In the absence of external electric fields parity, the symmetry under space-fixed inversion, is a good quantum label. This therefore enables the factorisation of the field-free Hamiltonian matrix. The operator for space-fixed inversion, E^*, has the following effect on a state or function of the space-fixed coordinates (X,Y,Z) :

$$E^* f(X,Y,Z) = f(-X,-Y,-Z) \qquad (3.4.1)$$

A careful consideration of the definition of the Euler angles indicates that their transformation under E* may be written[4] :

$$E^* f(\alpha,\beta,\gamma) = f(\pi+\alpha,\pi-\beta,\pi-\gamma) \qquad (3.4.2)$$

It should be noted that (3.4.2) is not unique in defining the effect of E* on the Euler angles. Application of (3.4.2) to the direction cosine matrix, (Appendix A3.2)[17] relating the molecule-fixed coordinates of Figure 3.2 to a space-fixed set (X,Y,Z), leads to the further relations :

$$E^* f(a,b,c) = f(a,b,-c) \qquad (3.4.3)$$

$$E^* f(x,y,z) = f(x,-y,z) \qquad (3.4.4)$$

$$E^* f(r,\theta,\phi) = f(r,\theta,-\phi) \qquad (3.4.5)$$

Hence the symmetry of the wavefunctions chosen in section (3.3) may be examined.

Manipulation of the rotation matrices[13] (defined by Brink and Satchler) leads to the following properties for the symmetric rotor functions :

$$E^* \mathcal{D}^{*(J)}_{M_j, K_a}(\alpha,\beta,\gamma) = \mathcal{D}^{*(J)}_{M_j, K_a}(\pi+\alpha,\pi-\beta,\pi-\gamma) \qquad (3.4.6)$$

$$= (-1)^{J-K_a} \mathcal{D}^{*(J)}_{M_j,-K_a}(\alpha,\beta,\gamma)$$

Therefore, $E^* |J\ K_a\ M_j\rangle = (-1)^{J-K_a} |J\ -K_a\ M_j\rangle$

The effect of E* on the molecule-fixed electronic spin functions is determined by relating them to a space-fixed function.[4]

$$E^* |S\ \Sigma\rangle = E^* \sum_{M_s} \mathcal{D}^{(S)}_{M_s,\Sigma}(\alpha,\beta,\gamma) |S;M_s\rangle \qquad (3.4.7)$$

$$= \sum_{M_s} \mathcal{D}^{(S)}_{M_s,-\Sigma}(\alpha,\beta,\gamma) |S,M_s\rangle \times (-1)^{S-\Sigma}$$

$$= (-1)^{S-\Sigma} |S\ -\Sigma\rangle$$

Inspection of the Φ-dependent part of the spherical harmonics describing the orbital functions indicates their symmetry under E*. For Σ states ($\Lambda=0$) there is no azimuthal dependence;[18] the symmetry under E* is then conventionally chosen and indicated by a right hand superscript, $\Sigma^{\pm}$. Hence,

$$E^* |\eta\ \Lambda\rangle = (-1)^{\Lambda+s} |\eta\ -\Lambda\rangle \qquad (3.4.8)$$

where s is an even integer for Σ^+ states, odd for Σ^- states and zero for all other states.

E* has no effect on the space-fixed nuclear spin functions nor on the vibrational part of the Hamiltonian. (It is also assumed that the ground electronic state of the rare gas atom is symmetric under E*.) The full symmetry of the basis functions is therefore :

$$E^* |\eta\ \Lambda;S\ \Sigma;J\ K_a\ M_j\rangle = (-1)^{\Lambda+s+S-\Sigma+J-K_a} |\eta\ -\Lambda;S\ -\Sigma;J\ -K_a\ M_j\rangle \qquad (3.4.9)$$

and eigenfunctions of E* with eigenvalues ± 1 are :

$$\langle \eta\ |\Lambda|;J\ |K_a|\ M_j;\pm\rangle\ =$$

$$1/\sqrt{2}\left\{|\eta\ \Lambda;S\ \Sigma;J\ K_a\ M_j\rangle \pm (-1)^{\Lambda+s+S+J-\Sigma-K_a}|\eta\ -\Lambda;S\ -\Sigma;J\ -K_a\ M_j\rangle\right\}$$

(3.4.10)

If desired matrix elements could be evaluated in a parity conserving basis :

$$\langle \eta\ |\Lambda'|;J'\ |K_a'|\ M_j;\pm|\ H\ |\eta\ |\Lambda|;J\ |K_a|\ M_j;\pm\rangle\ =$$

$$\langle \eta\ \Lambda';S\ \Sigma';J\ K_a'\ M_j|\ H\ |\eta\ \Lambda;S\ \Sigma;J\ K_a\ M_j\rangle$$

$$\pm(-1)^{\Lambda+s+S+J-\Sigma-K_a}\langle \eta\ \Lambda';S\ \Sigma';J\ K_a'\ M_j|\ H\ |\eta\ -\Lambda;S\ -\Sigma;J\ -K_a\ M_j\rangle$$

(3.4.11)

The phase factor reduces to $(-1)^{J-S+s}$ if Ka is set equal to (Λ + Σ), and this is the familiar parity appropriate to open-shell linear molecules with a $^2\Pi$ ground state.[26]

3.5 The Molecular Hamiltonian

It was shown in section (3.2) that the molecular Hamiltonian for the rotational spectrum of an open-shell molecule can be divided into the following terms :

$$H = H_r^n + H_{fs} + H_{hf} + H_z + H_e$$

The form of each of these together with the corresponding matrix elements will now be discussed.

3.5 a) The Rotation of the Nuclear Framework, Hr

From the preceding discussion and in particular from Equations (3.2.4) and (3.3.1) the suitable form for Hr is :

$$H_r^n = AR_a^2 + BR_b^2 + CR_c^2 \qquad (3.5.1)$$

$$= A(J_a - L_a - S_a)^2 + B(J_b - L_b - S_b)^2 + C(J_c - L_c - S_c)^2 \qquad (3.5.2)$$

This is analogous to the conventional rotational expression for NO but has been modified to an asymmetric top form appropriate for ArNO and NeNO. A,B and C are the rotational constants defined in terms of the moments of inertia about the principal axes ;

$$A = \frac{h\{JS\}.10^{-6}}{8\Pi^2.I_{aa}\{Kgm^2\}} \quad MHz \qquad (3.5.3)$$

with analogous expressions for B and C. Equation (3.5.2) is best treated by a further partitioning of the terms that arise from its expansion :

$$H_r^n = H_{r1}^n + H_{r2}^n + H_{r3}^n + H_{r4}^n \qquad (3.5.4)$$

$$H_{r1}^n = AJ_a^2 + BJ_b^2 + CJ_c^2 \qquad (3.5.5)$$

$$= \{A-1/2(B+C)\}J_a^2 + 1/2(B+C)J^2 + 1/4(B-C)(J^{+2} + J^{-2}) \qquad (3.5.6)$$

The final expression has been cast in a form suitable for calculating matrix elements using the raising and lowering operators defined in Equation (3.3.7).

$$H^n_{r2} = A(L_a^2 + S_a^2) + B(L_b^2 + S_b^2) + C(L_c^2 + S_c^2) \qquad (3.5.7)$$

$$\begin{aligned} &= A\left\{(L_x^2+S_x^2)\cos^2\theta + (L_z^2+S_z^2)\sin^2\theta - ([L_x,L_z]^+ + [S_x,S_z]^+)\sin\theta\cos\theta\right\} \\ &+ B\left\{(L_x^2+S_x^2)\sin\theta + (L_z^2+S_z^2)\cos\theta - ([L_x,L_z]^+ + [S_x,S_z]^+)\sin\theta\cos\theta\right\} \\ &+ C\left\{L_y^2 + S_y^2\right\} \end{aligned} \qquad (3.5.8)$$

$$\begin{aligned} &= 1/4\left(A\cos^2\theta + B\sin^2\theta - C\right)\left\{L^{+2}+L^{-2}+[L^+,L^-]^+ + S^{+2}+S^{-2}+[S^+,S^-]^+\right\} \\ &+ \left(A\sin^2\theta + B\cos^2\theta\right)\left\{L_z^2 + S_z^2\right\} \\ &+ (B-A)(1/2\sin\theta\cos\theta)\left\{[L^+,L_z]^+ + [L^-,L_z]^+ + [S^+,S_z]^+ + [S^-,S_z]^+\right\} \end{aligned} \qquad (3.5.9)$$

In the first line of (3.5.9) only the operators $L+^2$ and $L-^2$ are of importance and they are diagonal within the $^2\Pi$ electronic state. The anticommutators [L+,L-]+ and [S+,S-]+ yield a constant contribution to all rotational levels within this state and are therefore ignored. Since $\Sigma = \pm 1/2$ there are no non-zero matrix elements from the operators that are off-diagonal in Σ by two.

Of the remainder of the terms in (3.5.9) only the anticommutators [L+,Lz]+ and [L-,Lz]+ contribute to the rotational energy; they yield matrix elements off-diagonal in Λ by ± 1 and hence connect $^2\Sigma$ and $^2\Delta$ excited electronic states. Matrix elements of the corresponding electronic spin anticommutator all vanish within the $^2\Pi$ manifold.

$$H^n_{r3} = -2AJ_aL_a - 2BJ_bL_b - 2CJ_cL_c - \text{e.t.c.} \qquad (3.5.10)$$

$$\begin{aligned} &= -2AJ_a\{-(L_x+S_x)\cos\theta + (L_z+S_z)\sin\theta\} \\ &\quad -2BJ_b\{+(L_x+S_x)\sin\theta + (L_z+S_z)\cos\theta\} \\ &\quad -2CJ_c\{L_y + S_y\} \end{aligned} \qquad (3.5.11)$$

$$= AJ_a Cos\theta\{L^+ + L^- + S^+ + S^-\} \qquad (3.5.12)$$

$$-2AJ_a Sin\theta\{L_z + S_z\}$$

$$-BCos\theta\{J^+(L_z+S_z) + J^-(L_z+S_z)\}$$

$$-1/2(BSin\theta-C)\{J^+L^+ + J^-L^- + J^+S^+ + J^-S^-\}$$

$$-1/2(BSin\theta+C)\{J^+L^- + J^-L^+ + J^+S^- + J^-S^+\}$$

The second and third terms of (3.5.12) are diagonal within the $^2\Pi_{1/2}$ electronic state. They are primarily responsible for the behaviour of the rotational energy levels as Θ, the equilibrium structure angle of the complex (Figure 3.2), is varied. The other operators are all off-diagonal in electronic state.

$$H^n_{r4} = 2AL_aS_a + 2BL_bS_b + 2CL_cS_c \qquad (3.5.13)$$

$$= 2A\{(-L_xCos\theta + L_zSin\theta)(-S_xCos\theta + S_zSin\theta)\} \qquad (3.5.14)$$

$$+ 2B\{(+L_xSin\theta + L_zCos\theta)(+S_xSin\theta + S_zCos\theta)\}$$

$$+ 2C\{ L_yS_y \}$$

$$= (B-A)(Sin\theta Cos\theta)\{(L^+ + L^-)S_z + (S^+ + S^-)L_z\}$$

$$+1/2(ACos^2\theta+BSin^2\theta-C)\{L^+S^+ + L^-S^-\}$$

$$+1/2(ACos^2\theta+BSin^2\theta+C)\{L^+S^- + L^-S^+\}$$

$$+2(ASin^2\theta + BCos^2\theta)\{ L_zS_z \} \qquad (3.5.15)$$

The final two terms of Equation (3.5.15) are rotational terms similar to the diagonal and off-diagonal spin-orbit coupling.

Matrix elements of the operators of Hr_{1-4} which are diagonal within the $^2\Pi$ manifold are given in Table (3.1). The treatment of the terms off-diagonal in the electronic state and which lead to lambda-doubling is deferred until section (3.6) .

Table 3.1 : Matrix Elements of the Rotational and Spin-Orbit Hamiltonian Diagonal in Electronic State

$$\langle J\ K_a'\ \Lambda'\ \Sigma' | H | J\ K_a\ \Lambda\ \Sigma\rangle = \delta_{K_a', K_a} \times \delta_{\Lambda',\Lambda} \times \delta_{\Sigma',\Sigma} \times$$

$$\times \quad \{A-\tfrac{1}{2}(B+C)\}.K_a^{\,2} + \tfrac{1}{2}(B+C).J(J+1)$$

$$-2.A.\mathrm{Sin}(\theta).K_a.(\Lambda+\Sigma)$$

$$+(2.A.\mathrm{Sin}^2(\theta)+2.B.\mathrm{Cos}^2(\theta)+\zeta).\Lambda.\Sigma$$

$$\langle J\ K_a \pm 1\ \Lambda\ \Sigma | H | J\ K_a\ \Lambda\ \Sigma\rangle = -B.\mathrm{Cos}(\theta).(\Lambda+\Sigma).\{(J_{\mp}K_a).(J\pm K_a+1)\}^{\frac{1}{2}}$$

$$\langle J\ K_a \pm 2\ \Lambda\ \Sigma | H | J\ K_a\ \Lambda\ \Sigma\rangle = 1/4(B-C).\{(J_{\mp}K_a)(J_{\pm}K_a+1)(J_{\mp}K_a+1)(J_{\pm}K_a)\}^{\frac{1}{2}}$$

$$\langle J\ K_a\ \Lambda\ \Sigma \pm 1 | H | J\ K_a\ \Lambda\ \Sigma\rangle = \{A.K_a.\mathrm{Cos}(\theta) + (B-A).\mathrm{Sin}(\theta).\mathrm{Cos}(\theta).\Lambda\}$$

$$\times \{(S_{\mp}\Sigma)(S_{\pm}\Sigma+1)\}^{\frac{1}{2}}$$

$$\langle J\ K_a \pm 1\ \Lambda\ \Sigma \pm 1 | H | J\ K_a\ \Lambda\ \Sigma\rangle = -1/2.(B.\mathrm{Sin}(\theta) + C)$$

$$\times\{(J_{\mp}K_a)(J_{\pm}K_a+1)(S_{\mp}\Sigma)(S_{\pm}\Sigma+1)\}^{\frac{1}{2}}$$

$$\langle J\ K_a \pm 1\ \Lambda\ \Sigma \mp 1 | H | J\ K_a\ \Lambda\ \Sigma\rangle = -1/2.(B.\mathrm{Sin}(\theta) - C)$$

$$\times \{(J_{\mp}K_a)(J_{\pm}K_a+1)(S_{\pm}\Sigma)(S_{\mp}\Sigma+1)\}^{\frac{1}{2}}$$

3.5 b) The Fine Structure, Hfs

For an open-shell molecule with a single unpaired electron the spin-orbit interaction takes the simple form :

$$H_{fs} = \zeta L.S \qquad (3.5.16)$$

$$= \zeta\{L_x S_x + L_y S_y + L_z S_z\} \qquad (3.5.17)$$

$$= \zeta L_z S_z + 1/2\zeta\{L^+ S^- + L^- S^+\} \qquad (3.5.18)$$

The matrix elements of the diagonal part are accommodated with the rotational contributions of identical form from Equation (3.5.15). The off-diagonal part is likewise combined with (3.5.15) and is discussed more fully in section (3.6).

3.5 c) The Hyperfine Structure, Hhf

The magnetic moment associated with the nitrogen nucleus (I=1) may interact with those due to the spin and orbital motions of the unpaired electron and also with that due to the rotation of the nuclear framework. In addition the nucleus possesses an electric quadrupole moment. The splittings in the rotational energy levels that arise from these two effects are treated separately :

$$H_{hf} = H_{mag} + H_{quad} \qquad (3.5.19)$$

To facilitate the calculations the various angular momenta will be manipulated in terms of the algebra of irreducible spherical tensors.[19] The definition, construction and transformation properties of these tensors are summarised in Appendix A3.3 . It is important to note that since the molecule-fixed components of J commute with the anomalous sign of Equation (3.3.11), spherical tensors cannot be constructed for J in a straightforward fashion.[20] Although several workers[21] have devised

methods of applying this algebra to treat rotational angular momentum in a molecule-fixed representation, they all involve additional complexity and scope for confusion. Hence the foregoing treatment of Hr avoided the use of such techniques.

The Magnetic Hyperfine, Hmag $\quad H = H_{mag1} + H_{mag2} + H_{mag3}$

As discussed briefly in section (3.2) the form of the Hamiltonian for the hyperfine interactions in a molecule may be gained by introducing vector potentials for the magnetic moments of electrons and relevant nuclei and describing the former in terms of relativistic quantum mechanics. Frosch and Foley[22] presented the first full theory for the magnetic hyperfine structure of diatomic molecules. The Hamiltonian adopted for this work is similar to that used by Brown et al.[4] in their analysis of the OH electron paramagnetic resonance spectrum.

The coupling between the nuclear spin and electron orbital magnetic moments is given by an operator :

$$H_{mag1} = aT^1(\underset{\sim}{I}).T^1(\underset{\sim}{L}) \qquad (3.5.20)$$

$$a = 2.g_I\mu_B\mu_I < 1/r^3 >$$

The form of the Hamiltonian for the coupling of the electronic and nuclear spins may be introduced in the following way.[23] The classical magnetostatic expression for the interaction of two magnetic dipoles, $\mu(\underset{\sim}{I})$ and $\mu(\underset{\sim}{S})$ is :

$$E = \frac{\mu_0}{4\pi r^3}\left\{\mu(\underset{\sim}{I}).\mu(\underset{\sim}{S}) - \frac{3\mu(\underset{\sim}{I})(\underset{\sim}{\underset{\sim}{rr}})\mu(\underset{\sim}{S})}{r^2}\right\} \qquad (3.5.21)$$

where $(\underset{\sim}{\underset{\sim}{rr}})$ is a second rank cartesian tensor relating the positions of the two dipoles and μ_o is the permeability of free space. This interaction may alternatively be described in terms of $\mu(S)$ and the magnetic field due to $\underset{\sim}{I}$:

$$B(\underset{\sim}{I}) = - \frac{\mu_0}{4\pi r^3} \left\{ \mu(\underset{\sim}{I}) - \frac{3(\underset{\sim}{r}\underset{\sim}{r})\mu(\underset{\sim}{I})}{r^2} \right\} \qquad (3.5.22)$$

A suitable vector potential to describe this field is [23] :

$$A(\underset{\sim}{I}) = \left(\frac{\mu_0}{4\pi r^3} \right) \mu(\underset{\sim}{I}) \wedge \underset{\sim}{r} \qquad (3.5.23)$$

$$= \left(\frac{\mu_0 \mu_B}{4\pi r^3} \right) \underset{\sim}{I} \wedge \underset{\sim}{r}$$

On taking the curl of this vector potential two terms arise. The first, the Fermi Contact Interaction, involves the possibility that the unpaired electron has a non-zero probability density at the nitrogen nucleus (that is that it possesses some "s-orbital" character).

$$H_{mag2} = b_F T^1(\underset{\sim}{I}).T^1(\underset{\sim}{S}) \qquad (3.5.24)$$

$$\text{where,} \quad b_F = \frac{8\pi}{3} g_e g_I \mu_B \mu_I |\psi(r=0)|^2$$

The second effect corresponds to the simple dipolar mechanism depicted in Equation (3.5.22) and may be represented in a useful spherical tensor form by the operator :

$$H_{mag3} = - \sqrt{(10)} A' T^1(\underset{\sim}{I}).T^1(\underset{\sim}{S},\underset{\sim}{C}) \qquad (3.5.25)$$

where the surd is a scaling factor between cartesian and spherical tensor forms and $T^1(\underset{\sim}{S},\underset{\sim}{C})$ is a tensor product defined by :

$$T^1_q(\underset{\sim}{S},\underset{\sim}{C}) = \sqrt{3}.(-1)^{q-1} \sum_{q1,q2} \begin{pmatrix} 1 & 2 & 1 \\ q1 & q2 & -q \end{pmatrix} T^1_{q1}(\underset{\sim}{S}).C^2_{q2}(\theta_i,\phi_i)$$

$$A' = g_e g_i \mu_B \mu_I \langle 1/r_i^3 \rangle \qquad (3.5.26)$$

The origins of the Fermi Contact Interaction may also be deduced in a less circular but far more involved derivation based on the Dirac Equation.[10]

Thus the full magnetic hyperfine Hamiltonian may be written,

$$H_{mag} = T^1(\underset{\sim}{I}).\{aT^1(\underset{\sim}{L}) + b_F T^1(\underset{\sim}{S}) - \sqrt{(10)}A'T^1(\underset{\sim}{S},\underset{\sim}{C})\}$$

(3.5.27)

The advantage of this formulation is that matrix elements may be calculated by a simple separation of the scalar product.

$$\langle \eta\ \Lambda';S\ \Sigma';J'\ K_a';I\ F'\ M_f|H_{mag}|\eta\ \Lambda;S\ \Sigma;J\ K_a;I\ F\ M_f\rangle$$

$$= \delta_{F,F'}.(-1)^{J+I+F} \begin{Bmatrix} F & I & J' \\ 1 & J & I \end{Bmatrix} \langle I||T^1(\underset{\sim}{I})||I\rangle$$

$$\langle \eta\ \Lambda';S\ \Sigma';J'K_a'||aT^1(\underset{\sim}{L})+b_F T^1(\underset{\sim}{I})-\sqrt{10}.AT^1(\underset{\sim}{S},\underset{\sim}{C})||\eta\ \Lambda;S\ \Sigma;J\ K_a\rangle$$

(3.5.28)

The reduced matrix element of the nuclear spin operator is given by :

$$\langle I||T^1(I)||I\rangle = \{I(I+1)(2I+1)\}^{\frac{1}{2}} \qquad (3.5.29)$$

and the second reduced matrix element can be expressed in terms of the molecule-fixed components of the tensor operators.

$$\langle \eta\ \Lambda';S\ \Sigma';J'\ K_a'||aT^1(\underset{\sim}{L})+b_F T^1(\underset{\sim}{I})-\sqrt{10}.AT^1(\underset{\sim}{S},\underset{\sim}{C})||\eta\ \Lambda;S\ \Sigma;J\ K_a\rangle$$

$$= \sum_q (-1)^{J'-K_a'}.\{(2J+1)(2J'+1)\}^{\frac{1}{2}}.\begin{pmatrix} J' & 1 & J \\ -K_a' & q & K_a \end{pmatrix}$$

$$\langle \eta\ \Lambda';S\ \Sigma'|aT^1_q(\underset{\sim}{L})+b_F T^1_q(\underset{\sim}{S})-\sqrt{10}.AT^1_q(\underset{\sim}{S},\underset{\sim}{C})|\eta\ \Lambda;S\ \Sigma\rangle$$

(3.5.30)

This result is achieved by application of the Wigner-Eckart Theorem and evaluation of the resulting matrix elements of a rotation operator.

Unfortunately Equation (3.5.30) contains the components of electronic angular momentum operators in the molecule-fixed principal axis system. The corresponding wavefunctions refer to the (x,y,z) molecular axis system based on the NO sub-molecule. Thus a further rotation (about an axis perpendicular to the plane of the complex) is required in order to express the operators of (3.5.30) in terms of their components in the (x,y,z) space.

$$T^1_q(\underset{\sim}{L} \text{ or } \underset{\sim}{S} \text{ or } \underset{\sim}{S},\underset{\sim}{C}) = \sum_r d^1_{qr}(\gamma).T_r(\underset{\sim}{L} \text{ or } \underset{\sim}{S} \text{ or } \underset{\sim}{S},\underset{\sim}{C}) \qquad (3.5.31)$$

Here γ is the complement of θ as defined in Figure 3.2 . The $d^1_{q,r}(\gamma)$ rotation matrices are as defined by Brink and Satchler.[13] The matrix elements may now be evaluated explicitly.

Nuclear Spin-Orbit

Application of Equation (3.5.31) to the matrix element of the nuclear spin-orbit operator yields terms diagonal and off-diagonal in Λ by ± 1. The latter require the introduction of a new parameter el :

$$\begin{aligned}
&\langle \Lambda = 0 | aT^1_{r=-1}(L) | 1 \rangle = 1/\sqrt{2}\ e_1 \\
&\langle \Lambda = 1 | aT^1_{r=1}(L) | 0 \rangle = -1/\sqrt{2}\ e_1 \\
&\langle \Lambda = 0 | aT^1_{r=1}(L) | -1 \rangle = (-1)^s.1/\sqrt{2}\ e_1 \\
&\langle \Lambda = -1 | aT^1_{r=-1}(L) | 0 \rangle = (-1)^{1+s}.1/\sqrt{2}\ e_1
\end{aligned} \qquad (3.5.32)$$

$$\langle \Lambda' | aT^1_{r=0}(L) | \Lambda \rangle = \delta_{\Lambda',\Lambda} \cdot a.\Lambda$$

The last two expressions are obtained from the symmetry properties of the orbital wavefunctions discussed in section (3.4) .

For example the q=0 component of $T^1(\underset{\sim}{L})$ is evaluated as follows :

$$
\begin{aligned}
&\langle \eta\ \Lambda';S\ \Sigma' | aT^1_{q=0}(\underset{\sim}{L}) | \eta\ \Lambda;S\ \Sigma\rangle \\
&= \sum_r \langle \eta\ \Lambda';S\ \Sigma' | d^1_{0,r}(\gamma) T^1_r(\underset{\sim}{L}) | \eta\ \Lambda;S\ \Sigma\rangle \\
&= \langle\ "\ | d^1_{0,-1}(\gamma) T^1_{-1}(\underset{\sim}{L}) + d^1_{0,0}(\gamma) T^1_0(\underset{\sim}{L}) + d^1_{0,1}(\gamma) T^1_1(\underset{\sim}{L}) |\ "\ \rangle \\
&= -1/\sqrt{2}.\mathrm{Sin}(\gamma)\delta_{\Sigma'\Sigma}\delta_{\Lambda'\Lambda-1}.\langle \eta\ \Lambda' | aT^1_{-1}(\underset{\sim}{L}) | \eta\ \Lambda\rangle \\
&\quad + \mathrm{Cos}(\gamma)\delta_{\Sigma'\Sigma}\delta_{\Lambda'\Lambda}.\langle \eta\ \Lambda' | aT^1_0(\underset{\sim}{L}) | \eta\ \Lambda\rangle \\
&\quad + 1/\sqrt{2}.\mathrm{Sin}(\gamma)\delta_{\Sigma'\Sigma}\delta_{\Lambda'\Lambda+1}.\langle \eta\ \Lambda' | aT^1_1(\underset{\sim}{L}) | \eta\ \Lambda\rangle
\end{aligned}
\qquad (3.5.33)
$$

with Equation (3.5.32) providing the matrix elements of $T^1_r(\underset{\sim}{L})$. There is also a selection rule on Ka for each value of q which arises because of the restriction on the lower arguments of the three-j symbol of Equation (3.5.30). That is, the magnetic hyperfine matrix element will vanish unless :

$$-K_a' + q + K_a = 0 \qquad (3.5.34)$$

$$\text{or,}\quad q = K_a' - K_a$$

Fermi Contact Interaction

The components of $T^1(\underset{\sim}{S})$ in the (x,y,z) axis system are generated in exactly the same way as those for $T^1(\underset{\sim}{L})$. These matrix elements are then evaluated as :

$$
\begin{aligned}
&\langle \eta\ \Lambda';S\ \Sigma' | b_F T^1_r(S) | \eta\ \Lambda;S\ \Sigma\rangle \\
&= b_F.\delta_{\Lambda'\Lambda}.(-1)^{S-\Sigma'}.\{S(S+1)(2S+1)\}^{\frac{1}{2}} \\
&\quad x \begin{pmatrix} S & 1 & S \\ -\Sigma' & r & \Sigma \end{pmatrix}
\end{aligned}
\qquad (3.5.35)
$$

Spin-Spin Dipolar Interaction

The first rank tensor formed by coupling $T^1(\underset{\sim}{s})$ to $C^2(\Theta i, \phi i)$ was earlier defined by the equation :

$$T_r(\underset{\sim}{S},\underset{\sim}{C}) = \sqrt{3}.(-1)^{1-r} \sum_{r1,r2} T^1_{r1}(\underset{\sim}{S}).C^2_{r2}(\theta_i,\phi_i)$$

$$x \begin{pmatrix} 1 & 2 & 1 \\ r1 & r2 & -r \end{pmatrix}$$

where $C^2(\Theta i, \phi i)$ is a modified spherical harmonic relating the positions of the electronic and nuclear magnetic dipoles. $T^1(\underset{\sim}{S},\underset{\sim}{C})$ may be expressed in terms of the above components using Equation (3.5.31) . Thus its matrix element may be expanded :

$$-\sqrt{10}\,\langle \eta\ \Lambda';S\ \Sigma'|AT^1_q(\underset{\sim}{S},\underset{\sim}{C})|\eta\ \Lambda;S\ \Sigma\rangle$$

$$= -\sqrt{10} \sum_{r,r1,r2} \sqrt{3}.(-1)^{1-r} \begin{pmatrix} 1 & 2 & 1 \\ r1 & r2 & -r \end{pmatrix} d^1_{q,r}(\gamma)$$

$$x\langle \eta\ \Lambda'|AC^2_{r2}(\theta_i,\phi_i)|\eta\ \Lambda\rangle\langle S\ \Sigma'|T^1_{r1}(\underset{\sim}{S})|S\ \Sigma\rangle$$

$$= \sqrt{30} \sum_{r,r2} (-1)^r \begin{pmatrix} 1 & 1 & 2 \\ r & r2-r & -r2 \end{pmatrix} x\ d^1_{q,r}(\gamma)$$

$$x\ (-1)^{S-\Sigma'}.\{S(S+1)(2S+1)\}^{\frac{1}{2}} \begin{pmatrix} S & 1 & S \\ -\Sigma' & r-r2 & \Sigma \end{pmatrix}$$

$$x\ \langle \eta\ \Lambda'|AC^2_{r2}(\theta_i,\phi_i)|\eta\ \Lambda\rangle \qquad (3.5.36)$$

where the symmetry properties and argument constraints of the three-j symbol have been invoked.

The matrix elements of $A'C^2(\Theta i, \phi i)$ which are diagonal in the $^2\Pi$ manifold may be described in terms of the original c and d parameters of Frosch and Foley[22] and a modified parameter e2. (The "d" parameter used here is actually defined as twice that of Frosch and Foley to be consistent with more recent literature.)

$$c = 3/2.g_e g_I \mu_B \mu_N \langle (3\mathrm{Cos}^2\theta_i - 1)/r^3 \rangle$$

$$d = 3/2.g_e g_I \mu_B \mu_N \langle \mathrm{Sin}^2\theta_i / r^3 \rangle$$

$$e2 = \langle \Lambda=0 | \sqrt{3}/2.g_e g_I \mu_B \mu_N \mathrm{Sin}\theta_i \mathrm{Cos}\theta_i e^{-i\phi_i} | \Lambda=1 \rangle$$

From these definitions the matrix elements of $A'C^2(\theta i, \phi i)$ are :

$$\langle \eta\ \Lambda' | AC^2_{\pm 2}(\theta_i, \phi_i) | \eta\ \Lambda \rangle = -1/\sqrt{6}.\delta_{\Lambda' \Lambda \pm 2}.d$$

$$\langle \eta\ \Lambda' | AC^2_{0}(\theta_i, \phi_i) | \eta\ \Lambda \rangle = 1/3.\delta_{\Lambda' \Lambda}.c$$

$$\langle \eta\ 0 | AC^2_{-1}(\theta_i, \phi_i) | \eta\ 1 \rangle = \sqrt{2}/3.e_2$$

$$\langle \eta\ 1 | AC^2_{1}(\theta_i, \phi_i) | \eta\ 0 \rangle = -\sqrt{2}/3.e_2$$

$$\langle \eta\ 0 | AC^2_{1}(\theta_i, \phi_i) | \eta -1 \rangle = (-1)^s.\sqrt{2}/3.e_2$$

$$\langle \eta\ -1 | AC^2_{-1}(\theta_i, \phi_i) | \eta\ 0 \rangle = (-1)^{s+1}.\sqrt{2}/3.e_2$$

(3.5.37)

Full expressions for the magnetic hyperfine matrix elements within the $^2\Pi$ manifold are given in Appendix A3.4 .

Electric Quadrupole Interaction, Hquad

The electrostatic interaction between a nucleus and all the other charges in a molecule may be described by the Hamiltonian[15] :

$$H_{el} = \sum \frac{e_i e_p}{|\underset{\sim}{r}_i - \underset{\sim}{r}_p|} = \sum e_i e_p . \frac{r_p^l}{r_i^{l+1}} . P_l(\mathrm{Cos}\theta_{ip})$$

(3.5.38)

In this expression e_p and e_i denote charges of protons in the quadrupolar nucleus (subscript p) and of protons and electrons (labelled i) in the remainder of the molecule; r_p and r_i are the corresponding position vectors, the angle between which is θ_{ip}.

The quadrupolar contribution to this Hamiltonian is contained in the l=2 term. $P^l(\mathrm{Cos}(\theta_{ip}))$ may be expressed as a sum of Racah functions (The Spherical Harmonic Theorem) whereupon the

form of the electric quadrupole operator may be written as the scalar product of two second rank spherical tensors.

$$H_{quad} = T^2(\underset{\sim}{V}).T^2(\underset{\sim}{Q}) \qquad (3.5.39)$$

$$T^2(\underset{\sim}{V}) = \sum_i \frac{e_i}{r_i^3} C^2(\theta_i, \phi_i) \qquad (3.5.40)$$

$$T^2(\underset{\sim}{Q}) = \sum_p e_p r_p^2 C^2(\theta_i, \phi_i) \qquad (3.5.41)$$

Matrix elements of (3.5.39) may be evaluated by a procedure analogous to that used for Hmag.

$$\langle \eta\ \Lambda';S\ \Sigma';J'K_a';I\ F'|H_{quad}|\eta\ \Lambda;S\ \Sigma;JK_a;I\ F\rangle$$

$$= (-1)^{J+I+F} x\ \delta_{F'F} x \begin{Bmatrix} F & I & J' \\ 2 & J & I \end{Bmatrix}$$

$$x \langle \eta\ \Lambda';S\ \Sigma';J'K_a'||T^2(\underset{\sim}{V})||\eta\ \Lambda;S\ \Sigma;JK_a\rangle$$

$$x \langle I\ F'||T^2(\underset{\sim}{Q})||I\ F\rangle \qquad (3.5.42)$$

The reduced matrix element of $T^2(Q)$ is given by :

$$\langle I\ F||T^2(\underset{\sim}{Q})||I\ F\rangle = \qquad (3.5.43)$$

$$(-1)^{2I}.\frac{e}{2} \frac{\langle \beta\ I\ I|\sum_p (3z_p^2 - r_p^2)|\beta\ I\ I\rangle}{\begin{pmatrix} I & 2 & I \\ -I & 0 & I \end{pmatrix}}$$

whereupon evaluation of the three-j symbol and employing the conventional definition[15] of the quadrupole moment of a nucleus (β denotes all other relevant quantum numbers)

$$Q = \langle \beta\ I\ I| \sum_p (3z_p^2 - r_p^2)|\beta\ I\ I\rangle \qquad (3.5.44)$$

leads to the result :

$$\langle I\ F||T^2(\underset{\sim}{Q})||I\ F\rangle = eQ \Big/ 2.\sqrt{\frac{2I(2I-1)}{(2I+1)(2I+2)(2I+3)}} \qquad (3.5.45)$$

The reduced matrix element of $T^2(\underset{\sim}{V})$ is expressed in terms of its

molecule-fixed components using the procedure outlined for Equation (3.5.30). The result is :

$$\langle \eta\ \Lambda';S\ \Sigma';J'K_a' \| T^2(\underset{\sim}{V}) \| \eta\ \Lambda;S\ \Sigma;JK_a \rangle =$$

$$\delta_{\Sigma',\Sigma}(-1)^{J+K_a'} \{(2J+1)(2J'+1)\}^{\frac{1}{2}} \times \sum_q \begin{pmatrix} 2 & J & J' \\ -q & -K_a & K_a' \end{pmatrix}$$

$$\times \langle \eta\ \Lambda\ | T_q^2(\underset{\sim}{V}) | \eta\ \Lambda \rangle \qquad (3.5.46)$$

Once again it is necessary to transform the components of $T^2(\underset{\sim}{V})$ from the principal axis system to that based on the NO sub-molecule; this time the second rank matrices, $d^2_{q,r}(\gamma)$, are required.

$$T_q^2(\underset{\sim}{V}) = \sum_r d^2_{q,r}(\gamma).T_r^2(\underset{\sim}{V}) \qquad (3.5.47)$$

Hence the matrix elements of $T^2(\underset{\sim}{V})$, the electric field gradient tensor operator, can be evaluated as the conventional parameters. These are listed below.

$$\langle \eta\ \Lambda' | T^2_{r=0}(\underset{\sim}{V}) | \eta\ \Lambda \rangle = \langle \Lambda' | \sum_i e_i/r_i^3 C_0^2(\theta_i,\phi_i) | \Lambda \rangle$$

$$= \delta_{\Lambda'\Lambda} \langle \Lambda' | \sum_i e_i/r_i^3(3\cos^2\theta_i - 1)/2 | \Lambda \rangle = \delta_{\Lambda'\Lambda}.1/2q_0$$

$$\langle \eta\ \Lambda' | T^2_{\pm 2}(\underset{\sim}{V}) | \eta\ \Lambda \rangle = \delta_{\Lambda'\Lambda\pm 2}.q_2/2\sqrt{6}$$

$$\langle \eta\ \Lambda'=0 | T^2_{-1}(\underset{\sim}{V}) | \eta\ \Lambda=1 \rangle = \delta_{\Lambda'\Lambda-1}.q_1/\sqrt{6}$$

$$\langle \eta\ \Lambda'=1 | T^2_{+1}(\underset{\sim}{V}) | \eta\ \Lambda=0 \rangle = -\delta_{\Lambda'\Lambda+1}.q_1/\sqrt{6}$$

$$\langle \eta\ \Lambda'=0 | T^2_{+1}(\underset{\sim}{V}) | \eta\ \Lambda=-1 \rangle = \delta_{\Lambda'\Lambda+1}.(-1)^s.q_1/\sqrt{6}$$

$$\langle \eta\ \Lambda'=-1 | T^2_{-1}(\underset{\sim}{V}) | \eta\ \Lambda=0 \rangle = \delta_{\Lambda'\Lambda-1}.(-1)^{s+1}.q_1/\sqrt{6}$$

(3.5.48)

The conventional parameters q_0 , q_1 and q_2 [24] are defined by the relations :

$$q_0 = \delta_{\Lambda'\Lambda} \langle\Lambda'| \sum_i e_i/r_i^3(3\mathrm{Cos}^2\theta_i - 1)|\Lambda\rangle$$

$$q_1 = \delta_{\Lambda'\Lambda-1} \langle\Lambda'| \sum_i e_i/r_i^3 . 3\mathrm{Sin}\theta_i \mathrm{Cos}\theta_i e^{-i\phi_i}|\Lambda\rangle$$

$$q_2 = \delta_{\Lambda'\Lambda\pm2} \langle\Lambda'| \sum_i e_i/r_i^3 . 3\mathrm{Sin}^2\theta_i . e^{\pm 2i\phi_i}|\Lambda\rangle$$

(3.5.49)

Explicit expressions for the matrix elements of Hquad are given in Appendix A3.5 .

3.5 d) The Zeeman Interaction, Hz

Although the effects of magnetic fields were not investigated, they are included here for completeness. To a good approximation the interaction between an open-shell molecule and a magnetic field consists of four terms [19] :

$$H_z = \mu_B T^1(\underset{\sim}{B}).\{g_L T^1(\underset{\sim}{L}) + g_e T^1(\underset{\sim}{S})\}$$
$$+ g_I \mu_N T^1(\underset{\sim}{B}).T^1(\underset{\sim}{I}) + g_r^N \mu_B T^1(\underset{\sim}{B}).T^1(\underset{\sim}{J}-\underset{\sim}{L}-\underset{\sim}{S})$$

(3.5.50)

The effect on the spectrum of the first two electronic terms is usually greater than those due to the nuclear rotational magnetic moments. Matrix elements will therefore only be derived here for the former.

Application of the Wigner-Eckart Theorem allows the factorisation of the matrix element into a reduced part multiplied by a three-j symbol which contains all the spatial dependence.

$$\langle \eta\Lambda';S\Sigma';J'K_a';IF'M_F'|\mu_B T^1(\underset{\sim}{B}).\{g_L T^1(\underset{\sim}{L})+g_e T^1(\underset{\sim}{S})\}|\eta\Lambda;S\Sigma;JK_a;IFM_F\rangle$$

$$= \sum_p (-1)^p x (-1)^{F'-M_F'} x \begin{pmatrix} F' & 1 & F \\ -M_F' & p & M_F \end{pmatrix} x \mu_B x T^1_{-p}(B)$$

$$x \langle \eta\Lambda';S\Sigma';J'K_a';IF'||g_L T^1(\underset{\sim}{L})+g_e T^1(\underset{\sim}{S})||\eta\Lambda;S\Sigma;JK_a;IF\rangle$$

(3.5.51)

The nuclear part of the matrix element may be separated since the electronic operators have no effect on it.

$$\langle \eta\Lambda';S\Sigma';J'K_a';IF'||g_L T^1(\underset{\sim}{L})+g_e T^1(\underset{\sim}{S})||\eta\Lambda;S\Sigma;JK_a;IF\rangle$$

$$= (-1)^{J'+I+F+1} x \{(2F'+1)(2F+1)\}^{\frac{1}{2}} x \begin{Bmatrix} I & J' & F' \\ 1 & F & J \end{Bmatrix}$$

$$x \langle \eta\Lambda';S\Sigma';J'K_a'||g_L T^1(\underset{\sim}{L})+g_e T^1(\underset{\sim}{S})||\eta\Lambda;S\Sigma;JK_a\rangle$$

(3.5.52)

The reduced matrix element of (3.5.52) is related to the principal axis components of $T^1(\underset{\sim}{L})$ and $T^1(\underset{\sim}{S})$ as was done for the hyperfine interaction. Likewise a transformation to the (x,y,z) components of these operators is then used to generate the final matrix element :

$$\langle \eta\Lambda';S\Sigma';J'K_a';IF'M_F'|H_z|\eta\Lambda;S\Sigma;JK_a;IFM_F\rangle$$

$$= \sum_p (-1)^{I+F+F'+K_a'-M_F'+p+1} x \mu_B x T^1_{-p}(B)$$

$$x \{(2J'+1)(2J+1)(2F'+1)(2F+1)\}^{\frac{1}{2}} x \begin{pmatrix} F' & 1 & F \\ -M_F' & p & M_F \end{pmatrix} x \begin{Bmatrix} I & J' & F' \\ 1 & F & J \end{Bmatrix}$$

$$x \sum_{q,r} \begin{pmatrix} J' & 1 & J \\ -K_a' & q & K_a \end{pmatrix} x \begin{Bmatrix} \delta_{\Sigma'\Sigma}\langle \eta\Lambda'|d^1_{q,r}(\gamma) g_L T^1_r(\underset{\sim}{L})|\eta\Lambda\rangle \\ +\delta_{\Lambda\Lambda}\langle S\Sigma'|d^1_{q,r}(\gamma) g_e T^1_r(\underset{\sim}{S})|S\Sigma\rangle \end{Bmatrix}$$

(3.5.53)

If the space-fixed Z-axis is chosen to lie parallel to the applied magnetic field, that is if p=0, it can be seen that M_F is a good quantum number. Furthermore, since $|g_l| \sim g_s$ for the ground $^2\Pi_{1/2}$ state, the diagonal matrix elements of (3.5.53) are very close to zero.

3.5 e) The Stark Effect, He

The Hamiltonian operator for the effect of an electric field is given by the simple expression :

$$H_e = - T^1(\underset{\sim}{\mu}).T^1(\underset{\sim}{E}) \qquad (3.5.54)$$

Assuming that the electric field is along the space-fixed Z-axis the matrix element of He may be evaluated by a procedure entirely analogous to that just described for the Zeeman Effect.

$$\begin{aligned}
&\langle \eta\Lambda';S\Sigma';J'K_a';IF'M_F'|H_e|\eta\Lambda;S\Sigma;JK_a;IFM_F\rangle \\
&= (-1)^{I+F+K_a'+F'-M_F'} \times \{(2J'+1)(2J+1)(2F'+1)(2F+1)\}^{\frac{1}{2}} \\
&\times \begin{pmatrix} F' & 1 & F \\ -M_F' & 0 & M_F \end{pmatrix} \times \begin{Bmatrix} I & J' & F' \\ 1 & F & J \end{Bmatrix} \times E_z \\
&\times \sum_q \begin{pmatrix} J' & 1 & J \\ -K_a' & q & K_a \end{pmatrix} \times \delta_{\Lambda'\Lambda} \times \delta_{\Sigma'\Sigma} \times T_q^1(\underset{\sim}{\mu})
\end{aligned} \qquad (3.5.55)$$

If required the molecule-fixed components of the dipole moment may be expressed in the NO axis system. Thus in terms simply of the NO dipole moment (that is, neglecting all induced moments) :

$$\mu_a = \mu_{NO}.\mathrm{Sin}\theta \qquad (3.5.56)$$

$$\mu_b = \mu_{NO}.\mathrm{Cos}\theta$$

Since the non-zero matrix elements of the dipole moment give the selection rule for allowed transitions, it is appropriate

here to consider the symmetry of $T^1(\underset{\sim}{\mu})$ under the space-fixed inversion operator. Considering its space-fixed components :

$$E^* \, T^1_p(\underset{\sim}{\mu}) = - \, T^1_p(\underset{\sim}{\mu}) \qquad (3.5.57)$$

Matrix elements of $T^1_p(\underset{\sim}{\mu})$ must be invariant to this symmetry operation in free space. Hence this leads to a selection rule based on the parity of states connected by the electric dipole moment operator.

$$+ \leftrightarrow - \; ; \; - \leftrightarrow + \; ; \; \pm \leftrightarrow \pm \qquad (3.5.58)$$

This is in contrast to the Zeeman Effect which is parity conserving.

3.5 f) The Quenching Potential, Hq

In the non-rotating limit, the theory developed so far has effectively assumed an axial symmetry for the orbital motion of the unpaired electron about the NO internuclear axis. Clearly the presence of the weakly bound rare gas atom removes this symmetry; that is, it lifts the degeneracy of the Π_x and Π_y NO molecular orbitals. To model this unique interaction, not observed in conventional open-shell, non-linear triatomic molecules for which the orbital motion is predominantly quenched, an analogy is drawn with the Renner-Teller Effect.[1,2]

The Renner-Teller Effect is a coupling of vibrational and electronic motions in linear triatomic molecules with a degenerate ground state. The interaction arises because the doubly-degenerate bending vibration lifts the electronic degeneracy ; consequently the Born-Oppenheimer separation of the vibrational and electronic wavefunctions proves inappropriate for

interpreting the spectra.

In a rare gas - nitric oxide complex the orbital degeneracy is lifted by the presence of the rare gas atom. By analogy with the theory of the Renner-Teller Effect this may be modelled by a series expansion in the azimuthal angle of the odd electron as defined by the orbital basis set. Thus :

$$H_Q = \varepsilon_1 \mathrm{Cos}\phi + \varepsilon_2 \mathrm{Cos}\phi + \ldots \qquad (3.5.59)$$

This expansion again contains the correct symmetry with respect to a reflection in the molecular plane. The expansion coefficients will be functions of the van der Waals bond length, r, and the structural angle, t (Figure 3.2).

The most important term in (3.5.59) will be the second for its action is diagonal within the $^2\Pi$ manifold. Its matrix elements are deduced from the form of the orbital function to be,

$$\langle \Lambda' = \pm 1 | \varepsilon_2 \mathrm{Cos}2\phi | \Lambda = \mp 1 \rangle = -\varepsilon_2/2 \qquad (3.5.60)$$

The first term in (3.5.59) connects the $^2\Pi$ ground state to other electronic states differing in Λ by ± 1, that is to $^2\Sigma$ and $^2\Delta$ states. Matrix elements to the $^2\Sigma$ states would vanish for a pure precession model except that the coefficients ε_i also contain some dependence on the electronic polar angle θ_i.

3.6 Treatment of Terms Off-Diagonal in Electronic State and Estimation of Hyperfine Parameters

In section (3.5) the construction of Hr and Hfs led to various combinations of raising and lowering operators for the electronic angular momentum. In addition certain parts of Hhf and the leading term of Hq contain matrix elements which can connect the $X^2\Pi$ ground state to $^2\Sigma^+$, $^2\Sigma^-$ and $^2\Delta$ excited electronic states. The effect of these matrix elements on the rotational spectrum of the ground vibronic state may be evaluated from second order perturbation theory. The interactions that arise involve either a $\Lambda = \pm 1$ state in the $X^2\Pi$ manifold connected with itself via the excited state or a cross term between the states $\Lambda = +1$ and $\Lambda = -1$. As a result of the symmetry properties of the orbital wavefunctions contained in Equation (3.4.8), the matrix elements of the cross terms involving the states, $^2\Sigma^+$ and $^2\Sigma^-$, have opposite signs; that is, they are parity dependent. These terms are partly responsible for lifting the degeneracy of the $X^2\Pi^+$ and $X^2\Pi^-$ parity states in rare gas-nitric oxide complexes and for the lambda-doubling in NO itself.

The terms connecting a $\Lambda = \pm 1$ state with itself are parity independent and contributions to the ground state energies from the states, $^2\Sigma^+$ and $^2\Sigma^-$, have the same sign and hence reinforce each other. Excited $^2\Delta$ states can also contribute to these terms but not to the cross terms. The parity independent, non-adiabatic perturbations are responsible for an electronic contribution to the rotational constants and may also cause an appreciable spin-rotation interaction.

In general the theories used to fit the lambda-doubling spectra of NO have treated these non-adiabatic terms by

degenerate perturbation theory (that is they have included a van Vleck transformation). Operators that raise or lower Λ by +1 strictly cause interaction between the ground state and all excited $^2\Sigma$ states of the molecule. Hence the parameters included in the effective Hamiltonian correspond to sums over all the excited $^2\Sigma$ (and sometimes $^2\Delta$) states. In an early paper Mulliken and Christy[25] evaluated the second order lambda-doubling contributions to the effective Hamiltonian for a $^2\Pi$ ground state in terms of the parameters :

$$p^2 = -4 \sum_{\eta'} (-1)^S . \frac{\langle \eta\ \Lambda=1 | AT^1_1(\underset{\sim}{L}) | \eta\ \Lambda=0 \rangle \langle \eta\ \Lambda=0 | BT^1_{-1}(\underset{\sim}{L}) | \eta\ \Lambda=1 \rangle}{E_{\eta\,^2\Pi} - E_{\eta'\,^2\Pi}}$$

$$q^2 = 4 \sum_{\eta'} (-1)^S . \frac{|\langle \eta\ \Lambda=1 | BT^1_1(\underset{\sim}{L}) | \eta'\Lambda=0 \rangle|^2}{E_{\eta\,^2\Pi} - E_{\eta'\,^2\Pi}} \qquad (3.6.1)$$

where A and B are the spin-orbit and rotational constants and the quantum number η' runs over all $^2\Sigma$ states. (s has the usual definition.) Brown et al.[4] have pointed out that it is possible to derive similar parameters containing contributions from the higher orders of degenerate perturbation theory also.

The use of such a transformation can have disadvantages, however. For even a relatively simple molecule like NO (where each order of the theory was calculated separately) Meerts and Dymanus[26] needed to introduce a plethora of molecular constants. Many of these were found to make little difference to the fit of the spectrum.[27] Furthermore a large number of correctly assigned measured lines is required before such a procedure is rewarding. The problems associated with recording the spectra of rare gas - NO complexes made it unlikely that a large number of constants could be fitted. It was therefore decided to attempt to model the most important non-adiabatic effects by including a single

excited $^2\Sigma^-$ state in the Hamiltonian matrix. Unfortunately a single state chosen to mimic the phase dependent lambda-doubling terms will not properly model the phase independent terms. The latter should be of lesser importance and would be partly accounted for (to second order) as corrections to the definitions of the rotational constants.

The phase independent part of the spin-rotation interaction would not be included by this procedure. However this was estimated to be a small term (for a near T-shaped geometry) because of the comparatively small values of the B rotational constants in the complexes. In principle a second $^2\Sigma$ state of opposite parity could be included in the matrix but the effects of the two states are difficult to separate and hence the extra parameterised matrix elements could not be estimated.

Thus the procedure adopted in this work was somewhat analogous to the application of the closure approximation or the use of a mean excitation energy as proposed by Unsold and others. This technique has been widely used for polarisability calculations and in the theory of intermolecular forces.[28] It is reasonable to include a $^2\Sigma$ state without reference to $^2\Delta$ states as the latter do not affect lambda-doubling up to second order. (They can, however, provide small electronic contributions to the rotational constants and to any spin-rotation interaction.) Evidence for this statement is provided by the work of Neumann.[29] He fitted the lambda-doubling spectrum of NO to 50kHz without reference to $^2\Delta$ states in his perturbation expressions. Also Meerts et al.[26] found that the inclusion of such parameters did not improve their better fit of the same remeasured spectrum.

Recent work by Miescher[30] has confirmed the ordering of the lambda doublets in the $X\,^2\Pi_{1/2}$ ground state of NO to be as suggested

by Huber and Herzberg[12]; that is, that the "e" or (+)-parity state lies lowest in J=1/2. (The labels "e" and "f" are defined by Brown et al.[31]) This implies that the dominant contribution to the lambda-doubling comes from a $^2\Sigma^-$ state or states. By attempting to account for the effects of all $^2\Sigma^+$ and $^2\Sigma^-$ states using a single excited $^2\Sigma^-$ state in the matrix, the "mean excitation energy" will cease to have much physical meaning. This is because the states, $^2\Sigma^+$ and $^2\Sigma^-$, have opposite effects on the lambda-doubling. The chosen effective excitation energy therefore has to be considerably larger if it is to mimic the sum over all $^2\Sigma$ states that an exact calculation would contain.

To evaluate the matrix elements of Hr2-4 (anticipating this approach the hyperfine matrix elements have already been given) the following parameters are introduced :

$$\langle \Lambda' = 1 | AL^+ | 0 \rangle = \langle A^+ \rangle \qquad (3.6.2)$$

$$\langle \Lambda' = 0 | AL^- | 1 \rangle = \langle A^+ \rangle$$

$$\langle \Lambda' = -1 | AL^- | 0 \rangle = (-1)^S . \langle A^+ \rangle$$

$$\langle \Lambda' = 0 | AL^+ | -1 \rangle = (-1)^S . \langle A^+ \rangle$$

and similarly for $\langle B+ \rangle$, $\langle C+ \rangle$ and $\langle \zeta + \rangle$. It is assumed that the rotational constants and trigonometric functions of θ (Figure 3.2) are not operators on the excited vibronic wavefunctions that appear in the perturbation expression modelled by the single excited $^2\Sigma^-$ state. This may not be a very good approximation but is necessary to avoid introducing too large a number of empirical parameters whose magnitude would be difficult to estimate or fit. In many cases the procedure may be justified by invoking a closure approximation and assuming a Born-Oppenheimer separation of vibrational and electronic wavefunctions. Thus, for example, a typical perturbation matrix element might be :

$$\sum_{\eta,v} \frac{\langle \Lambda=1, v=0 | BL^{+} | \Lambda=0, v \rangle \langle \Lambda=0, v | BL^{-} | \Lambda=1, v=0 \rangle}{E_{\eta,v} - E_{0,0}}$$

Assuming vibrational separations are small compared with electronic intervals, the two parts of the matrix element may be separated to give :

$$\sum_{\eta} \frac{\langle \Lambda=1 | L^{+} | \Lambda=0 \rangle \langle \Lambda=0 | L^{-} | \Lambda=1 \rangle}{E_{\eta,0} - E_{0,0}} \times \sum_{v} \langle 0 | B | v \rangle \langle v | B | 0 \rangle$$

$$= \sum_{\eta} \frac{\langle \Lambda=1 | L^{+} | \Lambda=0 \rangle \langle \Lambda=0 | L^{-} | \Lambda=1 \rangle}{\Delta E} \times \langle B^{2} \rangle$$

Thus provided that this separation is valid, we can model the sums over η (all $^{2}\Sigma$ states)by a single state and use the ground state value of B. The latter is justified if a harmonic potential is assumed since ,

$$\langle 1/(\mu R_e^{2}) \rangle \approx \langle 1/(\mu^{2} R_e^{4}) \rangle^{\frac{1}{4}} \quad \text{or,} \quad \langle B \rangle \approx \langle B^{2} \rangle^{\frac{1}{2}}$$

The matrix elements of Hr2-4 expressed in terms of the parameters $\langle A+ \rangle$, $\langle B+ \rangle$, $\langle C+ \rangle$ and $\langle \zeta+ \rangle$ are listed in Table 3.2 .

A Computer program was written in the I.C.L. language Algol 68 to calculate the eigenvalues and wavefunctions of the Hamiltonian matrix described so far. By introducing the constraint that $Ka = \Lambda + \Sigma$ and letting the angle Θ=90 degrees, this program should then be suitable for calculating the rotational spectra of diatomic molecules with $^{2}\Pi$ ground states. In order to estimate the hyperfine and lambda-doubling parameters for the rare gas complexes and also to test the validity of the single perturbing state, a fit was attempted of the NO lambda-doubling spectrum of Meerts et al.

All 62 frequencies reported by Meerts[26] for the $^{2}\Pi_{1/2}$ and the excited $^{2}\Pi_{3/2}$ states of NO were included in the least squares fit.

TABLE 3.2 : Matrix Elements of the Rotational and Spin-Orbit Hamiltonian Off-Diagonal in Electronic State

$$\langle J\ K_a\ \Lambda=1\ \Sigma|H|J\ K_a\ \Lambda=0\ \Sigma\rangle = (b+ - a+).\mathrm{Sin}(\theta).\mathrm{Cos}(\theta).(\Sigma + \tfrac{1}{2}) + a+ .K_a.\mathrm{Cos}(\theta)$$

$$\langle J\ K_a\ \Lambda=-1\ \Sigma|H|J\ K_a\ \Lambda=0\ \Sigma\rangle = (-1)^S.(b+ - a+).\mathrm{Sin}(\theta).\mathrm{Cos}(\theta).(\Sigma - \tfrac{1}{2}) + (-1)^S.a+ .K_a.\mathrm{Cos}(\theta)$$

$$\langle J\ K_a \pm 1\ \Lambda=1\ \Sigma|H|J\ K_a\ \Lambda=0\ \Sigma\rangle = \tfrac{1}{2}\{(J \mp K_a)(J \pm K_a+1)\}^{\frac{1}{2}}.(-b+ .\mathrm{Sin}(\theta) \mp c+)$$

$$\langle J\ K_a \pm 1\ \Lambda=-1\ \Sigma|H|J\ K_a\ \Lambda=0\ \Sigma\rangle = \tfrac{1}{2}\{(J \mp K_a)(J \pm K_a+1)\}^{\frac{1}{2}}.(-1)^S.(-b+ \mathrm{Sin}(\theta) \pm c+)$$

$$\langle J\ K_a\ \Lambda=1\ \Sigma=\pm\tfrac{1}{2}|H|J\ K_a\ \Lambda=0\ \Sigma=\mp\tfrac{1}{2}\rangle = \tfrac{1}{2}(\tfrac{1}{2}\zeta+ \mp \tfrac{1}{2}\zeta+) + \tfrac{1}{2}(a+ .\mathrm{Cos}^2(\theta) + b+ .\mathrm{Sin}^2(\theta) \mp c+)$$

$$\langle J\ K_a\ \Lambda=-1\ \Sigma=\pm\tfrac{1}{2}|H|J\ K_a\ \Lambda=0\ \Sigma=\mp\tfrac{1}{2}\rangle = \tfrac{1}{2}.(-1)^S.(\tfrac{1}{2}\zeta+ \pm\tfrac{1}{2}\zeta+) + \tfrac{1}{2}.(-1)^S.(a+ .\mathrm{Cos}\ (\theta) + b+ .\mathrm{Sin}\ (\theta) \pm c+)$$

Where, $a+ \equiv \langle A+ \rangle$, $b+ \equiv \langle B+ \rangle$ e.t.c.

The data were weighted according to the reported uncertainties in Meerts' measurements. The values for ζ and $B(^2\Pi_{1/2})$ for NO were those used in his later paper, namely :

$$B(^2\Pi_{\frac{1}{2}}) = 50844.97 \text{ MHz}$$

$$\zeta = 123.16 \text{ cm}^{-1}$$

A single $^2\Sigma^-$ state was included in the Hamiltonian matrix. The energy separation between this and the ground state was arbitrarily chosen to be :

$$E_{\Sigma\Pi} = 131897.1 \text{ cm}^{-1}$$

This separation is approximately three times higher in energy than the lowest ($A^2\Sigma^+$) excited state of NO; such a choice has the advantage that the fitted matrix elements of $L\pm$ are close to the "pure precession" values.

By floating the hyperfine (diagonal in electronic state) and lambda-doubling parameters, a final fit was obtained with the largest discrepancy between observed and calculated frequencies being 104 kHz. The root mean square error was 0.0312 MHz. The fit obtained is shown in Table 3.3 . The final values of the floated parameters are shown below.

$$eQq_0 = -1.8728 \text{ MHz}$$

$$eQq_2 = 23.2145 \text{ MHz}$$

$$a = 84.2755 \text{ MHz}$$

$$b_F = 22.0330 \text{ MHz}$$

$$c = -58.4277 \text{ MHz}$$

$$d = 112.6125 \text{ MHz}$$

$$\langle 0|BL^-|1\rangle = 75250.4329 \text{ MHz}$$

$$\langle 0|\zeta L^-|1\rangle = 9212254.3572 \text{ MHz}$$

The hyperfine parameters agreed within one per cent with the equivalent ones of Neumann[29] and Meerts.[26] Since the definition of these parameters in the present work differed slightly from the

perturbation treatments of previous authors, a small discrepancy was to be expected. As an additional check, the ratio of the two fitted lambda-doubling constants was compared with the analogous parameters of Neumann;[29] the latter are given below :

$$A_1 = \sum_{\eta} (-1)^s . \frac{\langle 0|(B+1/2.\zeta)L^-|1\rangle\langle 0|BL^+|-1\rangle}{E(^2\Sigma) - E(X^2\Pi)} = 88.9033 \text{ MHz}$$

$$A_2 = \sum_{\eta} (-1)^s . \frac{\langle 0|BL^+|-1\rangle^2}{E(^2\Sigma) - E(X^2\Pi)} = 1.4148 \text{ MHz} \qquad (3.6.3)$$

The final ratio should be approximately equal to that of the fitted lambda-doubling parameters of this work :

$$\frac{\langle 0|BL^-|1\rangle}{\langle 0|\zeta L^-|1\rangle} = 122.421$$

The discrepancy between the two ratios is about one per cent. Once again this may be rationalised in terms of the difference in the definitions of Neumann's parameters and those of Equation (3.6.2).

The fitting of Meerts' NO data to this model Hamiltonian was valuable in two respects. Firstly, it demonstrated that the approximations made were not so drastic as to preclude a reasonable fit to experimental data. Secondly, the hyperfine and lambda-doubling parameters were well determined for NO; these were found useful as initial estimates for the equivalent parameters in rare gas - nitric oxide van der Waals molecules.

Table 3.3 : Fit of NO Lambda-Doubling Spectrum

$\Omega = \pm 1/2$ J=	F+	F-	Observed Freq./MHz	(Obs. - Calc.)/kHz
1/2	3/2	3/2	431.1905	-8.7
	3/2	1/2	411.2056	-68.4
	1/2	3/2	225.9357	80.9
3/2	1/2	1/2	560.8538	23.2
	3/2	3/2	651.5425	11.7
	5/2	5/2	801.1936	-8.1
	3/2	5/2	758.9106	18.3
	5/2	3/2	693.8282	-14.6
	1/2	3/2	624.6494	36.9
	3/2	1/2	587.7467	-2.2
5/2	3/2	3/2	929.2590	25.6
	7/2	7/2	1160.7768	-4.8
	7/2	5/2	1114.6770	54.0
	5/2	7/2	1072.5960	-48.5
	5/2	3/2	991.7338	67.2
	3/2	5/2	964.0230	-29.6
7/2	9/2	9/2	1514.7680	2.1
	9/2	7/2	1434.5880	-69.2
	7/2	9/2	1467.5110	91.8
	7/2	5/2	1325.2990	-48.7
	5/2	7/2	1348.4590	104.1

(Continued Overleaf)

Table 3.3 Continued

$\Omega = \pm 3/2$ / J=	F+	F-	Observed Freq./MHz	(Obs. - Calc.)/kHz
3/2	3/2	3/2	0.6120	0.2
	5/2	5/2	1.0290	0.6
	3/2	5/2	74.9310	-37.7
	5/2	3/2	73.2860	-42.4
	1/2	3/2	46.4640	-23.2
5/2	5/2	5/2	3.1210	1.5
	7/2	7/2	3.9230	2.0
	7/2	5/2	47.2110	-18.6
	5/2	7/2	40.1720	-17.1
	5/2	3/2	34.3900	4.2
7/2	7/2	9/2	39.2110	-26.4
	5/2	7/2	31.5500	5.5
9/2	11/2	9/2	40.5120	0.4
	9/2	7/2	35.0450	5.3
11/2	9/2	9/2	31.1240	6.1
	11/2	11/2	30.2650	5.9
	13/2	13/2	32.4250	8.3
	11/2	13/2	48.7860	7.1
	13/2	11/2	13.9050	8.1
13/2	11/2	11/2	49.4050	6.1
	13/2	13/2	48.5780	6.4
	15/2	15/2	51.2600	7.4
	15/2	13/2	63.6400	9.9
	13/2	15/2	36.1960	1.9
	13/2	11/2	59.7420	16.0
	11/2	13/2	38.2430	-1.5

(Continued Overleaf)

Table 3.3 Continued

$\Omega = \pm 3/2$ $J =$	F+	F-	Observed Freq./MHz	(Obs. - Calc.)/kHz
15/2	13/2	13/2	73.5400	2.5
	15/2	15/2	72.7860	2.4
	17/2	17/2	76.0250	4.0
	15/2	17/2	85.2550	9.2
	17/2	15/2	63.5520	-6.8
	13/2	15/2	81.5470	16.4
	15/2	13/2	64.7780	-12.5
17/2	15/2	15/2	104.2160	-7.1
	17/2	17/2	103.5750	-7.8
	19/2	19/2	107.4000	-7.5
	19/2	17/2	114.0240	5.9
	17/2	19/2	96.9510	-21.2
	17/2	15/2	110.3060	10.2
	15/2	17/2	97.4830	-27.1

3.7 A Simplified Picture of the Fine Structure

The foregoing parts of this chapter have shown how the fine and hyperfine rotational energy levels may be calculated by the diagonalisation of a rather complicated matrix. Whilst this sort of procedure is straightforward to achieve with a digital computer, it is instructive to try to extract those terms in the Hamiltonian that dominate the spectrum. Hence a simplified view of the fine structure will be developed in this section and treated by perturbation theory. The effects of lambda-doubling (non-adiabatic) and hyperfine interactions will not be included. Attention will be focussed on the lowest rotational energy levels (Ka=1/2) as these will be predominantly populated following a supersonic expansion.

To achieve a simplification of the fine structure it is advantageous to construct symmetrised wavefunctions from the basis set described in section (3.3) The parity of suitable wavefunctions may be determined from Equation (3.4.10) and is given below for the kets denoting $|Ka, \Omega = \Lambda + \Sigma >$.

(3.7.1)

	Parity J=1/2	Parity J=3/2 etc.
$\|Q\rangle = 1/\sqrt{2}\{ \|1/2, 1/2\rangle + \|-1/2,-1/2\rangle\}$	+	-
$\|R\rangle = 1/\sqrt{2}\{ \|1/2, 1/2\rangle - \|-1/2,-1/2\rangle\}$	-	+
$\|S\rangle = 1/\sqrt{2}\{ \|1/2,-1/2\rangle + \|-1/2, 1/2\rangle\}$	-	+
$\|T\rangle = 1/\sqrt{2}\{ \|1/2,-1/2\rangle - \|-1/2, 1/2\rangle\}$	+	-
$\|U\rangle = 1/\sqrt{2}\{ \|1/2, 3/2\rangle + \|-1/2,-3/2\rangle\}$	-	+
$\|V\rangle = 1/\sqrt{2}\{ \|1/2, 3/2\rangle - \|-1/2,-3/2\rangle\}$	+	-
$\|W\rangle = 1/\sqrt{2}\{ \|1/2,-3/2\rangle + \|-1/2, 3/2\rangle\}$	+	-
$\|X\rangle = 1/\sqrt{2}\{ \|1/2,-3/2\rangle - \|-1/2, 3/2\rangle\}$	-	+

The phase factor included in the definition of the parity states may be written $(-1)^{J-S}.(-1)^{\Omega-K_a}$; this leads to the alternation of parities with J for |Q> to |X>.

A further factorisation of the matrix may be performed at $\theta = 0$ (the T-shaped configuration for a complex) by taking appropriate symmetric and antisymmetric combinations of kets of like parity. The combination leading to the simplest matrices are given below in terms of the original unsymmetrised functions :

$$|Q+T\rangle = 1/2\{+|1/2,1/2\rangle + |-1/2,-1/2\rangle + |1/2,-1/2\rangle - |-1/2,1/2\rangle\}$$

$$|Q-T\rangle = 1/2\{+|1/2,1/2\rangle + |-1/2,-1/2\rangle - |1/2,-1/2\rangle + |-1/2,1/2\rangle\}$$

$$|V+W\rangle = 1/2\{+|1/2,3/2\rangle - |-1/2,-3/2\rangle + |1/2,-3/2\rangle + |-1/2,3/2\rangle\}$$

$$|V-W\rangle = 1/2\{+|1/2,3/2\rangle - |-1/2,-3/2\rangle - |1/2,-3/2\rangle - |-1/2,3/2\rangle\}$$

$$|R+S\rangle = 1/2\{+|1/2,1/2\rangle - |-1/2,-1/2\rangle + |1/2,-1/2\rangle + |-1/2,1/2\rangle\}$$

$$|R-S\rangle = 1/2\{+|1/2,1/2\rangle - |-1/2,-1/2\rangle - |1/2,-1/2\rangle - |-1/2,1/2\rangle\}$$

$$|U+X\rangle = 1/2\{+|1/2,3/2\rangle + |-1/2,-3/2\rangle + |1/2,-3/2\rangle - |-1/2,3/2\rangle\}$$

$$|U-X\rangle = 1/2\{+|1/2,3/2\rangle + |-1/2,-3/2\rangle - |1/2,-3/2\rangle + |-1/2,3/2\rangle\}$$

(3.7.2)

Using the fine structure matrix elements developed in section (3.5) the matrices for Ka=1/2 were calculated for the unsymmetrised wavefunctions and for the parity combinations given in (3.7.1) and (3.7.2). These matrices are shown in Tables 3.4 to 3.6 and are valid for J=1/2. For J>1/2 the Ka=3/2 manifold should be included in the matrix since elements off-diagonal in Ka by $\pm$ 1 may have a significant effect on the spectrum. (The Ka=3/2 manifold lies approximately 2[A-1/2(B+C)] MHz above Ka=1/2.)

The application of degenerate perturbation theory[19] to the matrix elements connecting the two fine structure states for each parity block permits a further reduction of the problem into four (2 x 2) matrices. From these explicit expressions may be

developed for the energies and wavefunctions of the Ka=1/2 fine structure states. The resulting (2 by 2) matrices are shown in Table 3.7. At the T-shaped geometry these matrices are diagonal leading to simple approximate expressions for the Ka=1/2 rotational fine structure energy levels :

$$|Q+T\rangle,\ E_{rot} - \tfrac{1}{2}\zeta' + B/2(J+\tfrac{1}{2}) - 1/(4\zeta')\{A+C(J+\tfrac{1}{2})-\varepsilon_2'\}^2$$

$$|R-S\rangle,\ E_{rot} - \tfrac{1}{2}\zeta' + B/2(J+\tfrac{1}{2}) - 1/(4\zeta')\{A+C(J+\tfrac{1}{2})+\varepsilon_2'\}^2$$

$$|R+S\rangle,\ E_{rot} - \tfrac{1}{2}\zeta' - B/2(J+\tfrac{1}{2}) - 1/(4\zeta')\{A-C(J+\tfrac{1}{2})-\varepsilon_2'\}^2$$

$$|Q-T\rangle,\ E_{rot} - \tfrac{1}{2}\zeta' - B/2(J+\tfrac{1}{2}) - 1/(4\zeta')\{A-C(J+-)+\varepsilon_2'\}^2$$

(3.7.3)

where,

$$E_{rot} = \{A-\tfrac{1}{2}(B+C)\}K_a^2 + \tfrac{1}{2}(B+C)J(J+1)$$

$$\zeta' = 2A\mathrm{Sin}^2\theta + 2B\mathrm{Cos}^2\theta + \zeta = 2B + \zeta$$

$$\varepsilon_2'/2 = \varepsilon_2/2 + 1/4\{A\mathrm{Cos}^2\theta + B\mathrm{Sin}^2\theta - C\}\langle\pm1|L\pm^2|\mp1\rangle$$

(3.7.4)

	| 1/2, 1/2>	|-1/2,-1/2>	| 1/2,-1/2>	|-1/2, 1/2>	| 1/2, 3/2>	|-1/2,-3/2>	| 1/2,-3/2>	|-1/2, 3/2>
< 1/2, 1/2|	$E_{rot}-\frac{1}{2}A\sin\theta$ $-\frac{1}{2}\zeta'$	0	0	$-\frac{1}{2}B\cos\theta.(J+\frac{1}{2})$	$(B-A).\sin\theta.$ $\cos\theta+\frac{1}{2}A\cos\theta$	0	$-\frac{1}{2}\varepsilon_2'$	$\frac{1}{2}(C-B\sin\theta).$ $(J+\frac{1}{2})$
<-1/2,-1/2|		$E_{rot}-\frac{1}{2}A\sin\theta$ $-\frac{1}{2}\zeta'$	$\frac{1}{2}B\cos\theta.(J+\frac{1}{2})$	0	0	$-(B-A)\sin\theta.$ $\cos\theta-\frac{1}{2}A\cos\theta$	$\frac{1}{2}(C-B\sin\theta.$ $(J+\frac{1}{2})$	$-\frac{1}{2}\varepsilon_2'$
< 1/2,-1/2|			$E_{rot}+\frac{1}{2}A\sin\theta$ $-\frac{1}{2}\zeta'$	0	$-\frac{1}{2}\varepsilon_2'$	$-\frac{1}{2}(C+B\sin\theta).$ $(J+\frac{1}{2})$	$-(B-A).\sin\theta.$ $\cos\theta+\frac{1}{2}A\cos\theta$	0
<-1/2, 1/2|				$E_{rot}+\frac{1}{2}A\sin\theta$ $-\frac{1}{2}\zeta'$	$-\frac{1}{2}(C+B\sin\theta).$ $(J+\frac{1}{2})$	$-\frac{1}{2}\varepsilon_2'$	0	$+(B-A)\sin\theta.$ $\cos\theta-\frac{1}{2}A\cos\theta$
< 1/2, 3/2|					$E_{rot}-3A/2.$ $\sin\theta+\frac{1}{2}\zeta'$	0	0	$-3/2.B\cos\theta.$ $(J+\frac{1}{2})$
<-1/2,-3/2|						$E_{rot}-3A/2.$ $\sin\theta+\frac{1}{2}\zeta'$	$+3/2.B\cos\theta.$ $(J+\frac{1}{2})$	0
< 1/2,-3/2|							$E_{rot}+3A/2.$ $\sin\theta+\frac{1}{2}\zeta'$	0
<-1/2, 3/2|								$E_{rot}+3A/2.$ $\sin\theta+\frac{1}{2}\zeta'$

Table 3.4

	| Q >	| R >	| S >	| T >	| U >	| V >	| W >	| X >
< Q |	$E_{rot} - \frac{1}{2}A\sin\theta - \frac{1}{2}\zeta'$	0	0	$+\frac{1}{2}B\cos\theta.(J+\frac{1}{2})$	0	$+(B-A)\cos\theta.\sin\theta + \frac{1}{2}A\cos\theta$	$+\frac{1}{2}(C-B\sin\theta).(J+\frac{1}{2}) - \frac{1}{2}\epsilon_2'$	0
< R |		$E_{rot} - \frac{1}{2}A\sin\theta - \frac{1}{2}\zeta'$	$-\frac{1}{2}B\cos\theta.(J+\frac{1}{2})$	0	$+(B-A)\sin\theta.\cos\theta + \frac{1}{2}A\cos\theta$	0	0	$-\frac{1}{2}(C-B\sin\theta).(J+\frac{1}{2}) - \frac{1}{2}\epsilon_2'$
< S |			$E_{rot} + \frac{1}{2}A\sin\theta - \frac{1}{2}\zeta'$	0	$-\frac{1}{2}(C+B\sin\theta).(J+\frac{1}{2}) - \epsilon_2'$	0	0	$-(B-A)\sin\theta.\cos\theta + \frac{1}{2}A\cos\theta$
< T |				$E_{rot} + \frac{1}{2}A\sin\theta - \frac{1}{2}\zeta'$	0	$+\frac{1}{2}(C+B\sin\theta).(J+\frac{1}{2}) - \epsilon_2'$	$-(B-A)\sin\theta.\cos\theta + \frac{1}{2}A\cos\theta$	0
< U |					$E_{rot} - 3A/2.\sin\theta + \frac{1}{2}\zeta'$	0	0	$+3B/2.\cos\theta.(J+\frac{1}{2})$
< V |						$E_{rot} - 3A/2.\sin\theta + \frac{1}{2}\zeta'$	$-3B/2.\cos\theta.(J+\frac{1}{2})$	0
< W |							$E_{rot} + 3A/2.\sin\theta + \frac{1}{2}\zeta'$	0
< X |								$E_{rot} + 3A/2.\sin\theta + \frac{1}{2}\zeta'$

Table 3.5

	$\|Q+T\rangle$	$\|Q-T\rangle$	$\|V+W\rangle$	$\|V-W\rangle$	$\|R+S\rangle$	$\|R-S\rangle$	$\|U+X\rangle$	$\|U-X\rangle$
$\langle Q+T\|$	$E_{rot} - \frac{1}{2}\zeta' + \frac{1}{2}B\cos\theta.(J+\frac{1}{2})$	$-A/2.\sin\theta$	$\frac{1}{2}(A\cos\theta-\varepsilon_2') + \frac{1}{2}C(J+\frac{1}{2})$	$+(B-A)\sin\theta\cos\theta + \frac{1}{2}B\sin\theta.(J+\frac{1}{2})$	0	0	0	0
$\langle Q-T\|$		$E_{rot} - \frac{1}{2}\zeta' - \frac{1}{2}B\cos\theta.(J+\frac{1}{2})$	$+(B-A)\sin\theta\cos\theta - \frac{1}{2}B\sin\theta.(J+\frac{1}{2})$	$\frac{1}{2}(A\cos\theta+\varepsilon_2') - \frac{1}{2}C(J+\frac{1}{2})$	0	0	0	0
$\langle V+W\|$			$E_{rot} + \frac{1}{2}\zeta' - 3B/2.\cos\theta(J+\frac{1}{2})$	$-3A/2.\sin\theta$	0	0	0	0
$\langle V-W\|$				$E_{rot} + \frac{1}{2}\zeta' + 3B/2-\cos\theta(J+\frac{1}{2})$	0	0	0	0
$\langle R+S\|$					$E_{rot} - \frac{1}{2}\zeta' - \frac{1}{2}B\cos\theta.(J+\frac{1}{2})$	$-A/2.\sin\theta$	$\frac{1}{2}(A\cos\theta-\varepsilon_2') - \frac{1}{2}C(J+\frac{1}{2})$	$+(B-A)\sin\theta\cos\theta - \frac{1}{2}B\sin\theta.(J+\frac{1}{2})$
$\langle R-S\|$						$E_{rot} - \frac{1}{2}\zeta' + \frac{1}{2}B\cos\theta.(J+\frac{1}{2})$	$+(B-A)\sin\theta\cos\theta + \frac{1}{2}B\sin\theta.(J+\frac{1}{2})$	$\frac{1}{2}(A\cos\theta+\varepsilon_2')$
$\langle U+X\|$							$E_{rot} + \frac{1}{2}\zeta' + 3B/2.\cos\theta(J+\frac{1}{2})$	$-3A/2.\sin\theta$
$\langle U-X\|$								$E_{rot} + \frac{1}{2}\zeta' - 3B/2.\cos\theta(J+\frac{1}{2})$

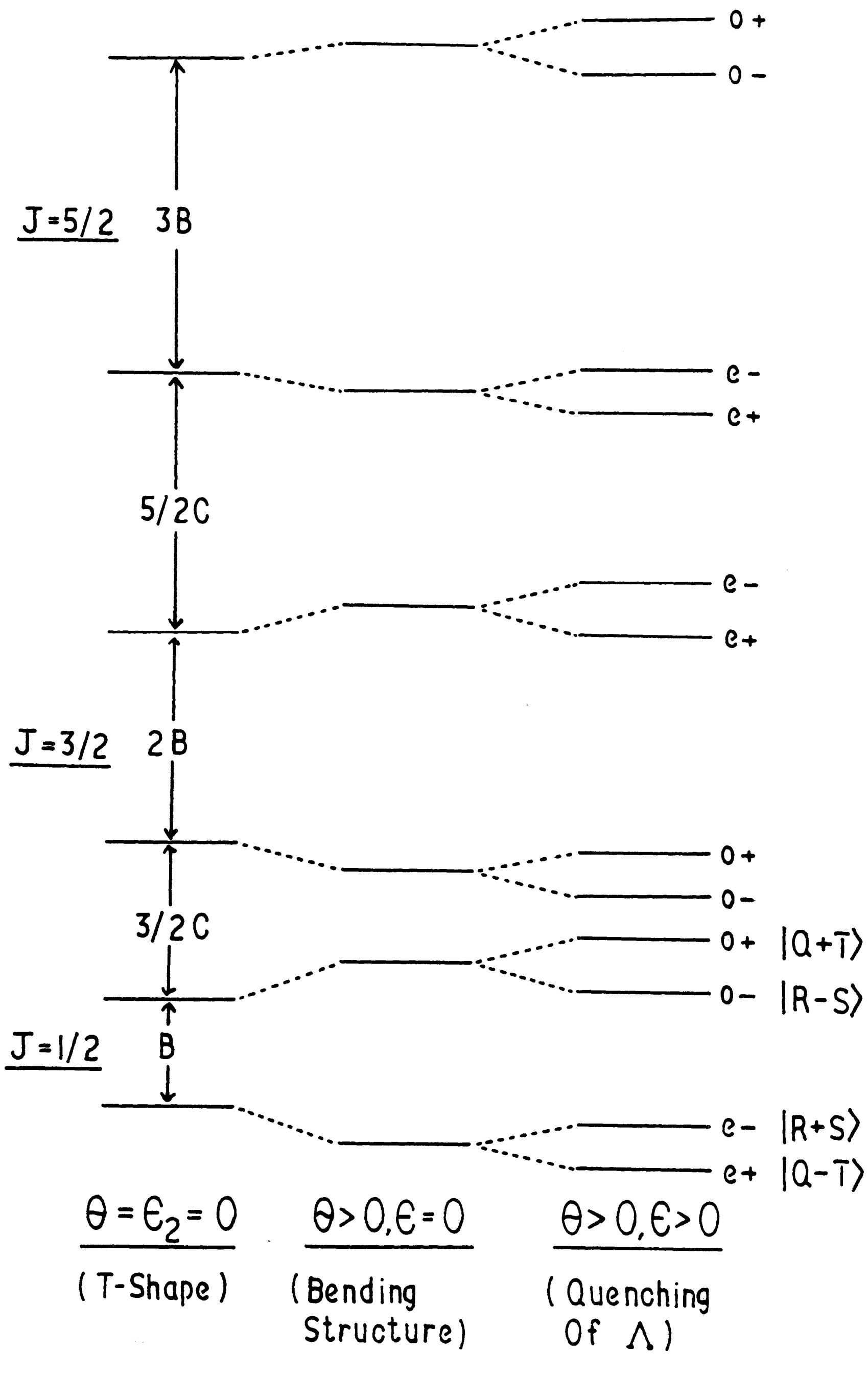
Table 3.6

	$\lvert Q + T\rangle$	$\lvert Q - T\rangle$
$\langle Q+T\rvert$	$E_{ROT} - 1/2.\zeta'$ $+ \frac{1}{2}B.\cos(\theta).(J+\frac{1}{2})$ $-1/\zeta'.\{((A.\cos(\theta)-\varepsilon_2')/2 + \frac{1}{2}C(J+\frac{1}{2}))^2$ $+((B-A)\sin(\theta)\cos(\theta) + \frac{1}{2}B.\sin(\theta)(J+\frac{1}{2}))^2\}$	$-1/2.A.\sin(\theta)$ $-1/\zeta'.\{A.\cos(\theta).(B-A)\sin(\theta)\cos(\theta)$ $+ \frac{1}{2}B.\sin(\theta)(J+\frac{1}{2})(\varepsilon_2' - C(J+\frac{1}{2}))\}$
$\langle Q-T\rvert$	$E_{ROT} - 1/2.\zeta'$ $- \frac{1}{2}B.\cos(\theta).(J+\frac{1}{2})$ $-1/\zeta'.\{((A.\cos(\theta)+\varepsilon_2')/2 - \frac{1}{2}C(J+\frac{1}{2}))^2$ $+((B-A)\sin(\theta)\cos(\theta) - \frac{1}{2}B.\sin(\theta)(J+\frac{1}{2}))^2$	

	$\lvert R + S\rangle$	$\lvert R - S\rangle$
$\langle R+S\rvert$	$E_{ROT} - 1/2.\zeta'$ $- \frac{1}{2}B.\cos(\theta).(J+\frac{1}{2})$ $-1/\zeta'.\{((A.\cos(\theta)-\varepsilon_2')/2 - \frac{1}{2}C(J+\frac{1}{2}))^2$ $+((B-A)\sin(\theta)\cos(\theta) - \frac{1}{2}B.\sin(\theta)(J+\frac{1}{2}))^2\}$	$-1/2.A.\sin(\theta)$ $-1/\zeta'.\{A.\cos(\theta).(B-A)\sin(\theta)\cos(\theta)$ $+ \frac{1}{2}B.\sin(\theta)(J+\frac{1}{2})(-\varepsilon_2' - C(J+\frac{1}{2}))\}$
$\langle R-S\rvert$	$E_{ROT} - 1/2.\zeta'$ $+ \frac{1}{2}B.\cos(\theta).(J+\frac{1}{2})$ $-1/\zeta'.\{((A.\cos(\theta)+\varepsilon_2')/2 + \frac{1}{2}C(J+\frac{1}{2})))^2$ $+((B-A)\sin(\theta)\cos(\theta) + \frac{1}{2}B.\sin(\theta)(J+\frac{1}{2}))^2$	

TABLE 3.7

Figure 3.3: RgNO Energy Levels



In the absence of a quenching potential, that is when $\varepsilon_2 = 0$, the spacing of the rotational energy levels depends predominantly upon B and C as shown on the left hand side of Figure 3.3 . When the equilibrium structure deviates from $\theta=0$ there is a strong interaction between the pairs $|Q\pm T\rangle$ and $|R\pm S\rangle$ the origin of which is most evident in Table 3.6 . The double degeneracy of each of these states is then lifted by the quenching interaction as shown on the right hand side of Figure 3.3 . The splittings thus caused are asymmetric between the pairs of states $|Q+T\rangle, |R-S\rangle$ and $|R+S\rangle, |Q-T\rangle$. At $\theta=0$ the major contribution to these splittings may be evaluated from the perturbation expression given in Equation (3.7.3).

$$E\{|Q+T\rangle\} - E\{|R-S\rangle\} \approx (1/\zeta').\varepsilon_2'.\{A+C(J+\tfrac{1}{2})\}$$

$$E\{|R+S\rangle\} - E\{|Q-T\rangle\} \approx (1/\zeta').\varepsilon_2'.\{A-C(J+\tfrac{1}{2})\}$$

(3.7.5)

On the right hand side of Figure 3.3 is indicated the correlation between the energy levels and the corresponding symmetrised wavefunctions. In the following chapters the prime on the diagonal quenching parameter will be omitted for convenience. It should be remembered, however, that the spectroscopically significant quantity still contains a rotational contribution.

3.8 Electric Dipole Transition Intensities

The intensity of an electric dipole transition between two states $|i\rangle$ and $|f\rangle$ is proportional to the sum of the squares of the transition dipole moments.[19] That is :

$$I_{if} \propto \sum_{p} |\langle i|T^1_p(\underset{\sim}{\mu}).T^1_{-p}(\underset{\sim}{E})|f\rangle|^2 \qquad (3.8.1)$$

where $T^1(E)$ denotes the magnitude of a component of the electric field vector of the radiation at a given point in space. The general form of such matrix elements has already been given in Equation (3.5.56). Although the molecular beam electric resonance spectrometer does not yield reliable relative intensities (because of focussing considerations), it is desirable to have a qualitative picture of the line strengths. The most straightforward approach is to use the symmetrised functions developed in the previous section which are good approximations to the eigenfunctions at, or close to, $\Theta=0$.

For μ_a allowed transitions the relevant part of the transition dipole moment that requires examination is :

$$\sum_{p} (-1)^{I+F+F'+p+1-M_F'}.(-1)^{K_a'} \times \sum_{q} \begin{pmatrix} J' & 1 & J \\ -K_a' & q=0 & K_a \end{pmatrix} \times \delta_{\Lambda'\Lambda}$$
$$\times \delta_{\Sigma'\Sigma} \times T^1_{-p}(E) \times \langle \beta' K_a' \Omega' | T^1_{q=0}(\underset{\sim}{\mu}) | \beta K_a \Omega \rangle$$

where the labels β and β' denote all other quantum numbers and are hereafter omitted for clarity. Hence we can evaluate an expression for the μ_a transition moment between any pair of symmetrised states as exemplified below :

$$\sum_{p} \langle Q+T|T^{1}_{q=0}(\underset{\sim}{\mu})|R+S\rangle \quad \propto \quad (3.8.2)$$

$$+(-1)^{I+F+F'+p+1-M_F'}.(-1)^{K_a'=\frac{1}{2}} x\begin{pmatrix} J' & 1 & J \\ -\frac{1}{2} & 0 & \frac{1}{2} \end{pmatrix} x \langle \tfrac{1}{2},\tfrac{1}{2}|\mu_a|\tfrac{1}{2},\tfrac{1}{2}\rangle$$

$$+(-1)^{I+F+F'+p+1-M_F'}.(-1)^{K_a'=\frac{1}{2}} x\begin{pmatrix} J' & 1 & J \\ -\frac{1}{2} & 0 & \frac{1}{2} \end{pmatrix} x \langle \tfrac{1}{2},-\tfrac{1}{2}|\mu_a|\tfrac{1}{2},-\tfrac{1}{2}\rangle$$

$$-(-1)^{I+F+F'+p+1-M_F'}.(-1)^{K_a'=-\frac{1}{2}} x\begin{pmatrix} J' & 1 & J \\ \frac{1}{2} & 0 & -\frac{1}{2} \end{pmatrix} x \langle -\tfrac{1}{2},-\tfrac{1}{2}|\mu_a|-\tfrac{1}{2},-\tfrac{1}{2}\rangle$$

$$-(-1)^{I+F+F'+p+1-M_F'}.(-1)^{K_a'=-\frac{1}{2}} x\begin{pmatrix} J' & 1 & J \\ \frac{1}{2} & 0 & -\frac{1}{2} \end{pmatrix} x \langle -\tfrac{1}{2},\tfrac{1}{2}|\mu_a|-\tfrac{1}{2},\tfrac{1}{2}\rangle$$

Thus, since the lower two components (with Ka'=-1/2) will contribute a phase factor of opposite sign to the upper pair, the transition moment will be non-zero provided that the three-j symbols are equal. From the symmetry properties of these symbols as given by Brink and Satchler, the two are related thus :

$$\begin{pmatrix} J' & 1 & J \\ -\frac{1}{2} & 0 & \frac{1}{2} \end{pmatrix} = (-1)^{J+J'+1} x \begin{pmatrix} J' & 1 & J \\ \frac{1}{2} & 0 & -\frac{1}{2} \end{pmatrix} \qquad (3.8.3)$$

Therefore the matrix elements connecting the states $|Q+T\rangle$ and $|R+S\rangle$ are only non-zero when :

$$J + J' + 1 = \text{EVEN INTEGER} \qquad (3.8.4)$$

The matrix elements of μ_b may be obtained from the relation:

$$\mu_b = 1/\sqrt{2}\{ T^{1}_{-1}(\underset{\sim}{\mu}) - T^{1}_{1}(\underset{\sim}{\mu}) \} \qquad (3.8.5)$$

and hence selection rules on μ_a and μ_b allowed transitions between all the symmetrised states may be derived. The non-zero matrix elements for μ_a and μ_b are as follows :

μ_a		μ_b		
$\langle Q+T\vert$	$\leftrightarrow \vert R+S\rangle$	$\langle Q+T\vert$	$\leftrightarrow \vert R-S\rangle$	$\Delta J = 0$
$\langle Q-T\vert$	$\leftrightarrow \vert R-S\rangle$	$\langle Q-T\vert$	$\leftrightarrow \vert R+S\rangle$	
$\langle Q+T\vert$	$\leftrightarrow \vert Q+T\rangle$	$\langle Q+T\vert$	$\leftrightarrow \vert Q-T\rangle$	$\Delta J = \pm 1$
$\langle Q-T\vert$	$\leftrightarrow \vert Q-T\rangle$	$\langle R+S\vert$	$\leftrightarrow \vert R-S\rangle$	
$\langle R+S\vert$	$\leftrightarrow \vert R+S\rangle$			
$\langle R-S\vert$	$\leftrightarrow \vert R-S\rangle$			

(3.8.6)

In addition to the above there is the general parity selection rule given in Equation (3.5.58). To simplify the notation, new symmetry labels "e" and "o" are introduced which correlate with the symmetrised wavefunctions already derived :

	J=1/2,5/2,9/2	J=3/2,7/2,11/2
$\vert Q+T\rangle$ and $\vert R-S\rangle$	o	e
$\vert Q-T\rangle$ and $\vert R+S\rangle$	e	o

(3.8.7)

Recalling the alternating parity with J for the symmetrised states, the full notation for J=1/2 is :

$$\vert Q+T\rangle \equiv o(+)$$
$$\vert Q-T\rangle \equiv e(+)$$
$$\vert R+S\rangle \equiv e(-)$$
$$\vert R-S\rangle \equiv o(-) \qquad (3.8.8)$$

and hence the full selection rules for a T-shaped complex are :

μ_a		μ_b		
$e(+)$	$\leftrightarrow o(-)$	$e(+)$	$\leftrightarrow e(-)$	(3.8.9)
$e(-)$	$\leftrightarrow o(+)$	$o(+)$	$\leftrightarrow o(-)$	

The allowed transitions for a pair of adjacent J manifolds are

indicated in Figure 3.4 .

It is important to note the range of applicability of these selection rules. Those based on parity (+ to -) are entirely rigorous for electric dipole transitions (in the absence of perturbing electric fields) and are independent of the equilibrium structure of the complex. The rules relating to the e,o labels are rigorous only at $\theta=0$ but may be expected to give a qualitative guideline for predicting strong transitions for geometries deviating by only a few degrees from a T-shape. For such geometries the largest component of μ is expected to be that along the b-axis arising mainly from the projection of the nitric oxide dipole moment. The e,o labels are used in the following chapters to denote states correlating with those of Equation (3.8.7).

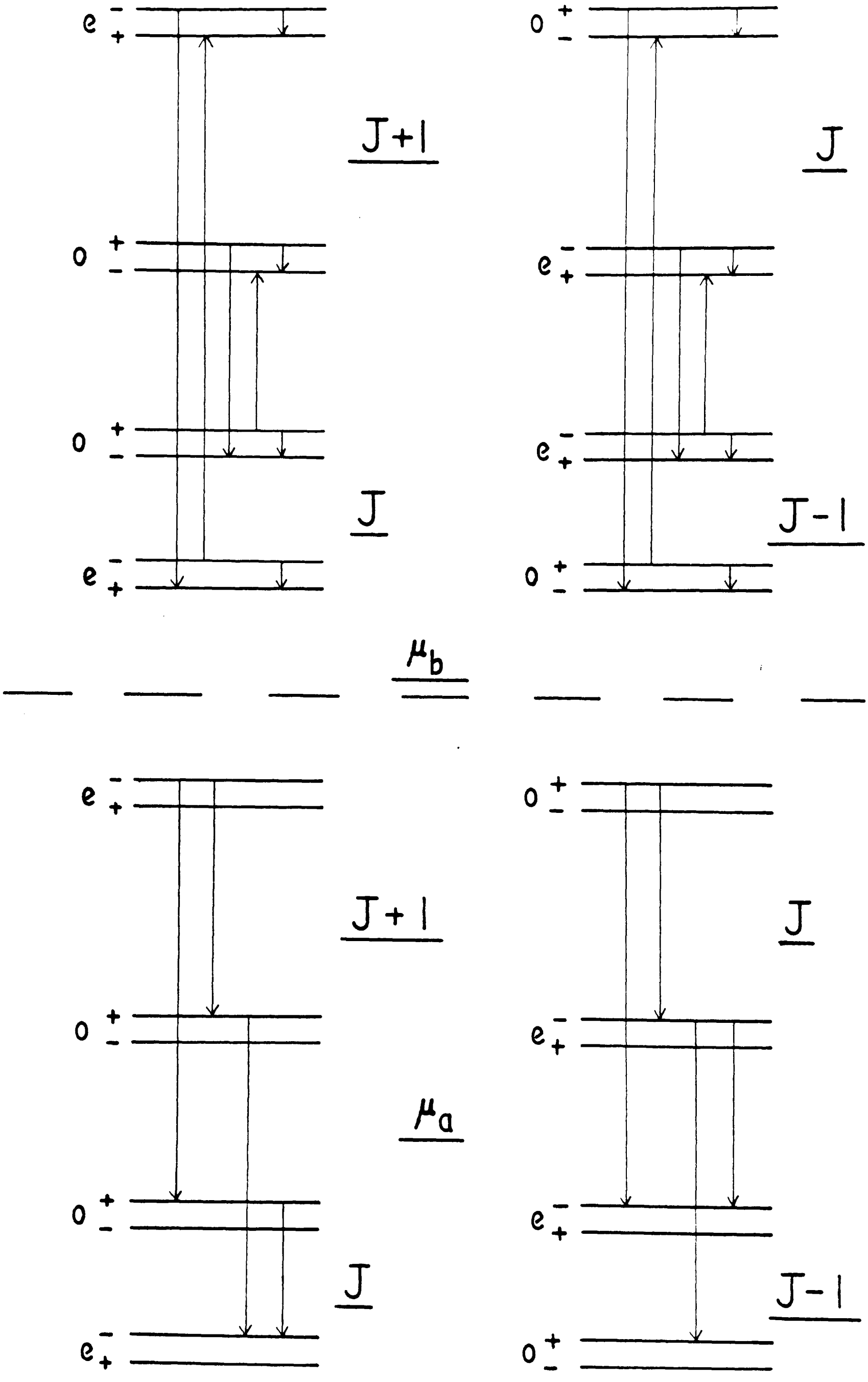


Figure 3.4

3.9 Postscript - Contributions from the Vibrational Hamiltonian

In defining the structural angles θ and γ and the rotational constants, the theory presented so far has effectively assumed that the rare-gas - nitric oxide molecule may be regarded as a rigid rotor. This assumption is usually adopted in deriving expressions for the rotational energy levels of conventional molecules. The deviations that arise from these rigid rotor expressions are attributable to the accompanying, much faster vibrational motion. (This represents a breakdown of the separation of the rotational and vibrational motions of the nuclear framework implied in Equation 3.2.3.[10]) Thus, for example, the inverse moments of inertia contained in the definition of the rotational constant should more accurately be interpreted as a vibrational average of the instantaneous quantity defined in Equation (3.5.3). In classical terms the moment of inertia of a non-rigid body would be expected to change with the speed of rotation because of the elongation due to centrifugal forces. The quantum mechanical picture ascribes rotational quantum number dependence to the structural parameters of a molecule. This is equivalent to admixture of excited vibrational states into the ground state of the molecule.[19] Thus the concomitant corrections to the rotational constants may be formulated in terms of second order perturbation theory.

The contributions from the vibrational Hamiltonian are generally more significant in van der Waals molecules than in their chemically-bound counterparts. This is because the stretching and bending force constants are appreciably smaller for the former; this results in large amplitude deformation of the equilibrium structure and a pronounced coupling of the

rotational and vibrational motion.

For the rare gas - nitric oxide complexes considered in this thesis the above considerations lead to two important effects on the rotational spectra. The first is that all the structural parameters, in particular those relating to the projection of quantities associated with the NO diatom, are averages over wide amplitude vibrations. The structural angles derived from rotational constants and the projections of the various NO internal angular momenta will represent vibrational averages of different trigonometric functions. This is exemplified in the structural analysis of the complex ArHBr by Jackson et al.[32] They determined two vibrationally averaged values for their angle γ (analogous to the angle γ of Figure 3.2) :

$$\text{Arc Cos } \sqrt{\langle \text{Cos}^2\gamma \rangle} = 42.11^{\,0} \qquad (3.9.1)$$

$$\text{Arc Cos } \langle \text{Cos } \gamma \rangle = 50.38^{\,0}$$

Thus any attempt to characterise the rotational spectrum of ArNO or NeNO by a single average θ or γ represents an over-simplification. Discrepancies for these species should not be quite so significant as in (3.8.1), however, since the vibrations in ArHBr represent the wide amplitude motion of the hydrogen atom. (The corresponding quantities for ArDBr differ by ~ 1.3 degrees.[32])

The second ramification arises from the very strong dependence of the "e" and "o" pairs on the structure angle that is displayed schematically in Figure 3.4. Centrifugal distortion of this angle may well result in a far greater perturbation of the rigid rotor energy levels than has previously been observed.

Chapter 3 : References

1.A.Carrington,A.R.Fabris,B.J.Howard and N.J.D.Lucas, Magnetic Resonance, Plenum Press, (1970)

2.A.Carrington,A.R.Fabris,B.J.Howard and N.J.D.Lucas, MP, 20, 961, (1971)

3.P.G.Favero, A.M.Mirri and W.Gordy, Phys.Rev. 114, 1534, (1959)

4.J.M.Brown,M.Kaise,C.M.L.Kerr and D.J.Milton, MP, 36, 553, (1978)

5.I.C.Bowater,J.M.Brown and A.Carrington, Proc.R.Soc.Lond.A. 333, 265, (1973)

6.G.C.Nielson,G.A.Parker and R.T.Pack, JCP, 66, 1396, (1977)

7.B.R.Figgis, Introduction to Ligand Fields, New York, (1966)

8.P.D.A.Mills, Part II Thesis, Oxford University, (1980)

9.M.Born and R.Oppenheimer, Ann.Physik. 84, 457, (1927)

10.A.Carrington,D.H.Levy and T.A.Miller, Adv.Chem.Phys. 18, 149, (1970)

11.B.J.Howard and R.E.Moss, MP, 19, 433, (1970)

12.K.P.Huber and G.Herzberg, Constants of Diatomic Molecules, V.N.R. (1979)

13.D.M.Brink and G.R.Satchler, Angular Momentum, Clarendon Press, (1979)

14.E.U.Condon and G.H.Shortley, The Theory of Atomic Spectra, C.U.P. (1964)

15.A.R.Edmonds, Angular Momentum in Quantum Mechanics, Princeton, (1974)

16.J.H.van Vleck, Rev.Mod.Phys. 23, 213, (1951)

17.E.B.Wilson,J.C.Decius and P.C.Cross, Molecular Vibrations, (1955)

18.J.T.Hougen, Natn.Bur.Stand.Monogr. 115, (1970)

19.H.W.Kroto, Molecular Rotation Spectra, Wiley, (1975)

20.J.M.Brown and B.J.Howard, MP, 31, 1517, (1976)

21.J.-L.Femenias and C.Athenour, Can.J.Phys. 53, 533, (1975)

22.R.A.Frosch and H.M.Foley, Phys.Rev. 88, 1337, (1952)

23.P.W.Atkins, Molecular Quantum Mechanics, Part III, Clarendon Press, (1970)

24.C.M.Western,P.R.R.Langridge-Smith,B.J.Howard and S.E.Novick, MP, 44, 145, (1981)

25.R.S.Mulliken and A.Christy, Phys.Rev. 38, 87, (1931)

26.W.L.Meerts and A.Dymanus, J.Mol.Spec. 44, 320, (1972)

27.W.L.Meerts, CP, 14, 421, (1976)

28.H.Margenau and N.R.Kestner, Theory of Intermolecular Forces, Pergamon (1971)

29.R.M.Neumann, Astrophys.J. 161, 779, (1970)

30.E.Miescher, JCP, 73, 3088, (1980)

31.J.M.Brown et al. J.Mol.Spec. 55, 500, (1975)

32.K.C.Jackson,P.R.R.Langridge-Smith and B.J.Howard, MP, 39, 817, (1980)

Chapter 4 : ArNO - An Open-Shell Van Der Waals Molecule.

4.1 Introduction

4.2 A Review of Previous Work on the Ar-NO System

4.3 Prediction of the ArNO Spectrum

4.4 Experimental Work - The M.B.E.R. Spectrum

4.5 The Assignment of the Spectrum and Further Confirmatory Experiments

4.6 Fitting the Spectrum of ArNO

4.7 Discussion and Conclusions

Chapter 4 : ArNO - An Open-Shell Van Der Waals Molecule

4.1 Introduction

The first part of this chapter involves the description of a long series of experiments aimed at recording the rotational spectrum of the van der Waals species, ArNO. Although the conditions necessary for searching and measuring the spectrum proved both tortuous and time consuming, the positions of some sixty radiofrequency and microwave transitions were accurately determined. Even so the resulting energy level pattern was found to be far from complete.

The major objectives of this study were twofold. Firstly, such a spectrum would be suitable for testing the Hamiltonian described in Chapter 3 and in particular the validity of the basic assumption that the orbital angular momentum remains predominantly unquenched in these complexes. In the latter part of the chapter attempts to fit the recorded spectrum to this Hamiltonian are described and its value in accounting for the spectra is appraised.

The second feature of interest concerns the hyperfine structure associated with the diatomic constituent, nitric oxide; the parameters that characterise this interaction depend critically upon the NO electronic wavefunction. A comparison may be made between the projections of the known parameters of free NO and those that best fit the observed spectrum of ArNO. Differences between the two are then attributable to the effects of complex formation. Thus the hyperfine interaction provides a probe with which an attempt may be made to understand the nature of the van der Waals bond.

Although there have been no reports of high resolution rotational spectra of open-shell van der Waals species in the literature, a few workers have contributed information about the Ar-NO intermolecular potential. The results of these are considered in the next section.

4.2 A Review of Previous Work on the Ar-NO System

There has been relatively little work published concerning the actual van der Waals molecule, ArNO. In an early paper on the electric deflection of weakly bound complexes, Dyke et al.[1] reported that the species ArNO refocussed strongly but no spectroscopy was attempted. More recently the fluorescence excitation spectrum of the complex was recorded by Langridge-Smith, Carrasquillo and Levy.[2] They produced a molecular beam by expansion of 2% NO in Ar through a 50 micron nozzle and detected the fluorescence resulting from excitation at around 44,000 cm-1. A weak, broad feature was observed at slightly higher frequency than the $A^2\Sigma^+(v'=0) - X^2\Pi_{1/2}(v''=0)$ band of NO itself. The former feature was interpreted in terms of an electronic transition to the repulsive wall of the equivalent excited electronic state in the complex. Dispersion of the fluorescence showed that it originated from NO following direct photodissociation.

This result was of interest for two reasons. It was the first observation of direct photodissociation of a van der Waals molecule. Secondly the fact that vibrational states of the repulsive wall were populated indicates that the potential curve for the excited electronic state is shifted outward relative to the ground state.[2]

Considerably more research has been published regarding the intermolecular potential energy surface between NO and rare gas atoms and in particular argon. A number of workers have studied the effect of broadening by argon on the linewidths of nitric oxide transitions. French and Arnold[3] determined argon- and self-broadened linewidths for the ten hyperfine components of the J=1/2 - 3/2 microwave transitions using a Fabry-Perot resonator.

The results due to argon corresponded to impact parameters which were larger than values from kinetic theory; long range forces were therefore presumed to be of importance in the broadening mechanism. It was demonstrated that the observed linewidths were too large to be accounted for solely by dipole-induced dipole interactions. French and Arnold concluded that a quadrupole-induced dipole mechanism was operative. Pressure broadening of several P- and R-branch lines in the NO infrared spectrum has been reported by Urban[4] and coworkers. No attempt was reported to derive information regarding the intermolecular potential, however.

The most useful piece of theoretical research in this context has been the publication of an Ar-NO intermolecular potential surface by Nielson, Parker and Pack.[5] They used the electron gas model (described in Chapterl) and considered two energy surfaces, V+(r,θ) and V-(r,θ), with the unpaired electron lying respectively in and out of the triatomic plane. Although the model was originally recommended for the calculation of potentials deriving from closed-shell species, Nielson et al. argued that Ar-NO was a suitable candidate since extensive charge transfer or configuration mixing was unlikely.

Hartree-Fock wavefunctions were used to calculate the electron density of the Ar and NO species. The interaction energy difference between V+ and V- was found to be much smaller than either one, hence (for fitting purposes) average and difference potentials were defined :

$$V_a = 1/2(V^+ + V^-) \qquad (4.2.1)$$

$$V_d = 1/2(V^+ - V^-)$$

Both Va and Vd depend upon a sum of contributions from S.C.F. and correlation energies :

$$V^{(i)} = V^{(i)}_{SCF} + V^{(i)}_{COR} \qquad (4.2.2)$$

where i = a or d. Each of the terms on the right hand side of (4.2.2) was expanded in terms of Legendre (for Va) or associated Legendre (for Vd) functions :

$$V_{ja} = \sum_n v_n^{ja}(r).P_n(Cos\theta) \qquad (4.2.3)$$

$$V_{jd} = \sum_n v_n^{jd}(r).P_n^2(Cos\theta)$$

where j denotes the S.C.F. or correlation potential energy. The various coefficients were fitted to the calculation by least squares and Gauss-Legendre quadrature and the final potentials expressed in the analytic forms :

$$v_n^{SCF,i}(r) = A^i_{n1}.\exp(A^i_{n2}.r + A^i_{n3}.r^2) \qquad (4.2.4)$$

$$v_n^{COR,i}(r) = -B^i_{n1}.\exp(B^i_{n2}.r + B^i_{n3}.r^2)$$

To correct for the shortcomings of the electron gas method a modified form for the correlation energy contribution was spliced into the potential at larger r using C6 and D6 values from an earlier paper.[6]

A computer plot of the average N.P.P. surface is shown in Figure 4.1. It is quite anisotropic and has a potential minimum at r=7.43 Bohr radii and Θ = 89.3 degrees. The depth of Va at the minimum was quoted to be $2.3x10^{-4}$ a.u. (50.6 cm-1) by the authors, however they estimated that the calculation had probably significantly underestimated this quantity. (Comparison with Ar-CO and Ar-CO surfaces suggested a figure of about 83.6 cm-1 for the well depth.) The difference surface, Vd, shown in Figure 4.2 was assessed to be qualitatively reasonable with a maximum well depth of only $4.5x10^{-6}$ a.u. (that is, about 1cm-1). It was

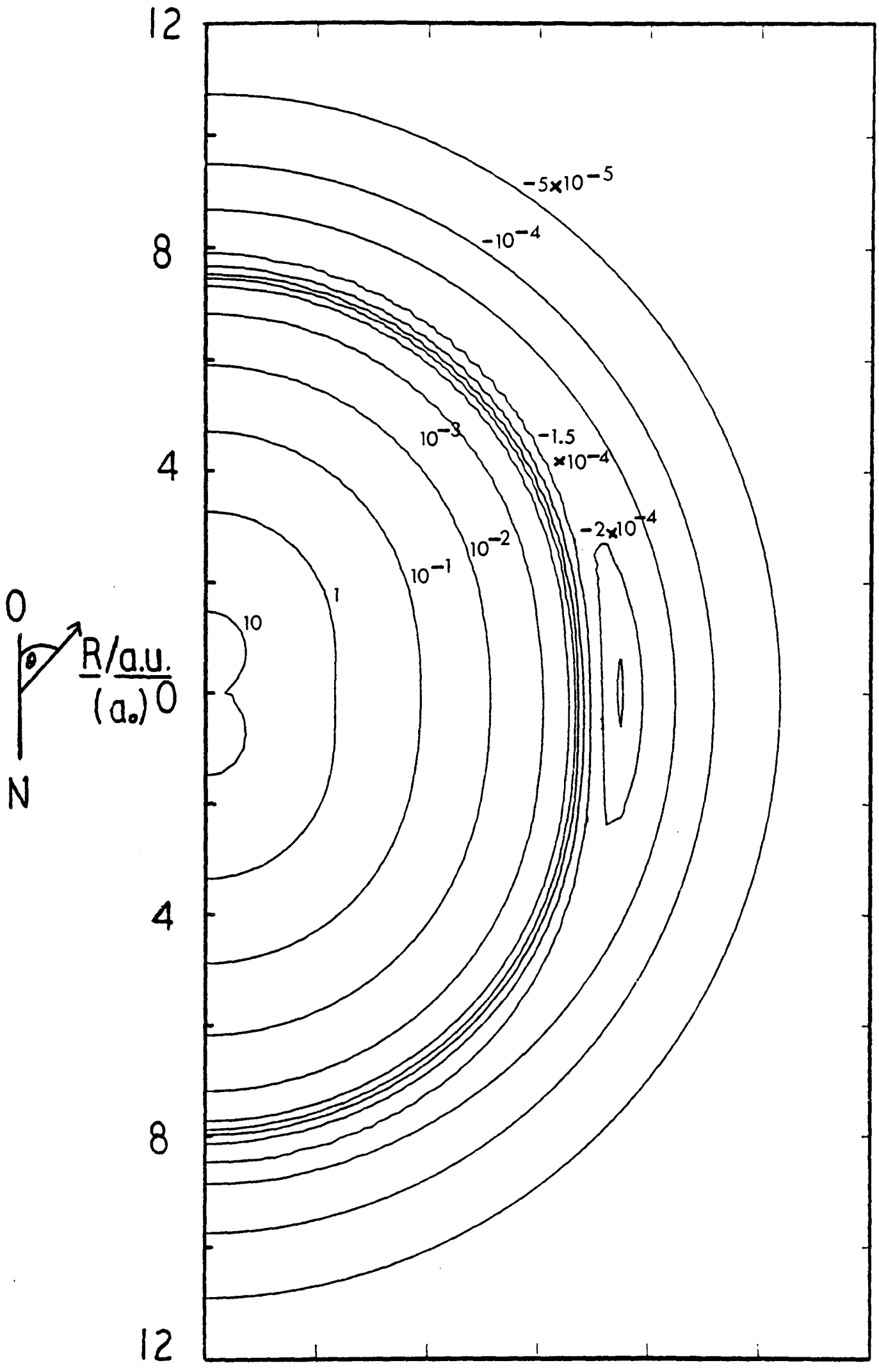


Figure 4.1

ArNO N.P.P. Average Potential.
(Contours in atomic units)

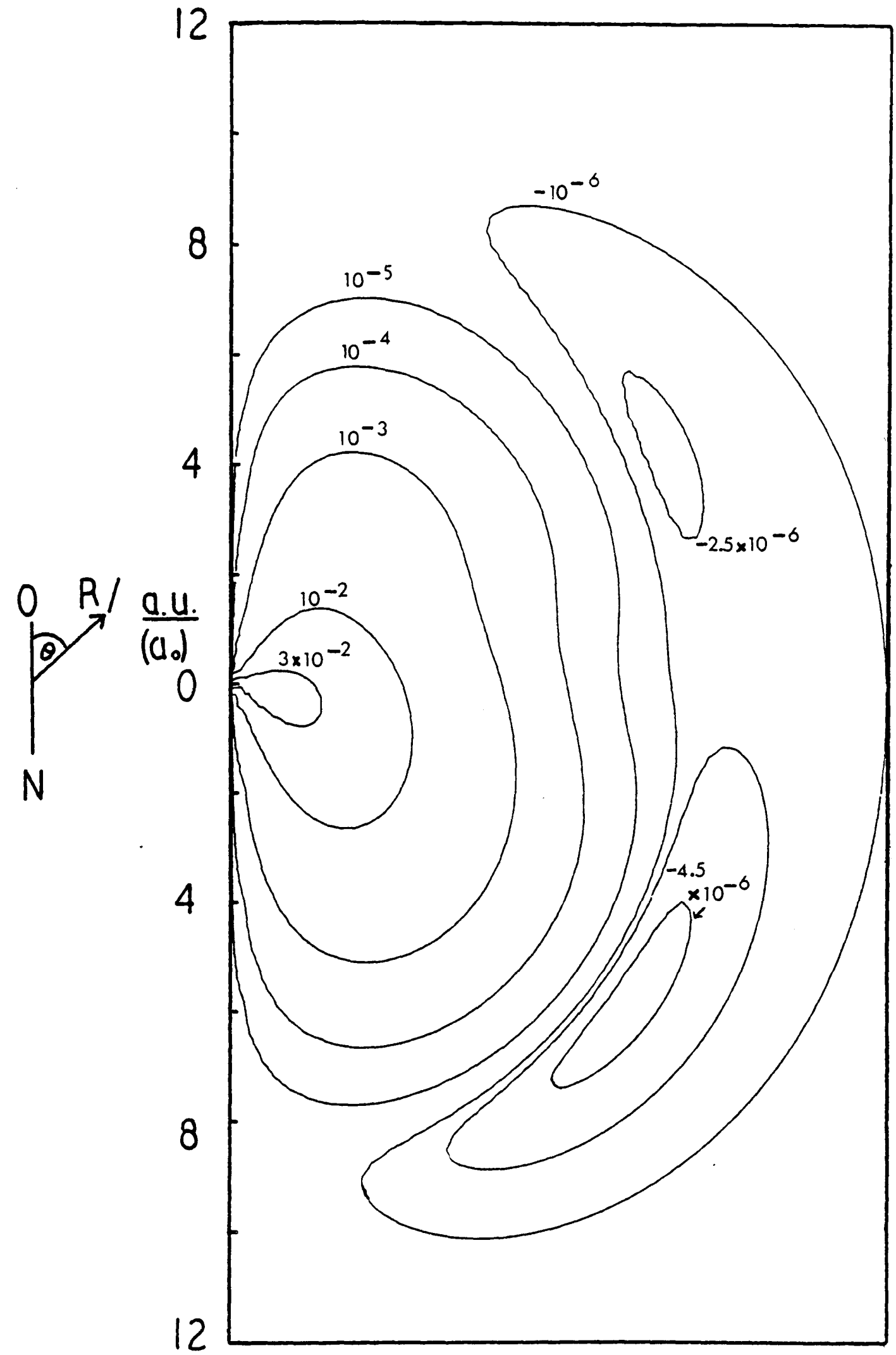


Figure 4.2

ArNO N.P.P. Difference Potential

(Contours in atomic units)

stressed that this latter figure was only of qualitative value. These details are considered in the next section to predict the spectrum of ArNO.

Another very fruitful source of information on the anisotropic Ar-NO potential energy surface has been the field of molecular beam scattering experiments. The most exhaustive work to date has been reported in a series of papers by Reuss and coworkers.[7-9] Their experiments measured the total collision cross section as a function of relative velocity for beams of NO and various rare gases. The nitric oxide beam was prepared by seeded supersonic expansion through a 200 micron nozzle. The molecules were then state-selected ($J= \Omega =Mj=3/2$) by a "wobbling" sixpole electrostatic field and orientated either parallel or perpendicular to the beam direction by magnetic coils. The secondary argon beam was generated in an effusive source and then collimated.

Thuis, Stolte and Reuss measured total collision cross sections, $\sigma_{\parallel}$ and $\sigma_{\perp}$, for NO molecules orientated parallel and perpendicular to the relative velocity. They then defined the anisotropy, A, as[7]:

$$A = (\sigma_{\parallel} - \sigma_{\perp})/\bar{\sigma} \qquad (4.2.5)$$

$$\bar{\sigma} = 1/3(\sigma_{\parallel} + 2\sigma_{\perp})$$

A nine disk velocity selector was placed before an ioniser and magnetic sector analyser which comprised the detector. This permitted the determination of A as a function of the relative velocity both with and without state selection.

An absolute value of the total collision cross section was also determined. From these measurements, and in particular the Glory structure, the data were fitted to anisotropic potential forms using the "sudden approximation". In the earlier paper[8] a

simple Lennard-Jones potential was used to fit the results for beams of NO with Ne, Ar, Kr and Xe :

$$V = V_0 + V_2(R).P_2(\cos\theta) \qquad (4.2.6)$$

$$= \varepsilon\{(R_e/R)^{12} - 2(R_e/R)^6\}$$

$$+ \varepsilon.P_2(\cos\theta)\{q_{2,12}(R_e/R)^{12} - 2q_{2,6}(R_e/R)^6\}$$

The following values resulted from the fit for argon :

$$\varepsilon = 1.91\times10^{-14} \text{ erg} \qquad (4.2.7)$$

$$R_e = 3.62 \text{ A}$$

$$q_{2,6} = 0.20$$

$$q_{2,12} = 0.40$$

A later paper including the results of further similar experiments[9] produced a more complete analysis in terms of a modified Maitland-Smith potential. This included the hitherto neglected $P^1(\cos\theta)$ term which the work of Nielson, Parker and Pack[6] had shown to be small but not negligible. The functional form of the potential and best fitted values are given below :

$$V(R,\theta) = V_0(R) + V_1(R).P_1(\cos\theta) + V_2(R).P_2(\cos\theta) \qquad (4.2.8)$$

where,

$$V_0(R) = \varepsilon\{(6/(n-6))(R_e/R)^n - (n/(n-6))(R_e/R)^6\}$$

$$V_1(R) = \varepsilon.q_{1,r}.(6/(n-6))(R_e/R)^n$$

$$V_2(R) = \varepsilon\{q_{2,r}.(6/(n-6))(R_e/R)^n - q_{2,a}.(n/(n-6))(R_e/R)^6\}$$

$$n = 13 + \gamma.(R/R_e - 1) \quad ; \quad \gamma = 10$$

$$\varepsilon = 1.85\times10^{-21} \text{ J}$$

$$R_e = 3.86 \text{ A}$$

$$q_{1,r} = 0.10$$

$$q_{2,r} = 0.75$$

$$q_{2,a} = 0.20$$

A plot of the resultant potential energy surface is shown in Figure 4.3 .

Two other scattering studies warrant a brief mention.

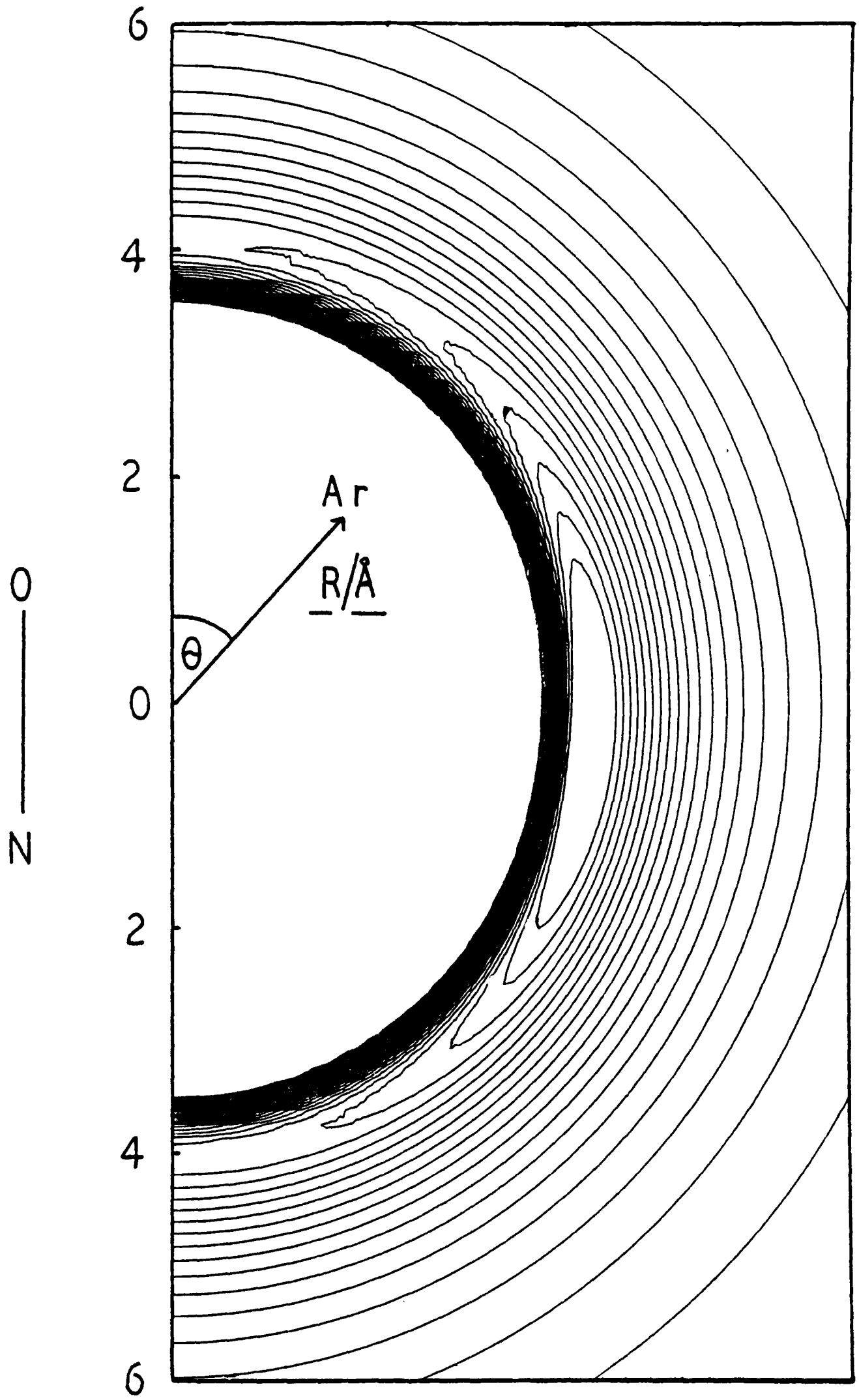


Figure 4.3

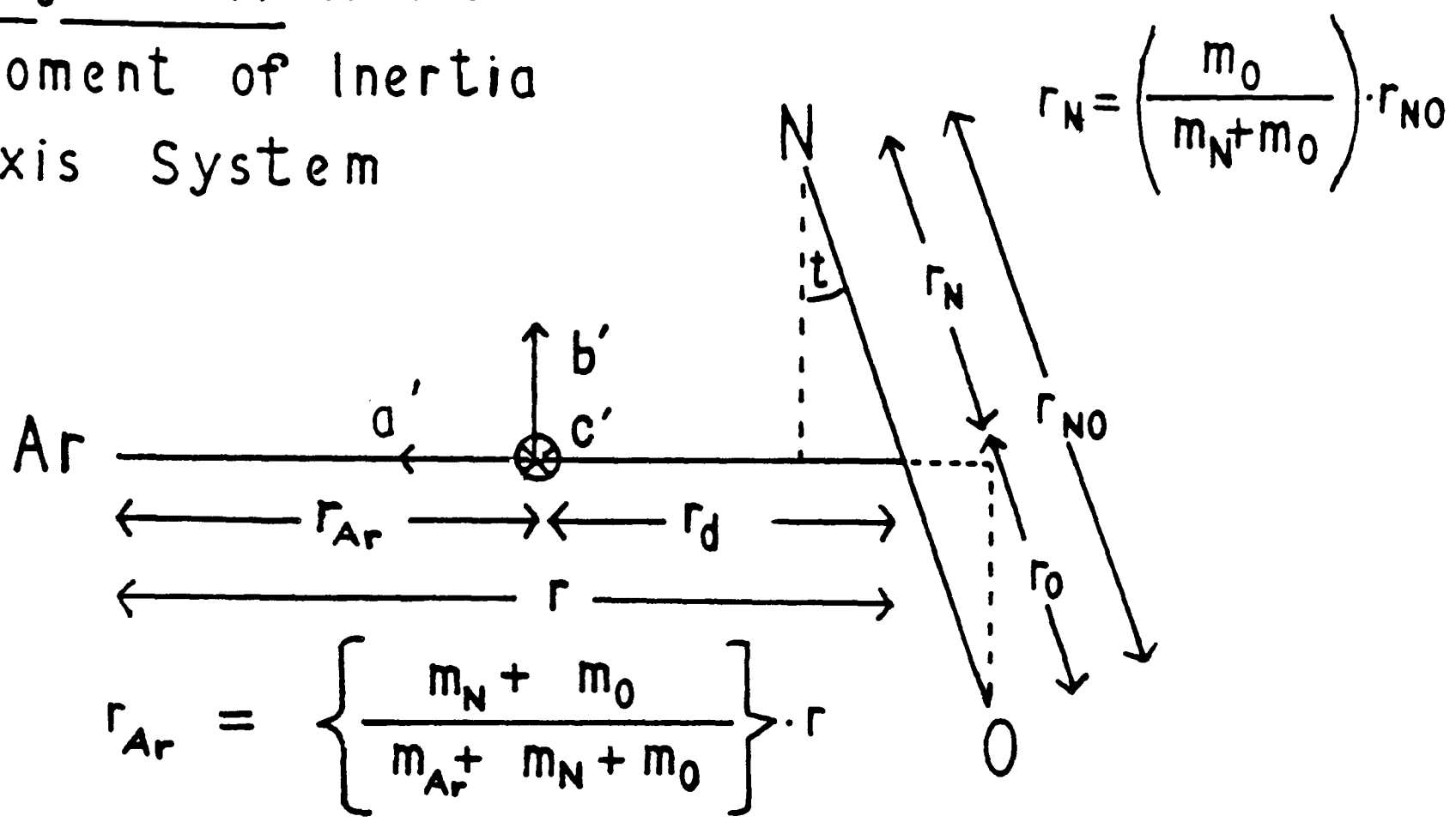
ArNO Potential of Thuis et al.

(Contours at 5 cm^{-1})

Kalinin, Khromov and Leonas[10] have measured Ar-NO differential scattering cross sections at small angles and found reasonable agreement with values predicted from the N.P.P. potential surface. In a brief communication Andresen, Joswig, Pauly and Schinke[11] outline the results of an experiment yielding state to state integral cross sections for the rotational excitation of NO (N''=0) by argon. They probed the state of the scattered NO molecules using laser induced fluorescence measured by a photomultiplier tube. An alternation in the density of final NO state populations was noted with maxima in even N' at low N'. A considerable population of N'=14 and 15, at just below the energy conservation limit, was observed; this was taken as evidence for strong coupling between rotational and translational motions. Coupled state calculations, again on the N.P.P. surface, reproduced qualitatively the alternation in populations which were attributed to the asymmetry of the heteronuclear diatom.

The authors claimed that the interference effects measured in this work are extremely sensitive to the anisotropy of the intermolecular potential predicting a much improved Ar-NO surface in the future. Unfortunately further analysis of the data has indicated that they are really only sensitive to the repulsive wall of the potential.[12]

Figure 4.4 ArNO : Moment of Inertia Axis System



ATOM	a'	b'	c'
Ar	r_{Ar}	0	0
N	$r_N Sin(t) - r_d$	$r_N Cos(t)$	0
O	$r_O Sin(t) + r_d$	$- r_O Cos(t)$	0

TABLE 4.1 ArNO : Atomic Coordinates.

$$
\begin{array}{c|cc}
 & a' & b' \\
\hline
a' & m_N.(r_N.Cos(t))^2 + m_O.(r_O.Cos(t))^2 & m_N.(r_N.Sin(t) - r_d).r_N.Cos(t) - m_O.(r_O.Sin(t) + r_d).r_O.Cos(t) \\
\hline
b' & & m_{Ar}.r_{Ar}^2 + m_N.(r_N.Sin(t) - r_d)^2 + m_O.(r_O.Sin(t) + r_d)^2
\end{array}
$$

$$
I_{cc} = m_{Ar}.r_{Ar}^2 + m_N\{(r_N.Sin(t) - r_d)^2 + r_N^2.Cos^2(t)\} + m_O\{(r_O.Sin(t) + r_d)^2 + r_O^2.Cos^2(t)\}
$$

TABLE 4.2 ArNO : Moment of Inertia Matrix

4.3 Prediction of the ArNO Spectrum

From the intermolecular potential energy surfaces of Thuis and of Nielson, Parker and Pack it is possible to estimate the equilibrium geometry of the van der Waals molecule. Inspection of Figures 4.1 and 4.3 show that both potential minima correspond to a structure which is quite close to a T-shaped geometry. The values for Re range from 3.62 and 3.86 Angstroms respectively for Thuis' Lennard-Jones[8] and Maitland-Smith[9] potentials to 3.9 Angstroms for that of Nielson et al.[6] In view of the slightly dubious applicability of the electron gas model to an open-shell system perhaps the scattering data is to be preferred. For the present work then an initial estimate of the rotational constants was based on a van der Waals bond length of 3.65 to 3.75 Angstroms and equilibrium angle, Θ, of approximately 90 degrees. The internuclear separation in the NO sub-molecule was fixed at a value of 1.1538 Angstroms such that it reproduced the B(NO) value used by Meerts[13] in his fit of the NO lambda-doubling spectrum ($B(^2\Pi_{1/2})$=50844.97 MHz).

To calculate rotational constants the inverse principal moments of inertia of the complex are substituted into Equation (3.5.3). Figure 4.4 shows the axis system used to derive the moment of inertia tensor. The axis a' runs between the argon nucleus and the NO centre of mass and b' is orthogonal to it also passing through the centre of mass of the complex. The coordinates in terms of this axis system are given in Table 4.1 . The elements of the moment of inertia tensor may be evaluated from the standard definition[14]:

$$I_{ij} = \sum_{\alpha} m_{\alpha}\{\delta_{ij} \sum_{k} x^2_{\alpha,k} - x_{\alpha,i}x_{\alpha,j}\} \qquad (4.3.1)$$

Substitution of the coordinates and masses of the atoms yields

Icc directly. Iaa and Ibb are obtained from the eigenvalues of the 2 x 2 symmetric matrix given in Table 4.2 .

The relationship between the angles θ and t of Figure 3.2 is established from the eigenvectors of the matrix of Table 4.2 . The two differ by less than a degree for small angles. For a T-shaped equilibrium geometry with a van der Waals bond length of 3.65 Angstroms (a value consistent with the scattering data of Thuis) the rotational constants are :

$$A = 50845.0 \text{ MHz} \qquad (4.3.2)$$

$$B = 2213.8 \text{ MHz}$$

$$C = 2121.4 \text{ MHz}$$

Modest variations in Re change the B and C rotational constants by a relatively small fraction (about 100 MHz for 0.1 Angstroms or about 5%) and have a negligible effect on the A constant. In contrast to this the pattern of rotational energy levels is very strongly dependent on the equilibrium angle, θ, as explained in Chapter 3. This is demonstrated in Figure 4.5 which contains only fine structure contributions to the energy and neglects the quenching and hyperfine effects. The positions of the potential minima in the work of Thuis and Nielson et al. predict that the geometry of ArNO will lead to an energy level pattern with θ fairly close to zero, that is, towards the left hand side of the figure.

Values for the hyperfine parameters and lambda-doubling constants which best fit Meerts' NO data have already been given in section (3.6). In order to predict the spectrum of ArNO the same hyperfine parameters were used as initial estimates and the various Coriolis matrix elements off-diagonal in electronic state were assumed to scale with the A, B and C rotational constants. Since the off-diagonal hyperfine parameter, el, was not needed in

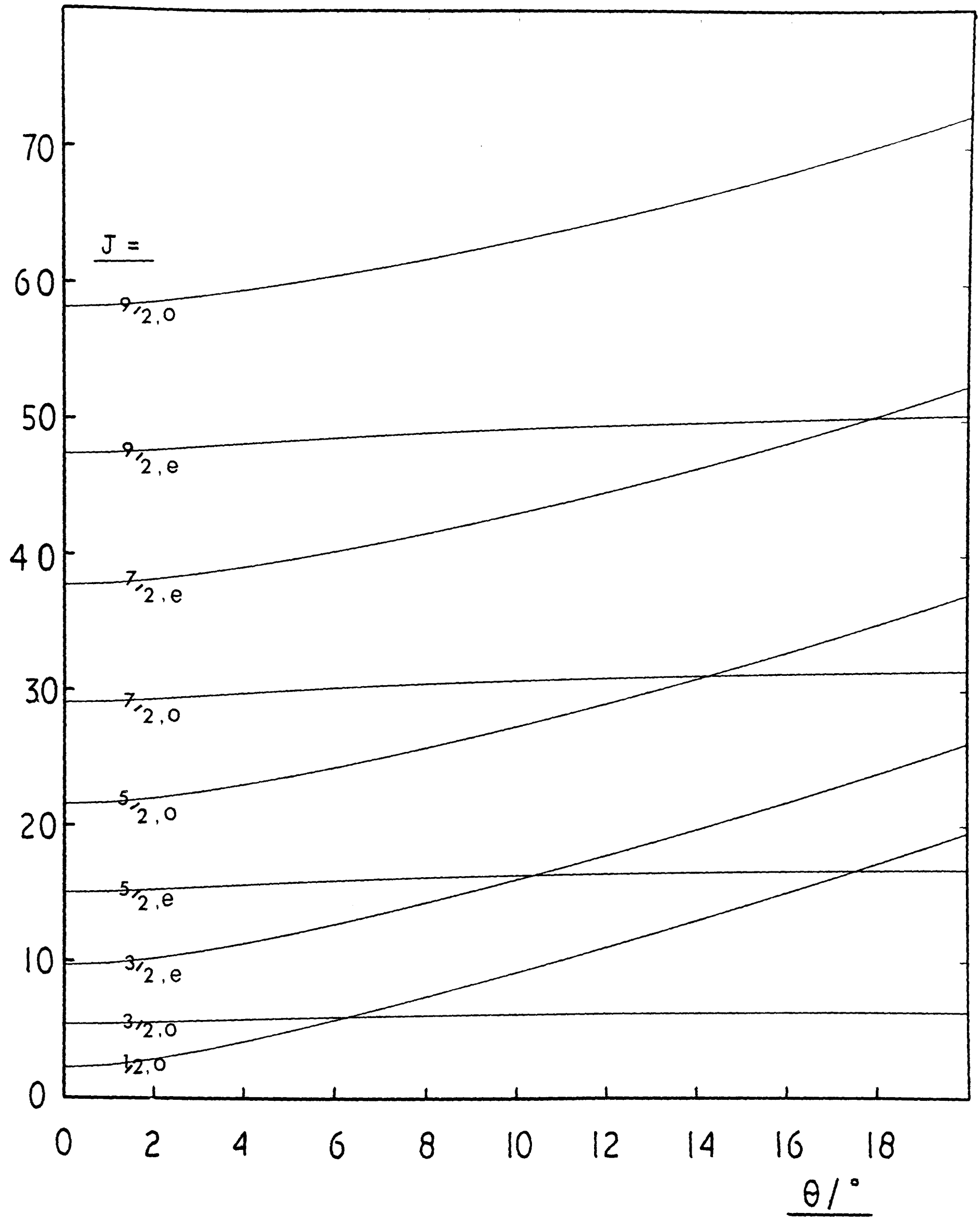


Figure 4.5 : ArNO Energy Levels as $F(\theta)$.

$\epsilon_2 \sim 0$

the NO fit its magnitude could not be estimated.

The only other parameters needed to estimate the spectrum are those of the quenching part of the Hamiltonian, ε_1 and ε_2 . In Figure 4.2 the depth of the minimum in the difference potential of Nielson, Parker and Pack was about 1 cm-1. The authors cautioned against the use of this potential in other than a qualitative sense but these data indicate that the magnitude of the diagonal quenching contribution, ε_2 , is likely to be at the most a few cm-1.

In fact in the subsequent chapters only the diagonal quenching term, ε_2 , will be considered even though the leading term, ε_1 , may be large and responsible in 2nd. order for the magnitude of the N.P.P. difference surface. The reasons for this neglect of ε_1 are twofold. The first derives from the phase relationships of its matrix elements :

$$\langle 0|\varepsilon_1 \mathrm{Cos}(\phi)|1\rangle = \langle 1|\varepsilon_1 \mathrm{Cos}(\phi)|0\rangle = \varepsilon_1'$$

$$\langle 0|\varepsilon_1 \mathrm{Cos}(\phi)|-1\rangle = \langle -1|\varepsilon_1 \mathrm{Cos}(\phi)|0\rangle = (-1)^{1+s}.\ \varepsilon_1' \qquad (4.3.3)$$

These have the opposite phase to the matrix elements of the non-adiabatic operators from the rotational, spin-orbit and hyperfine parts of the Hamiltonian of Chapter 3. Important cross terms between the two in 2nd. order perturbation theory will therefore vanish. For example,

$$\begin{aligned}\Delta E = -1/E_{\Sigma\Pi}\ .\{&\langle \Lambda=-1,\Sigma=\tfrac{1}{2}|\zeta L^- S^+|0,-\tfrac{1}{2}\rangle\langle 0,-\tfrac{1}{2}|\varepsilon_1 \mathrm{Cos}(\phi)|1,-\tfrac{1}{2}\rangle \\ &+ \langle -1,\tfrac{1}{2}|\varepsilon_1 \mathrm{Cos}(\phi)|0,\tfrac{1}{2}\rangle\langle 0,\tfrac{1}{2}|\zeta L^- S^+|1,-\tfrac{1}{2}\rangle \quad \}\end{aligned}$$

$$= -1/E_{\Sigma\Pi}\ .\{\varepsilon_1'.(-1)^s.\langle 0|\zeta L^-|1\rangle + (-1)^{1+s}.\varepsilon_1'.\langle 0|\zeta L^-|1\rangle\}$$

$$= 0 \qquad (4.3.4)$$

The second reason for not explicitly including ε_1 is that

in 2nd. order it has exactly the same effect on the spectrum as a much smaller positive value of the diagonal parameter, thus :

$$\Delta E = -1/E_{\Sigma\Pi} \cdot \{<-1|\varepsilon_1 \mathrm{Cos}(\phi)|0><0|\varepsilon_1 \mathrm{Cos}(\phi)|1>\}$$

$$= (-1)^s . \varepsilon_1'^2 \; / \; E_{\Sigma\Pi} \qquad (4.3.5)$$

The effect of the quenching parameter, ε_2 , on the fine structure energy levels is illustrated in Figure 4.6 .

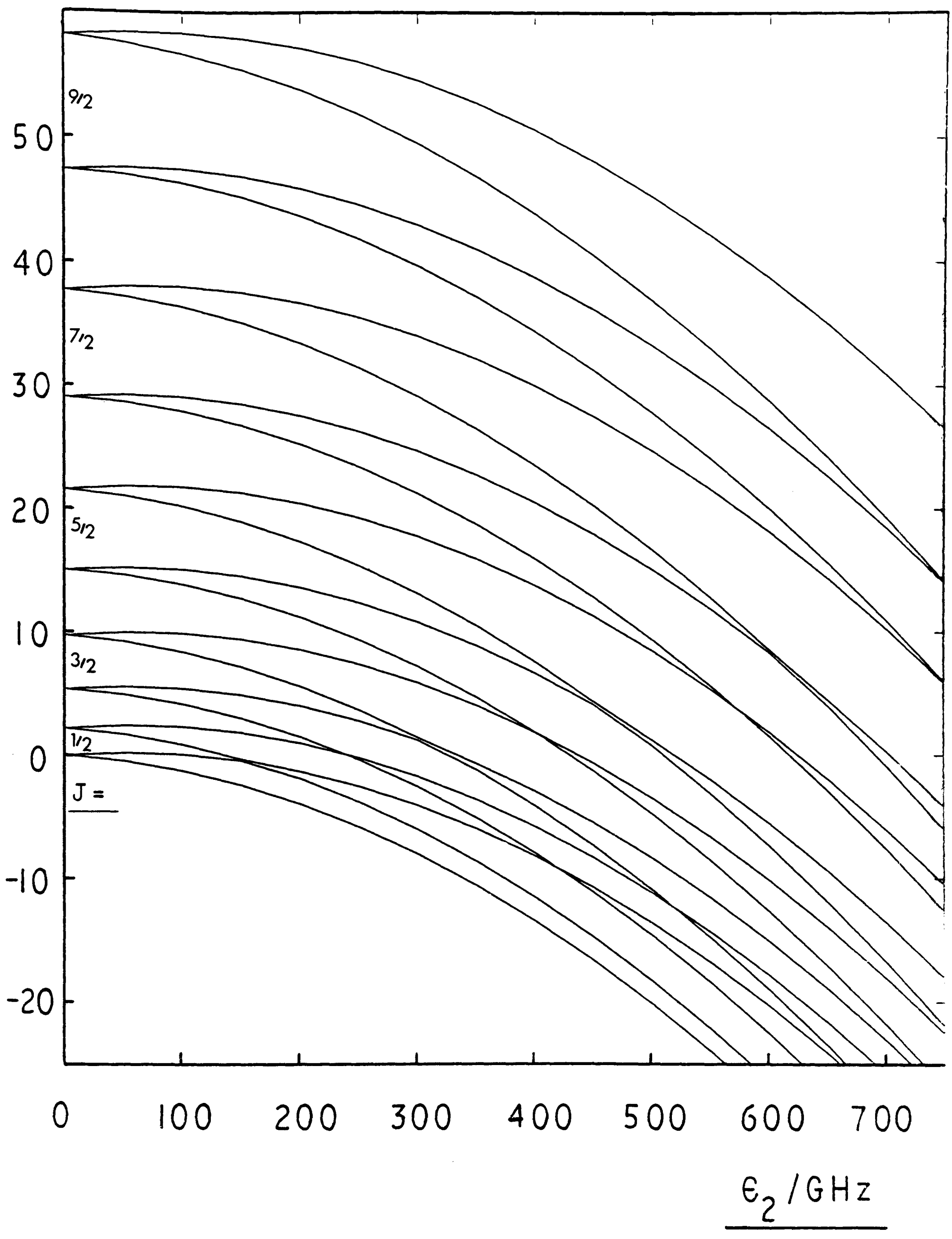
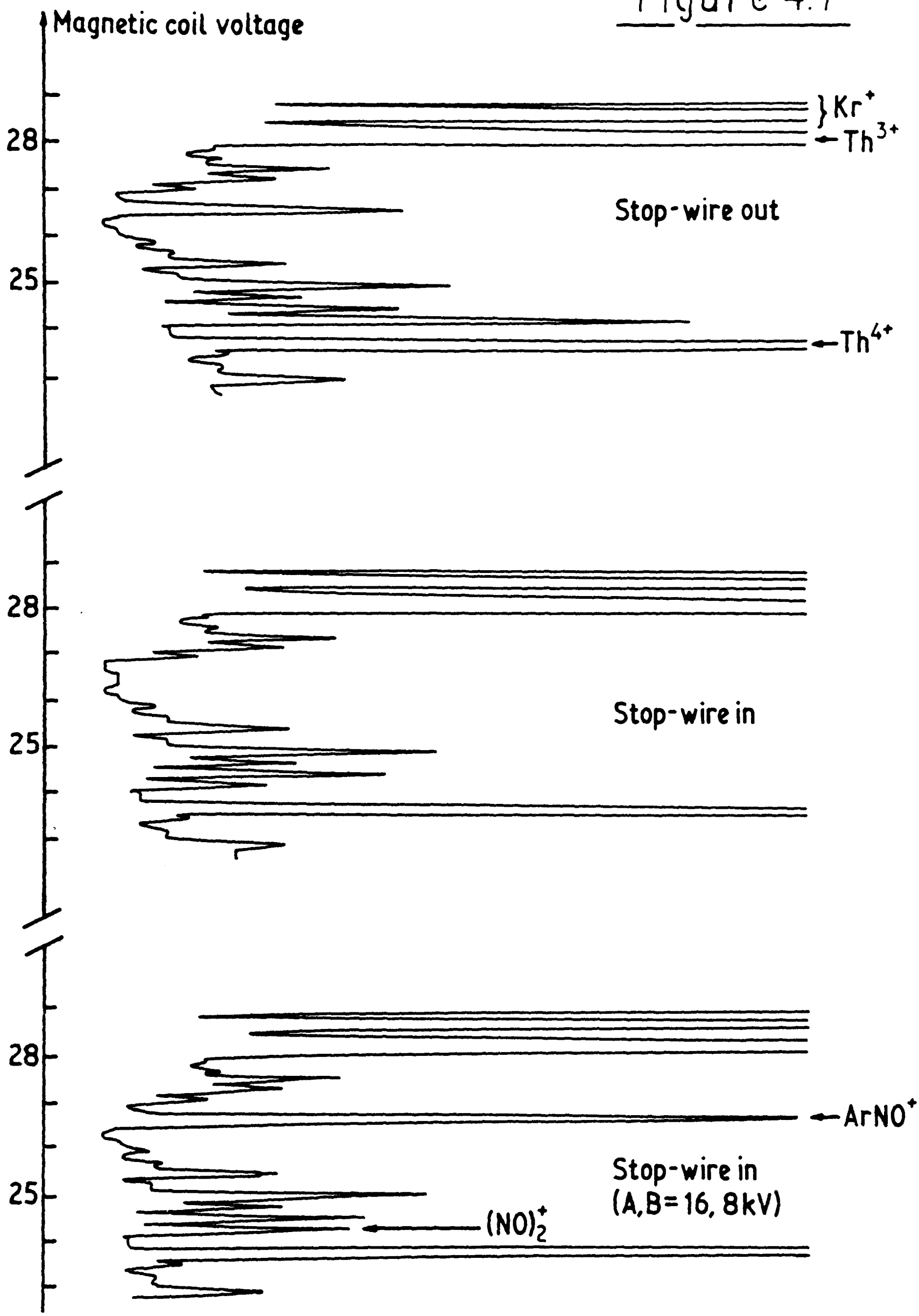


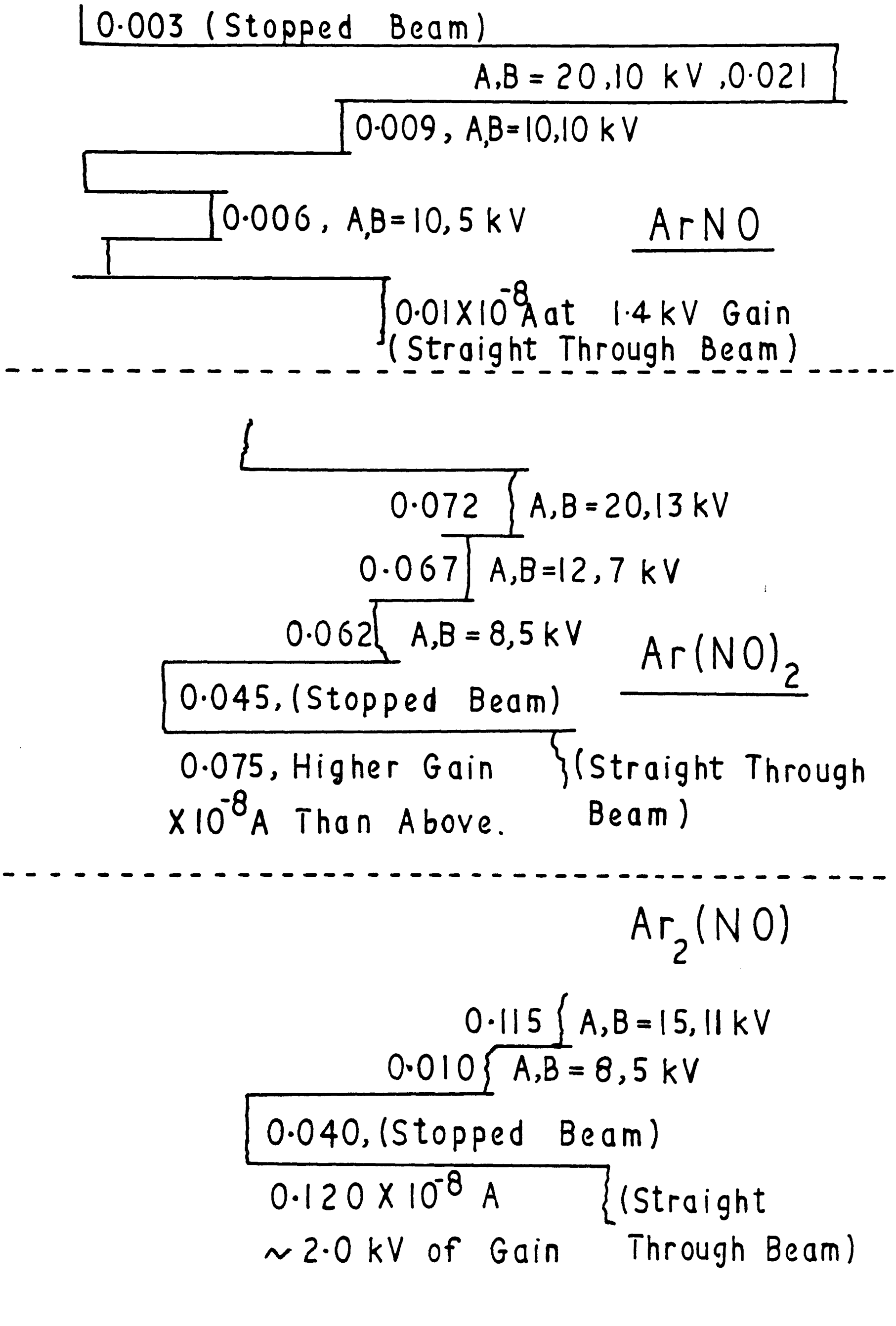
Figure 4.6 : ArNO Energy Levels as $F(\epsilon_2)$

Figure 4.7



ArNO: Mass spectra

Figure 4.8 : Refocussing Traces



4.4 Experimental Work - The M.B.E.R. Spectrum

4.4 a) The Expansion Conditions, Polarity of ArNO and General Experimental Details

As had been established previously[15], an 8% mixture of NO in Ar produced strong beams of ArNO in the supersonic expansion. The van der Waals dimer, $(NO)_2$[16], was also present in appreciable concentration. A typical section of the mass spectrum is reproduced in Figure 4.7 and indicates the presence of these two species. The polarity and concentration of ArNO produced by expansion through 40, 50 and 70 micron pinhole nozzles (manufactured by Agar Aids Ltd.) was assessed. The two smaller apertures were found to induce the most effective rotational cooling with the 50 micron nozzle being less prone to blockage. The latter nozzle was therefore used for all experimental work.

In agreement with the reports of Novick[1], ArNO was found to be a highly polar species with refocussing considerably in excess of 200% being easily attained. It was assumed that the behaviour of the percentage refocussing as conditions were altered would reflect the efficiency of rotational cooling being achieved. Hence the polarity was carefully investigated as a function of stagnation pressure (Pst) and nozzle temperature (Tn). Some representative traces and data are presented in Figure 4.8 . Although Pst and Tn were optimised before each experiment, operating conditions were fairly constant being typically :

$$P_o = 6 \times 10^{-5} \text{ torr} \qquad (4.4.1)$$

$$T_n = 140 \text{ K}$$

where Po was the background pressure in the source chamber. Under these conditions the supersonic expansion was frequently

reasonably stable for periods of up to six or eight hours allowing very long searches to be feasible.

The high polarity of ArNO may be attributed to a Stark interaction between the near-degenerate energy levels of opposite parity shown in Figure 3.3 . For such species with close interacting states, the Stark Effect is expected to be predominantly first order in electric field. Consistent with this was the observation of a smooth variation in refocussing as a function of A and B Field voltages. The fields that produced the maximum percentage refocussing appeared to depend somewhat upon the geometric configuration of the quadrupole rods inside the main chamber (the position of these required occasional alteration). However, a maximum normally appeared within the range :

A = 13 to 15 kV

B = 9 to 11 kV

Initial searches were usually conducted with the A and B Field voltages set to within the above ranges. The Buffer Fields were operated at a potential of 1.5 kV although this seemed to have only a small effect on the measured refocussing.

All spectra were recorded by monitoring the molecular flux at the mass peak m/e = 70. The parent peak was used because the Ar peak (m/e = 40) carried a high background and that due to NO could yield resonances due to the lambda-doubling spectrum of the uncomplexed molecule. Although the background at mass 70 was comparatively low, it proved advantageous to reduce it further by cryo-pumping the detector chamber with liquid nitrogen. Before spectroscopy was attempted, the voltages of the Weiss Ioniser and deflecting plates were optimised to yield the largest electrometer current at mass 70 such that oscillations in the

Ioniser were absent. From the gain of the electron multiplier an estimate of the flux of ArNO+ ions being detected is possible. Typically this flux was of the order of 2.5×10^5 ions per second.

Since it is possible that higher molecular weight clusters would fragment and contribute to the spectrum recorded at m/e = 70, the polarity of the two most obvious candidates, Ar_2NO and $Ar(NO)_2$, was examined by looking at their respective parent mass peaks (m/e = 110 and 100). Species at these higher mass peaks were indeed found to be polar though not so much as ArNO itself. Refocussing traces are given in Figure 4.8 . It was subsequently demonstrated that fragments arising from the mass peaks at 100 and 110 were not responsible for some representative examples of the strong radiofrequency transitions located. It was concluded that the origin of these lines was the simplest mixed dimer, ArNO.

4.4 b) The Radiofrequency Spectrum

As explained in section (3.1) a number of radiofrequency transitions had been reported by the author from a preliminary study of the molecule. Although the whole of the radiofrequency region had been covered in this previous work, the conditions employed had been such that only the strongest lines could be observed. It was decided to search selected portions of the radiofrequency spectrum much more slowly in order to locate some of the many transitions that had been missed. Old traces from the earlier work were carefully inspected to indicate the most likely regions for further searches.

In this work scans were usually of only 10 MHz with the radiation broadened to produce a linewidth of 0.5 to 2.0 MHz. The

Varian Computer was used to digitise and store spectra averaged over six to eight scans using a 10 second integration time. Every 10 MHz signal-averaged interval was repeated twice with different voltages on the A and B quadrupolar fields so that searches were conducted with the following combinations : (A,B) = (9,4), (14,7) and (20,15) kV. A full noise broadened search of a 10 MHz interval therefore typically took between 30 and 60 minutes (depending on the frequency modulation applied to the radiation). A complete recording of the radiofrequency region under these conditions was therefore impractical and hence only some 200 MHz (900 - 1100 MHz) in all was scanned. In addition many of the lines reported in the earlier work were rescanned to yield more accurate measurements of the line centres.

A number of new transitions were found and their frequencies located accurately using a phase-locked oscillator. Some of these (for example, transition "A") were only observed with the highest radiation powers (0.5 MHz of frequency modulation) and at just one of the field settings (A,B = 9,4 kV). A complete list of the accurate frequencies of all the ArNO radiofrequency transitions is given in Table 4.3 (including the new measurements of those determined in the previous study); also indicated are the approximate frequencies of features which proved too weak for phase-locked measurements to be successful.

Spectroscopy was also attempted to cover the range between 150 and 400 MHz (the range below 150 MHz had previouly been searched thoroughly) using 2 MHz of modulation, a 30 second time constant and the quadrupole voltages set to (A,B) = (9,5) kV. These voltages had produced the best signal to noise ratios for the lowest frequency transitions at 395 and 400 MHz. No new lines were observed. Very careful searching between 380 and 420 MHz

Table 4.3 : ArNO Radiofrequency Transitions

Label	Frequency/MHz	Label	Frequency/MHz
a	395.1945	v	1079.5500
b	395.3467	r	1085.9334
c	400.5537	B	1088.7382
d	572.2895	s	1091.7336
e	578.9335	Z	1141.4060
E	664.6966		
h	844.9642	----------	
i	914.6376	Double Resonance Transitions	
j	919.9944		
k	956.9572	Label	Frequency/MHz
l	958.0195		
m	959.5611	δ	480.9577
D	962.0869	ε	481.1099
n	1001.9334	η	658.0526
o	1003.3561	α	775.8211
t	1012.6811	β	775.9689
w	1013.2625	γ	952.9159
x	1016.1969		
p	1016.7021	----------	
q	1023.3473		
y	1028.5810	Weak Features,	Approximate Freq./MHz
z	1037.5088		
C	1043.5505		968.04
A	1065.7505		986.99
u	1077.6827		992.30

(The Attribution of the alphabetic labels represents the approximate chronological order in which the R.F. transitions were discovered.)

---

was also attempted to locate any possible further hyperfine components of transitions "a", "b" and "c" but none were found. Further, much less thorough, searching above 1100 MHz revealed transition "Z".

4.4 c) Early Attempts to Measure the Microwave Spectrum

Attempts were now made to search the microwave region. A compromise was required in the rate of scanning so that weak features might be detected without the expenditure of very long search times. The conditions employed were the use of 2 MHz of frequency modulation of the radiation source with a 10 second integration time. This corresponded to a search rate of about 200 MHz per hour. The entire region from 2.0 to 6.5 GHz (the full range of one of the solid-state oscillators) was covered under these conditions with many 100 MHz sections being scanned twice. Two transitions were located and their line centres determined accurately by the phase-locking technique. Extensive, even more careful, searching of the 200 MHz sections centred on these transitions (3751.1932 and 5847.4333 MHz) failed to locate any hyperfine structure associated with these lines.

Although the region from 6.5 to 12.4 GHz fell within the range of the next available solid-state oscillator, this device was not used for searching due to its relatively low power output (~10 mW for an H.P.86245a). Instead a Varian X-13 reflex klystron was employed to cover its full range from 8.0 to 12.4 GHz with typical output powers specified at greater than 200 mW. The radiation was frequency modulated with 5 MHz of noise broadening; focussing fields of (A,B) = (14,10) kV were used.

Due to the difficulties associated with very slow

mechanically-tuned frequency sweeping only a 10 second time constant could be employed. (Signal averaging with such klystron sources has not proved possible on the Oxford spectrometer.) Although some very weak features were observed, at between 9.7 and 9.8 GHz, they could not be reproduced with any reliability.

It was concluded that still higher incident powers, together with longer integration times, would be required if further searching in the microwave region were to prove fruitful.

4.4 d) The Use of a Travelling Wave Tube Amplifier between 8 and 18 GHz

At this stage in the work a Hughes Travelling Wave Tube (T.W.T) Amplifier was kindly made available by Southampton University. The amplification of the microwave source enabled more noise broadening to be employed with a concomitant improvement in the rate of scanning. The experimental arrangement for these investigations was as described in Chapter 2.

An initial search was made scanning down in frequency from 11.5 GHz using a 10 second time constant and fields of (A,B) = (14,10) kV. The attenuation between the solid-state oscillator and the T.W.T. amplifier was adjusted to provide an output power of 1 to 2 Watts; 20 MHz of noise broadening was employed. A weak feature was observed at about 8.7 GHz with a signal to noise ratio of about 2:1. This transition could be seen with a much improved signal to noise ratio on doubling the power (10 MHz of broadening) and using a 30 second integration time. The signal was also increased by slightly reducing the focussing voltages to (A,B) = (11,8) kV. These modified conditions were then used to search the whole frequency range of the amplifier at a rate of



Figure 4.9 ArNO : Phase Lock Measurement of M12.

about 1 GHz every 3 hours. In several regions great difficulty was encountered in levelling the output of the solid-state oscillator and in providing sufficient power to drive the amplifier at saturation.

A number of transitions were observed and for each of these further careful searches were made to try and locate any additional hyperfine structure. The exact frequencies of all these lines were determined using a phase-locked oscillator (without amplification) and are given in Table 4.4 . In the 9.8 GHz and 17.2 GHz manifolds additional lines were located by searching with amplified, phase-locked radiation. In several cases (see Table 4.4) only a single hyperfine component of a given manifold was ever observed.

An interesting additional feature was the occurrence of resonances having the opposite sign (corresponding to an increase in detected molecular flux) to the transitions of Table 4.4 . The positions of these resonances shifted when the quadrupolar field voltages were altered. It was presumed that these features were due to transitions occurring in the vicinity of the A and B quadrupole regions and therefore Stark shifted by these large electric fields.

An example of a phase-locked microwave transition is given in Figure 4.9 .

4.4 e) Further Work with High Power Radiation Sources : 4 to 8 GHz

The work described in the previous section had indicated that a high power source of microwaves was essential if long searches were to be of value. Following an S.R.C. research grant

application a second T.W.T (Keltec) was purchased to cover the microwave region from 4 to 8 GHz. The latter item only became available during the final stages of this experimental work but proved invaluable in enabling a more complete spectrum to be recorded.

The search conditions were similar to those found suitable during the work with the Hughes (8 - 18 GHz) amplifier. Focussing fields of (A,B) = (14,7) kV and a 30 second detection time constant were used. The applied power was typically 1 to 2 Watts with 5 or 10 MHz of noise broadening. The entire region from 3.6 up to 7.9 GHz was searched in this fashion. As in previous work, very careful scanning was undertaken around known transitions to try and locate as many hyperfine components of each manifold as possible.

Several new hyperfine components of the microwave transitions at 3751.1932 and 5847.4333 GHz (section 4.4 c) were discovered and measured accurately. The precise frequencies of three components of a new transition at about 6.7 GHz were also determined. In addition single, very weak resonances were detected at frequencies close to 7286 MHz and 7420 MHz with the former requiring a 100 second time constant to achieve a signal to noise ratio of 2:1! The latter lines were not phase-locked. The frequencies of all these transitions are given in Table 4.4 .

A number of experimental difficulties were encountered in these searches in the C- to X-band region. Microwave power was reflected by the stripline C-Field or microwave horn and this caused considerable heating of the circulator which was used to protect the amplifier. This frequently caused delay in waiting for the circulator to cool to within its operating range (293 to 300K). A second, more serious problem was the appearance of

strong resonance patterns in the spectrum particularly between 6 and 7.8 GHz. These patterns consisted of a series of oscillations (both positive and negative) in the output of the lock-in amplifier. The magnitude of these features was quite comparable with that of previously recorded spectra and hence they could mask the presence of genuine transitions. The spurious resonance patterns were present when either the stripline field or the microwave horn was used to deliver radiation to the beam. The problem was somewhat lessened by reducing the incident microwave power. To maintain the power per unit bandwidth this remedy necessitated using reduced noise broadening and consequently slowed down the scan rate.

It was thus very important to be able to distinguish these "beat patterns" from molecular transitions. The most reliable method of effecting this distinction was to test whether the signal from the lock-in amplifier was still present when a different mass peak (of similar intensity) was observed at the detector. This procedure was used to investigate all spectral features with intensity appreciably above the noise level.

Table 4.4 : ArNO Microwave Transitions

Label	Frequency/MHz	Label	Frequency/MHz
M25	3642.8229	M8	10902.3883
M26	3652.0504	M9	11793.1334
M27	3664.5994	M11	17139.5139
M1	3751.1932	M12	17154.4091
M2	5847.4333	M13	17164.5821
M28	5862.3295	M14	17229.4388
M21	5947.7212	M15	17239.6094
M22	6697.1315	M16	17303.3983
M23	6767.4132		
M24	6772.1636	----------	
M3	7854.6168		
M18	7868.1721	Weak Features,	Approximate Freq./MHz
M4	7952.1683		
M5	8702.9168		7286.0
M17	9708.0145		7420.0
M19	9716.6979		
M20	9727.9400	----------	
M6	9788.3334		
M10	9799.5847		
M7	9882.4116		

(Once again the numerical ordering reflects the approximate chronological order of discovery of the transitions.)

4.5 The Assignment of the Spectrum and Further Confirmatory Experiments

4.5 a) Common Difference Analysis

In order to gain an assignment and energy level scheme for the transitions contained in Tables 4.3 and 4.4, all the frequencies were tested for common sums and differences. For a large number of transitions the use of a computer program for this purpose is advantageous. The program possessed by the Oxford group calculates all possible sums and differences and then performs a "shell-sort" (an efficient sorting algorithm) on the resulting numbers. Where the sums or differences of two pairs of transition frequencies fall within a preset threshold value (typically about 30 kHz) a common relationship is recorded. The results of such an analysis are given in Table 4.5 together with, Δ , the deviation in kHz from a perfect match.

It has been found empirically that under favourable conditions the position of a line centre may normally be calculated with an uncertainty of approximately one tenth of a linewidth. The linewidths of most of the phase-locked measurements of Tables 4.3 and 4.4 ranged from between 10 to 30 kHz and so for a genuine common pattern Δ should be of the order of 6 kHz or less. With such a large number of transitions the occurrence of coincidental common differences (unrelated to the pattern of energy levels) becomes likely. Those marked with a double asterisk are differences which are incompatible with patterns derived from those above; the former are assumed to correspond to such coincidental occurrences.

Table 4.5 : Common Differences

Transitions Involved	Δ /kHz	
g - f = b - a	4.4	
c - b = h - g	2.1	
j - i = h - f	0.1	
h - f = c - a	2.3	
e - d = q - p	1.2	
i - f = s - p	1.2	
d - c = p - h	2.1	
p - h = s - j	1.3	
d - b = p - g	4.3	
p - f = d - a	0.1	
d - a = s - i	1.1	
e - c = q - h	3.3	
e - b = q - g	5.5	
e - a = q - f	1.1	
d - c = s - j	3.4	
M16 - M15 = q - m	2.7	
M14 - M12 = j - h	0.5	
M14 - M12 = M15 - M13	2.4	
M24 - M22 = s - p	0.6	
M24 - M22 = M14 - M12	2.4	
M28 - M2 = M12 - M11	1.0	
M20 - M19 = M10 - M6	9.2	
M6 - M19 = y - k	11.7	
M4 - M18 = r - n	3.8	
M21 - M28 = B - o	9.6	
M1 - M27 = C - k	0.5	
M4 - M18 = C - m	6.8	**
M9 - M7 = h + A	6.9	**
M6 - M3 = h + B	14.2	**
n - m = r - C	10.6	**
M2 - M1 = p + v	12.1	**

4.5 b) The Fine Structure Assignment of the Spectrum

For most closed-shell, atom-diatom van der Waals molecules (for example, the rare gas-hydrogen halide systems) the assignment of the M.B.E.R. rotational spectrum has proved fairly straightforward. For ArNO (and NeNO) the additional complexity in the fine and hyperfine structure due to the unpaired electron rendered an assignment of the transitions of Tables 4.3 and 4.4 far from obvious. Since the eventual "best fit" of the spectrum was not within the estimated experimental error, the considerations that led to the final assignment are presented here in some detail.

Using the parameters that fitted the NO lambda-doubling spectrum it was shown that the hyperfine splittings for ArNO were only likely to be of the order of 100 MHz or less. The coarse pattern of the energy levels is therefore determined mainly by the equilibrium structure of the complex (described by the van der Waals bond length, r, and the related structural angles, θ and t) and by the splittings of the (+) and (-) components of each fine structure level. (These effects were illustrated in Figure 3.3 .) The latter structure is dominated by the diagonal term of the quenching potential, ε_2 . The variation of the energy levels with this parameter was given in Figure 4.6 . It may be recalled that its magnitude was estimated by Nielson, Parker and Pack[6] to be at most a few cm-1.

An initial crude estimate of the magnitude of ε_2 may be gained from the observed radiofrequency spectrum. Nearly all the frequencies contained in Table 4.3 fall within the range 900 to 1150 MHz. The common difference analysis showed that those at lower frequency (except "E") all arose from the same manifold

which also contained some transitions at ~1 GHz. With reference to Figure 3.3 it can be seen that this observed pattern of R.F. transitions is compatible only with a small value of ε_2 that is, a magnitude of less than 5 cm-1. The scale of the diagram is approximately 2 mm. to 1 GHz. There are no other reasonable values of ε_2 that permit a number of these radiofrequency stacks at about 1 GHz without other independent manifolds at much lower frequency. The careful radiofrequency searches described in section (4.4 b) had revealed no lower frequency transitions that were not found to be part of a 1 GHz manifold.

A more detailed examination of the common differences contained in Table 4.5 reveals that no fewer than 14 transitions (a,b,c,d,e,f,g,h,i,j,m,q,p,s) arise from a single, common 1 GHz manifold. Since for J>=3/2 the maximum of hyperfine components (allowed by the general selection rule $\Delta F=0,\pm1$) for a $\Delta J=0,\pm1$ stack are 7 and 6 respectively, it is evident that this pattern must involve a nearly degenerate pair of fine structure states. In Figure 4.10 is illustrated the variation of fine structure state energies with the angle θ and a quenching value of ε_2 ~3 cm-1. The rotational constants used for this plot are those estimated in Equation (4.3.2); hyperfine and lambda-doubling effects have been omitted.

The common differences of Table 4.5 also reveal connections between these 14 R.F. transitions and hyperfine components of the microwave transitions at 5.8, 6.7 and 17.2 GHz. Four possible fine structure energy level schemes are compatible with the common difference data and are shown in Figure 4.11; the rotation of each of these four by 180 degrees will also yield a possible energy scheme.

The arguments of section (4.3) indicated that the

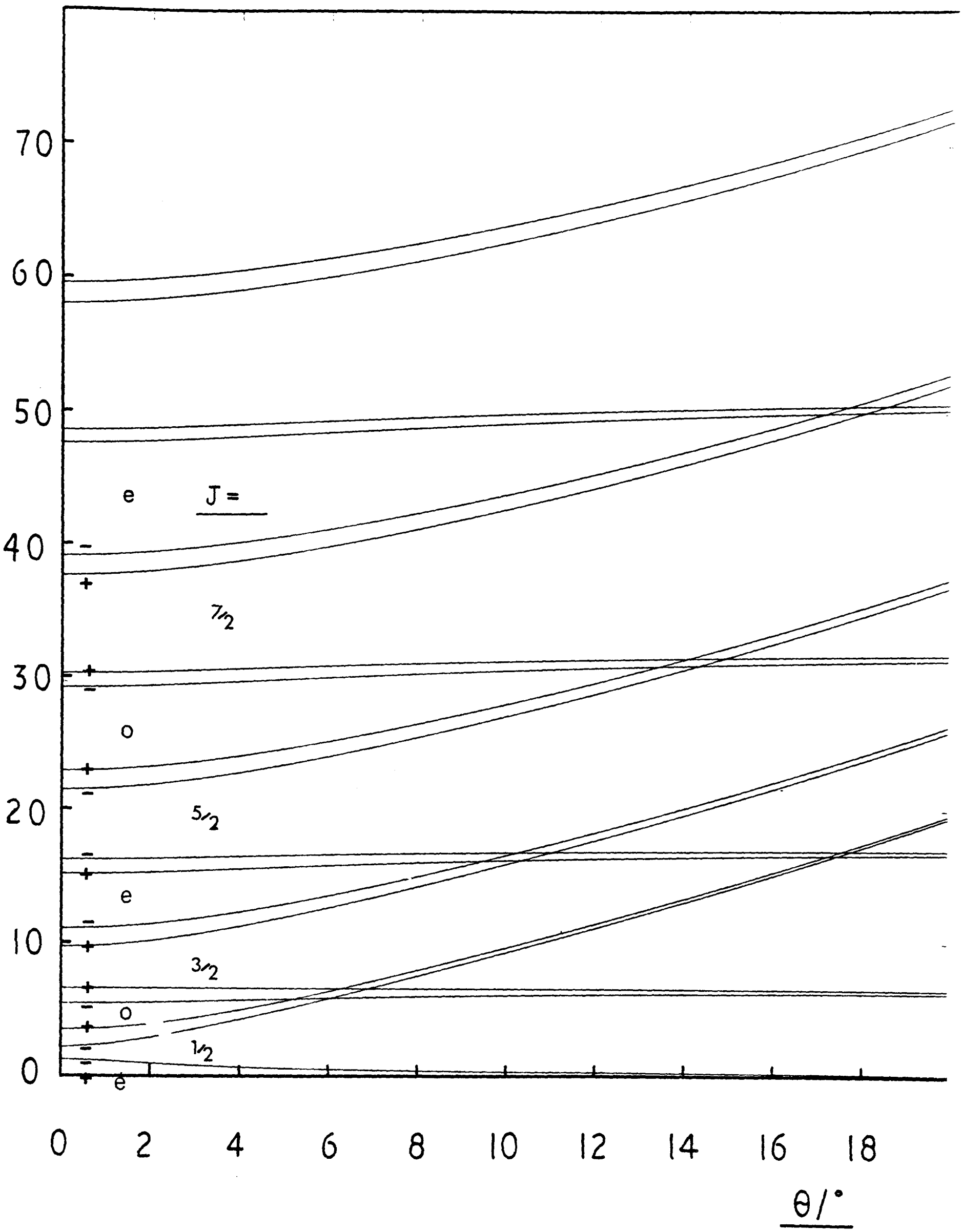


Figure 4.10: ArNO Energy Levels as $F(\theta)$ With $\epsilon_2 \sim 3\,cm^{-1}$.

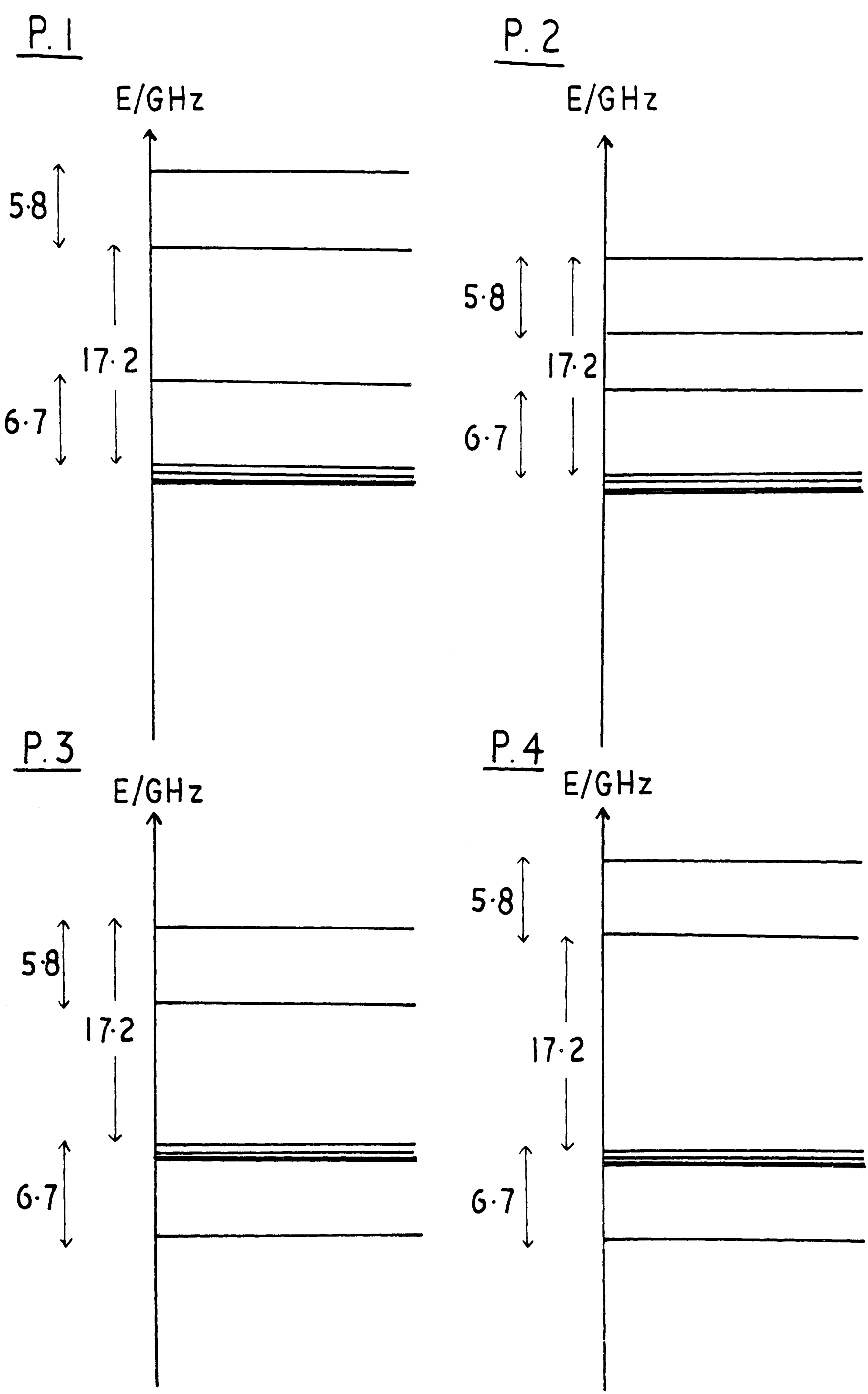

P.1
E/GHz
5·8
17·2
6·7
P.2
E/GHz
5·8
17·2
6·7
P.3
E/GHz
5·8
17·2
6·7
P.4
E/GHz
5·8
17·2
6·7

Figure 4.11

equilibrium geometry of ArNO would be within the scope of Figure 4.10 and probably towards the left hand side of the diagram. Comparison of Figures 4.10 and 4.11 reveals a number of plausible assignments where different J levels become nearly degenerate. Of the five J-crossings the one at about 17 degrees may be rejected immediately because some of the 14 R.F. lines within such a system would have to involve forbidden $\Delta J=2$ transitions. The crossings close to Θ = 14 and 18 degrees involve states rather higher in energy for which the populations following a supersonic expansion would be expected to be low. The signal to noise ratios were better (typically 5:1 for a 10 second time constant) for these 14 R.F. transitions than for the other lines observed and so an assignment with moderately low J is to be preferred. Moreover neither of these two possibilities could account for all of the 5.8, 6.7 and 17.2 GHz manifolds in the patterns of Figure 4.11 .

Only the inverted form of Pattern 2 of Figure 4.11 is at all compatible with the crossing at Θ = 10 degrees. The next nearest candidate, Pattern 3, is compatible with the 6.7 and 17.2 GHz manifolds but deviates by at least 2.5 GHz for the transitions that would have to be assigned to the 5.8 GHz set. In fact the inverse of Pattern 2 is also ruled out because it requires the six 17.2 GHz transitions to be assigned to a J=1/2 to 3/2 or 5/2 group. The latter is forbidden by the selection rule on J and the former can yield a maximum of only 5 hyperfine components.

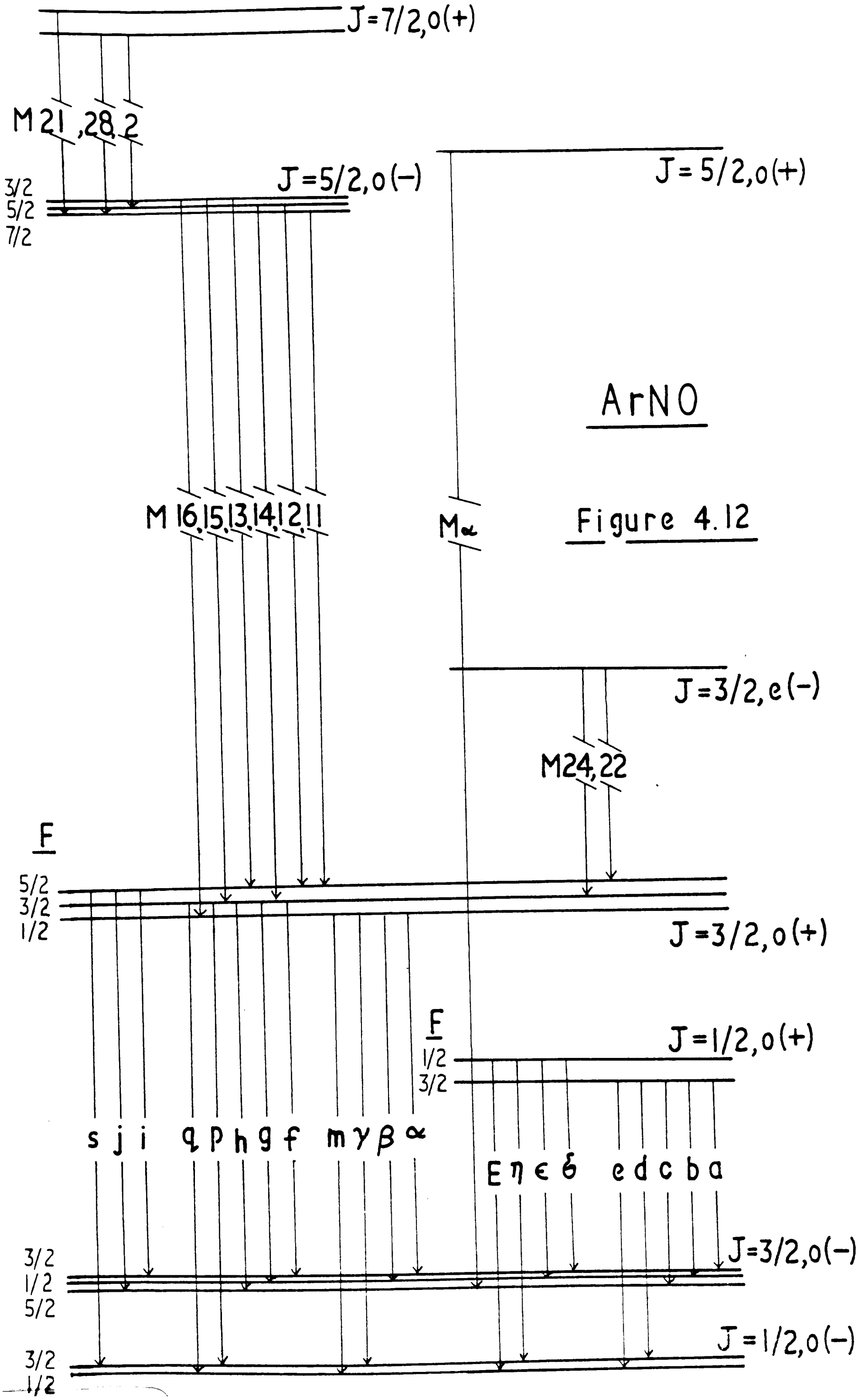
Finally the crossing of the J = 1/2,(O) and 3/2,(O) levels at about 6 degrees must be considered. This angle would be in best agreement with the structural predictions based on the potentials of previous workers discussed in section (4.2) . Inspection of (4.11) shows that Patterns 1 and 4 are in

reasonable agreement with the lower rotational energy levels of Figure 4.10 near to θ = 6 degrees. Simple fine structure calculations indicated that the former (Pattern 1) accommodated the 6.7 GHz transitions more easily. (This choice was later confirmed by the double resonance experiments.)

4.5 c) Assignment of Hyperfine Structure - The sign of ε_2

As explained earlier (see Equation 3.7.5), in the absence of non-adiabatic effects, a change in the sign of ε_2 has no effect on the fine structure eigenvalues; it merely interconverts the (+) and (-) parity states. The sign of ε_2 does have a profound effect on the hyperfine intervals, however. Calculations using the values of a, b_F, c, d, eQq_0 and eQq_2 which best fit the NO spectrum (section 3.6) and a positive ε_2 reveal large hyperfine intervals (tens of MHz) for o(+) and e(-) states and smaller intervals (a few MHz) for o(-) and e(+). The magnitudes of these splittings are reversed by a change in the sign of ε_2. An energy level pattern may be derived for the transitions involved in the common differences in the top part of Table 4.5 . Assuming that the hyperfine parameters of ArNO are similar to those derived from the NO spectrum, a positive value of ε_2 provides a hyperfine pattern in qualitative agreement with the observed experimental one. This information together with the selection rules allowed a tentative assignment also of the F quantum numbers.

The observed energy level pattern together with this hyperfine assignment is presented in Figure 4.12 . A series of further experiments were then performed to confirm this assignment.


J=7/2,0(+)
M21,28,2
J=5/2,0(-)
3/2
5/2
7/2
J=5/2,0(+)
ArNO
M16,15,13,14,12,11
Mα
Figure 4.12
J=3/2,e(-)
M24,22
F
5/2
3/2
1/2
J=3/2,0(+)
F
J=1/2,0(+)
1/2
3/2
s j i q p h g f m γ β α
E η ϵ δ e d c b a
J=3/2,0(-)
3/2
1/2
5/2
J=1/2,0(-)
3/2
1/2

4.5 d) Further Confirmatory Experiments

The energy level pattern of Figure 4.12 was constructed on the basis of the common differences contained in Table 4.5 . In order to confirm these relationships a series of double resonance experiments were attempted. The first two of these were to verify the existence of common energy levels between the 17.2 GHz microwave set and the radiofrequency stack of 4.11 . To test for such common energy levels one of the 17.2 GHz components was pumped with a phase-locked solid-state oscillator and no attenuation of the power. This pump transition was observed using phase-sensitive detection by frequency modulating the output of the solid-state oscillator at 14 Hz. Continous wave radiofrequency radiation with about 0.5 MHz of noise broadening was then switched on and off and the effect on the pump signal was noted. The frequency of the applied R.F. was chosen to correspond with the various transitions of Table 4.3 . The results are shown in Table 4.6 . Other transitions, α , β , and γ were also confirmed in this fashion thus verifying this assignment; these lines had not previously been observed. The absence of a resonance at 781.1779 MHz also supported the assignment of the F quantum numbers. All of the remaining R.F. transitions of Table 4.3 were tried as probes with the M11 pump transition but no further double resonance signals were seen.

Similar radiofrequency-microwave investigations were subsequently used to verify the connection between M22 and M24, of the 6.7 GHz set, and the radiofrequency stack. The results of these are summarised in Experiment 3 of Table 4.6. For these later experiments an R.F. amplifier was available making saturation of the R.F. transition more facile. For some cases

Table 4.6 : Double Resonance Experiments

Expt. 1 (T=10s)

Pump Transition	Probe Transition								
	f	g*	h*	i	j	m	p	q	s
M11	N	N	N	D	D	-	N	-	D
M14	D	D	D	N	N	N	D	D	N

* - No noise broadening on R.F. source.

Expt. 2 (T=10s)

Pump Transition	Probe Frequency/MHz				
	959.5611	959.9159	775.9689*	775.8211*	781.1779
M16	D	D	D	D	N

Expt. 3 (T=30s)

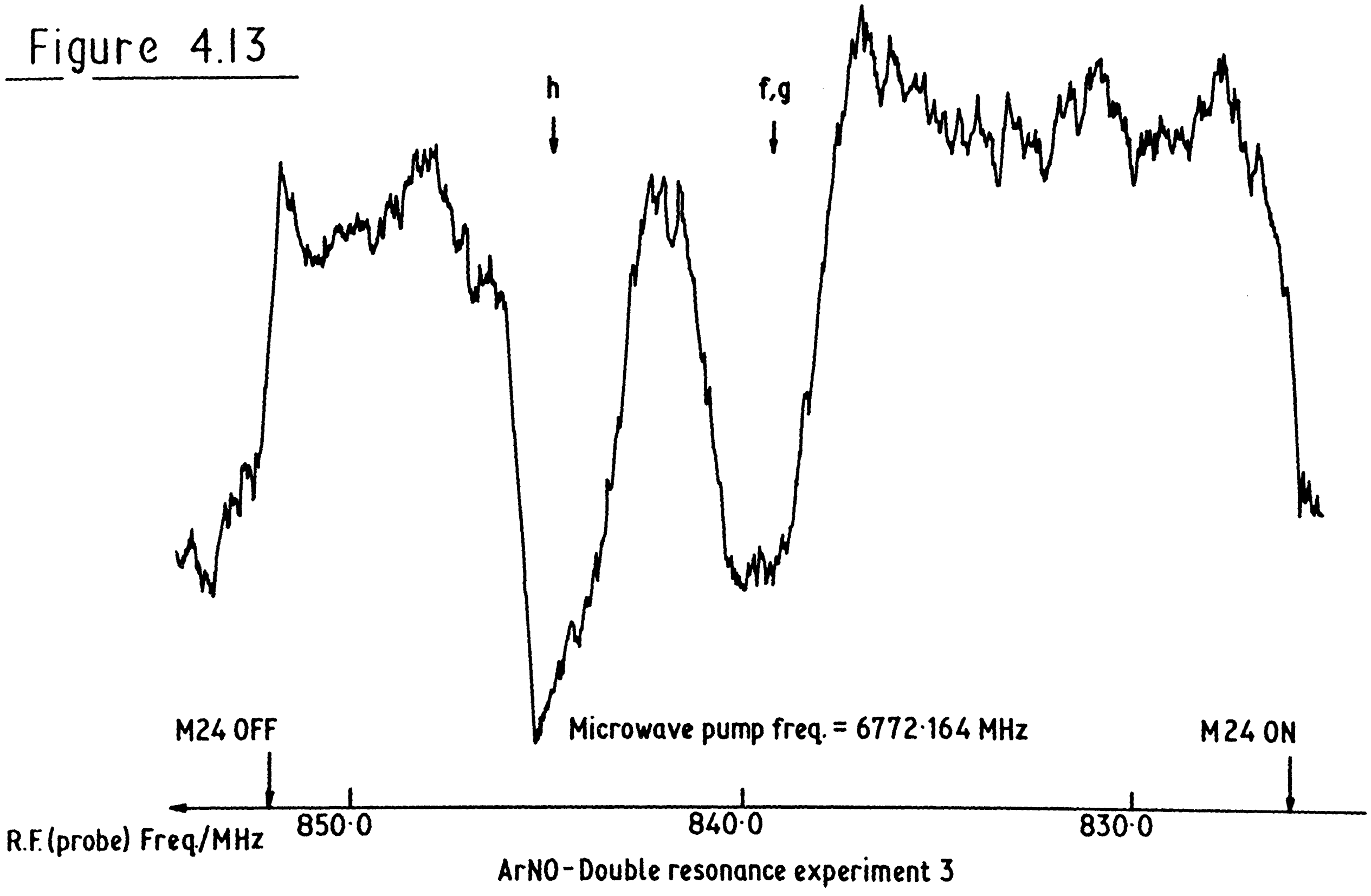
Pump Transition	Probe Transition				
	f	g*	h*	i	j
M22	N	N	N	D	D
M24	D	D	D	N	N

Expt. 4 (T=10s)

Pump Transition	Probe Transition		
	M2	M21	M28
M11	N	D	D

N.B. "D" denotes a decrease and "N" no change in the magnitude of the Pump signal on irradiation with the Probe frequency.

Figure 4.13



ArNO - Double resonance experiment 3

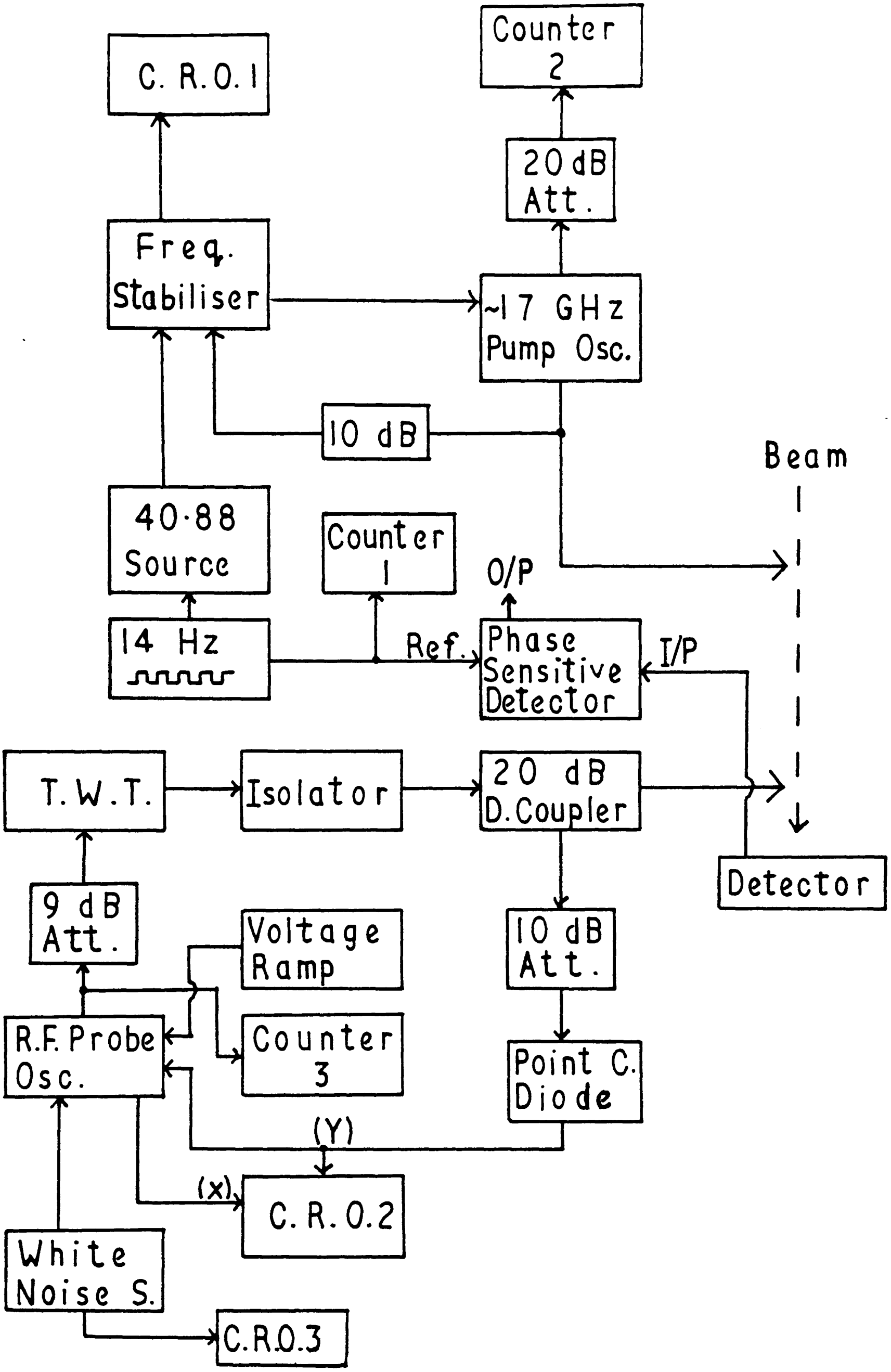


Figure 4.14: Double Resonance Experiment

therefore it was feasible to obtain a double resonance spectrum by ramping the R.F. frequency. An example of such a scan is shown in Figure 4.13 .

To confirm the common difference beween the transitions M2, M28, M11 and M12 a microwave-microwave double irradiation was required. This required a small modification of the main chamber to allow simultaneous application of two microwave sources. Amplification of the probe radiation also proved necessary and the somewhat involved arrangement of apparatus used for Experiment 4 is displayed schematically in Figure 4.14 . Considerable difficulty was encountered with this experiment (due to a lack of stability in the phase-locked loop) but the results given in Table 4.6 were satisfactorily reproducible.

The results of these four experiments not only confirm the validity of the common differences used to construct 4.12, they also indicate that the adoption of Pattern 1 of Figure 4.11 was correct.

Following the confirmation of the assignment an attempt was made to locate the transitions marked M_a on Figure 4.12 corresponding to J=3/2,o(-) to J=5/2,o(+). Approximate fine structure calculations based on reasonable values of the rotational constants and ε_2 indicated that this group of lines would occur at a frequency around 19.2 GHz. Unfortunately this frequency fell outside the upper range of the available solid-state oscillators and the travelling wave tube amplifier. An OKI 20V10 klystron was therefore used as the microwave source with a typical output power of some 200 mW. The entire region from 18.5 up to 20.0 GHz was searched with a 10 second time constant, focussing fields of (A,B) = (11,8) kV and 5 MHz of noise broadening. Sections of the scan around 19.0 to 19.6 GHz which

had showed interesting features were then re-examined with reduced noise broadening (2 MHz) of the radiation. Some very weak features were observed at 19.15 GHz and in the region around 19.5 GHz with the former being closer to the estimated position of the J=3/2,o(-) to J=5/2,o(+) transition. Further attempts to reproduce these features with a respectable signal to noise ratio (2:1 or better), or to locate their position more accurately, were unsuccessful.

The failure of these searches at around 19 GHz involves two factors. With the available stepping motor and gear systems it was not possible to mechanically sweep the klystron frequency at slower rates than were used above. To employ electronic tuning would have required a major modification of the klystron power supply. Hence neither longer integration times nor greater incident powers (by using less noise broadening) could be utilised. To support this explanation it should be pointed out that the comparatively strong 17GHz transitions (initially located with the amplified output from a solid-state oscillator) were not discovered in earlier searches with a similar klystron source.

As a control a microwave transition in the related van der Waals complex, $(NO)_2$, also present in the beam at mass 60, was tested. The 2_{02} to 2_{11} (F'=4 to F=4) resonance at 22268.8212 MHz was easily found under similar conditions (with a signal to noise ratio in excess of 5:1) thus verifying that correctly modulated microwave power was reaching the C-Field region.

The final experiments attempted on the ArNO system involved the tentative assignment of transition "E" as shown in Figure 4.12 . Consideration of the selection rules on the F quantum number indicates that further transitions should be allowed at

480.9577 MHz (δ), 481.1099 MHz (ε) and 658.0526 MHz (η). Using one Watt of amplified R.F. radiation with 5 to 10 MHz of noise broadening each of these resonances was observed. With a 30 second time constant the transitions, δ and ε , yielded a signal to noise ratio of about 6:1. The failure to find these transitions earlier must therefore have been due to a lack of power.

With this conclusion in mind further searches using 10 MHz of noise broadened, amplified radiation and a 30 second time constant were made between 400 and 900 MHz. Just four new resonances were found all of which could not be saturated with the very highest powers available in contrast to the other R.F. transitions of Table 4.3 . Inspection of their approximate frequencies (501.4, 507.6,538.5 and 544.5 MHz) showed them to be (within experimental error) just one half of the frequencies of transitions "n" or "o", "x" or "p", "u" and "B". As confirmation of this the second resonance was carefully measured under phase-locked conditions. It had an exact frequency of 508.3509 MHz to be compared with 1016.7021 MHz for "p". Further this line exhibited little evidence of power broadening even with no attenuation of the phase-locked source. The need for caution in interpreting or attempting assignment of resonances induced by very high power sources is evident.

4.6 Fitting the Spectrum of ArNO

4.6 a) The Fine Structure

In the previous section an assignment was made for about 26 transitions from a total of some 60 measured for ArNO. For the group of lines occurring in the radiofrequency region and the six transitions at 17.2 GHz, an assignment of the initial and final F quantum numbers was also possible. Unfortunately a similar hyperfine assignment was not straightforward for the transitions at 5.8 and 6.7 GHz because only three out of a possible six components had been found in each case. It was therefore decided to attempt to fit approximate fine structure energy intervals initially; from this it was hoped that further hyperfine assigments could be deduced.

In these calculations the Hamiltonian was that described in Chapter 3 but with the hyperfine interactions suppressed. Fitting was achieved using the standard least squares criterion. For this derivatives of the eigenvalues of the Hamiltonian matrix with respect to each fitted parameter are required. For a parameter, p, which occurs linearly in the Hamiltonian, the derivatives can be calculated using the Hellmann-Feynman Theorem.

$$dE/dp = \langle dH/dp \rangle = \sum_{i,j} c_i c_j . \langle i | dH/dp | j \rangle \qquad (4.6.1)$$

where the coefficients, ci and cj, are known from the matrix diagonalisation. The resulting large number of multiplications of eigenvector coefficients makes the calculation of derivatives a time consuming operation.

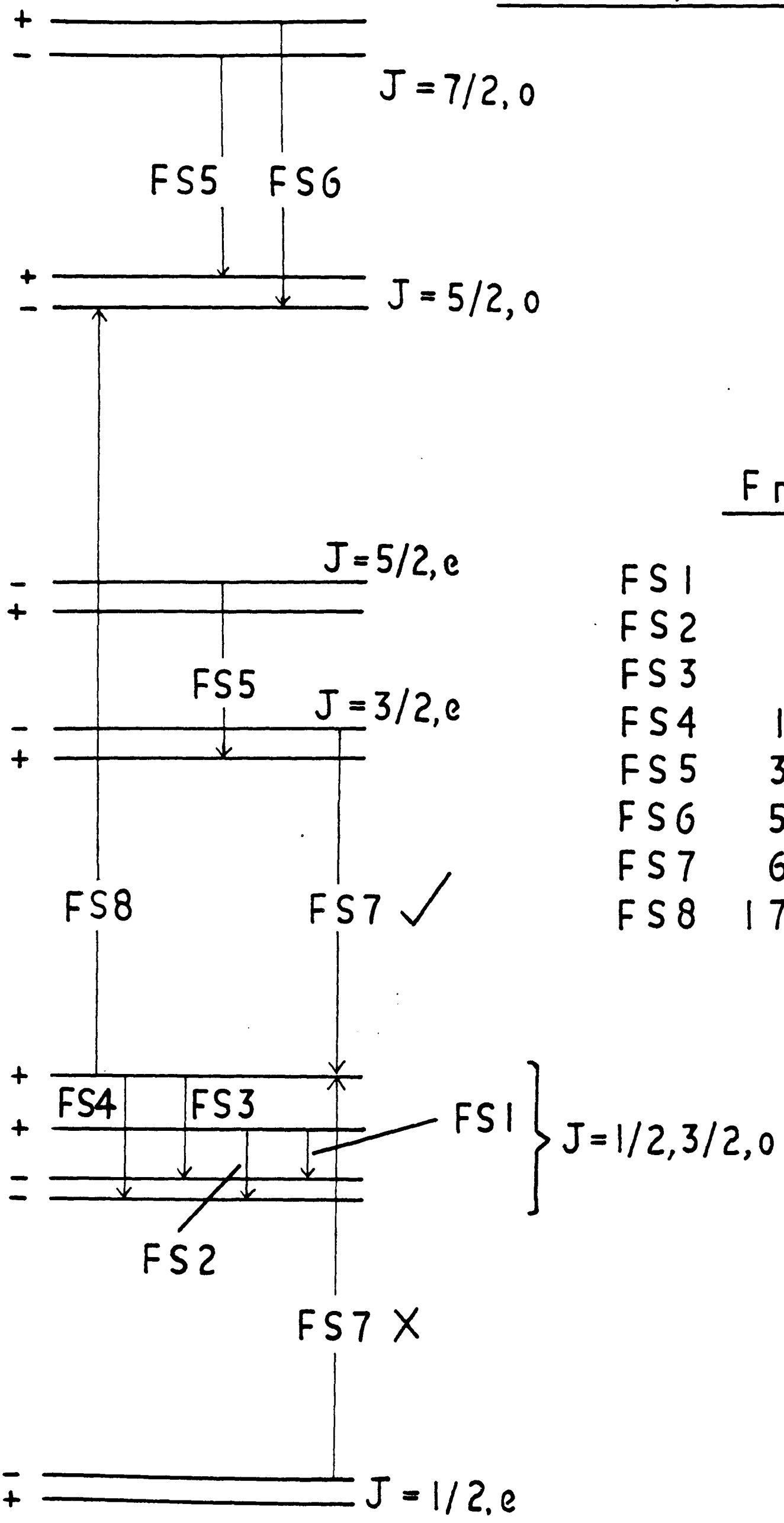
The other parameters, such as the structural angle, θ, which do not occur linearly are calculated from the definition of the differential coefficient. This involves incrementing the

parameter by a small amount and performing a second diagonalisation to yield the change in the eigenvalues of interest. This process too is clearly expensive in computer time for matrices of appreciable size. To try and alleviate this problem the effect on the Ka=1/2 levels of truncating the number of Ka states in the matrix was investigated. It was found that a calculation which included only the Ka=1/2 manifold introduced truncation errors of 20 to 50 MHz for J=3/2,5/2 etc. The origins of the important terms off-diagonal in Ka by ± 1 were discussed in Chapter 3.7 . The inclusion of the Ka=3/2 states caused the discrepancy in the Ka=1/2 eigenvalues, compared with a full calculation, to fall to only 50 kHz. Thus most of the fits described here involved diagonalisation of matrices including just Ka=1/2 and 3/2.

The general fine structure assignment, together with observed fine structure frequencies used, FS1 to 8, are shown in Figure 4.15 . Where the full hyperfine assignment was known the fine structure frequency is a simple average of the transitions. For the 3.7, 5.8 and 6.7 GHz manifolds it was arbitrarily taken to be the mean of the observed components with the highest and lowest frequencies. This somewhat crude treatment was adopted for two reasons. For the radiofrequency transitions the hyperfine interaction off-diagonal in J is probably significant and so an F-weighted average would still be misleading. Also the uncertainty in the hyperfine assignment of some transitions made a weighted average difficult. It should be mentioned that the tacit assumption has been made that M1, M25, M26 and M27 originate from a single fine structure transition and that M23 is part of the same manifold as M22 and M24.

Due to a lack of evidence from common differences the

ArNO, θ ~ 5°



	Freq./MHz
FS1	440·9
FS2	618·5
FS3	847·9
FS4	1025·7
FS5	3697·0
FS6	5897·6
FS7	6734·7
FS8	17221·5

Figure 4.15

transitions FS5 had not been given an assignment (though two possibilities are indicated in the figure) and hence were not included in the initial attempts at a fit of the fine structure. As a starting point the parameters B, C, θ and ε_2 were floated in a crude calculation that omitted all non-adiabatic effects. Although B and C were strongly correlated (93%) a final R.M.S. error of 47 MHz was obtained. On inclusion of a $^2\Sigma^-$ state in the matrix with the scaled matrix elements described in Chapter 3.6, this error was reduced to 37 MHz. The values of the fixed parameters used in this fit together with the final values of those floated are given below :

$$A = 51251.4 \text{ MHz} \qquad (4.6.2)$$

$$B = 2667.6 \text{ MHz}$$

$$C = 1553.1 \text{ MHz}$$

$$\theta = 4.94^{\circ}$$

$$\varepsilon_2 = 69819.2 \text{ MHz}$$

$$\zeta = 3692243.9 \text{ MHz}$$

For a planar molecule only two rotational constants should be independent and the moments of inertia from which they are derived are related by the expression[17] :

$$\Delta = I_C - I_A - I_B \qquad (4.6.3)$$

where Δ is the inertial defect. For planar molecules with four or more atoms the latter arises as a result of vibrations that lift the symmetry of reflection in the molecular plane; it is, however, normally fairly close to zero. For such a zero inertial defect Equation (4.6.3) leads to the following relation for the rotational constants :

$$B - C = B.C/A \qquad (4.6.4)$$

For example in the van der Waals species[18] ArN_2O Δ has a value of 2.2 a.m.u. $\mathring{A}^2$ and this corresponds to a discrepancy of 6% between

the observed value of (B-C) and that predicted by (4.6.4). In view of this the values for the ArNO rotational constants in (4.6.2) are totally inconsistent with each other and with θ. In particular the value of (B-C) for small angles should be of the order of 100 MHz.

From the van der Waals bond length,r , and angle, t, of Figure 4.4 the rotational constants and θ can be calculated. Thus these structural parameters together with ε_2 were floated in fits both with and without the perturbing $^2\Sigma^-$ state. The results of the former, slightly better, fit are shown in Fit 1 of Table 4.7. The same value of the spin-orbit coupling constant, ζ ,was used and r,t and ε_2 floated to :

$$r = 3.719 \text{ A} \qquad (4.6.5)$$

$$t = 5.650^{\,0}$$

$$\varepsilon_2 = 57453.9 \text{ MHz}$$

Although these are quite reasonable values for the parameters, the large R.M.S. error of 288 MHz is quite outside that expected from the approximate frequencies used for FS1 to FS8. The alternative assignments discussed in section 4.5 b) were shown to be invalid or to introduce much greater inconsistencies. Thus the origin of the discrepancy must lie in the fine structure Hamiltonian.

Apart from the size of the rotational constants and the quenching parameter, the major parameter that will influence the behaviour of the relevant fine structure states is the angle, θ. It was pointed out in the final section of Chapter 3 that centrifugal distortion of this angle would have a very significant effect on the spectrum. On the other hand modest variations in r due to centrifugal distortion will only cause small corrections to the rotational constants and hence have much

Table 4.7 : Fine Structure Fits

Transition	Lower State	Upper State	Observed/MHz	(Obs.-Calc.)/MHz Fit 1	Fit 2
FS1	J=3/2,o(-)	J=1/2,o(+)	440.9	51.5	31.7
FS2	J=1/2,o(-)	J=1/2,o(+)	618.5	227.9	-7.8
FS3	J=3/2,o(-)	J=3/2,o(+)	847.9	284.2	29.3
FS4	J=1/2,o(-)	J=3/2,o(+)	1025.7	460.8	-10.0
FS6	J=5/2,o(-)	J=7/2,o(+)	5897.6	-466.8	-0.4
FS7	J=3/2,o(+)	J=3/2,e(-)	6734.7	14.7	-67.7
FS8	J=3/2,o(+)	J=5/2,o(-)	17221.5	135.9	26.5
			R.M.S. Error	288.9	32.3

Transition	Lower State	Upper State	Observed/MHz	(Obs.-Calc.)/MHz Fit 3	Fit 4
FS1	J=3/2,o(-)	J=1/2,o(+)	440.9	30.0	16.2
FS2	J=1/2,o(-)	J=1/2,o(+)	618.5	-3.3	-21.4
FS3	J=3/2,o(-)	J=3/2,o(+)	847.9	34.6	14.3
FS4	J=1/2,o(-)	J=3/2,o(+)	1025.7	1.4	-23.1
FS5(Fit3)	J=3/2,e(+)	J=5/2,e(-)	3697.0	-25.9	-
FS5(Fit4)	J=5/2,o(+)	J=7/2,o(-)	3697.0	-	-23.9
FS6	J=5/2,o(-)	J=7/2,o(+)	5897.6	11.3	19.7
FS7	J=3/2,o(+)	J=3/2,e(-)	6734.7	-68.3	-76.5
FS8	J=3/2,o(+)	J=5/2,o(-)	17221.5	27.3	30.7
			R.M.S. Error	32.2	33.9

less effect. It was therefore decided to model as simply as possible just the centrifugal distortion of the structural angle by ascribing a dependence on the total angular momentum (excluding nuclear spin), J :

$$\theta = \theta_e + \Delta\theta.J(J+1) \qquad (4.6.6)$$

The reasoning for the model is as follows. The structure of the complex results from a combination of short range repulsive and long range attractive forces. The repulsive interaction is smaller for a geometry close to a T-shape enabling this structure to be stabilised by enhanced dispersion forces resulting from a shorter van der Waals bond length. For a simple atom-hetero diatom interaction the form of the long range interaction (neglecting small r^{-8} terms) has been given by Margenau and Kestner[19] :

$$\Delta E(r,t) = -\frac{(a_0 + a_2/3)}{r^6} \qquad (4.6.7)$$

$$-\frac{(6a_0 + 14/5.a_2 + 3a_3/5).d.\mathrm{Cos}(t)}{r^7}$$

$$-\frac{\{16(d/r)^2 a_0 + (26/7).(d/r)^2 + 2a_2/3\}(3\mathrm{Cos}^2 t-1)/2}{r^6}$$

where,

$$a_0 = \frac{3}{2}\,\frac{I_1.I_2}{I_1+I_2}.\,\alpha_{Ar}.\,\frac{\alpha_{\parallel}+5\alpha_{\perp}}{6} + \frac{\alpha_{Ar}.\mu^2}{2}$$

$$a_2 = \frac{3}{2}\,\frac{I_1.I_2}{I_1+I_2}.\,\alpha_{Ar}.\,\frac{\alpha_{\parallel}-\alpha_{\perp}}{2} + \frac{3\alpha_{Ar}.\mu^2}{2}$$

$$a_3 = 3.\alpha_{Ar}.\mu.Q$$

and I_1, I_2 are mean ionisation energies for Ar and NO. The α terms are polarisabilities and Q denotes the quadrupole moment of the NO molecule. From (4.6.7) it is clear that the attractive interaction energy is greatest for a linear configuration when t=0; this is true for both the dipole- and quadrupole-induced

dipole contributions. Likewise a collinear equilibrium geometry is also favoured by attractive dispersion forces. When the van der Waals bond is elongated by centrifugal effects the longer range attractive part of the potential becomes more important in determining the equilibrium structure. Hence as the rotational motion gets faster the equilibrium structure relaxes towards a linear geometry.

A crude estimate of the magnitude of $\Delta\theta$ may now be made. Assuming a typical well depth for ArNO of about 100 cm-1, then the onset of rotational dissociation will occur when :

$$BJ(J+1) \sim 100 \text{ cm}^{-1} \qquad (4.6.8)$$

which corresponds to a J value of about 30 to 40. Now the assumption is made that the relaxation to a linear geometry is approximately linear in J(J+1) and complete just prior to dissociation. From this the estimate of $\Delta\theta$ follows the limiting behaviour of (4.6.6) :

$$\pi/2 \sim \Delta\theta.(\text{well depth})/B \sim 1500.\Delta\theta \qquad (4.6.9)$$

$$\Delta\theta \sim 10^{-3} \text{ radians}$$

Thus the program described in Chapter 3 was modified to incorporate the J dependence of the angle θ and another attempt made to fit the seven fine structure transitions. The effect of this new term on the fine structure states is illustrated in Figure 4.16 . Four parameters were floated : r, t, ε_2 and $\Delta\theta$. The latter was given the initial value of (4.6.9). This fit (Fit 2) is also given in Table 4.7 where it can be seen that a great improvement resulted with the R.M.S. error falling to 32 MHz. The four parameters floated to the following values :

$$r = 3.709 \text{ A} \qquad (4.6.10)$$

$$t = 4.951^{\,0}$$

$$\varepsilon_2 = 91387.5 \text{ MHz}$$

$$\Delta\theta = 3.3\text{x}10^{-3} \text{ radians}$$

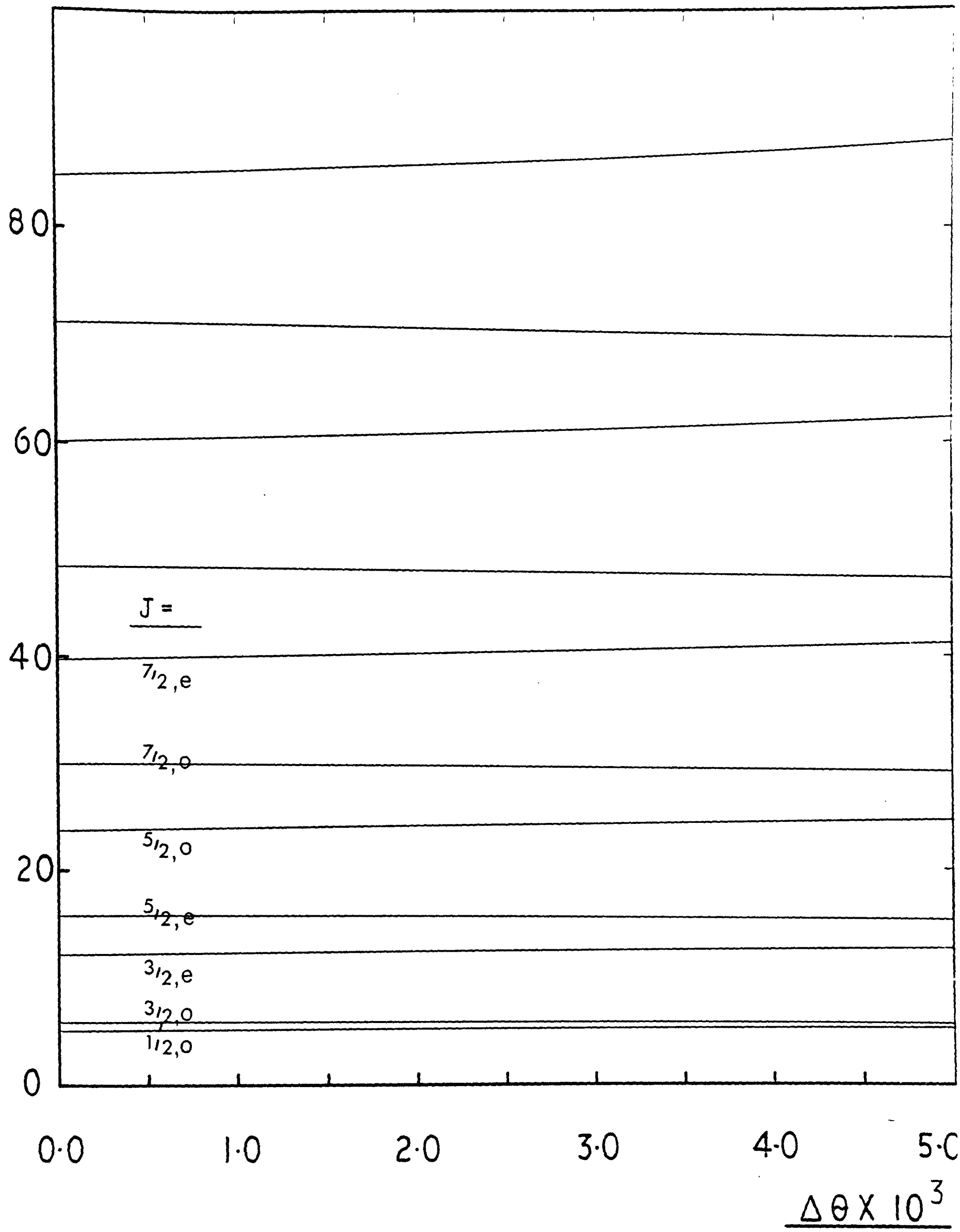


Figure 4.16 : ArNO Effect of $\Delta\theta$ on Fine Structure Energy Levels.

This fit was considered reasonable in the light of the approximate values derived for the fine structure intervals. It was noticed that the largest residual error was associated with FS7. Omitting this transition from a similar fit reduced the R.M.S. error to just 10 MHz with only minor changes to the floated parameters.

Finally the two possible assignments for the transitions denoted FS5 were tried in similar fits. The results are shown in Fit 3 and Fit 4 of Table 4.7 . For both assignments the R.M.S. error was much the same as in Fit 2 and so it must be concluded that either (or possibly both) could be responsible for the transitions at around 3.7 GHz. The final values of the floated parameters are given below for these two fits with the latter in brackets :

$$r = 3.710 \quad (3.709)\ A \qquad (4.6.11)$$

$$t = 4.960 \quad (4.931)\ ^{0}$$

$$\varepsilon_2 = 90783.5\ (93531.3)\ MHz$$

$$\Delta\theta = 3.3\times10^{-3}(3.4\times10^{-3})\ radians$$

4.6 b) Fitting the Radiofrequency and 17.2 GHz Transitions

In attempting a fit of the hyperfine structure of ArNO the pattern of energy levels containing just the assigned radiofrequency and 17.2 GHz transitions was investigated first. This was because a complete assignment of the relevant F quantum numbers had been made and extensively verified by the confirmatory experiments of section 4.5 d). A number of early attempts were made to obtain a good fit of all the known transitions by floating both fine and hyperfine parameters. These

first attempts were not very successful with large residual errors attributable in part to statistical correlation between some of the parameters.

In order to try and separate the effects of the fine and hyperfine parts of the Hamiltonian, the influence of the relevant parameters on the hyperfine intervals was studied. To do this the values of r, t and ε_2 from the best fine structure fit, (4.6.11), were held constant and the hyperfine parameters floated. The dependence of these intervals on the fine structure separations (and hence on the structural parameters) is small provided that the major contribution to the hyperfine structure is diagonal in J. This should be a good approximation except for the J=1/2,o and J=3/2,o hyperfine structure where the fine structure intervals are of the same order of magnitude as the hyperfine energy. Nevertheless this procedure was followed for the radiofrequency transitions but with the possibility of strong r, t and ε_2 dependence on the hyperfine splittings being kept in mind.

The R.M.S. error for the eight hyperfine intervals associated with the J=1/2,o(+) and o(-), J=3/2,o(+) and o(-) and J=5/2,o(-) states was found to be 7.10 MHz when using the unperturbed NO values for a, b_F, c, d, eQq_0 and eQq_2. This error could not be substantially reduced by changes in the value of t or ε_2 so it was concluded that a modification of the hyperfine parameters was necessary. In fact for the magnetic hyperfine only d and one from a, b_F and c could be floated without severe correlation problems. This is because, as for NO, only the combination $(a-1/2b_F-1/3c)$ is determined for the $^2\Pi_{1/2}$ ground electronic state.

When a and d were floated in a least squares fit the R.M.S. error on the same eight hyperfine intervals only fell to 6.6. MHz

and to 7.1 MHz for the six pertaining to the radiofrequency transitions. These results are compared with the discrepancies found for the unperturbed values of a and d in Table 4.8 . Similar fits attempted with modest changes to r, t and ε_2 also failed to produce significantly smaller residual errors. The electric quadrupole parameters, eQq_0 and eQq_2, although well decorrelated from a and d, required large changes from their values in NO to significantly reduce the residuals.

At this point the angular dependence of the complete magnetic and electric hyperfine matrix elements was re-examined. These are to be found in Appendices 3.4 and 3.5 . Apart from those which are completely diagonal in J, Ka, Λ and Σ all the magnetic hyperfine matrix elements have an angular dependence which may be expressed in terms of Cos(θ). For the electric quadrupole interaction the matrix elements are all functions of Cos(θ), $Cos^2(\theta)$ or Sin(θ).Cos(θ) . Now for an equilibrium geometry and bending vibrations that correspond to fairly small values of the angle θ, the above functions may be approximated by the leading terms in their power series expansions. Thus as discussed in Chapter 3 the large amplitude motion will lead to vibrational averages of the form :

$$< \mathrm{Cos}\theta > \quad < 1 - -/2.\theta^2 > \qquad (4.6.12)$$

$$< \mathrm{Cos}^2\theta > \quad < 1 - \theta^2 + 1/4.\theta^4 >$$

$$< \mathrm{Sin}\theta.\mathrm{Cos}\theta > \quad < \theta - 5/6.\theta^3 >$$

Since the magnetic effects are much larger it will be the vibrational average of θ^2 which dominates much of the hyperfine structure although the diagonal magnetic interaction and part of the quadrupole interaction is projected as the vibrational average of θ.

In contrast to this the dominant fine structure term,

$-2A.\sin(\theta).Ka.\Omega$, projects with an angle characteristic of the average of θ. In Chapter 3.9 it was pointed out that a model of the rotational spectrum in terms of a single vibrationally averaged angle was likely to prove erroneous. The introduction of a series of parameters to represent vibrational averages of all the trigonometric functions found in Appendices A3.4 and A3.5 was not attempted because there was insufficient experimental data to determine them. Instead a modification was made to the computer program to enable the angle characteristic of the projection of relevant parts of the NO hyperfine structure to be floated independently. For clarity it should be pointed out that this angle, γ ,which is defined in Figure 3.2 and discussed in section 3.6 c) is the complementary angle to θ, the latter appearing in the above discussion and in A3.4 and A3.5 . Thus it is the complement of γ which, when floated independently, is to be interpreted as the expectation value of θ^2. In Figure 4.17 is shown the effect of variation in the angle γ on the energy of the assigned radiofrequency stack. It can be seen that the frequency of these transitions is a rather slow function of this angle.

When a, d and γ were similarly floated in a fit of the eight hyperfine intervals a much better fit was obtained with an R.M.S. error of 0.71 MHz. This is also shown in Table 4.8 . In view of the approximation that all the hyperfine can be characterised by just one extra vibrationally averaged angle parameter and the omission of hyperfine terms off-diagonal in electronic state ($e1=e2=eQq_1=0$), this agreement is quite satisfactory.

A complete fit of all the assigned radiofrequency and 17.2 MHz transitions was now made using fixed values of a, d and γ

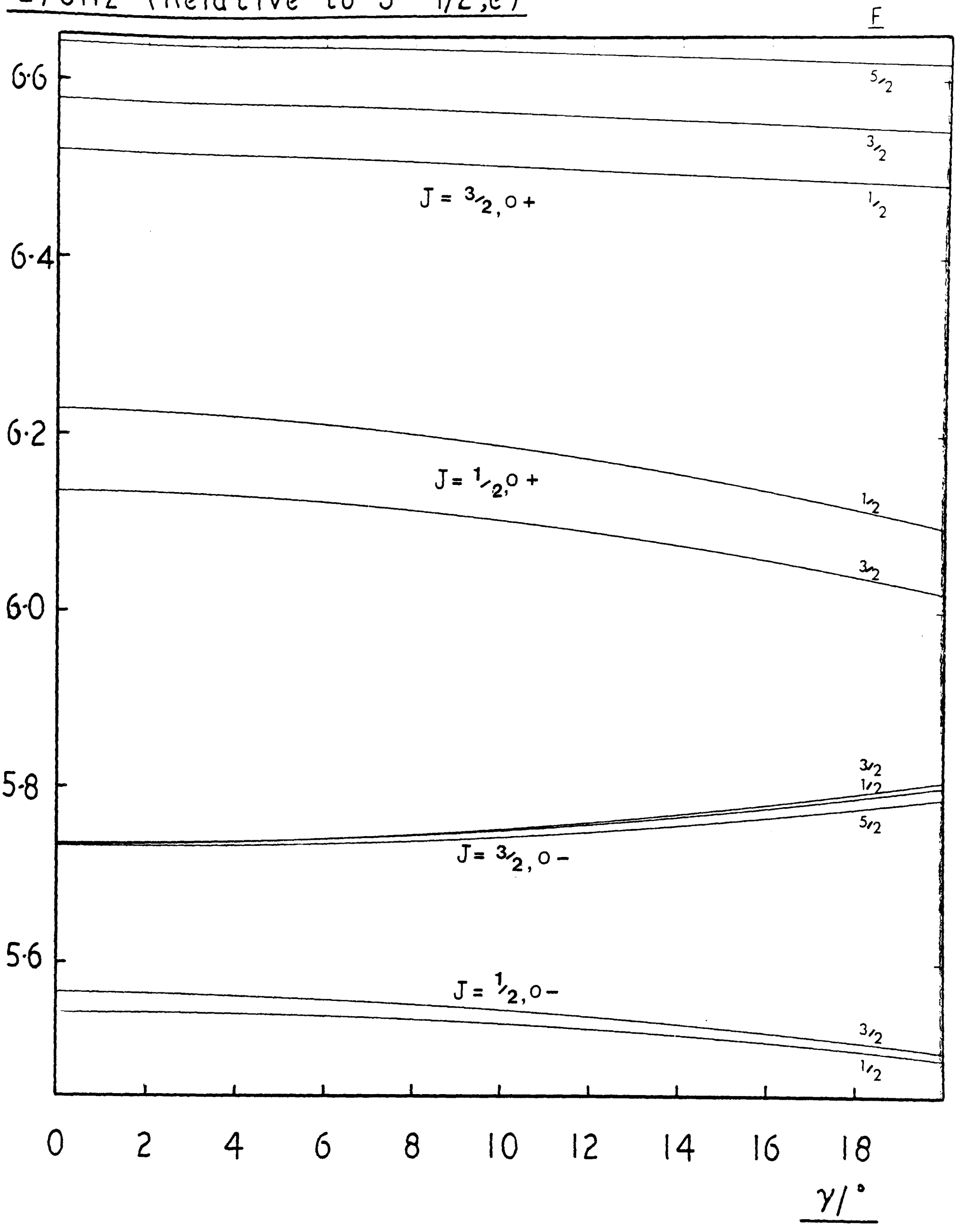


Figure 4.17: ArNO Variation of RF Hyperfine Energy with γ.

Table 4.8 : Fit of Hyperfine Intervals

Hyperfine Interval	Observed Interval (MHz)	Obs.-Calc. (NO params.) (MHz)	Obs.-Calc. (Float a,d) (MHz)	Obs.-Calc. (Float a,d,γ) (MHz)
J=1/2,o(-);F=1/2,3/2	6.6440	-12.9792	-11.5893	0.0225
J=3/2,o(-);F=5/2,1/2	5.2070	-0.9561	4.1336	-0.2427
J=3/2,o(-);F=1/2,3/2	0.1522	0.6322	-1.0184	1.2879
J=1/2,o(+);F=3/2,1/2	85.7631	-3.2252	-6.6762	-0.5918
J=3/2,o(+);F=1/2,3/2	63.7862	5.1613	4.0922	0.5426
J=3/2,o(+);F=3/2,5/2	75.0315	10.8350	9.8797	0.7096
J=5/2,o(-);F=7/2,5/2	14.8957	7.2442	5.2121	-0.9374
J=5/2,o(-);F=5/2,3/2	10.1706	5.2382	3.7795	-0.5715

Final Values of Fit :

a = 98.4549 MHz

d = 111.0153 MHz

γ = 72.1923 degrees.

Table 4.9 : Fit of R.F. and 17 GHz Transitions

Transition	Lower State	F"	Upper State	F'	Observed (MHz)	Obs.-Calc. (MHz)
a	J=3/2,o(-)	3/2	J=1/2,o(+)	3/2	395.195	-1.52
b	"	1/2	"	3/2	395.347	-1.84
c	"	5/2	"	3/2	400.554	1.16
d	J=1/2,o(-)	3/2	"	3/2	572.290	-8.36
e	"	1/2	"	3/2	578.934	-15.32
E	"	1/2	"	1/2	664.697	-40.16
f	J=3/2,o(-)	3/2	J=3/2,o(+)	3/2	839.607	10.44
g	"	1/2	"	3/2	839.755	10.11
h	"	5/2	"	3/2	844.964	13.12
i	"	3/2	"	5/2	914.638	5.66
j	"	5/2	"	5/2	919.995	8.34
m	J=1/2,o(-)	1/2	"	1/2	959.561	10.10
p	"	3/2	"	3/2	1016.702	3.60
q	"	1/2	"	3/2	1023.347	-3.37
s	"	3/2	"	5/2	1091.734	-1.18
M11	J=3/2,o(+)	5/2	J=5/2,o(-)	7/2	17139.514	10.55
M12	"	5/2	"	5/2	17154.409	5.62
M13	"	5/2	"	3/2	17164.582	2.12
M14	"	3/2	"	5/2	17229.439	0.83
M15	"	3/2	"	3/2	17239.609	-2.67
M16	"	1/2	"	3/2	17303.398	-16.13
					R.M.S. Error	11.86

from the final fit of Table 4.3 and floating r, t and ε_2. $\Delta\theta$ was fixed at its value determined in the previous section. Finally the hyperfine parameters were allowed to float also. The best fit obtained of this data is given in Table 4.9 and yielded an R.M.S. error of 11.9 MHz. The final values of the floated parameters were as follows :

$$r = 3.694 \text{ A} \qquad (4.6.13)$$

$$t = 5.094^{0}$$

$$\varepsilon_2 = 106676.7 \text{ MHz}$$

$$a = 128.79 \text{ MHz}$$

$$d = 136.86 \text{ MHz}$$

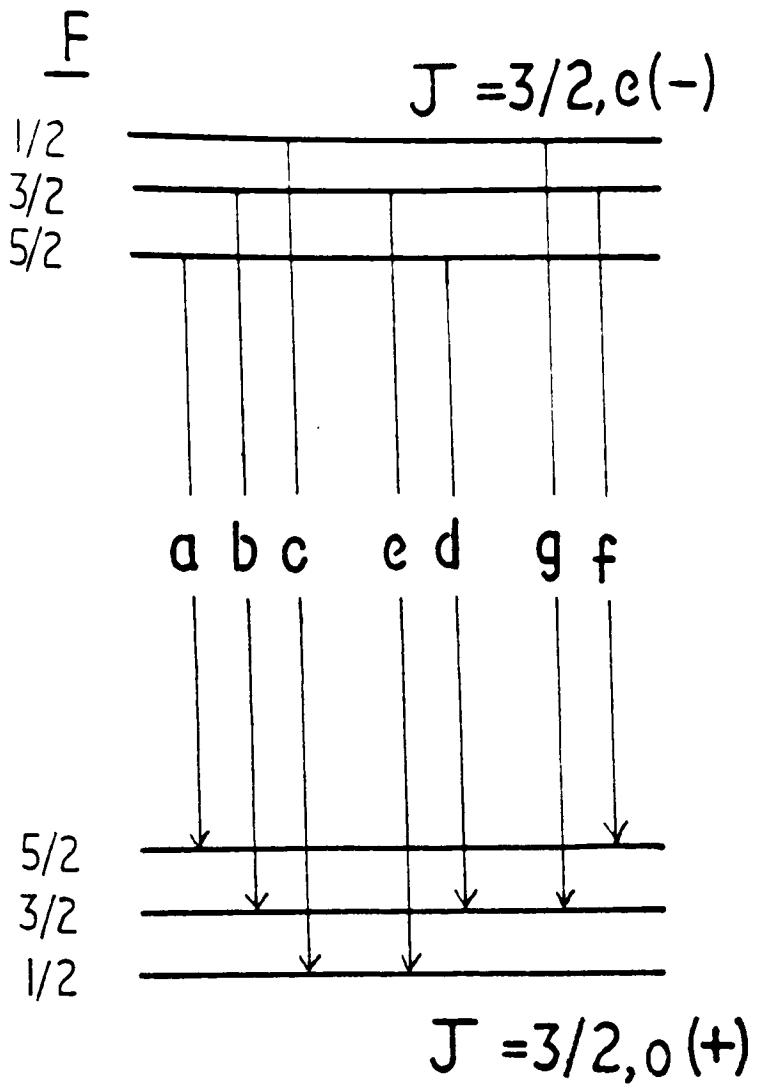
$$\gamma = 71.786^{0}$$

The fact that quite reasonable fitting of the hyperfine intervals did not lead to a better overall fit may indicate further shortcomings in the fine structure treatment. With reasonable estimates of γ and the hyperfine parameters it was now considered worthwhile to attempt the full assignment and fitting of the remaining transitions of Figure 4.12 .

4.6 c) The Full Assignment and Fitting of the 3.7, 5.8 and 6.7 GHz Transitions

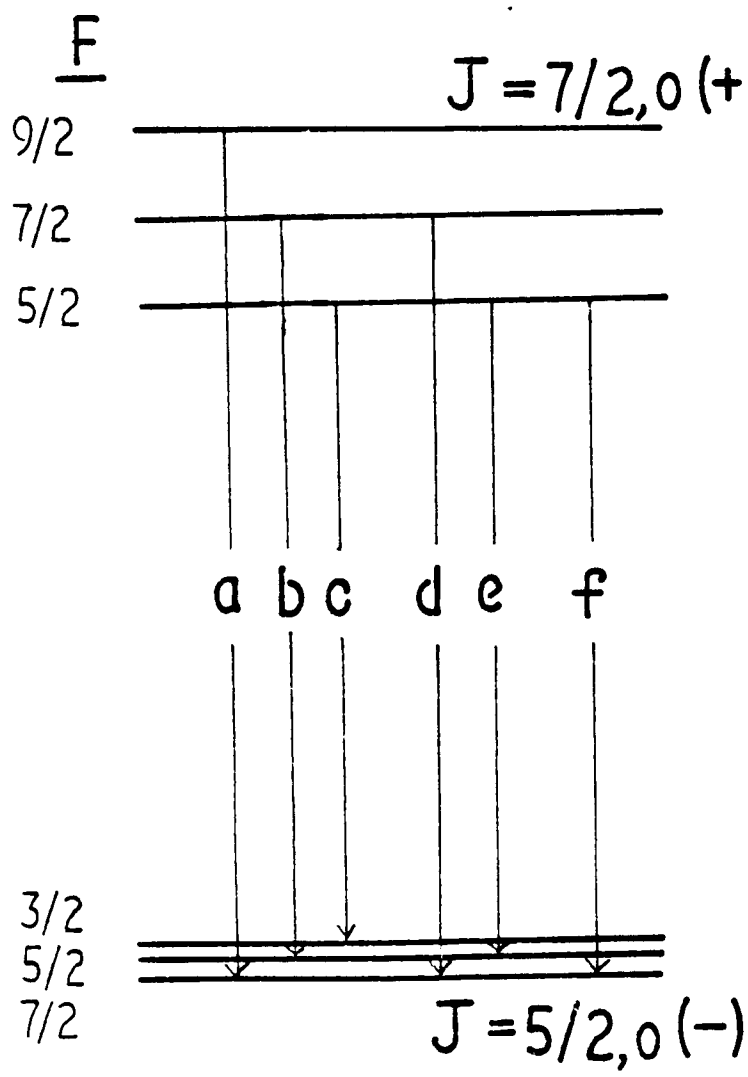
In section 4.6 a) the three transitions at 6.7 GHz were assigned as J=3/2,o(+) to J=3/2,e(-) . For the reasons described previously both of these fine structure states are characterised by large hyperfine splittings of the order of a few tens of MHz. In addition the double resonance experiments had indicated the F quantum number for the lower states associated with M22 and M24. In Figure 4.18a) are shown the calculated hyperfine splittings based on the unperturbed nitric oxide parameters and approximate

a) 6·7 GHz Set



Freq./MHz	
a	= 6733·7
d	= 6797·5
f	= 6803·1
b	= 6866·9
g	= 6909·4
e	= 6925·2
c	= 6967·7

b) 5·8 GHz Set



Freq./MHz	
c	= 5815·2
e	= 5820·2
f	= 5827·8
b	= 5884·2
d	= 5891·8
a	= 5970·5

Figure 4 18a) and b)

values of r, t and ε_2 . Beneath are given the calculated frequencies of all the seven ΔF allowed components. Since M22 and M24 arise from a common upper state and connect to F=3/2 and 5/2 in the lower state, they must correspond to one of the pairs (a,d) or (b,f) of that diagram. The difference between the frequencies of M23 and M24 is only ~5 MHz. For the latter pair M23 would have to be assigned to another hyperfine component very close in frequency to M24. This is impossible without very drastic changes in the hyperfine parameters or the sign of ε_2 .However, if M22 is identified with (a) and M24 with (d) then with only a minor perturbation of the splittings of Figure 4.18a), M23 may be associated with (f).

That is, the full assignment for these transitions is :

J=3/2,o(+),F=5/2 to J=3/2,e(-),F=5/2 : M22

J=3/2,o(+),F=5/2 to J=3/2,e(-),F=3/2 : M23

J=3/2,o(+),F=3/2 to J=3/2,e(-),F=5/2 : M24

For the 5.8 GHz set the hyperfine assignment is not quite so clear. This time the F numbering of the lower state is known for all three measured lines : M2, M21 and M28. Again M2 and M28 must arise from a common state which therefore can only be F=5/2 or 7/2. Hence M2 and M28 must be assigned to one of the pairs (b,d) or (e,f) shown in Figure 4.18b). For the former pair the remaining transition, M21, can only be assigned to transition (a). For the second pair this line is best associated with transition (d). The two schemes are therefore :

J=5/2,o(-),F=5/2 to J=7/2,o(+),F=7/2 : M2

Scheme 1 J=5/2,o(-),F=7/2 to J=7/2,o(+),F=7/2 : M28

J=5/2,o(-),F=7/2 to J=7/2,o(+),F=9/2 : M21

J=5/2,o(-),F=5/2 to J=7/2,o(+),F=5/2 : M2

Scheme 2 J=5/2,o(-),F=7/2 to J=7/2,o(+),F=5/2 : M28

J=5/2,o(-),F=7/2 to J=7/2,o(+),F=7/2 : M21

There are several factors which, a priori, favour Scheme 1. It had been established that a frequent reason for the failure to observe some hyperfine components was the lack of microwave power. As shown by Gordy and Cook[20] the largest transition moments for hyperfine patterns are obtained for those components with $\Delta J = \Delta F$. For Scheme 1 two out of the three resonances satisfy this relationship. For Scheme 2 two transitions have $\Delta F = \Delta J + 1$ and the third $\Delta F = -\Delta J$. If all other factors were equal these would be expected to be the least easily observed of the six possible hyperfine components of this manifold.

Further evidence in favour of adopting Scheme 1 comes from the predicted focussing characteristics of the focussing state, J=7/2,o(+). The hyperfine levels with the highest F quantum numbers are expected to contain the greatest number of focussing M_F states. Since the signal to noise ratio depends strongly upon the number of molecules refocussed, Scheme 1 is again to be preferred. Finally the exact positions of further lines could be deduced if Scheme 2 were valid; no evidence of these extra components was found in the recorded spectra.

Once again a fit of the hyperfine intervals seemed worthwhile to test these assignments. Scheme 1 for the 5.8 GHz set indeed produced the better fit which is shown in Table 4.10 . The R.M.S. error of this fit was 0.86 MHz with only slight alteration of the hyperfine parameters and the angle γ from the

Table 4.10 : Fit of Hyperfine Intervals

Hyperfine Interval	Observed Interval (MHz)	Obs.-Calc. (Without 3.7 GHz) (MHz)	Obs.-Calc. (With 3.7 GHz) (MHz)
J=1/2,o(-);F=1/2,3/2	6.6440	-0.2891	-0.0473
J=3/2,o(-);F=5/2,1/2	5.2070	-0.0349	0.0973
J=3/2,o(-);F=1/2,3/2	0.1522	1.1944	1.1584
J=1/2,o(+);F=3/2,5/2	85.7631	-1.1065	-1.0680
J=3/2,o(+);F=1/2,3/2	63.7862	0.3909	0.3682
J=3/2,o(+);F=3/2,5/2	75.0315	0.7905	0.6524
J=5/2,o(-);F=7/2,5/2	14.8957	-0.8599	-1.0148
J=5/2,o(-);F=5/2,3/2	10.1706	-0.5174	-0.6280
J=3/2,e(-);F=5/2,3/2	70.2817	1.5838	1.6103
J=7/2,o(+);F=7/2,9/2	85.3917	-0.7059	-0.7859
J=3/2,e( );F=5/2,3/2	12.5490	-	-0.2374
J=3/2,e( );F=3/2,1/2	9.2275	-	1.8878
R.M.S. Error		0.87	0.97

values found in Table 4.8 . Thus it was concluded that the assignment of the F quantum numbers had been made correctly.

Since the hyperfine structure could now be predicted to within 1 MHz R.M.S. error, the hyperfine patterns were calculated for the two possible manifolds for the 3.7 GHz transitions using the parameters of Table 4.10 . Denoting the frequency of the lowest component by F MHz, the ordered frequencies of the twelve hyperfine components are given in Figure 4.19. It should be recalled that the transitions M1 and M27 were related by a common difference and hence would be expected to share a common hyperfine level. Also shown are the four observed frequencies. Assignment of M1, M27 and M26 to (a,d,b) of the J=3/2,e(+) to J=5/2,e(-) manifold gives good agreement with the observed pattern. It therefore follows that the R.F. transitions, "C" and "k", which yielded that common difference belong to J=5/2,e(+) to e(-).

As discussed for the Scheme 1 assignment for the 5.8 GHz transitions, this choice is favoured by considering the transition moments and focussing properties. It can be seen that M25 with a frequency close to M26 and M27 cannot be accommodated into the same pattern. It must therefore originate from the fine structure states, J=5/2,o(+) to J=7/2,o(-); no firm conclusions can be drawn regarding its hyperfine assignment, however. A final fit including these new hyperfine intervals was made and the results are shown in Table 4.10 . The best fit values of the hyperfine parameters are as follows :

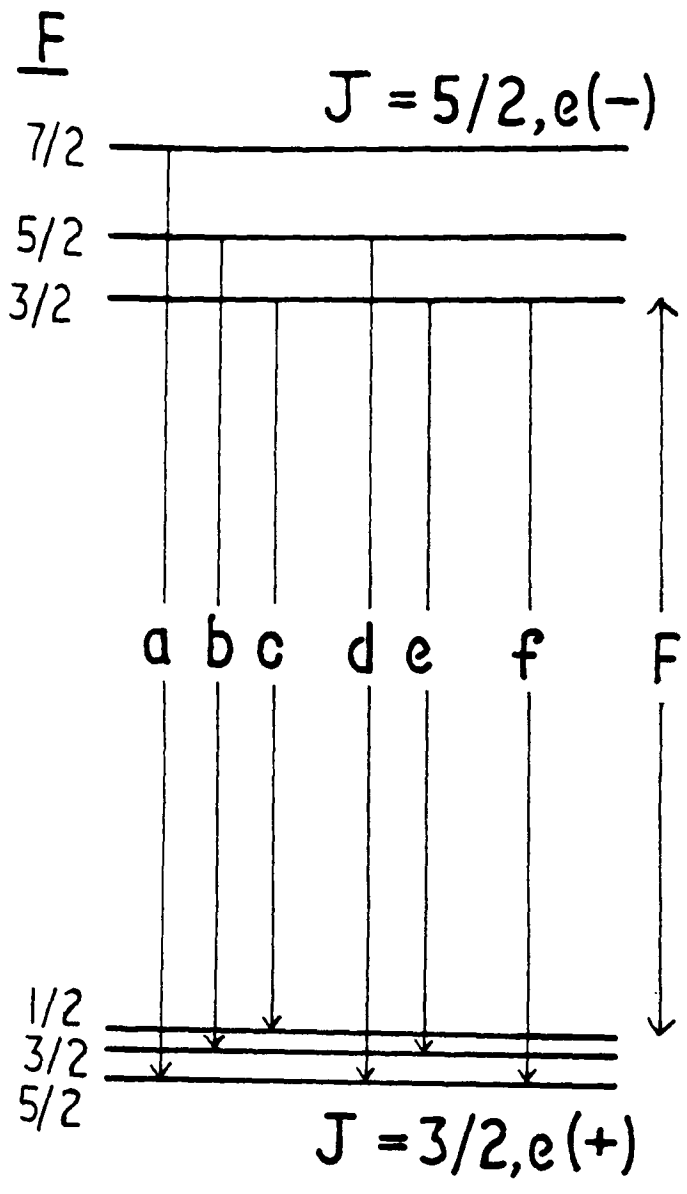
$$a = 98.841 \text{ MHz}$$

$$d = 111.228 \text{ MHz}$$

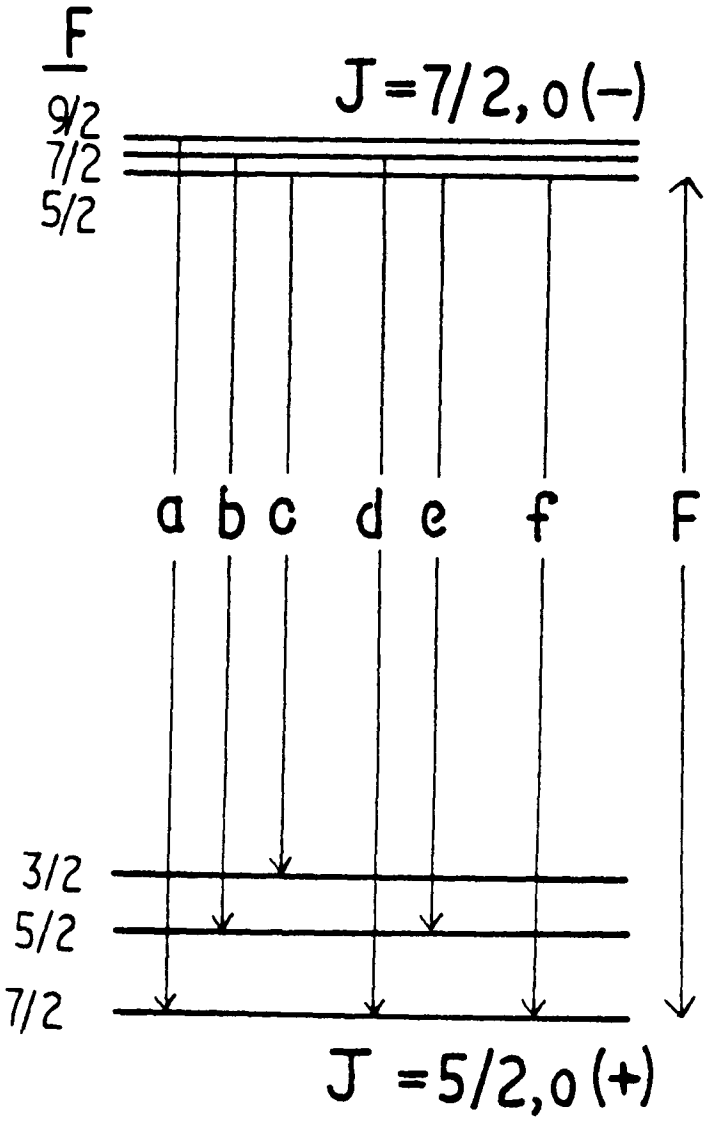
$$\gamma = 72.362^{\circ}$$

Following the successful determination of the hyperfine

ArNO - 3·7 GHz Set



Freq./ MHz		
c	=	F
e	=	F + 7·3
f	=	F + 20·1
b	=	F + 73·4
d	=	F + 86·2
a	=	F + 172·8



Freq/ MHz		
c	=	F
e	=	F + 48·5
b	=	F + 56·8
f	=	F + 115·6
d	=	F + 123·9
a	=	F + 133·3

Figure 4.19

Table 4.11 : ArNO - Fit Floating Structure Parameters

Transition	Lower State	F"	Upper State	F'	Observed (MHz)	Obs.-Calc. (MHz)
a	J=3/2,o(-)	3/2	J=1/2,o(+)	3/2	395.195	4.19
b	"	1/2	"	3/2	395.347	5.18
c	"	5/2	"	3/2	400.554	5.26
δ	"	3/2	"	1/2	480.958	1.65
ε	"	1/2	"	1/2	481.110	2.64
η	J=1/2,o(-)	3/2	J=1/2,o(+)	1/2	658.053	-20.42
E	"	1/2	"	1/2	664.697	-25.99
d	"	3/2	"	3/2	572.290	-17.88
e	"	1/2	"	3/2	578.934	-23.45
f	J=3/2,o(-)	3/2	J=3/2,o(+)	3/2	839.607	33.98
g	"	1/2	"	3/2	839.755	34.96
h	"	5/2	"	3/2	844.964	35.05
i	"	3/2	"	5/2	914.638	40.62
j	"	5/2	"	5/2	919.995	41.68
m	J=1/2,o(-)	1/2	J=3/2,o(+)	1/2	959.561	4.98
p	"	3/2	"	3/2	1016.702	11.92
q	"	1/2	"	3/2	1023.347	6.35
s	"	3/2	"	5/2	1091.734	18.55
M11	J=3/2,o(+)	5/2	J=5/2,o(-)	7/2	17139.514	2.58
M12	"	5/2	"	5/2	17154.409	3.64
M13	"	5/2	"	3/2	17164.582	4.48
M14	"	3/2	"	5/2	17229.439	10.27
M15	"	3/2	"	3/2	17239.609	11.11
M16	"	1/2	"	3/2	17303.398	12.49

(Continued Overleaf)

Table 4.11 Continued

Transition	Lower State	F"	Upper State	F'	Observed (MHz)	Obs.-Calc. (MHz)
M22	J=3/2,o(+)	5/2	J=3/2,e(-)	5/2	6697.132	-36.50
M23	"	5/2	"	3/2	6767.413	-35.23
M24	"	3/2	"	5/2	6772.164	-29.86
M2	J=5/2,o(-)	5/2	J=7/2,o(+)	7/2	5847.433	18.02
M28	"	7/2	"	7/2	5862.330	19.08
M21	"	7/2	"	9/2	5947.721	20.22
M26	J=3/2,e(+)	3/2	J=5/2,e(-)	5/2	3652.050	-47.88
M27	"	5/2	"	5/2	3664.599	-45.52
M1	"	5/2	"	7/2	3751.193	-43.45

---

parameters, a full fit of all the assigned transitions was made. Initially r, t, ε_2 and $\Delta\theta$ were floated. The hyperfine parameters were then re-floated to produce the fit of Table 4.11 . The R.M.S. error of 25.1 MHz again seemed to be largely resident in the fine structure part of the calculation.

4.6 d) Further Effects of Centrifugal Distortion

The fits of the previous section indicated that most of the residual errors were attributable to shortcomings in the fine structure treatment of the problem. Unfortunately the recorded spectrum is not complete enough to be able to easily isolate the source of the remaining discrepancies. The necessity of ascribing a J-dependence to θ, Equation (4.6.6), demonstrated the importance of centrifugal distortion effects. Whilst a rigorous treatment of these terms would introduce much more complexity than is justified by the experimental data, it was considered worthwhile examining such effects in a little more detail.

The first modification that was investigated concerned Equation (4.6.6). This relation assumes that the stretching in the van der Waals bond, which allows relaxation towards the linear structure, is proportional to J(J+1). Considering for simplicity the harmonic elongation in the T-shaped complex, there are centrifugal stretching forces due to rotation about the B and C inertial axes. The assumption is made that these forces are proportional to the corresponding rotational angular momenta and also that the electronic angular momenta are strongly quantised along the b or NO internuclear axis. The centrifugal force operating therefore follows the proportionality :

$$F \propto B^2(J_b - L_b - S_b)^2 + C^2J_c^2$$

where the constant of proportionality contains the atomic masses and distances.

The analogous expression for θ may now be written in the form :

$$\theta = \theta_e + \Delta\theta' \qquad (4.6.14)$$

where,

$$\Delta\theta' = \theta_d \left\{ \frac{B^2(J_b - L_b - S_b)^2 + C^2J_c^2}{1/2.(B^2 + C^2)} \right\} \qquad (4.6.15)$$

The denominator is a scaling factor which yields angular units for θ_d . Equation (4.6.15) may be expanded in the form :

$$\Delta\theta' = \theta_d.\{1/2(B^2+C^2)(J^2-J_a^2) + 1/4(B-C)(J^{+2}+J^{-2}) + B^2\Omega^2 - B^2(\Lambda+\Sigma)(J^+ + J^-)\} \Big/ 1/2(B^2+C^2)$$

(4.6.16)

In this expression the first term is entirely analogous to Equation (4.6.6) except for a factor of 1/4 which merely slightly modifies the interpretation of θ_d. The second term being off-diagonal in Ka by ± 2 will have a negligible effect on the spectrum. Likewise the third term is discounted because it gives a constant contribution to the $^2\Pi_{1/2}$ electronic state. Thus the only term that warrants further investigation is the last one in the equation.

In the manipulation of the rotational Hamiltonian of Chapter 3 it was assumed that the quantum mechanical operators for the various angular momenta commuted with functions of the angle θ. For the above model of θ, which allows for some centrifugal distortion effects, this assumption is no longer valid. If the constant terms of (4.6.16) are neglected the expression for θ can

be rewritten :

$$\theta = \theta_e + \theta_d.(J^2-J_a^2) + \theta_d.\left\{\frac{-2B^2}{B^2+C^2}\right\}(L_z+S_z)(J^+ + J^-) \qquad (4.6.17)$$

The diagonal contribution has already been incorporated. The off-diagonal corrections to the trigonometric functions of θ (assuming small θ) are therefore as follows :

$$\mathrm{Sin}\theta = \mathrm{Sin}\theta_e + K'.(\Lambda+\Sigma).(J^+ + J^-) \qquad (4.6.18)$$

$$\mathrm{Cos} = \mathrm{Cos}\theta_e - K.(\Lambda+\Sigma).(J^+ + J^-)$$

where,

$$K' = \mathrm{Cos}\theta_e.\theta_d.\left\{\frac{-2B^2}{B^2+C^2}\right\} \sim 3.5\times10^{-3}$$

$$K = \mathrm{Sin}\theta_e.\theta_d.\left\{\frac{-2B^2}{B^2+C^2}\right\} \sim 3.5\times10^{-4}$$

Also indicated are rough estimates of the magnitudes of the constants K and K' derived from the value of $\Delta\theta$ found in the fits based on Equation (4.6.6). These expressions for Sin(θ) and Cos(θ) were then applied to the rotational Hamiltonian of Chapter 3, Equation (3.5.1). Evaluation of the resulting expressions generated a very large number of terms. These were qualitatively inspected to determine which might yield large corrections to the calculated spectrum. The largest effects would be expected to arise from terms involving the A rotational constant and K'. Many of the terms were estimated to contribute the order of a few MHz but to accommodate these would have required very extensive modification of the computer program. However, the largest single correction term which would dominate these centrifugal distortion effects was shown not to contribute in the Ka=1/2 manifold. This is the matrix element that is responsible for the fast divergence

of the "e" and "o" fine structure states as the angle θ is increased.

$$H'_{1c} = A\{J_a - (L_z+S_z).\mathrm{Sin}\theta\}^2 \qquad (4.6.19)$$

and using the relations above :

$$H''_{1c} = -A\left\{ J_a(L_z+S_z).\{\mathrm{Sin}\theta_e + K'(\Lambda+\Sigma)(J^+ + J^-) + (L_z+S_z).\{\mathrm{Sin}\theta_e + K'(\Lambda+\Sigma)(J^+ + J^-)\}J_a\right\} \qquad (4.6.20)$$

Inspection of (4.6.20) reveals that the corrections to the rigid rotor part of Hlc involve the anticommutator :

$$\left[J_a, J^{\pm}\right]^+$$

the matrix elements of which were shown to be zero for Ka=±1/2 in Chapter 3. It must therefore be concluded that the original form for the centrifugal distortion of θ, Equation (4.6.6), already contains the largest terms. This more thorough treatment generates a large number of terms of smaller magnitude.

The above approach to the treatment of the centrifugal distortion of the complex clearly proves very cumbersome. In order to investigate the effect of the largest contributions in a simpler way, the relative magnitudes were assessed using second order perturbation theory. This formulation of centrifugal distortion, well described by Kroto, involves the admixture of excited vibrational states into the rotational wavefunctions of the ground vibrational state. Accurate estimates of such terms are difficult because the bending frequencies of similar van der Waals molecules are not generally known. This procedure does indicate their relative magnitudes, however. Inspection of the rotational Hamiltonian of Chapter 3 indicates that two of the largest corrections will arise from the following cross terms in

perturbation theory :

$$E_{cd1} = \sum \frac{\langle O|\tfrac{1}{2}(B+C).J(J+1)|n\rangle\langle n|2A\sin\theta.J_a(L_z+S_z)|O\rangle}{E_n - E_O}$$

$$E_{cd2} = \sum \frac{-\langle O|B\cos\ (J^+ + J^-)(L_z+S_z)|n\rangle\langle n|2A\sin\theta.J_a(L_z+S_z)|O\rangle}{E_n - E_O}$$

(4.6.21)

Here the n subscript denotes an excited (bending) vibrational state. The above contributions correspond to those terms that have already been considered. The former leads to the J-dependence of Θ and the latter has zero matrix elements in the Ka=±1/2 manifold.

The only other sources of potentially large corrections were those containing cross terms from Hlc of Chapter 3 such that they were diagonal in electronic state. These were of the form :

$$\sum \frac{\langle O|A\cos\theta.J_a(L^+ + S^+)|n\rangle\langle n|(-\tfrac{1}{2}B\sin\theta+\tfrac{1}{2}C).J^-(L^- + S^-|O\rangle}{E_n - E_O} + H.C.$$

$$\sum \frac{\langle O|A\cos\theta.J_a(L^+ + S^+)|n\rangle\langle n|-\tfrac{1}{2}(B\sin\theta+C).J^+(L^- + S^-)|O\rangle}{E_n - E_O} + H.C.$$

(4.6.22)

The important non-vanishing contributions arising from (4.6.22) may then be shown to yield the functional form :

$$K''.A.\tfrac{1}{2}C\cos\theta.(J^+ + J^-)(L_z+S_z) \qquad (4.6.23)$$

where K'' is a constant. This term mimics the following term in the original Hamiltonian :

$$-B\cos\theta.(J^+ + J^-)(L_z+S_z) \qquad (4.6.24)$$

and hence merely provides a modification of the definition of B.

A furtner correction to the values of the A and B rotational constants arises from the angular dependence in their definitions; this does not apply to C. These corrections together with the large residual errors in the fine structure separations of the rotational energy levels (which also depend on B and C) prompted a further fit floating these constants and θ instead of the bond length and angle. This procedure should also take account of other contributions to the inertial effect defined in Equation (4.6.3). A slight reduction in the R.M.S. error from 25.1 MHz to 16.1 MHz was obtained with the final values of the floated parameters being :

$$A = 51244.7301 \text{ MHz} \qquad (4.6.25)$$

$$B = 2299.3785 \text{ MHz}$$

$$C = 1899.6407 \text{ MHz}$$

$$\theta = 5.1077^{o}$$

$$\varepsilon_2 = 95496.8957 \text{ MHz}$$

4.6 e) The Assignment of the Remaining Transitions.

Of the sixty transitions of Tables 4.3 and 4.4 many remain unassigned. Seventeen of these are radiofrequency transitions the frequencies of which correspond to the (+) and (-) splittings of the various states. It is not possible to make a definite assignment for the majority of these without further common difference information. It can be seen from Table 4.5, however, that the transitions "r" and "n" share common energy levels with the three lines near 7.8 GHz. A calculation based on the parameters given in Equation (4.6.25) led to a satisfactory fine structure assignment (Obs. - Calc. ~ 100 MHz) for these 7.8 GHz transitions. Furthermore the calculated hyperfine intervals (from

the floated parameters of Table 4.10) gave good agreement for the full assignment of M3, M4 and M18 being as follows :

J=7/2,e(+),F=7/2 to J=9/2,e(-),F=9/2 : M3

J=7/2,e(+),F=9/2 to J=9/2,e(-),F=9/2 : M18

J=7/2,e(+),F=9/2 to J=9/2,e(-),F=11/2 : M4

In a similar pattern the R.F. lines "B" and "o" connect with the upper fine structure state of the 5.8 GHz manifold. In Figure 4.20 is given the most likely assignments for these remaining R.F. lines for which common difference information exists. These assignments were deduced from the selection rules and predicted hyperfine patterns using the best fitted parameters given at the end of the preceding section. In each case a tentative suggestion is made for a further R.F. line (t, w and D) that could be part of the same pattern by virtue of the predicted splittings.

A comparison was now made between the observed frequencies of the R.F. lines of Figure 4.12 and 4.20 and those calculated in the fit which floated B, C and Θ. A J-dependent discrepancy was found as exemplified below :

J=9/2,e, (Obs. - Calc.) ~ 100 MHz

J=7/2,o, (Obs. - Calc.) ~ 80 MHz

J=5/2,e, (Obs. - Calc.) ~ 50 MHz

J=3/2,o, (Obs. - Calc.) ~ 24 MHz

J=1/2,o, (Obs. - Calc.) ~ -20 MHz

Thus a final similar fit was attempted but allowing the value of the lambda-doubling matrix element to float away from the scaled value determined for NO. The fit, given in Table 4.12, was much

improved with an R.M.S. error of just 6.7 MHz. The rotational constants were little changed but the matrix element of $L^{\pm}$ floated to a value of 3.12 to be compared with 1.48 for NO.

$$B = 2280.1791 \text{ MHz} \qquad (4.6.26)$$

$$C = 1916.2739 \text{ MHz}$$

$$\theta = 5.1240^{o}$$

$$\varepsilon_2 = 80546.4774 \text{ MHz}$$

$$< L^{\pm} > = 3.1240$$

In fact this matrix element was 99% correlated with the parameter for the off-diagonal spin-orbit coupling which, when floated, was also approximately doubled in magnitude leading to a similar improvement in the fit. An inspection of Table 4.12 shows that the largest residual errors are associated with the higher J states of the 3.7 and 5.8 GHz transitions.

Nine unassigned phase-locked microwave transitions remain. Of these the set at about 9.8 GHz exhibit hyperfine structure characteristic of an "outer", predominantly μ_b-allowed transition. Although agreement was far from good this set was best assigned to the fine structure states J=9/2,o(-) to J=11/2,o(+). For M5, M8 and M9 no hyperfine structure was found. For these the following associations are those most compatible with calculations using the best fitted parameters :

J=5/2,e(-) to J=5/2,o(+) :M5 (~ 8702 MHz)

J=7/2,o(+) to J=7/2,e(-) :M8 (~ 10902 MHz)

J=1/2,e(-) to J=3/2,e(+) :M9 (~ 11793 MHz)

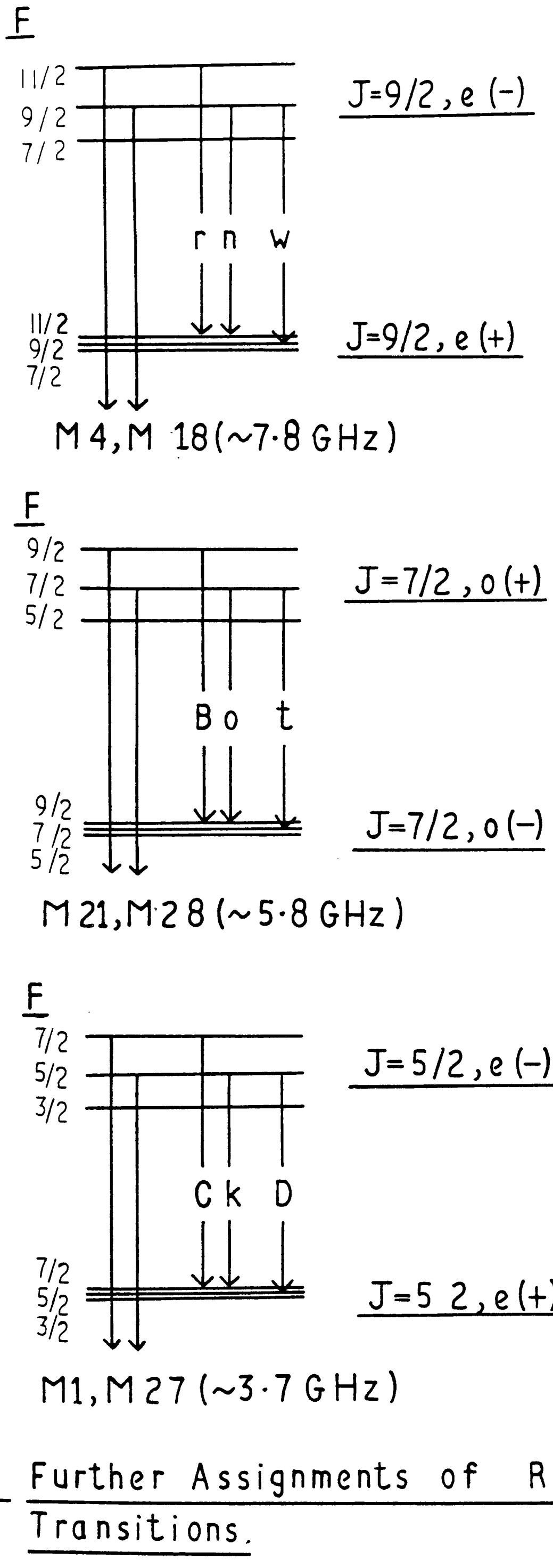


Figure 4.20 Further Assignments of R.F. Transitions.

Table 4.12 : ArNO - Fit Floating Lambda Doubling Parameters

Transition	Lower State	F"	Upper State	F'	Observed (MHz)	Obs.-Calc. (MHz)
a	J=3/2,o(-)	3/2	J=1/2,o(+)	3/2	395.195	-2.19
b	"	1/2	"	3/2	395.347	-1.12
c	"	5/2	"	3/2	400.554	-1.90
δ	"	3/2	"	1/2	480.958	-3.16
ε	"	1/2	"	1/2	481.110	-2.09
η	J=1/2,o(-)	3/2	J=1/2,o(+)	1/2	658.053	-1.86
E	"	1/2	"	1/2	664.697	-0.36
d	"	3/2	"	3/2	572.290	-0.89
e	"	1/2	"	3/2	578.934	0.61
f	J=3/2,o(-)	3/2	J=3/2,o(+)	3/2	839.607	1.72
g	"	1/2	"	3/2	839.755	2.78
h	"	5/2	"	3/2	844.964	2.01
i	"	3/2	"	5/2	914.638	3.42
j	"	5/2	"	5/2	919.995	3.71
m	J=1/2,o(-)	1/2	J=3/2,o(+)	1/2	959.561	5.03
p	"	3/2	"	3/2	1016.702	3.02
q	"	1/2	"	3/2	1023.347	4.52
s	"	3/2	"	5/2	1091.734	4.72
M11	J=3/2,o(+)	5/2	J=5/2,o(-)	7/2	17139.514	-1.67
M12	"	5/2	"	5/2	17154.409	-1.53
M13	"	5/2	"	3/2	17164.582	-1.31
M14	"	3/2	"	5/2	17229.439	0.17
M15	"	3/2	"	3/2	17239.609	0.38
M16	"	1/2	"	3/2	17303.398	-0.12

(Continued Overleaf)

Table 4.12 Continued

Transition	Lower State	F"	Upper State	F'	Observed (MHz)	Obs.-Calc. (MHz)
M22	J=3/2,o(+)	5/2	J=3/2,e(-)	5/2	6697.132	1.44
M23	"	5/2	"	3/2	6767.413	3.00
M24	"	3/2	"	5/2	6772.164	3.14
M2	J=5/2,o(-)	5/2	J=7/2,o(+)	7/2	5847.433	10.51
M28	"	7/2	"	7/2	5862.330	10.66
M21	"	7/2	"	9/2	5947.721	10.47
M26	J=3/2,e(+)	3/2	J=5/2,e(-)	5/2	3652.050	-17.72
M27	"	5/2	"	5/2	3664.599	-18.36
M1	"	5/2	"	7/2	3751.193	-18.41

4.7 Discussion and Conclusions

The analysis of the measured spectrum of ArNO has yielded a number of useful molecular parameters. Although the final fits of the spectrum involved floating B, C and θ, the structural parameters of the molecule are given better by the results of the fit summarised in Table 4.11 . The molecule has a vibrationally averaged bond length of 3.711 A with an average structure angle, $\langle\theta\rangle$, deviating from a T-shape by 5.175 degrees. From the projection of the NO hyperfine structure on the complex, an angle of 17.405 degrees is obtained for the vibrational average of θ^2. These two angles may be regarded as equivalent to those derived for other van der Waals molecules from the expectation values of $P_1(\text{Cos }\theta)$ and $P_2(\text{Cos }\theta)$.[21]

The other structural parameter of interest is the centrifugal distortion of the average angle $\Delta\theta$. The spectrum was best fitted with a value of 3.3×10^{-3} radians for this parameter. Since the mechanism of this centrifugal distortion involves the coupling of the van der Waals stretching and bending motions, it provides a measure of the curvature of the minimum and the r-dependence of the bending force constants on the intermolecular potential energy surface. The extent of the latter terms has previously been extracted for species such as ArHCl[22] from the centrifugal distortion of the angle representing the projection of the chlorine quadrupole coupling constant. In ArNO it is the projection of the diatomic electronic angular momentum that yields a similar quantity.

The sign of $\Delta\theta$ indicates the expected relaxation towards linearity as the van der Waals bond is stretched. The implication of this is that the ordering of the atoms in the (presumed)

linear long range geometry allows a determination of the sign of $\langle\theta\rangle$ derived in this work. The Maitland-Smith potential of Thuis et al.[9] indicates a positive sign for this angle. The average N.P.P. potential[6] does not yield a conclusive result because the potential minimum is so close to a T-shaped configuration.

The value of ε_2 that best fitted the ArNO transitions was 80546.5 MHz. Residual errors in the calculated fine structure may have caused the floated value of this parameter to deviate slightly, however. There is a rotational contribution to the parameter which, in the limit of pure precession, would be expected to be of the order of (1/2)A or 25 GHz. The remainder arises from the vibrational average of the quenching interaction. If most of this quenching contribution arises from the diagonal part of H_Q , then the positive sign (Figure 3.2) implies that the configuration with the unpaired electron out of the plane is more stable. At small separations the unpaired electron will experience greater overlap repulsion in the π-orbital in the plane of the complex. If, however, long range forces are important, the greater polarisability of this arrangement would favour the preferred localisation of the electron in the plane. Since the measured effect is a vibrational average, both of these influences will be sampled. It may therefore be concluded that the repulsive forces are dominant in determining the orbital motion of the electron. It must not be overlooked, however, that a large ε_1 term of either sign could mimic in second order the fitted positive sign of ε_2.

Also of interest are the successes and shortcomings of the Hamiltonian of Chapter 3 in accounting for the observed spectra. The general pattern of transitions together with the fitted value of ε_2 vindicates the use of a Hamiltonian derived on the

assumption of slight quenching. The NO hyperfine Hamiltonian proved adequate in accounting for hyperfine intervals to within about 1 MHz. The residual errors in the fine structure separations were, however, considerably higher than could be accounted for by experimental error. The failing of the single excited electronic state in the matrix to model the parity-independent interactions (section 3.6) may be largely responsible. Further centrifugal distortion effects, as discussed in section 4.6 d), may also have contributed to the errors. A failure to treat these terms, plus other vibrational and electronic contributions, explains why the fitted values of B and C indicate such a large inertial defect.

It is not obvious why the matrix element of $L\pm$ floated to a value of 3.12 compared with 1.48 for the fit of the NO spectrum (section 3.6). One possible mechanism for this change concerns the centre of mass transformation discussed briefly in Appendix A3.1 . Strictly the components of L should be referred to the molecular centre of mass and this introduces correction terms additional to those treated in Chapter 3. The form of some of these terms is mimicked by the lambda-doubling matrix elements.

One of the most important results of this study is the need to considerably perturb the magnetic hyperfine parameters of NO in order to fit the spectrum of ArNO. The best fitted values of the combinations $a-1/2(b_F+2/3.c)$ and d were 107.300 MHz (92.735) and 111.228 MHz (112.613) with the values for NO as given in the brackets. This represents a change of about 15% for the first term with the second largely unaltered (~1%). Although it is difficult to draw firm conclusions about whether charge transfer effects are operative, this large change implies a substantial perturbation of the NO electronic wavefunction by the argon atom.

The evidence from the sign of the quenching parameter, ε_2 ,indicates that there could be a considerable sampling by the NO of a repulsive interaction due to the rare gas atom. There is experimental[23,24] and theoretical[25] evidence for the overlap of the electron clouds of nitric oxide and rare gas atoms arising from collisions in a bulk mixture of the gases. Jameson et al.[24] reported large downfield chemical shifts in the ^{129}Xe N.M.R. spectrum in the presence of NO. Thus it is possible that the perturbation of the NO magnetic hyperfine constants in the complex, ArNO, is partly due to overlap of the two charge clouds.

Chapter 4 : References

1.S.E.Novick,P.B.Davies,T.R.Dyke and W.Klemperer, JACS, 95, 8547, (1973)

2.P.R.R.Langridge-Smith,E.Carrasquillo.M. and D.H.Levy, JCP, 74, 6513, (1981)

3.I.P.French and T.E.Arnold, JCP, 48, 5720, (1968)

4.W.Rohrbeck,R.Winter,W.Herrmann,J.Wildt and W.Urban, MP, 39, 673, (1980)

5.G.C.Nielson,G.A.Parker and R.T.Pack, JCP, 66, 1396, (1977)

6.G.C.Nielson,G.A.Parker and R.T.Pack, JCP, 64, 2055, (1976)

7.S.Stolte,J.Reuss and H.L.Schwartz, Physica, 66, 211, (1973)

8.H.Thuis,S.Stolte and J.Reuss, CP, 43, 351, (1979)

9.H.Thuis,S.Stolte,J.Reuss,J.J.H.van den Biesen and C.J.N.van den Meijdenberg, CP, 52, 211, (1980)

10.A.P.Kalinin,V.N.Khromov and V.B.Leonas, MP, 47, 811, (1982)

11.P.Andresen,H.Joswig,H.Pauly and R.Schinke, JCP, 77, 2204, (1982)

12.R.Schinke, Personal Communication

13.W.L.Meerts, CP, 14, 421, (1976)

14.J.B.Marion, Classical Dynamics, Academic Press, (1967)

15.P.D.A.Mills, Part II Thesis, Oxford University, (1980)

16.C.M.Western,P.R.R.Langridge-Smith,B.J.Howard and S.E.Novick, MP, 44, 145, (1981)

17.H.W.Kroto, Molecular Rotation Spectra, Wiley, (1975)

18.C.H.Joyner,T.A.Dixon,F.A.Baiocchi and W.Klemperer, JCP, 75, 5285, (1981)

19.H.Margenau and N.R.Kestner, Theory of Intermolecular Forces, Pergamon Press, (1971)

20.W.Gordy and R.L.Cook, Microwave Molecular Spectra,

Interscience, (1970)

21.J.M.Hutson and B.J.Howard, MP, 43, 493, (1981)

22.B.J.Howard, Unpublished Work

23.C.J. and A.K.Jameson, MP, 20, 957, (1971)

24.C.J.Jameson,A.K.Jameson and S.M.Cohen, JCP, 65, 3397, (1976)

25.A.D.Buckingham and P.A.Kollman, MP, 23, 65, (1972)

Chapter 5 : The Rotational Spectrum And Analysis Of NeNO.

5.1 Introduction

5.2 Previous Studies of NeNO - Estimation of the Fine Structure Parameters

5.3 The NeNO M.B.E.R. Spectrum

5.4 The Assignment and Analysis of the Recorded Spectrum

5.5 Discussion and Conclusions

Chapter 5 The Rotational Spectrum and Analysis of NeNO

5.1 Introduction

In this chapter is described a series of attempts to record and analyse the M.B.E.R. spectrum of a second open-shell van der Waals molecule, NeNO. The initial motivation for this study arose when the work on ArNO was far from complete and hence its assignment still quite ambiguous. NeNO has B and C rotational constants which are some 50% larger than those of ArNO. Hence the pattern of energy levels, though qualitatively similar, is considerably more spaced. It was concluded that the M.B.E.R. spectrum of the former would show fewer transitions and that the assignment of these might prove more straightforward. The possibility that such an assignment would assist in unravelling the incomplete spectrum of ArNO was therefore a further incentive.

There are factors both in favour and against the choice of the neon complex as the subject of a second investigation. The larger rotational constants and correspondingly smaller rotational partition function will increase the relative populations of low lying rotational states. Transitions arising from these states are therefore more easily observed providing that the focussing behaviour is favourable. On the other hand the binding energy of the neon complex is expected to be smaller than that of argon, reflecting the influence of the rare gas polarisability (Ar=1.61$\mathring{A}^3$, Ne=0.39$\mathring{A}^3$)[1] on the magnitude of dispersion and induction forces. Assuming a non-linear geometry by analogy with ArNO, the magnitude of the induced μ_a dipole moment will also be smaller.

In practice the experimental difficulties encountered with this molecule proved even greater than those for ArNO. As a consequence the experimental work was less complete and a full analysis not possible. A comparison of the information gained with that from the argon molecule enabled some interesting and useful conclusions to be drawn, however.

5.2 Previous Studies of NeNO - Estimation of the Fine Structure Parameters

Much less work has been reported on the intermolecular potential between neon and nitric oxide than that already reviewed for the corresponding argon potential. In fact the only direct source of information for the position of the potential minimum has again come from the work of Thuis, Stolte and Reuss.[2] The experiment used to measure the anisotropy in the total scattering cross section for beams of neon and nitric oxide was essentially the same as that described in Chapter 4. Minor modifications were necessary to narrow the velocity distribution of the neon source.

The experimental results were analysed using the sudden approximation. From the spacings of the anisotropic glory features the product of the well depth and equilibrium distance was obtained :

$$\varepsilon . R_e = 3.11 \times 10^{-14} \text{ erg.A} \qquad (5.2.1)$$

Using a value for the C6 coefficient calculated from the Kirkwood relation, and assuming the Lennard-Jones form for the potential, Equation (4.2.6), Thuis et al. separated the two components of (5.2.1). The validity of this relation for rare gas-nitric oxide systems has been previously established by experiment for argon. Unfortunately there are serious errors in some of the entries in Table 1 of this reference. Assuming that the reported experimental quantity of (5.2.1) is as presented, the correct values for the isotropic parameters are :

$$\varepsilon = 0.92 \times 10^{-14} \text{ erg} \qquad (5.2.2)$$
$$= 46.3 \text{ cm}^{-1}$$
$$R_e = 3.39 \text{ A}$$

In principle Thuis et al. could have related the parameters for the attractive part of the anisotropy, $q_{2,6}$ to the non-glory part of the measured anisotropy. However, because of the high velocity of the neon atomic beam (a cooled effusive source was used), the total collision cross section was not very sensitive to the attractive part of the potential. The parameter was therefore set equal to that determined for the analogous systems Kr+NO and Xe+NO. The anisotropic repulsion coefficient, $q_{2,12}$, was then derived from the glory contribution to the measured anisotropy. The values given for the two anisotropy parameters are :

$$q_{2,6} = 0.20 \qquad (5.2.3)$$

$$q_{2,12} = 0.22$$

A plot of the potential derived from Equations (4.6.2), (5.2.2) and (5.2.3) is shown in Figure 5.1 . In view of the unsuitability of neon as the scattering partner in these investigations, the potential should be regarded only as a qualitative one.

The values of ε and Re above may be compared with the following estimates. The former is derived from combination rules.[3] The latter uses an average value for the difference in the effective rare gas radii from the known structures of the van der Waals species $(Ne)_2$, $(Ar)_2$[3], NeDCl[4,5] and ArDCl[6] and from van der Waals "b" values for argon and neon.[7] An approximate value of Re for ArNO from Chapter 4 then permits an estimate of that quantity for NeNO.

$$\varepsilon \sim 38.6 \quad cm^{-1} \qquad (5.2.4)$$

$$R_e \sim 3.70 - 0.28 \sim 3.42 \text{ A}$$

An estimate may be made of the equilibrium structure angle, θ, from that determined for ArNO. Assuming that the bending motion of the NO sub-molecule is simple harmonic, the amplitude

will depend on the one fourth power of the ratio of the reduced masses for the two complexes. A value of about 8 degrees is therefore estimated for the neon complex.

If the major contribution to the diagonal quenching term, ε_2, arises from the dispersion forces, its magnitude will be expected to scale with that of ArNO as the ratio of the rare gas polarisabilities, (0.24). This yields an estimate of about 20 GHz for the parameter. However, as explained the sign of this parameter in ArNO implies that repulsive forces are dominant at the equilibrium geometry. Thus for the neon complex a larger positive value seems likely though its magnitude is difficult to estimate accurately.

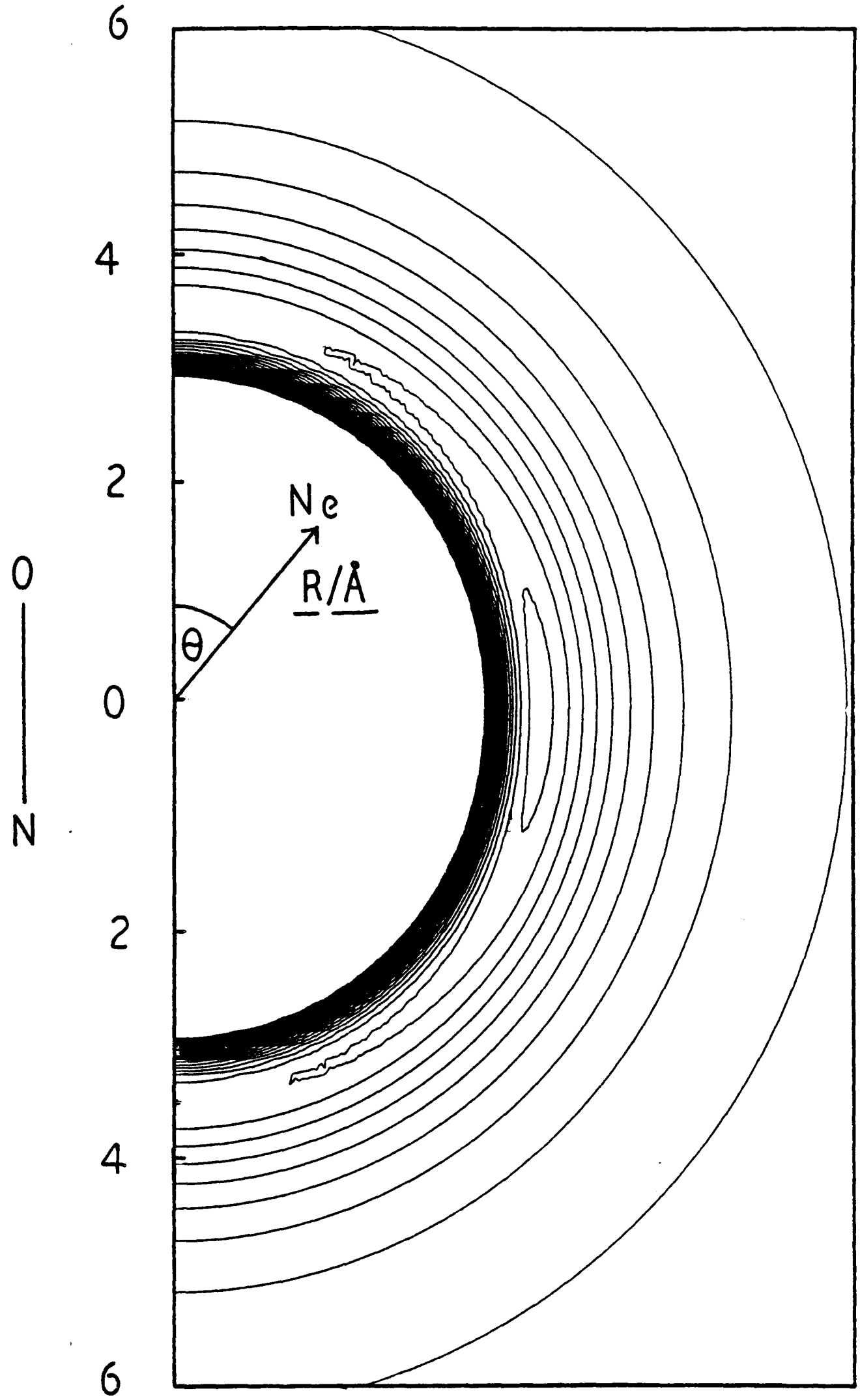


Figure 5.1 : NeNO Potential of Thuis et al.

(5 cm^{-1} Contours)

Figure 5.2

NeNO Refocussing as a F(T,P)

A,B = [kV]

0·023 (30,28)

0·019 (25,20)

0·017 (22,15)

0·016 (20,10)

0·015 Stopped Beam

0·018 X 10^{-8}A Straight Through Beam

P = 2·8 X 10^{-5} torr

T ~ 125K

0·013 X 10^{-8}A Straight Through Beam

0·017 (29,24) = A,B [kV]

(25,20)

(22,15)

(20,10)

0·010 Stopped Beam

P = 2·6 X 10^{-5} torr

T ~ 100K

0·017 X 10^{-8}A Straight Through Beam

0·021 (29,26) = A,B [kV]

(25,20)

(22,15)

(20,10)

0·012 Stopped Beam

P = 6·0 X 10^{-5} torr

T ~ 100 K

Gain = 1·95 kV

Figure 5.3

NeNO: Mass spectra

5.3 The NeNO M.B.E.R. Spectrum

5.3 a) Refocussing Behaviour and Expansion Conditions

Initial investigations of the refocussing behaviour of the complex were made with an 8% mixture of NO in standard research grade neon. A weak beam of a strongly polar species was found at m/e=50; this mass peak was used for all subsequent work for the same reasons as for ArNO. Attempts to enhance the refocussing further by seeding the neon expansion with some argon were unsuccessful since ArNO was formed in much greater concentration at the expense of the neon complex. Although the background at this parent mass peak was quite high, it could be reduced substantially by the cryo-pumping of the detector chamber. It is of interest that some of the species at this mass number originated from the main or buffer chamber but were not present in the nozzle expansion. This caused a build-up of the background mass spectrum which resulted in an increase in the noise present on the detected molecular flux at mass 50.

Following the experience of previous studies of neon containing van der Waals molecules, a slightly smaller nozzle aperture was tried. A 40 micron nozzle produced good refocussing, in excess of 250%, and was not so prone to blockage as smaller nozzles through dust particles carried from the vacuum line. A 50 micron nozzle (as used for ArNO) was also tried. This produced quite strong beams but with slightly poorer rotational cooling as measuring by the percentage refocussing. The former nozzle was therefore used for all spectroscopic experiments.

Much effort was invested at various stages of the study in finding the optimum conditions of temperature and pressure for

the expansion. It was discovered that, although the lowest temperatures available (~90 to ~100K) produced good refocussing, they very soon led to nozzle blockage through polymerisation and condensation. This problem was rarely encountered with the argon expansions; the difference in behaviour may be attributable to the use of a smaller aperture or even to impurities in the neon. A sample of refocussing traces at different temperatures, pressures and quadrupole field voltages is presented in Figure 5.2 . In order to prolong the life of the nozzle expansion before condensation occurred, a compromise of slightly higher temperatures and pressures was usually undertaken. Typical operating conditions were :

$$P_o = 2.5 \times 10^{-5} \text{ torr}$$

$$T_n = 150 \text{ K}$$

It should be noted that the sensitivity of the source chamber ion gauge is reduced by a factor of four in going from argon to neon. The above observed pressure is therefore actually higher than those typically employed in the work described in Chapter 4. Later it was discovered that the use of more dilute mixtures, typically 2% of NO in neon, lessened polymerisation without adversely affecting the refocussed beam.

Even at these higher temperatures the blocking of the nozzle was a constantly attendant problem causing much delay to the experiments. An expansion was rarely stable for more than three hours (in contrast to ArNO) and hence only selected portions of the microwave spectrum could be examined within reasonable time constraints. Furthermore, whilst using the 40 micron nozzle, it proved necessary to clean the vacuum line frequently in order to remove dust particles. Blockage induced by the carriage of these solid particles induced even greater periods of "down time" for

the spectrometer.

When the neon-nitric oxide system was first examined no maximum in refocussing was reached as the A and B Field voltages were increased. To enhance the refocussing of such species as these the length of the A field quadrupole rods was increased from 39 to 48 cms. during the later stages of the work. A maximum was just discernable with the longer field arrangement and the voltages used for most searches were slightly lower than those necessary to produce this maximum : (A,B) = (22,12) kV.

In Figure 5.3 is illustrated the mass spectrum in the region around mass 50. The effect of the focussing fields at this mass peak, as well as the high background, is easily observed. Also of interest is the polarity of the beam-carried species at m/e=52. This corresponds to the van der Waals molecule, ^{22}NeNO, at 8% natural abundance. Thus it is possible to investigate the isotopic shifts in the spectrum for this species without using enriched samples. Due to the long integration times required for ^{20}NeNO, however, the spectroscopy of the less abundant form was not attempted in the present project.

5.3 b) Spectroscopy in the Radiofrequency Region

For much of the early work in this region a high power source of radiation was not available. The small number of transitions thus found compared with the total eventually recorded is indicative of the value of R.F. and microwave amplifiers in the study of complexes with small dipole moments.

As indicated in section (5.2) the earliest estimates of ε_2 assumed that dispersion forces yielded the major contribution and hence predicted a smaller value for the neon complex. It was

therefore decided to search up through the radiofrequency region starting at the bottom of the frequency range of the appropriate solid-state oscillator. In order to achieve a reasonable scan rate a 10 second integration time and 10 MHz of noise broadening was used together with focussing fields of (A,B) = (23,20) kV. The spectrum from repeated scans was digitised and signal-averaged in 200 MHz sections using the Varian computer. The total time constant for each section ranged from 20 to 40 seconds.

In total the region from 100 MHz to 2300 MHz was covered in this way. Many features were re-examined but only three transitions, at 1.0 to 1.25 GHz, were confirmed and measured by phase-locking. The exact frequencies of these denoted "m", "o" and "p" are given in Table 5.1 . Much weaker features at ~1140 and 1174 MHz were only observed at low resolution. The use of multiple scans and reduced noise broadening failed to produce accurate estimates of their frequencies and so phase-locking was not attempted.

Further scans were attempted using 2.5 MHz of noise broadening, a 30 second time constant and focussing fields of (A,B) = (21,12) kV to extend the range covered up to 3 GHz. No further transitions were observed.

After this work had been completed a solid-state radiofrequency amplifier (range 0.1 to 350 MHz) was kindly made available by Dr. R. Freeman of this laboratory. This enabled careful searching of the lower frequency regions (5 to 350 MHz) but with much higher incident powers being typically 1 to 2 Watts. A and B Field voltages of (16,8) and (20,12) kV were used. Strong features were observed at about 200, 250 and 320 MHz. Further checks including attempts with phase-locked radiation sources failed to locate the precise frequencies of the two lower

Table 5.1 : R.F. and Microwave Transitions of NeNO

R.F.		Microwave	
Label	Frequency/MHz	Label	Frequency/MHz
a	318.7555	M4	4302.9517
b	342.5003	M5	4358.9530
c	357.0628	M6	4396.0486
d	428.4093	M7*	5549.0
e	466.7152	M1	9243.9252
f	659.3018	M2	9305.1281
g	681.5112	M3	10517.8338
h	729.9982		
i	752.2094		
j	790.9198		
k	808.5328		
s	1012.5171		
t	1014.5757		
l	1019.1657		
m	1027.4986		
u	1048.4593		
v	1049.7983		
w	1051.8493		
n*	1174.40		
o	1242.7305		
p	1244.0670		
---	---		
x	1246.1256		
q	1274.4649		
r	1276.5142		

N.B. "*" Denotes a transition not measured with a phase-locked oscillator.

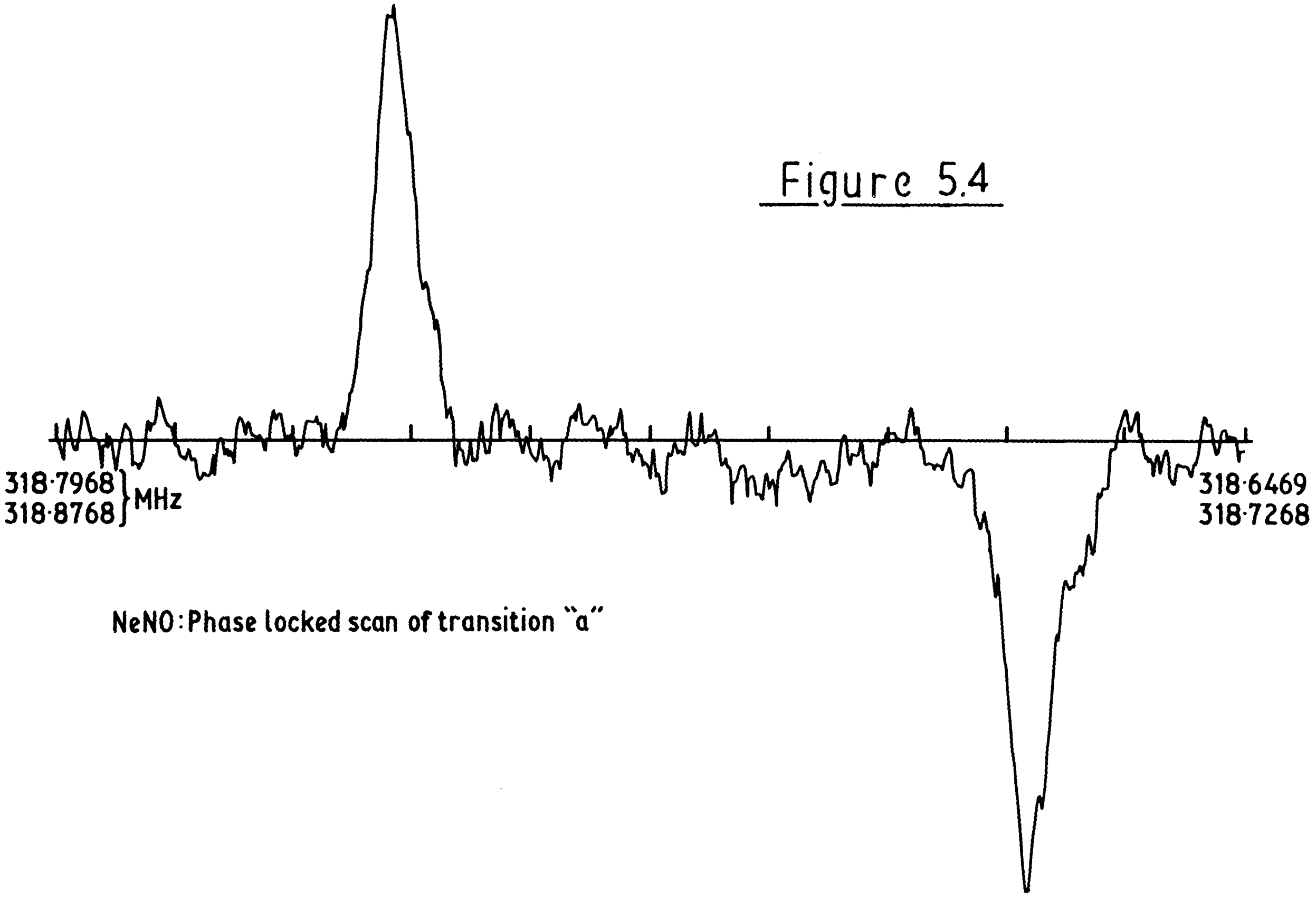
---

features. Subsequent tests showed them to be "beam resonances". The third structure was a genuine molecular transition denoted "a" in Table 5.1 .

Prompted by the discovery of "a" much more careful searching was carried out between 350 and 540 MHz using 2 MHz of noise broadening (since no amplification was available at this stage). Four more molecular resonances were located and their line-centres measured by phase-locking. It is of some interest that the linewidths (~7 kHz) and shapes achieved for this group of five transitions showed a considerable improvement compared with those measured for ArNO. A plausible explanation is that an improved signal to noise ratio resulted from the lower rotational partition function for NeNO. This then permitted a better assessment of the optimum power attenuation for the phase-lock measurement. An example of such a phase-locked line is given in Figure 5.4; it may be compared with Figure 4.9 .

Regrettably it was not until the final stages of the experimental work that the ENI 603L R.F. amplifier mentioned in the previous chapter became available. This provided powers of greater than 2 Watts at frequencies up to 1 GHz.The whole range of this amplifier was swept using multiple scans of 200 MHz sections with a 30 second time constant and 10 MHz of broadening. Although the spectroscopy was severely hampered by the presence of a number of "beam resonances" several new lines were observed. The possibility that other molecular resonances were masked by these artifacts, induced by the high power densities in the spectrometer, should not be overlooked, however. The ENI device also delivered slightly amplified radiation at between 1000 MHz and 1050 MHz. This led to the discovery of still more transitions also contained in Table 5.1 . A section of the noise broadened

Figure 5.4



NeNO: Phase locked scan of transition "a"

spectrum is reproduced in Figure 5.5 showing a triplet of lines.

A common difference analysis was now carried out on all the exact frequencies of the R.F. lines that had been measured so far; that is all those that lie above the horizontal line of Table 5.1 . The following difference relationships were found :

t-s = w-v = 2.0548 MHz ; Δ = 7.6 kHz

w-t = v-s = 37.2774 MHz ; Δ = 7.6 kHz

v-u = p-o = 1.3383 MHz ; Δ = 3.5 kHz

p-v = o-u = 194.2705 MHz ; Δ = 3.5 kHz

g-f = i-h = 22.2103 MHz ; Δ = 1.8 kHz

h-f = i-g = 70.6973 MHz ; Δ = 1.8 KHZ

e-d = b-a = 38.3066 MHz ; Δ = 1.4 kHz

e-b = d-a = 109.6531 MHz ; Δ = 1.4 kHz

The lower four relationships indicate two independent systems each of which comprises four connected energy levels. However, the occurrence of transition "v" in all of the other four cases implies a more involved pattern for these seven transitions. In fact eight plausible arrangements can be constructed from the common difference information. Each of these eight patterns predicts the possibility of transitions at two other frequencies which should be observable if they do not contravene the selection rules. The eight possible patterns and their predictions are shown in Figure 5.6 . As stated previously it should be recalled that the inverses of these patterns are also compatible with the data.

An experiment was now performed to determine which pattern or patterns described the energy levels of NeNO. A beam was set up with focussing fields of (A,B) = (25,15) kV. Using a phase-

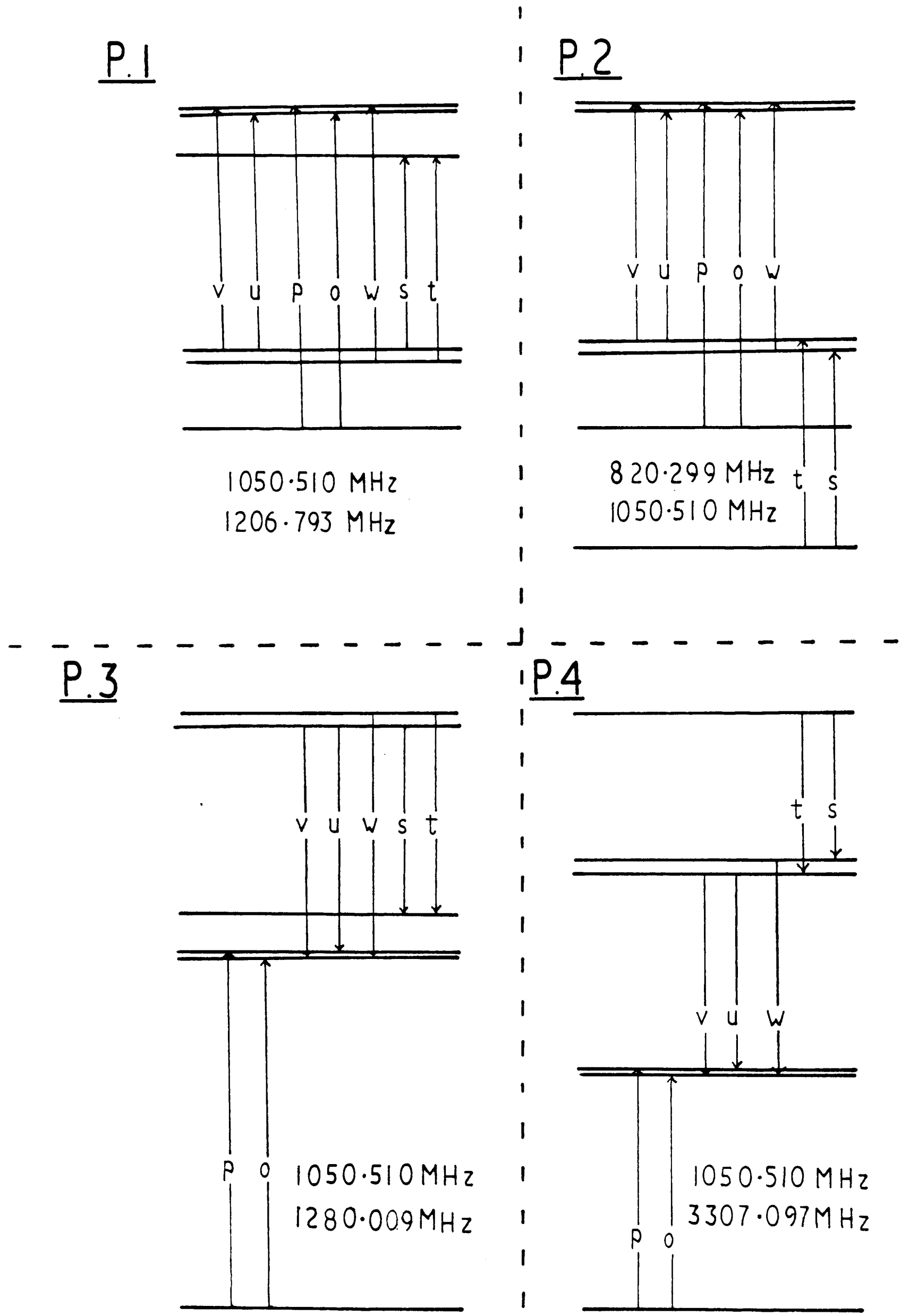
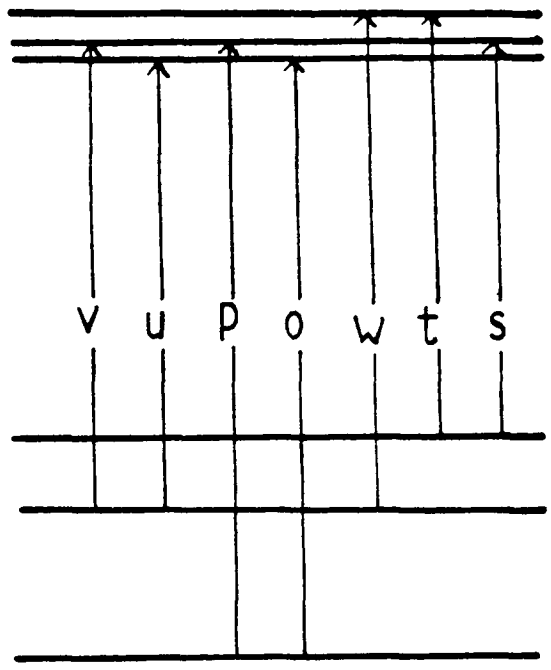


Figure 5.6 RF Patterns

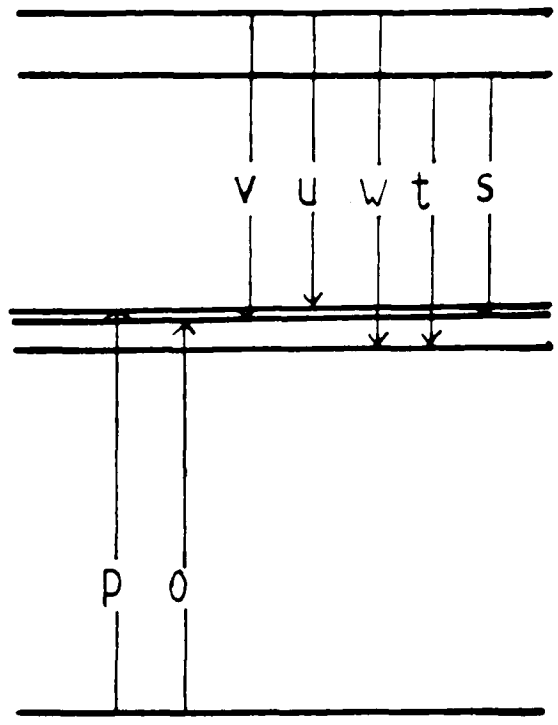
P.5

1011·178 MHz
1246·126 MHz

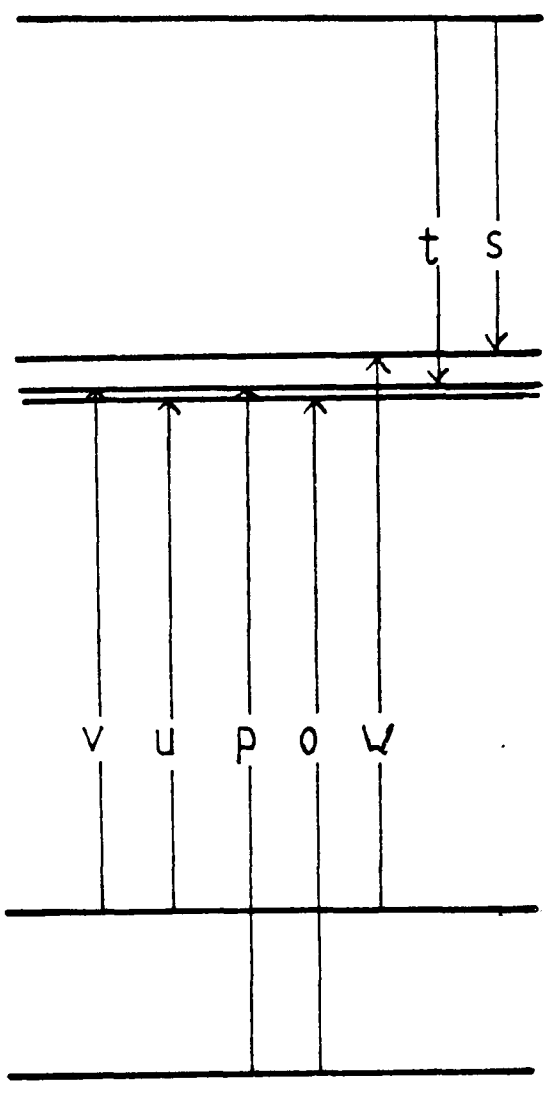


P.7

1011·178 MHz
1240·672 MHz

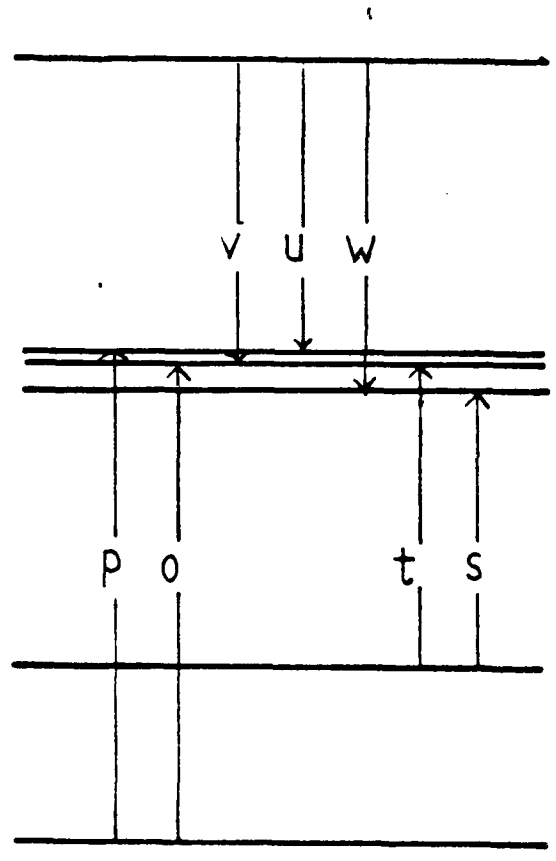


P.6



1015·915 MHz
1246·126 MHz

P.8



1015·915 MHz
1240·672 MHz

Figure 5.6 RF Patterns

locked source with no attenuation and a phase separation of 100 kHz , each of the possible new transition frequencies was irradiated in turn for some 180 seconds. A 30 second integration time was used and, to allow for errors in the measurements, frequencies displaced by 50 kHz either way from those of Figure 5.6 were also tested. Only radiation of 1246.1256 MHz produced a signal indicating that either Pattern 5 or 6 was the correct one. To try and distinguish the two, the experiment was repeated very carefully for the other two predicted frequencies of these patterns. Neither gave any indication of a resonance. Consideration of the magnitude of the hyperfine and quenching splittings led to the conclusion that Pattern 6 would require unreasonable molecular parameters for NeNO. Pattern 5 was therefore adopted.

Final, careful searching for further transitions around "o" and "p" revealed two more lines "q" and "r" which fitted in with, and hence confirmed, Pattern 5. Their frequencies together with that of the predicted transition "x" are shown below the horizontal line of Table 5.1 . Irradiation with phase-locked radiation of frequencies at 1273.1295 MHz, and 5 or 10 kHz displaced from this value, yielded no signal.

5.3 c) The Microwave Spectrum

For the reasons given in 5.3 a) it was considered impractical to search large regions of the microwave spectrum. Estimates of the rotational constants and ε_2 were therefore used to try to predict which transitions might be observed within the range of the two available T.W.T. amplifiers. For NeNO the μ_a dipole moment is expected to be small and so transitions

predominantly allowed by the b-moment were considered first. The two most feasible sets of transitions to search for were determined to be (in increasing frequency) J=3/2,e(- and +) to J=5/2,e(+ and -) and J=5/2,o(+ and -) to J=7/2,o(- and +).

From the estimates of the parameters it was deduced that the latter transitions should be located in the region around 10 GHz. The microwave spectrum between 9.0 GHz and 11.5 GHz was therefore scanned using the Hughes T.W.T. amplifier to provide about 1 Watt of power, although trouble was encountered with the power level at the highest frequencies. 10 MHz of noise broadening, a 30 second time constant and focussing fields of (A,B) = (24,15) kV were employed. Two weak transitions were located at about 9.25 and 9.30 GHz. These were eventually phase-locked with the measurements requiring 60 seconds of integration for even a poor signal to noise ratio. A further stronger line was found at around 10.5 GHz which, in contrast to the other two transitions, required substantial attenuation of the power of the phase-locked source for a good measurement. Extra searching, some under phase-locked conditions, was attempted to try and locate further hyperfine components associated with these transitions. Even though the power per unit bandwidth was increased by a factor of ten, no further lines were found.

The searches for the J=3/2,e to J=5/2,e lines required the Keltec T.W.T. amplifier and were therefore performed last. Fine structure calculations indicated that these two manifolds should lie between 4.0 and 6.5 GHz. This region was scanned using the same conditions and three transitions were located and measured by phase-locking at around 4.3 GHz. A section of the noise broadened spectrum is shown in Figure 5.7 .Further searching revealed no additional hyperfine information.

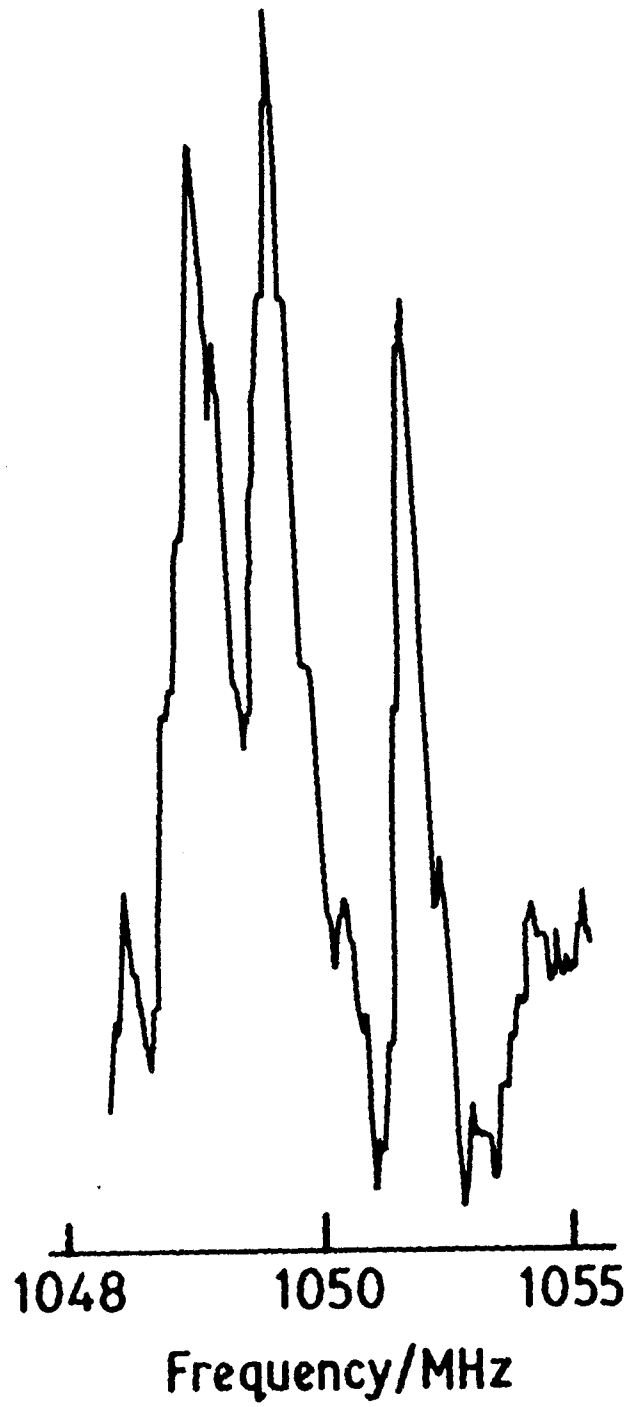


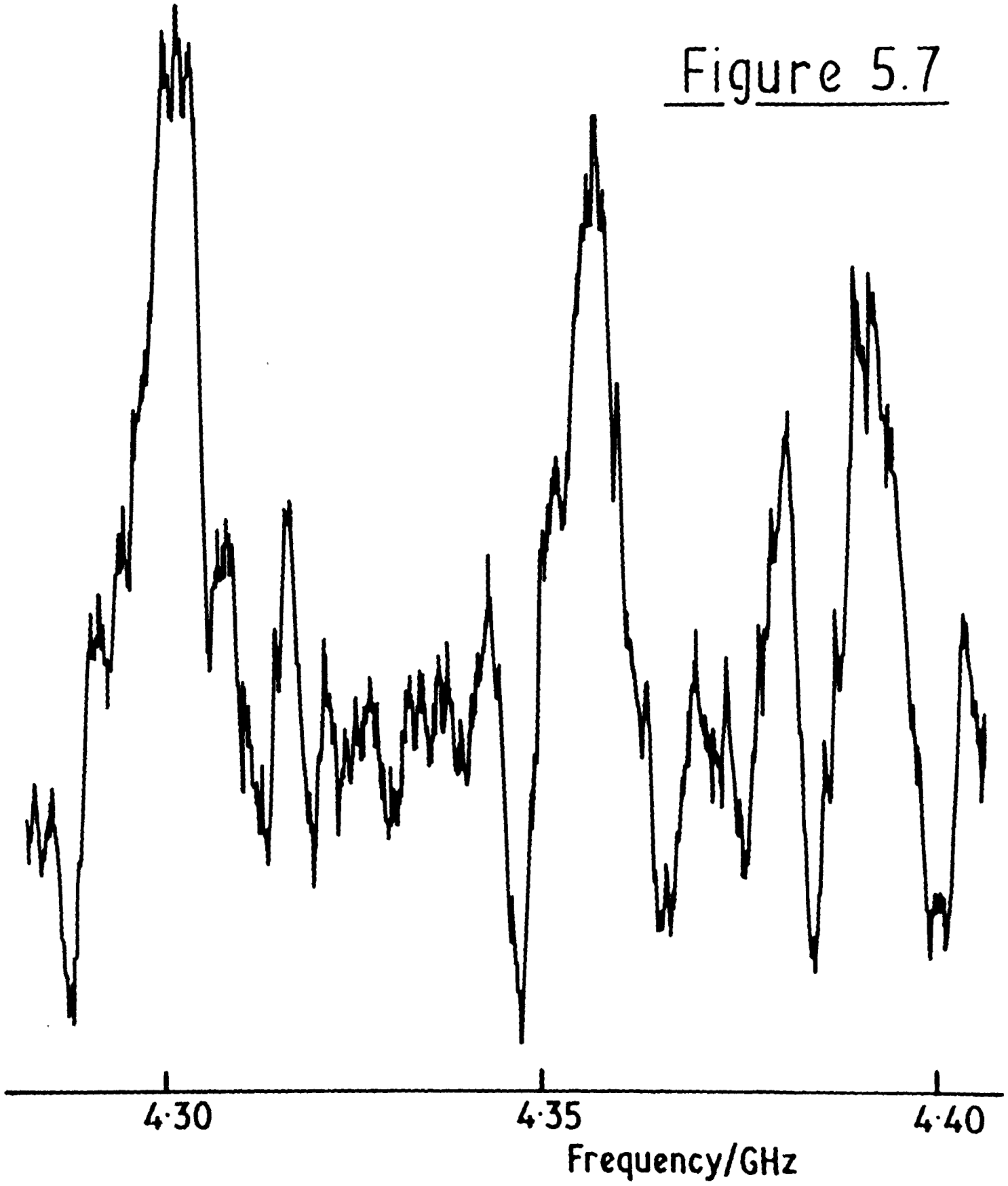
Figure 5.5

NeNO :

Left : Transitions u, v and w
(Noise broadened)

Right : Transitions M4,5,6
(Noise broadened)

Figure 5.7



Proceeding on the assumption (later found to be erroneous) that these lines at 4.3 GHz were components of the "inner", that is, J=3/2,e(-) to J=5/2,e(+) transition, the region from 5.2 to 5.8 GHz was scanned again more slowly. The power output of the T.W.T. amplifier was increased and the scan rate reduced to four time constants per linewidth of 10 MHz. A very weak transition was found at about 5.5 GHz with no accompanying hyperfine structure. A fairly good estimate of the centre frequency of this transition was obtained using 0.5 MHz of noise broadening. Many attempts to observe the line with a phase-locked source proved totally unsuccessful, however. The signal to noise ratio under noise broadened conditions was never better than 2 to 1 for a 30 second time constant. This was at least partly responsible for the failure to gain a precise measurement. Consideration of the frequencies of the other microwave transitions indicated that this line was unlikely to yield a further common difference relationship and so no further attempts were made to refine the measurement.

The frequencies of the seven microwave transitions are given in Table 5.1 .

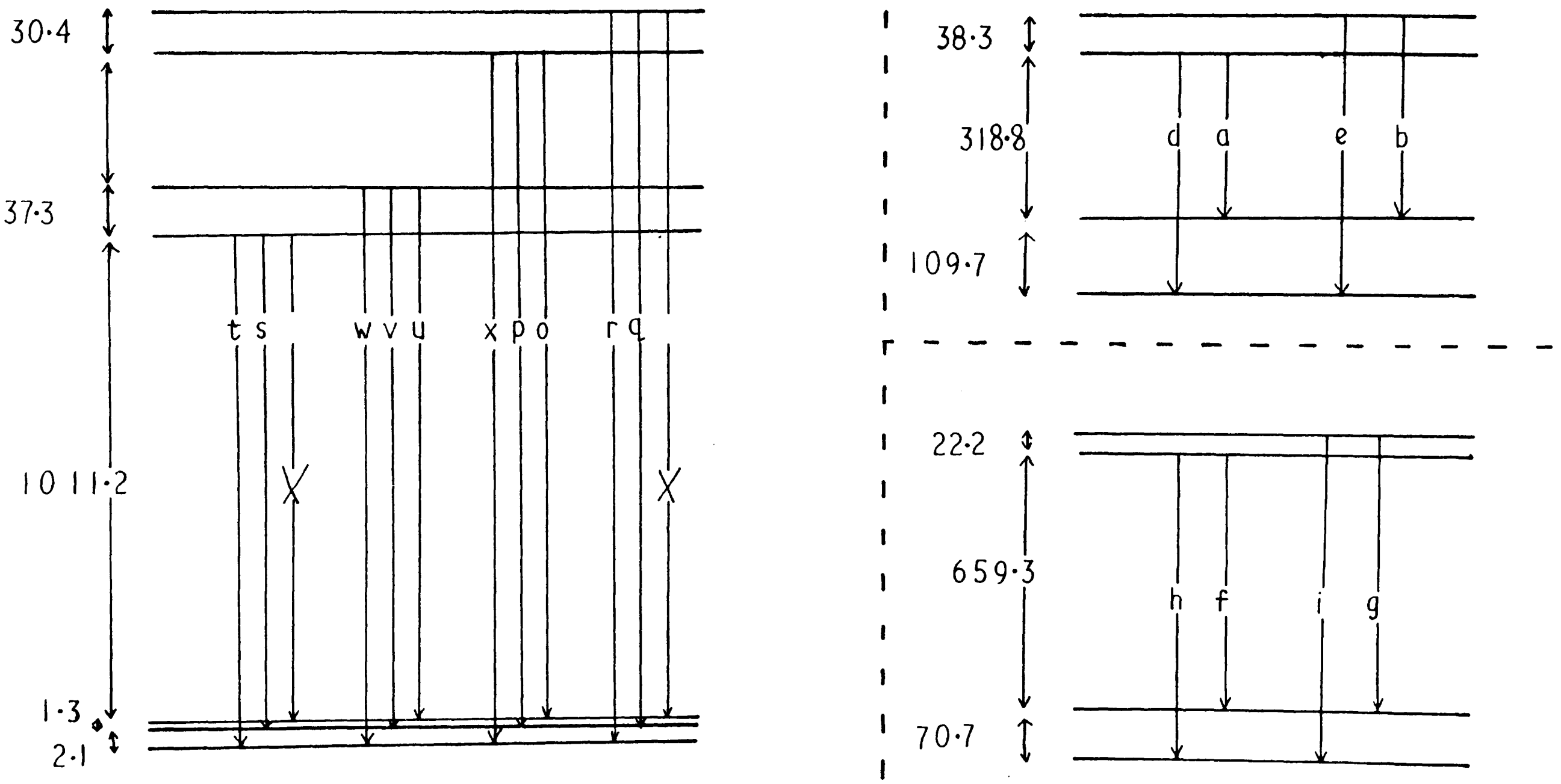


Figure 5.8 NeNO Transitions

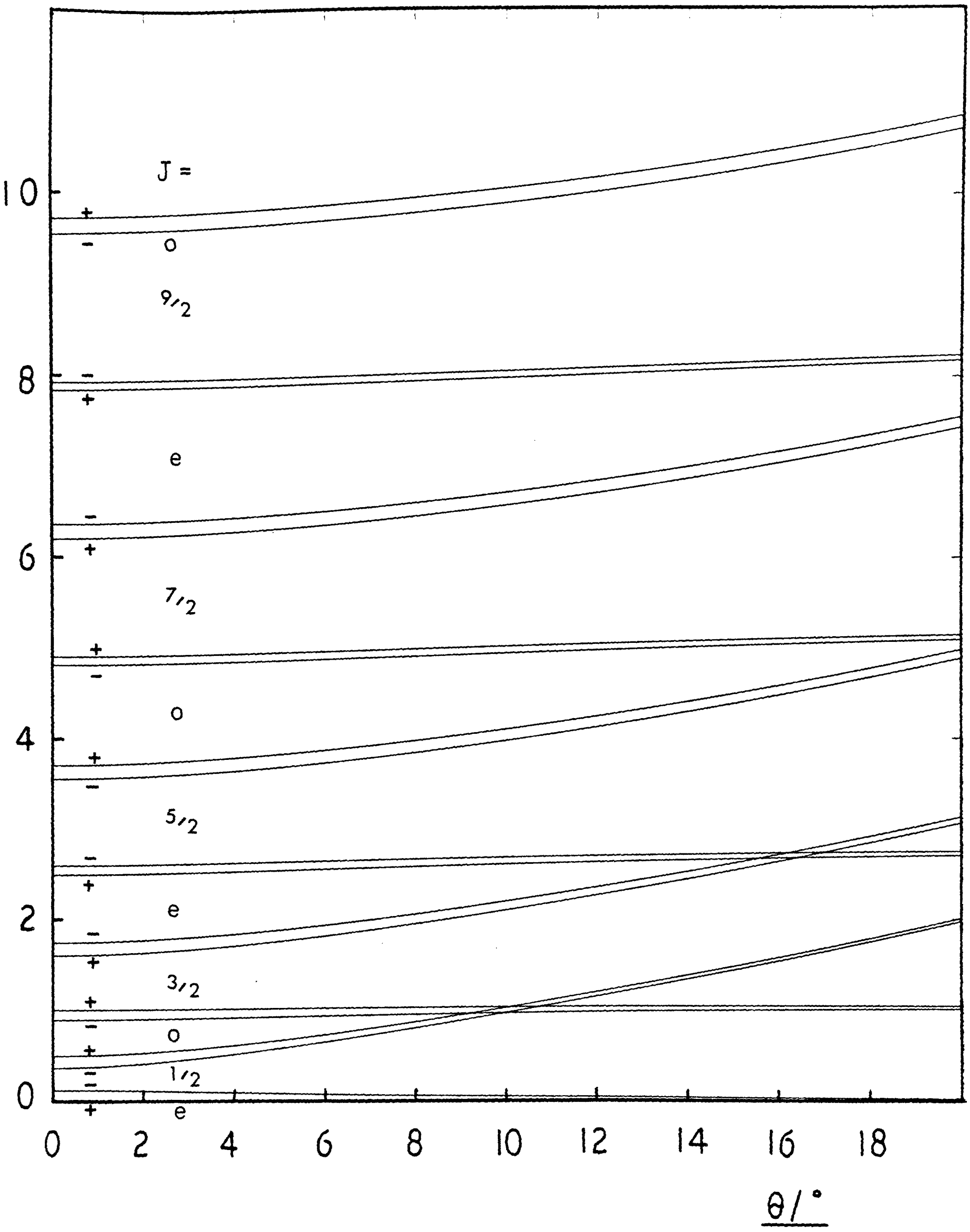


Figure 5.9 : NeNO Energy Levels as F(θ)

$\epsilon_2 \sim 3\ cm^{-1}$

5.4 The Assignment and Analysis of the Recorded Spectrum

5.4 a) Introduction

Although a total of some 31 transitions had been measured in the NeNO spectrum, the resulting picture was very incomplete. Two problems made the initial assignment of these transitions rather speculative. The first was the lack of hyperfine information; only for the radiofrequency transitions was any sort of energy level pattern forthcoming from common differences. The second disadvantage, the lack of a good prediction of the structure, arose because of the sparse coverage in the literature of the anisotropic potential for this system. Nevertheless from the available common difference patterns, summarised in Figure 5.8 , a number of general conclusions may be deduced.

The necessity of involving seven energy levels in the major pattern of Figure 5.8 means that, as found for the analysis of ArNO, a crossing of different fine structure states must be invoked. Considerations of the selection rules further dictate that the two pairs of levels of opposite parity must have adjacent J quantum numbers and be interleaved. That is, a "near crossing" of the fine structure states would not account for the observed transitions. The variation in the fine structure energies up to J=9/2 as a function of the angle θ is shown in Figure 5.9 . For this plot the van der Waals bond length was compatible with the results of Thuis (section 5.2) and the diagonal quenching parameter, ε_2 , was set equal to 90 GHz by analogy with ArNO. Non-adiabatic and hyperfine interactions were suppressed in this calculation. Inspection of the plot reveals plausible fine structure crossings at angles close to 10 degrees

and 16 degrees. Other crossings are possible at greater angles but are less likely to be responsible for the spectrum since they correspond to levels at higher energy or non adjacent J quantum numbers.

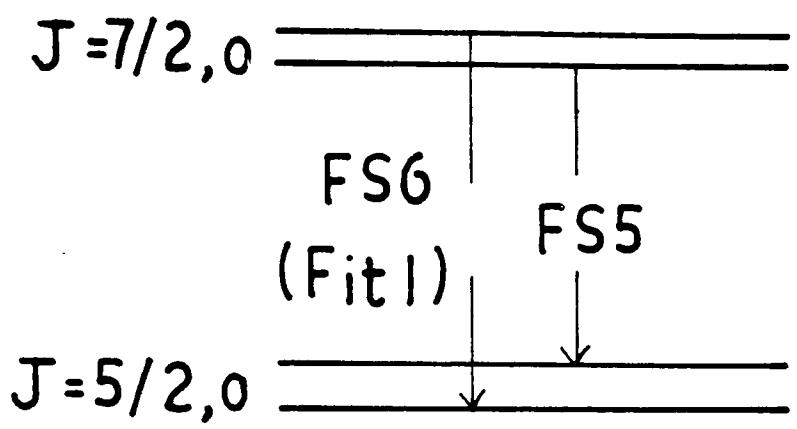
Another significant feature of Figure 5.8 is the spread in the splittings caused by the quenching and non-adiabatic interactions. For ArNO the $\Delta J=0$ transitions ranged in frequency from about 600 MHz to 1100 MHz. In the neon complex, however, equivalent quenching splittings of the order of 300 to 1050 MHz (or possibly even 1270 MHz) are apparent. The wider variation in the frequencies of the observed R.F. transitions proved a crucial feature in determining the fine structure assignment.

On the basis of the foregoing remarks it was decided to deduce a partial assignment by attempting fits of the fine structure transitions at the two angles of crossing in Figure 5.9 .

5.4 b) The Fine Structure

Three fine structure assignments were attempted for structural angles close to 10 degrees and these are indicated in Figure 5.10 together with the approximate frequencies used in the fitting. The three differ only in the attribution of the initial and final states for M4. Fit 1 corresponds to the predicted spectrum on which the microwave searching was based. All the transitions in this assignment are predominantly allowed by the μ_b component of the dipole moment in contrast to Fits 2 and 3 where M4 involves the μ_a component. The choice made for the two R.F. intervals is based on the most likely hyperfine pattern for a positive value of ε_2 . This point is discussed in the next

NeNO, $\theta \sim 10^{\circ}$



	Freq./GHz
FS1	1·030
FS2	1·260
FS3	4·350
FS4	5·550
FS5	9·275
FS6	10·520

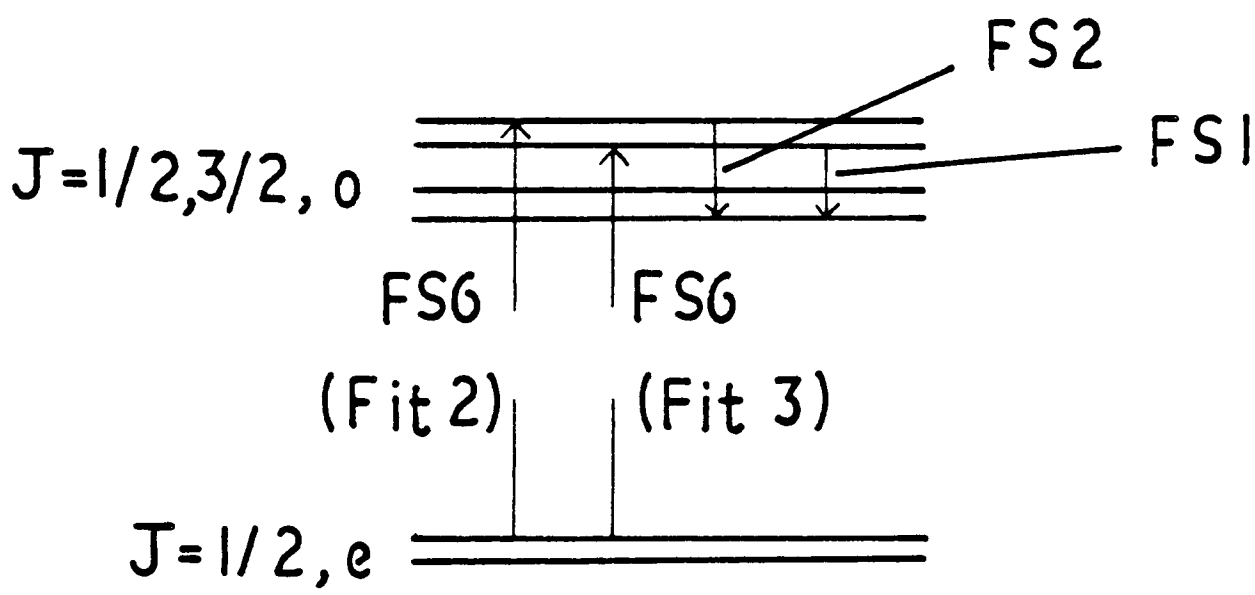


Figure 5.10

section. In these fits r, t and ε_2 were floated and the lambda doubling was held constant at the scaled values predicted from the NO fit of Chapter 3.6 . ε_2 was chosen to be positive.

Of the three, Fit 1 yielded the smallest R.M.S. error although this was still far too high at 240 MHz. An R.M.S. error of about 50 MHz might have been expected because of the lack of a proper hyperfine assignment. This fit is shown in Table 5.2 . Fits 2 and 3 yielded corresponding R.M.S. errors of 310 and 260 MHz respectively. The floated parameters of Fit 1 reached the following final values :

$$r = 3.19 \text{ A} \qquad (5.4.1)$$

$$t = 11.10^{\circ}$$

$$\varepsilon_2 = 56240.0 \text{ MHz}$$

Apart from the large R.M.S. error in Fit 1 there are other reasons which preclude it from being a realistic assignment. The value of the van der Waals bond length at 3.19 Angstroms is very considerably shorter than had been predicted in Equations (5.2.2) and (5.2.4). Also it can be seen from the distribution of the "Observed Minus Calculated" frequencies that there is a total failure to model the observed R.F transition frequencies. This is because the pairs FS3, FS4 and FS5, FS6 require quenching splittings of about 600 MHz whereas FS1 and FS2 exhibit a quenching interaction of about 1030 MHz. Figure 5.9 indicates that considerable variations in the quenching interaction with J are only obtained at larger angles. Floating the parameter for the centrifugal distortion of the angle, $\Delta\theta$, failed to appreciably improve Fit 1 . The R.M.S. error dropped by only 10 MHz with a further shrinkage in the fitted value of the bond length.

For the reasons just mentioned and in particular the failure

Table 5.2 : NeNO Fine Structure Fits.

Transition	Lower State	Upper State	Observed/MHz	Obs.-Calc./MHz
FS1	J=3/2,o(-)	J=3/2,o(+)	1030.0	525.5
FS2	J=3/2,o(-)	J=1/2,o(+)	1260.0	91.4
FS3	J=3/2,e(-)	J=5/2,e(+)	4350.0	130.8
FS4	J=3/2,e(+)	J=5/2,e(-)	5550.0	32.5
FS5	J=5/2,o(+)	J=7/2,o(-)	9275.0	101.6
FS6	J=5/2,o(-)	J=7/2,o(+)	10520.0	-183.0

R.M.S. Error = 240.3 MHz

FS1	J=3/2,e(+)	J=3/2,e(-)	1030.0	-25.7
FS2	J=3/2,e(+)	J=5/2,e(-)	1260.0	51.8
FS3	J=3/2,o(+)	J=1/2,o(-)	4350.0	42.9
FS4	J=3/2,o(-)	J=1/2,o(+)	5550.0	8.1
FS5	J=1/2,e(-)	J=3/2,o(+)	9275.0	-67.6
FS6	J=1/2,o(+)	J=3/2,e(-)	10520.0	35.0

R.M.S. Error = 42.9 MHz

NeNO, θ ~ 14°

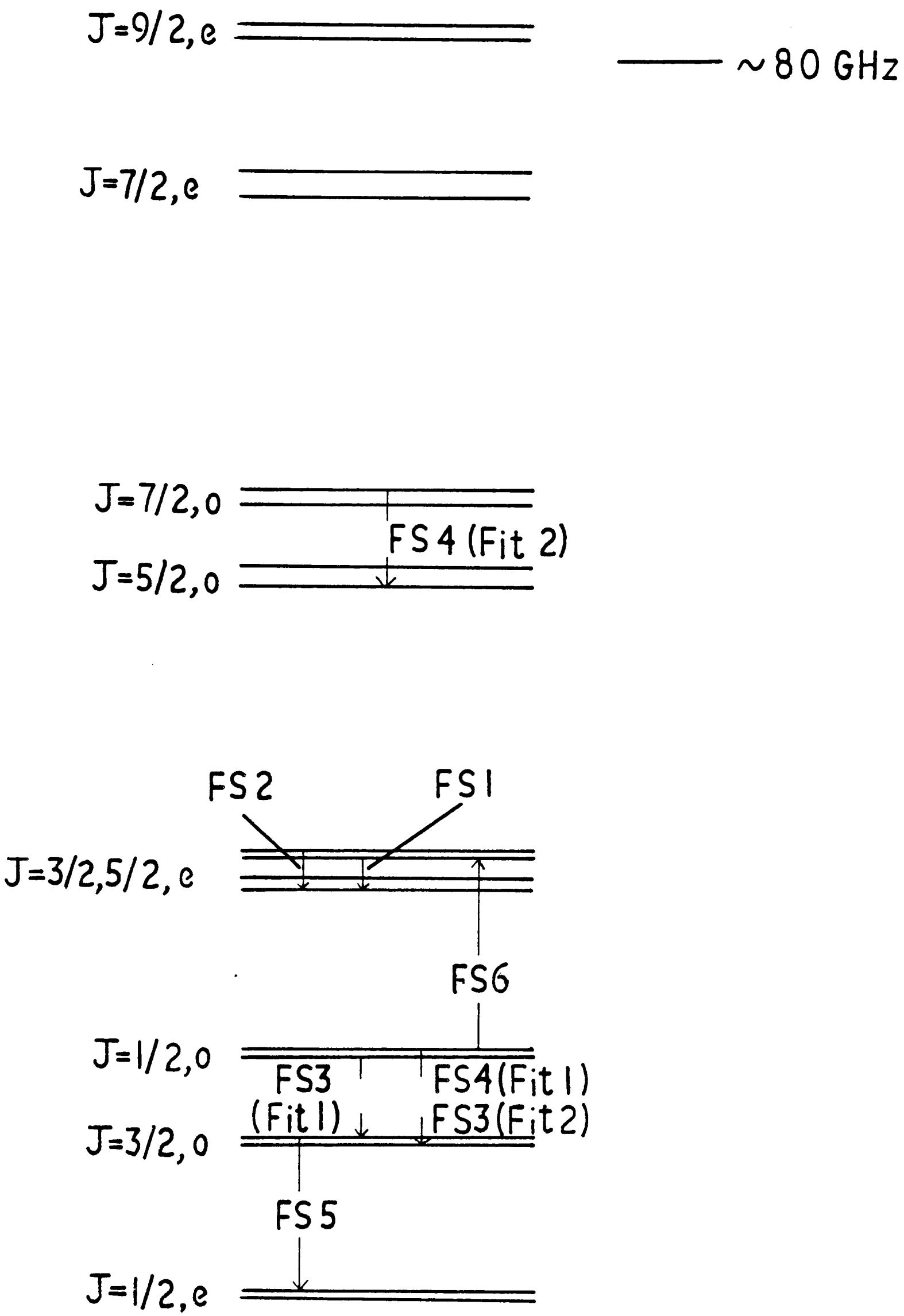


Figure 5.11

to model the spread in the quenching splittings, attention was then focussed on the crossing of J=3/2 and 5/2 near Θ=14 degrees. Figure 5.11 shows the best assignment of the fine structure transitions as denoted by Fit 1. The alternative assignment of FS5 and FS6 to the "inner" and "outer" components of J=7/2,e to J=9/2,e was disregarded since these states are comparatively high in energy (~80 GHz) and would only be sparsely populated after the supersonic expansion. Fit 1 gave a much improved R.M.S. error of only 42 MHz which is well within the limits expected by neglect of the hyperfine structure. The results are also given in Table 5.2 with the final values of the floated parameters being :

$$r = 3.53 \text{ A} \qquad (5.4.2)$$

$$t = 14.00^{\circ}$$

$$\varepsilon_2 = 122690.0 \text{ MHz}$$

Once again the positive value of the quenching parameter was arbitrarily chosen by analogy with ArNO. Its sign can only really be determined from its effect on the hyperfine structure which is discussed in the next section.

Further weight was added to this assignment at 14 degrees by the observation that the two hitherto unassigned R.F. patterns of Figure 5.8 could be associated with the following states :

(a,b,d,e) : J=1/2,e(+ to -)

(f,g,h,i) : J=1/2,o(+ to -)

or J=3/2,o(+ to -)

In particular, only the former assignment could account for the very large hyperfine splittings observed for the (a,b,d,e) set. Unfortunately, careful consideration of such a scheme, and of the number of observed hyperfine components for FS3 and FS5,

indicates that it is not totally compatible with the number of common differences observed. More of the latter would be expected if every aspect of the above assignments were correct. As an alternative scheme the possibility that FS3 and FS4 were from different J-manifolds was investigated with the assignment denoted Fit 2 . This fit was much less satisfactory with R.M.S. errors of 160 MHz even after the centrifugal distortion parameter, $\Delta\theta$, was allowed to float.

In conclusion, Fit 1 at the 14 degree crossing accounts well for the fine structure energy levels and in particular for the two R.F. sets of transitions. The predicted energy levels are compatible with the additional assignments but these would require verification by further searching or double resonance experiments. Thus good estimates of the van der Waals bond length and average angle, θ, may be taken from (5.4.2) . Although an estimate of the magnitude of ε_2 is likewise gained, the sign of this quantity must be derived from the hyperfine structure.

5.4 c) The Hyperfine Structure and the Sign of ε_2

Although extra hyperfine components were observed accompanying the transitions at 4.3 GHz and 9.3 GHz, there was a general lack of such structure on the microwave transitions. Hence no attempt was made to assign F quantum numbers to these lines. Instead some effort was concentrated towards trying to fit the hyperfine structure associated with the pattern of ten transitions of Figure 5.8 . This pattern involves seven energy levels deriving from only three fine structure states. Even with no transitions assigned to this "missing" state, quite a lot may be deduced provided that it is assumed that the hyperfine

structure is qualitatively similar to that predicted by the NO parameters. This assumption certainly proved to be justified for ArNO, and so is expected to be valid for the neon complex particularly as the predicted magnitude of ε_2 is only slightly larger.

If the ordering of hyperfine levels is the same as that predicted by the NO parameters, only certain assignments for the observed energy level patterns are compatible with the parity and ΔF selection rules. As an extra test of the fine structure assignment just given, all the possible hyperfine patterns for positive and negative values of ε_2 were considered at the two crossing points. In fact for three of these four cases only one assignment was possible without altering the ordering of the multiplets. For the fourth case, the assignment that involved the least perturbation of the hyperfine orderings predicted from NO, was taken. These four possibilities are shown in Figure 5.12 .

An attempt was made to fit both the hyperfine intervals and frequencies of the ten transitions for each of these cases. Due to the comparatively important hyperfine effects off-diagonal in J, the latter proved more valuable. In each case the four parameters floated were a, d, t and ε_2 with a van der Waals bond length of 3.53 Angstroms and all other parameters set to their NO values.

For the J=1/2, 3/2 crossing with ε_2 positive (Case 1) an R.M.S. error of 7.2 MHz resulted. To fit this assignment would require inversion of the J=3/2,o(-) multiplet which proved impossible for modest changes in the hyperfine parameters. Since ε_2 and t should fix the relative separations of the three fine structure states, the remaining discrepancy may be attributed to a failure to fit the hyperfine part properly. The values for the

parameters arising from this fit (7.2 MHz R.M.S. error) were :

$$t = 9.61^{\circ} \quad (\theta = 10.35^{\circ}) \qquad (5.4.3)$$

$$\varepsilon_2 = 161367.0 \text{ MHz}$$

$$a = 88.06 \text{ MHz}$$

$$d = 108.87 \text{ MHz}$$

Cases 2 and 3 of Figure 5.12 involved fits with a negative value for the quenching parameter. For the crossing near 10 degrees an R.M.S. error of 3.7 MHz was obtained with 6.0 MHz resulting for the other. However, the final values of the floated parameters, given below, indicate much larger magnitudes for ε_2 being in excess of 200 GHz. In both these cases no transitions would be possible at the low frequencies of the other R.F. patterns of Figure 5.8 . Both of these possibilities must therefore be rejected.

$t = 9.40^{\circ}$ $(\theta = 10.12^{\circ})$	$t = 14.67^{\circ}$ $(\theta = 15.66^{\circ})$
$\varepsilon_2 = -212855.2$ MHz	$\varepsilon_2 = -235320.5$ MHz
$a = 79.07$ MHz	$a = 71.51$ MHz
$d = 62.24$ MHz	$d = 64.86$ MHz

(5.4.4)

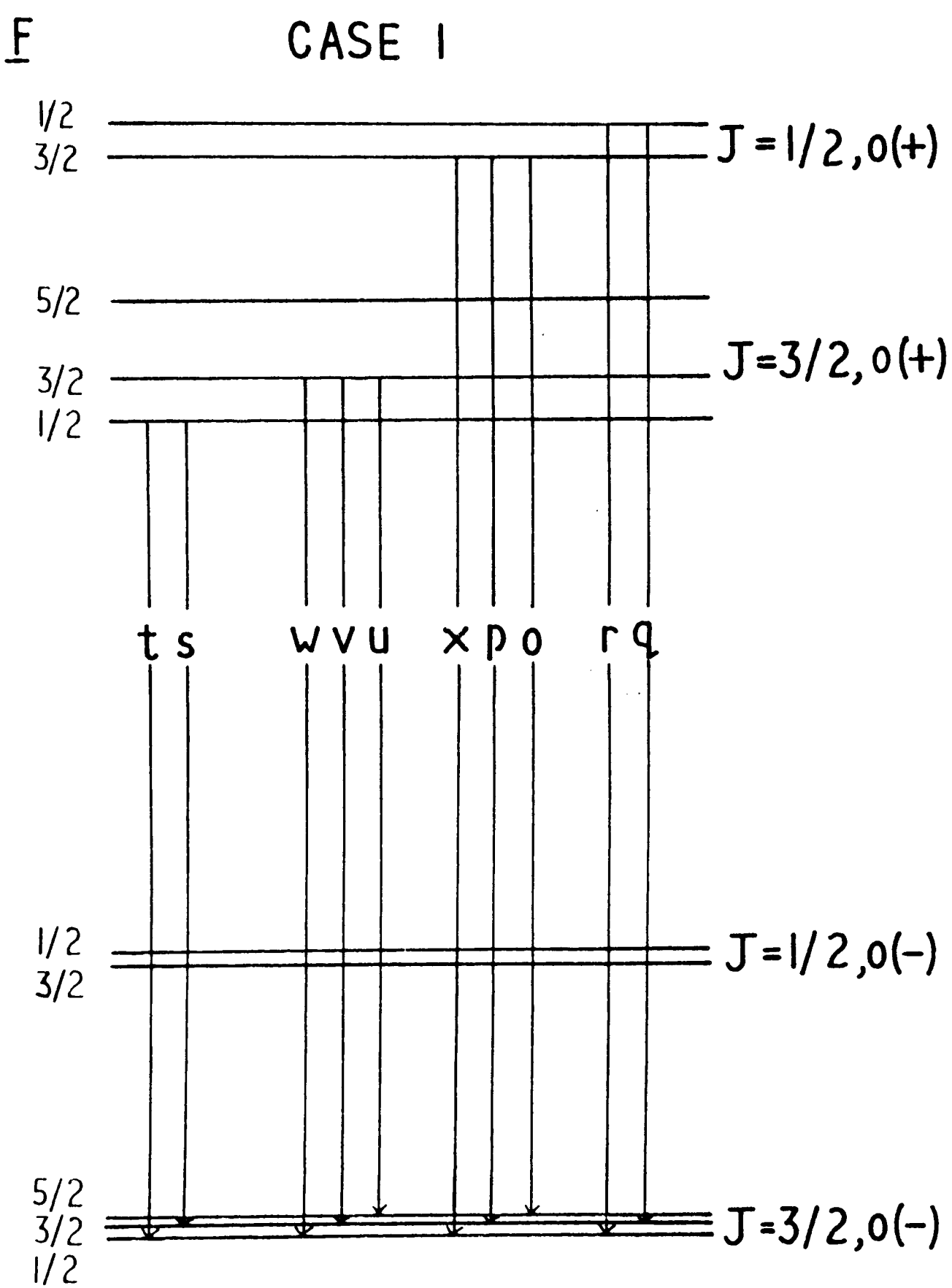
Case 4 yielded a much better fit with an R.M.S. error of only 1.5 MHz. This fit is shown in Table 5.3 . For a positive value of ε_2 at this crossing, the J=3/2 state must lie lowest. The parameters determined by the fit are reasonable and it can be seen that ε_2 is only a little increased from the value given by the best fit of the fine structure.

$$t = 14.03^{\circ} \quad (\theta = 14.98^{\circ}) \qquad (5.4.5)$$

$$\varepsilon_2 = 131824.5 \text{ MHz}$$

$$a = 124.57 \text{ MHz}$$

$$d = 149.31 \text{ MHz}$$


F
CASE 1
1/2
3/2
J = 1/2,0(+)
5/2
J=3/2,0(+)
3/2
1/2
t s
w v u
x p o
r q
1/2
3/2
J=1/2,0(-)
5/2
3/2
1/2
J=3/2,0(-)

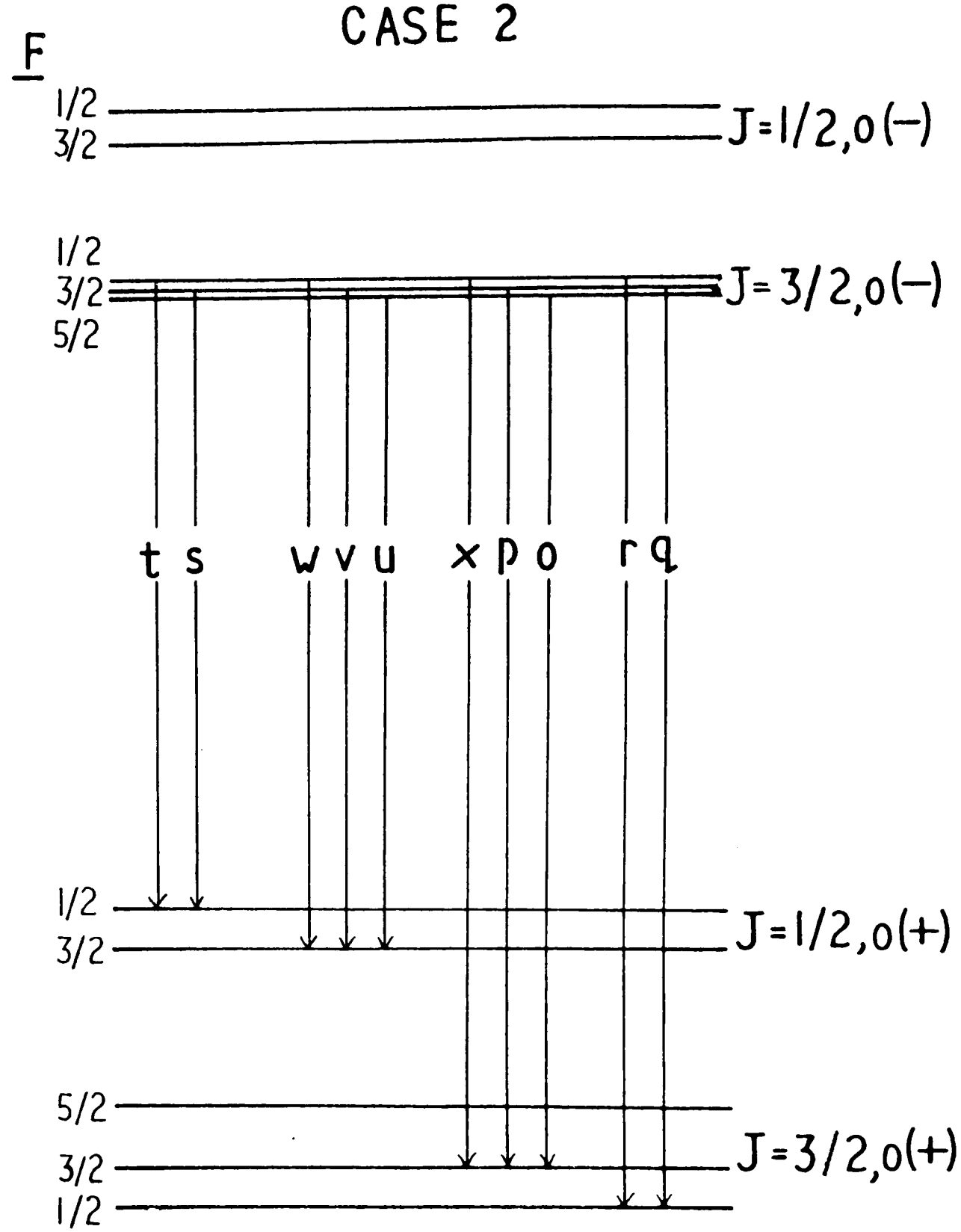
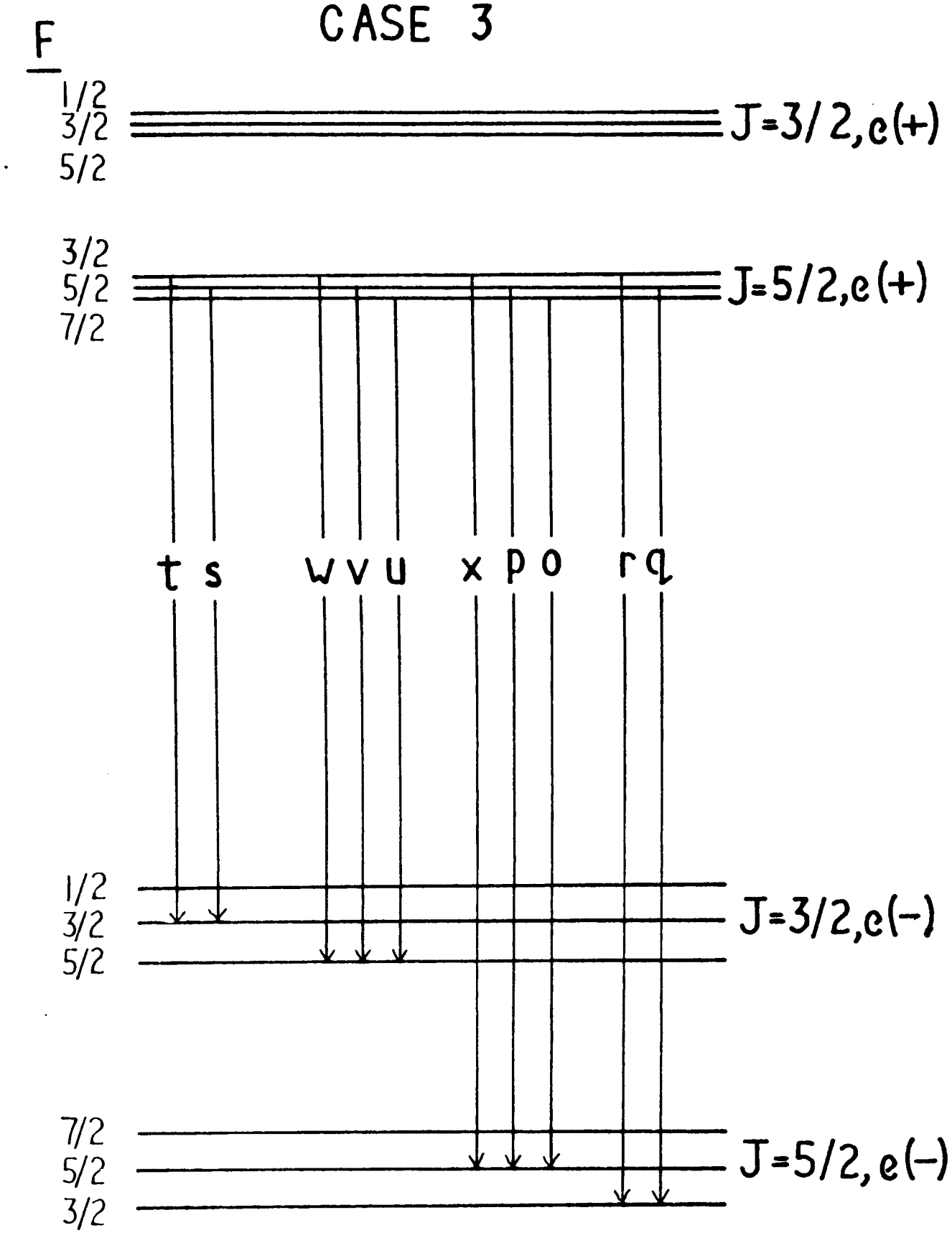

F
CASE 2
1/2
3/2
J=1/2,0(-)
1/2
3/2
5/2
J=3/2,0(-)
t s
w v u
x p o
r q
1/2
3/2
J=1/2,0(+)
5/2
3/2
1/2
J=3/2,0(+)

Figure 5.12


CASE 3
F
1/2
3/2
5/2
J=3/2,e(+)
3/2
5/2
7/2
J=5/2,e(+)
t s w v u x p o r q
1/2
3/2
5/2
J=3/2,e(-)
7/2
5/2
3/2
J=5/2,e(-)

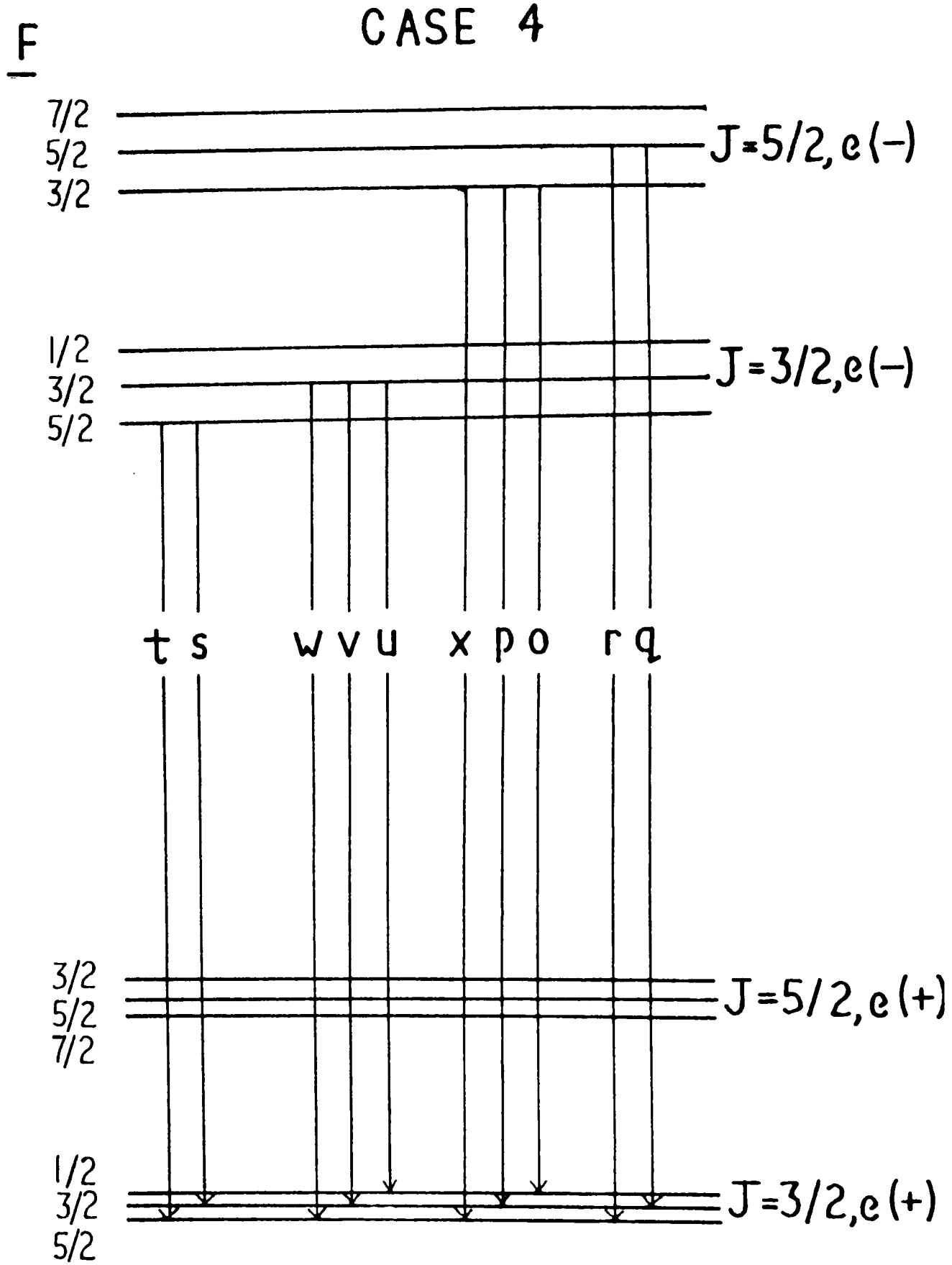

CASE 4
F
7/2
5/2
3/2
J=5/2,e(-)
1/2
3/2
5/2
J=3/2,e(-)
t s w v u x p o r q
3/2
5/2
7/2
J=5/2,e(+)
1/2
3/2
5/2
J=3/2,e(+)

Figure 5.12

Table 5.3 : NeNO fit of R.F. Transitions

Transition	Lower State	F"	Upper State	F'	Observed (MHz)	Obs.-Calc. (MHz)
s	J=3/2,e(+)	3/2	J=3/2,e(-)	5/2	1012.5171	-2.0750
t		5/2		5/2	1014.5757	-1.6910
u		1/2		3/2	1048.4593	1.2918
v		3/2		3/2	1049.7983	1.0133
w		5/2		3/2	1051.8493	1.3897
o	J=3/2,e(+)	1/2	J=5/2,e(-)	3/2	1242.7305	1.2842
p		3/2		3/2	1244.0670	1.0031
x		5/2		3/2	1246.1256	1.3871
q		3/2		5/2	1274.4649	-2.0204
r		5/2		5/2	1276.5142	-1.6457

R.M.S. Error = 1.522 MHz

Attempts to refine this fit further by floating, γ ,the angle representing the projection of the hyperfine were unsuccessful due to its correlation with the parameters a and d.

Thus Case 4 is the only scheme which is compatible with the observed data. This fit confirms that the R.F. transitions arise from the J=3/2,5/2 crossing and that the quenching parameter has the same sign as that determined for ArNO.

5.5 Discussion and Conclusions

The difficulties encountered in obtaining the rotational spectrum of NeNO rendered a full analysis very difficult. The absence of common differences to the microwave rotational transitions meant that the details of the final assignment could not be made with certainty. However, the evidence from fine and hyperfine structure very firmly favours the assignment with a structure angle close to 14 degrees and with a positive value for the quenching parameter.

The bond length, r, and bond angle, t, of the complex were determined to be 3.53 Å and 14.00 degrees. These molecular constants correspond to A, B and C rotational constants of 54231.4 , 3364.2 and 3167.7 MHz respectively. The limited experimental data did not permit a useful determination of the centrifugal distortion of Θ, $\Delta\Theta$, or the separate floating of the B and C rotational constants. Therefore the above rotational constants do not contain the contributions to the inertial defect that were presented for ArNO. The value of the structure angle, Θ , that arises from the above is 14.95 degrees but this is less well determined than that for ArNO because $\Delta\Theta$ was not evaluated.

One particularly interesting result from the spectra of NeNO is the fitted value of the quenching parameter, ε_2 = 122690.9 MHz. It should be recalled that the floated value of this parameter fell from about 95.5 GHz to ~ 80.5 GHz in ArNO when the matrix element of $L_{\pm}$ was floated. Since the latter matrix element could not be determined in NeNO, it was set to the scaled value from the NO spectrum. The value of ε_2 determined for NeNO may thus be a little too large. Even so, since the rotational contribution

(~(1/2)A in pure precession) is expected to be of a similar magnitude, the quenching interaction appears to be considerably larger in NeNO than ArNO. If repulsive forces dominate the value of this vibrationally averaged parameter, the increase for NeNO may be rationalised in terms of its tighter bound and less polarisable electron cloud.[1] Thus exchange repulsion effects might be expected to be larger.

The only assigned hyperfine structure was that associated with the R.F. transitions at the fine structure crossing. The failure to observe transitions from all the hyperfine energy levels meant that a separate determination of a, d and γ was not possible. However, when γ was fixed at a value corresponding to the complement of θ (close to the value of 90 - $\langle\theta^2\rangle$ in ArNO), the values of a and d needed to fit the hyperfine were again different from the NO values. Since the value of $\langle\theta^2\rangle$ will be larger than $\langle\theta\rangle$ the fitted values of a (124.6 MHz) and d (149.3 MHz) should be treated with caution. The hyperfine is a comparatively slow function of γ, however, (Figure 4.17) so once again it must be concluded that the hyperfine parameters of NO are very considerably perturbed upon complex formation. This adds further weight to the possibilities of a strong exchange repulsion or even a charge transfer interaction that were discussed at the end of Chapter 4. The former idea is supported by the increase in the quenching interaction and larger change in the hyperfine parameters that are observed for the neon complex.

Chapter 5 : References

1.H.Margenau and N.R.Kestner, Theory of Intermolecular Forces, Pergamon (1971)

2.H.Thuis,S.Stolte and J.Reuss, CP, 43, 351, (1979)

3.J.O.Hirschfelder,C.F.Curtiss and R.B.Bird, Molecular Theory of Gases and Liquids, Wiley (1964)

4.A.E.Barton,D.J.B.Howlett and B.J.Howard, MP, 41, 619, (1980)

5.J.M.Prout, Part II Thesis, Oxford University (1981)

6.S.E.Novick,P.B.Davies,S.J.Harris and W.Klemperer, JCP, 59, 2273, (1973)

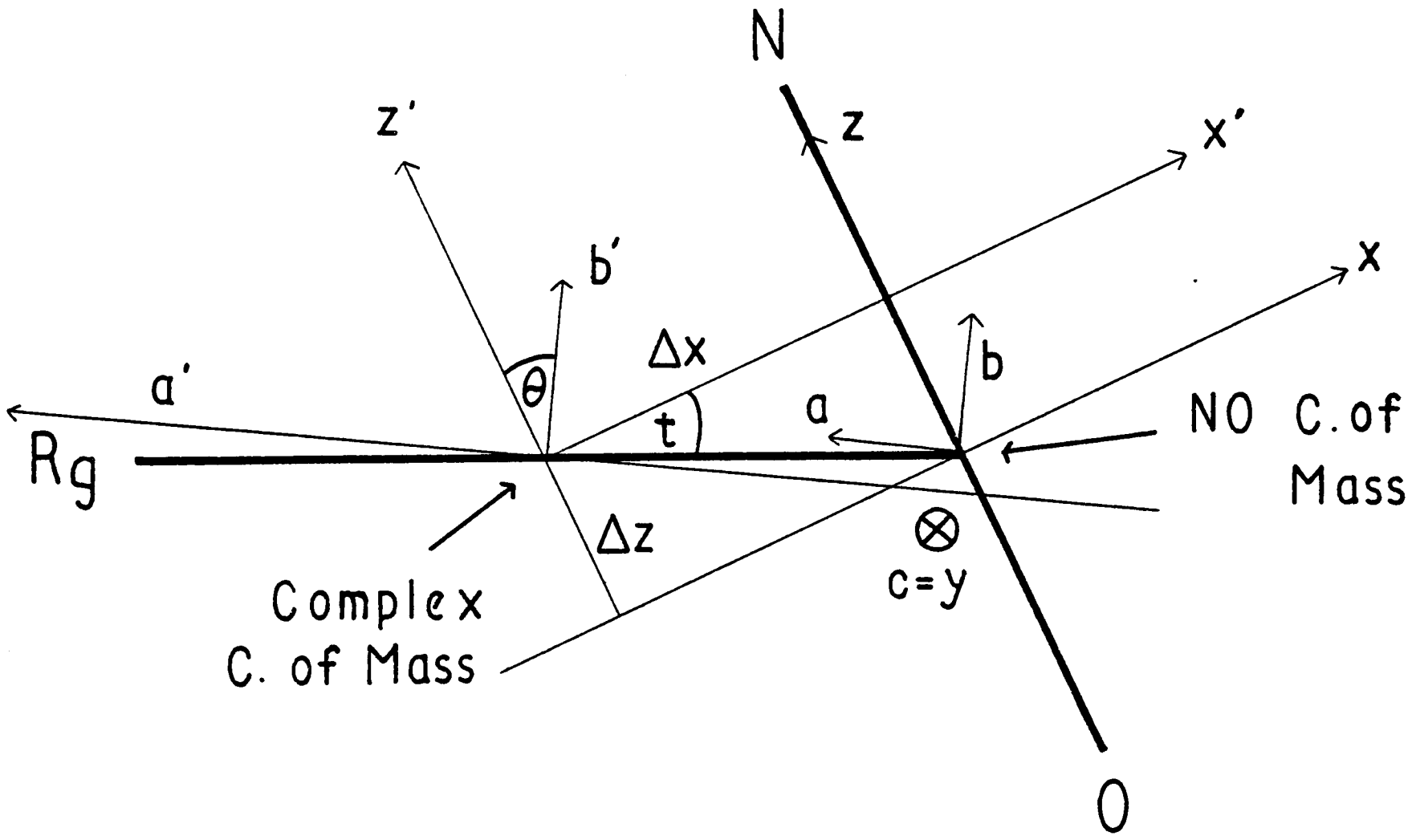
7.Handbook of Chemistry and Physics, Ed. R.C.Weast, CRC (1975)

APPENDICES

Appendix A3.1 : The Centre of Mass Transformation

In the fine structure Hamiltonian derived in Chapter 3 the internal electronic angular momenta of the NO diatom were related to the RgNO principal axis system by a rotation about the c- or y-axis. Although this treatment is correct for the electronic spin, a rigorous treatment of the orbital angular momentum should include the effects of the translational displacement between the NO and principal axis coordinate systems.

The diagram below illustrates this point with the two relevant pairs of axes; θ has been chosen to be positive and acute :



The primed and unprimed axis systems relevant to the electronic angular momenta are related by the centre of mass

transformation which may be defined by :

$$x' = x + \Delta x$$

$$y' = y$$

$$z' = z + \Delta z$$

From the definition of orbital and linear momenta :

$$\underset{\sim}{L} = \underset{\sim}{r} \times \underset{\sim}{p}$$

$$p_{\alpha i} = (h/i).d/d_{\alpha i}$$

the components of $\underset{\sim}{L}$ in the complex's centre of mass system may be expressed in the form :

$$L'_x = L_x - \Delta z.P_y$$

$$L'_y = L_y + \Delta z.P_x - \Delta x.P_z$$

$$L'_z = L_z + \Delta x.P_y$$

$$L'_a = L_a + (\Delta x.\mathrm{Sin}\theta + \Delta z.\mathrm{Cos}\theta).P_y$$

$$L'_b = L_b + (\Delta x.\mathrm{Cos}\theta - \Delta z.\mathrm{Sin}\theta).P_y$$

$$L'_c = L_c + \Delta z.P_x - \Delta x.P_z$$

Thus strictly the Hamiltonian expression of Equation (3.5.2) should refer to the components La', Lb' and Lc'. Hence in addition to the matrix elements presented in that chapter, a very large number of new terms and cross terms also exist. Although it was considered that the effect of these would be small, and their inclusion very tedious, it is worthwhile investigating what effect they might have on the spectrum.

Thus raising and lowering operators are introduced for P, the linear momentum, analogous to those of L :

$$p^{\pm} = P_x \pm i.P_y$$

The following commutation relations were shown to hold in the position representation :

$$\left[L_z, P_z\right] = \left[L^{\pm}, P^{\pm}\right] = 0$$
$$\left[L_z, P^{\pm}\right] = -\left[L^{\pm}, P_z\right] = \pm h.P^{\pm}$$
$$\left[L^{\pm}, P^{\mp}\right] = \pm 2.h.P_z$$

From these relations it may be deduced that the matrix elements of P are similar to those of L. In particular eigenstates of Lz will also be eigenstates of Pz. However, since the expectation value of the z component of linear momentum in any state must be zero, the matrix elements of Pz must obey the following :

$$\langle \eta' \Lambda' | P_z | \eta \Lambda \rangle = \delta_{\Lambda', \Lambda} \quad \text{and} \quad \eta' = | = \eta$$

In a similar way the commutation relations also show that the matrix elements of $P^{\pm}$ must connect the same eigenstates as those of the raising and lowering operators of L :

$$\langle \eta' \Lambda' | P^{\pm} | \eta \Lambda \rangle = \delta_{\Lambda', \Lambda \pm 1}$$

Therefore the effects of the centre of mass transformation only affect energies in the second order of perturbation theory or higher. In principal the extra matrix elements could be parameterised in a fashion analogous to those of L, and incorporated in the fine structure Hamiltonian together with the following relations for the translational displacements :

$$\Delta x = r.\mathrm{Cos}(t).\left\{m_{Rg}/m_{RgNO}\right\}$$
$$\Delta z = -r.\mathrm{Sin}(t).\left\{m_{Rg}/m_{RgNO}\right\}$$

Incorporating all cross terms to second order would, however, be a very awkward and involved exercise.

APPENDIX A3.2 The Direction Cosine Matrix

	X	Y	Z
X	$\cos(\alpha).\cos(\beta).\cos(\gamma)$ $-\sin(\alpha).\sin(\gamma)$	$\cos(\beta).\sin(\alpha).\cos(\gamma)$ $+\cos(\alpha).\sin(\gamma)$	$-\sin(\beta).\cos(\gamma)$
Y	$-\cos(\beta).\cos(\alpha).\sin(\gamma)$ $-\sin(\alpha).\cos(\gamma)$	$-\cos(\beta).\sin(\alpha).\sin(\gamma)$ $+\cos(\alpha).\cos(\gamma)$	$\sin(\beta).\sin(\gamma)$
Z	$\sin(\beta).\cos(\alpha)$	$\sin(\beta).\sin(\alpha)$	$\cos(\beta)$

Appendix 3.3 : The Definition, Construction and Manipulation of Spherical Tensor Operators

Many calculations, particularly those involving the coupling of several angular momenta, are simplified by transforming the operators from a cartesian to a spherical tensor basis. The latter incorporate the transformation properties of the spherical harmonics and such a tensor of the first rank may be defined by its components :

$$T^1_1(\underset{\sim}{A}) = -1/\sqrt{2}(A_x + iA_y)$$
$$T^1_0(\underset{\sim}{A}) = A_z$$
$$T^1_{-1}(\underset{\sim}{A}) = 1/\sqrt{2}(A_x - iA_y)$$

The space-fixed component of a general tensor of rank, k, is denoted $T^k_p(\underset{\sim}{A})$. For two such tensors of like rank the scalar product is defined as :

$$T^k(\underset{\sim}{A}).T^k(\underset{\sim}{B}) = \sum_p (-1)^p . T^k_p(\underset{\sim}{A}) . T^k_{-p}(\underset{\sim}{B})$$

In a similar way tensors of higher rank may be constructed from the form of the tensor product :

$$T^k_p(\underset{\sim}{A},\underset{\sim}{B}) = (-1)^{k1-k2+p}.(2k+1)^{1/2} \sum_{p1,p2} \begin{pmatrix} k1 & k2 & k \\ p1 & p2 & -p \end{pmatrix} x$$
$$x\ T^{k1}_{p1}(\underset{\sim}{A}) . T^{k2}_{p2}(\underset{\sim}{B})$$

The symbol in large brackets is the highly symmetric 3-j symbol as defined by Brink and Satchler or Edmonds.

The M_J dependence of the matrix element of a spherical tensor operator may be factorised off using the following form of the Wigner-Eckart Theorem :

$$\langle \gamma' J' M_J' | T^k_p(\underset{\sim}{A}) | \gamma J M_J \rangle = (-1)^{J'-M_J'} \begin{pmatrix} J' & k & J \\ -M_J' & p & M_J \end{pmatrix} \times \langle \gamma' J' || T^k(\underset{\sim}{A}) || \gamma J \rangle$$

Methods for evaluating the resulting reduced matrix element by considering a specific component, p, are illustrated in the text of Chapter 3. The matrix element in a coupled representation of the scalar product of two tensor operators may be expressed in terms of such reduced matrix elements and a 6-j symbol (also defined by Brink and Satchler) :

$$\langle \gamma' J_1' \; J_2' \; J' M' | T^k(\underset{\sim}{A}) . T^k(\underset{\sim}{B}) | \gamma \; J_1 \; J_2 \; J M \rangle$$

$$= (-1)^{J_1 + J_2' + J} . \delta_{J,J'} . \delta_{M,M'} . \begin{pmatrix} J' & J_2' & J_1' \\ k & J_1 & J_2 \end{pmatrix} \times \quad \text{6-j Symbol}$$

$$\times \sum_{\gamma''} \langle \gamma' J_1' || T^k(\underset{\sim}{A}) || \gamma'' J_1 \rangle \langle \gamma'' J_2' || T^k(\underset{\sim}{B}) || \gamma J_2 \rangle$$

The following expressions indicate the relationship between the space- and molecule-fixed components of a spherical tensor :

$$T^k_p(\underset{\sim}{A}) = \sum_q \mathcal{D}^{k\,*}_{p,q}(\omega) . T^k_q(A)$$

$$T^k_q(\underset{\sim}{A}) = \sum_p . (-1)^{p-q} . \mathcal{D}^{k\,*}_{-p,-q}(\omega) . T^k_p(A)$$

The properties and matrix elements of the rotation operators that arise in the above forms are given in Brink and Satchler.

Appendix A3.4 : The Magnetic Hyperfine Matrix Elements.

$$\langle J'\ K_a'\ \Lambda'\ \Sigma'\ I\ F|H_{mag}|J\ K_a\ \Lambda\ \Sigma\ I\ F\rangle = (-1)^{J+I+F+J'-K_a'}$$

$$\times \begin{Bmatrix} F & I & J' \\ 1 & J & I \end{Bmatrix} \times \{(2J+1)(2J'+1)\}^{\frac{1}{2}} \times \{I(I+1)(2I+1)\}^{\frac{1}{2}} \times$$

$$\times \sum_q \begin{pmatrix} J' & 1 & J \\ -K_a' & q & K_a \end{pmatrix} \times$$

$$+ \delta_{\Lambda,\Lambda'}.\delta_{\Sigma,\Sigma'} \times a \times \Lambda \times \begin{Bmatrix} -1/\sqrt{2}.\mathrm{Cos}(\theta).\delta_{q,1} \\ + \quad \mathrm{Sin}(\theta).\delta_{q,0} \\ +1/\sqrt{2}.\mathrm{Cos}(\theta).\delta_{q,-1} \end{Bmatrix}$$

$$+ \delta_{\Lambda,\Lambda'} \times b_F \times \{S(S+1)(2S+1)\}^{\frac{1}{2}} \times (-1)^{S-\Sigma'} \times$$

$$\begin{bmatrix} 1/\sqrt{2}.\mathrm{Cos}(\theta) \begin{pmatrix} S & 1 & S \\ -\Sigma' & 0 & \Sigma \end{pmatrix} \times \delta_{q,-1} \\ + \mathrm{Sin}^2(\theta/2) \begin{pmatrix} S & 1 & S \\ -\Sigma' & -1 & \Sigma \end{pmatrix} \times \delta_{q,-1} \\ + \mathrm{Cos}^2(\theta/2) \begin{pmatrix} S & 1 & S \\ -\Sigma' & 1 & \Sigma \end{pmatrix} \times \delta_{q,-1} \\ \\ -1/\sqrt{2}.\mathrm{Cos}(\theta) \begin{pmatrix} S & 1 & S \\ -\Sigma' & -1 & \Sigma \end{pmatrix} \times \delta_{q,0} \\ + \quad \mathrm{Sin}(\theta) \begin{pmatrix} S & 1 & S \\ -\Sigma' & 0 & \Sigma \end{pmatrix} \times \delta_{q,0} \\ +1/\sqrt{2}.\mathrm{Cos}(\theta) \begin{pmatrix} S & 1 & S \\ -\Sigma' & 1 & \Sigma \end{pmatrix} \times \delta_{q,0} \\ \\ + \mathrm{Cos}^2(\theta/2) \begin{pmatrix} S & 1 & S \\ -\Sigma' & -1 & \Sigma \end{pmatrix} \times \delta_{q,1} \\ -1/\sqrt{2}.\mathrm{Cos}(\theta) \begin{pmatrix} S & 1 & S \\ -\Sigma' & 0 & \Sigma \end{pmatrix} \times \delta_{q,1} \\ + \mathrm{Sin}^2(\theta/2) \begin{pmatrix} S & 1 & S \\ -\Sigma' & 1 & \Sigma \end{pmatrix} \times \delta_{q,1} \end{bmatrix}$$

Continued Overleaf.

$$+\ \delta_{\Lambda,\Lambda'} \times c/3 \times \{S(S+1)(2S+1)\}^{\frac{1}{2}} \times (-1)^{S-\Sigma'} \times$$

$$\left[\begin{array}{ll}
-\sin^2(\theta/2) & \begin{pmatrix} S & 1 & S \\ -\Sigma' & -1 & \Sigma \end{pmatrix} \times \delta_{q,-1} \\
+\sqrt{2}.\cos(\theta) & \begin{pmatrix} S & 1 & S \\ -\Sigma' & 0 & \Sigma \end{pmatrix} \times \delta_{q,-1} \\
-\cos^2(\theta/2) & \begin{pmatrix} S & 1 & S \\ -\Sigma' & 1 & \Sigma \end{pmatrix} \times \delta_{q,-1} \\
+1/\sqrt{2}.\cos(\theta) & \begin{pmatrix} S & 1 & S \\ -\Sigma' & -1 & \Sigma \end{pmatrix} \times \delta_{q,0} \\
+\quad 2.\sin(\theta) & \begin{pmatrix} S & 1 & S \\ -\Sigma' & 0 & \Sigma \end{pmatrix} \times \delta_{q,0} \\
-1/\sqrt{2}.\cos(\theta) & \begin{pmatrix} S & 1 & S \\ -\Sigma' & 1 & \Sigma \end{pmatrix} \times \delta_{q,0} \\
-\quad \cos^2(\theta/2) & \begin{pmatrix} S & 1 & S \\ -\Sigma' & -1 & \Sigma \end{pmatrix} \times \delta_{q,1} \\
-\quad \sqrt{2}.\cos(\theta) & \begin{pmatrix} S & 1 & S \\ -\Sigma' & 0 & \Sigma \end{pmatrix} \times \delta_{q,1} \\
-\quad \sin^2(\theta/2) & \begin{pmatrix} S & 1 & S \\ -\Sigma' & 1 & \Sigma \end{pmatrix} \times \delta_{q,1}
\end{array}\right]$$

$$+\ \delta_{\Lambda;\Lambda+2} \times d \times \{S(S+1)(2S+1)\}^{\frac{1}{2}} \times (-1)^{S-\Sigma'} \times$$

$$\left[\begin{array}{ll}
+\cos^2(\theta/2) & \begin{pmatrix} S & 1 & S \\ -\Sigma' & -1 & \Sigma \end{pmatrix} \times \delta_{q,-1} \\
1/\sqrt{2}.\cos(\theta) & \begin{pmatrix} S & 1 & S \\ -\Sigma' & -1 & \Sigma \end{pmatrix} \times \delta_{q,0} \\
+\sin^2(\theta/2) & \begin{pmatrix} S & 1 & S \\ -\Sigma' & -1 & \Sigma \end{pmatrix} \times \delta_{q,1}
\end{array}\right]$$

$$+\ \delta_{\Lambda;\Lambda-2} \times d \times \{S(S+1)(2S+1)\}^{\frac{1}{2}} \times (-1)^{S-\Sigma'} \times$$

$$\left[\begin{array}{ll}
+\sin^2(\theta/2) & \begin{pmatrix} S & 1 & S \\ -\Sigma' & 1 & \Sigma \end{pmatrix} \times \delta_{q,-1} \\
-1/\sqrt{2}.\cos(\theta) & \begin{pmatrix} S & 1 & S \\ -\Sigma' & 1 & \Sigma \end{pmatrix} \times \delta_{q,0} \\
+\cos^2(\theta/2) & \begin{pmatrix} S & 1 & S \\ -\Sigma' & 1 & \Sigma \end{pmatrix} \times \delta_{q,1}
\end{array}\right]$$

Appendix A3.5 : The Electric Quadrupole Matrix Elements.

$$\langle J'\ K_a'\ \Lambda'\ \Sigma'\ I\ F|H_{quad}|J\ K_a\ \Lambda\ \Sigma\ I\ F\rangle =$$

$$\delta_{\Sigma,\Sigma'} \times \begin{Bmatrix} F & I & J' \\ 2 & J & I \end{Bmatrix} \times \{(2J+1)(2J'+1)\}^{\frac{1}{2}} \times 1/2 \times \left\{\frac{(2I+1)(2I+2)(2I+3)}{2I(2I-1)}\right\}^{\frac{1}{2}}$$

$$\times \sum_q (-1)^{I+F-K_a'} \times \begin{pmatrix} 2 & J & J' \\ -q & -K_a & K_a' \end{pmatrix} \times$$

$$+\delta_{q,-2} \begin{pmatrix} \delta_{\Lambda,\Lambda'}.\sqrt{(3/8)}.\mathrm{Cos}^2(\theta).eQq_0/2 \\ +\ \delta_{\Lambda;\Lambda+2}.\sqrt{(1/24)}.\mathrm{Cos}^4(\theta/2).eQq_2 \\ +\ \delta_{\Lambda;\Lambda-2}.\sqrt{(1/24)}.\mathrm{Sin}^4(\theta/2).eQq_2 \end{pmatrix}$$

$$+\delta_{q,-1} \begin{pmatrix} \delta_{\Lambda,\Lambda'}.\sqrt{(3/2)}.\mathrm{Sin}(\theta).\mathrm{Cos}(\theta).eQq_0/2 \\ -\ \delta_{\Lambda;\Lambda+2}.\sqrt{(1/24)}.\mathrm{Cos}(\theta)\{\mathrm{Sin}(\theta)-1\}.eQq_2/2 \\ -\ \delta_{\Lambda;\Lambda-2}.\sqrt{(1/24)}.\mathrm{Cos}(\theta)\{\mathrm{Sin}(\theta)+1\}.eQq_2/2 \end{pmatrix}$$

$$+\delta_{q,0} \begin{pmatrix} \delta_{\Lambda,\Lambda'}.1/2\{3\mathrm{Sin}^2(\theta)-1\}.eQq_0/2 \\ +\ \delta_{\Lambda;\Lambda+2}.\sqrt{(3/8)}.\mathrm{Cos}^2(\theta).\sqrt{(1/24)}.eQq_2 \\ +\ \delta_{\Lambda;\Lambda-2}.\sqrt{(3/8)}.\mathrm{Cos}^2(\theta).\sqrt{(1/24)}.eQq_2 \end{pmatrix}$$

$$+\delta_{q,+1} \begin{pmatrix} -\delta_{\Lambda,\Lambda'}.\sqrt{(3/2)}.\mathrm{Sin}(\theta).\mathrm{Cos}(\theta).eQq_0/2 \\ +\ \delta_{\Lambda;\Lambda+2}.\sqrt{(1/24)}.\mathrm{Cos}(\theta)\{1+\mathrm{Sin}(\theta)\}.eQq_2/2 \\ +\ \delta_{\Lambda;\Lambda-2}.\sqrt{(1/24)}.\mathrm{Cos}(\theta)\{\mathrm{Sin}(\theta)-1\}.eQq_2/2 \end{pmatrix}$$

$$+\delta_{q,+2} \begin{pmatrix} \delta_{\Lambda,\Lambda'}.\sqrt{(3/8)}.\mathrm{Cos}^2(\theta).eQq_0/2 \\ +\ \delta_{\Lambda;\Lambda+2}.\sqrt{(1/24)}.\mathrm{Sin}^4(\theta/2).eQq_2 \\ +\ \ ;\ -2.\sqrt{(1/24)}.\mathrm{Cos}^4(\theta/2).eQq_2 \end{pmatrix}$$